Nanostructured Optical Fibre for use as Miniature Surface-enhanced Raman Scattering Sensors

A thesis submitted for the degree of

Doctor of Philosophy

by

Daniel Joshua White

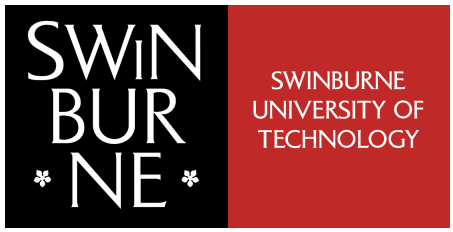

Centre for Atom Optics and Ultrafast Spectroscopy

Faculty of Engineering and Industrial Sciences

Swinburne University of Technology

Melbourne, Australia

October 2, 2008

"No effect that requires more than ten percent accuracy in measurement is worth investigating."

— *Walther Nernst (1864-1941)*

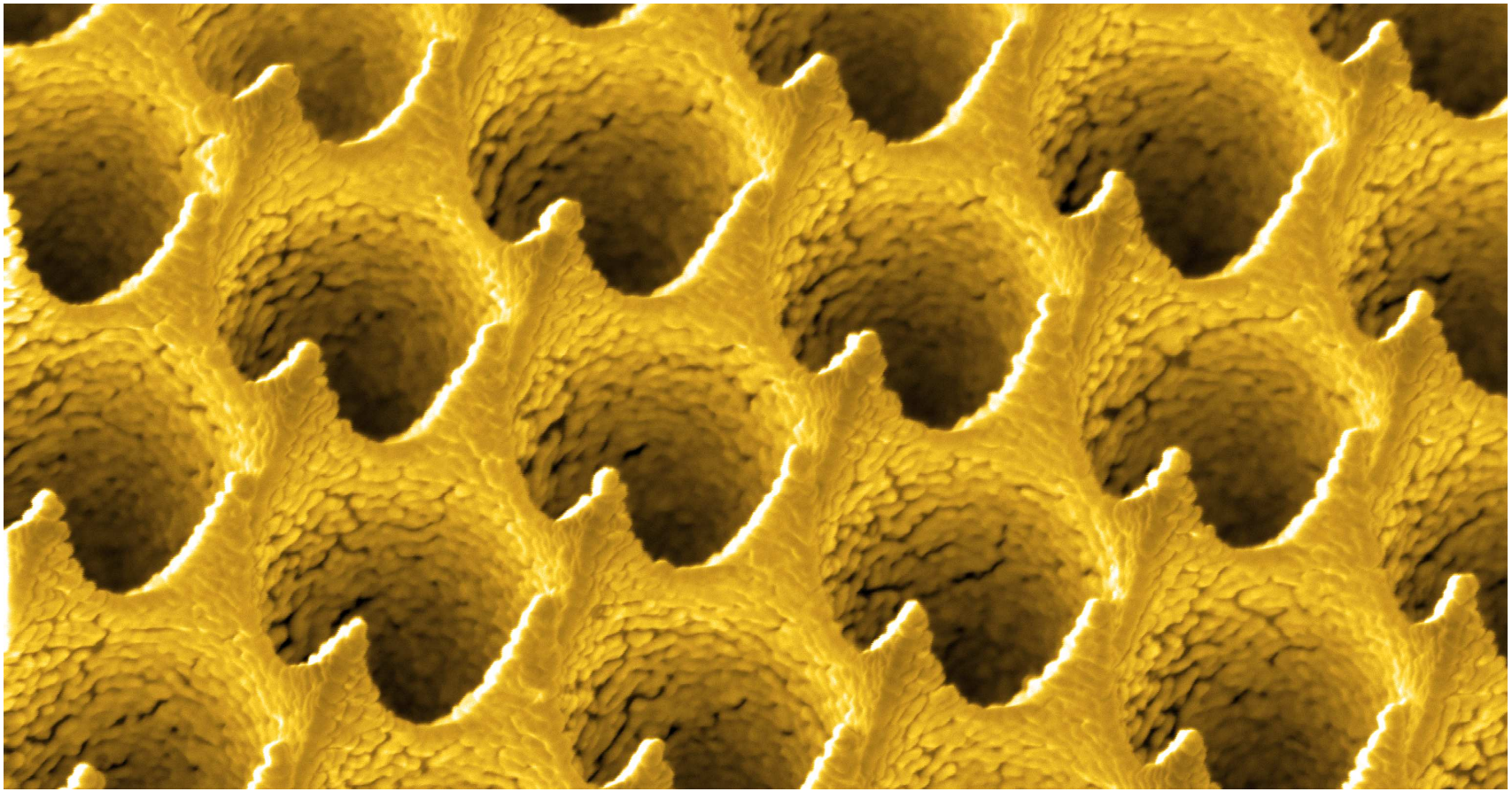

Fig. 1: False colour, high resolution SEM image of an etched nanostructured optical fibre with a metal coating. Field of view is approximately 1 μm $\times$ 2 μm.

Abstract

Surface-enhanced Raman scattering (SERS) is a powerful spectroscopic tool for detecting low concentrations of many substances. The SERS effect occurs when a Raman-active molecule interacts with the electromagnetic (EM) field generated by surface plasmon excitations in a metal surface having nanoscale structural features. As a result of the interaction, the typically weak Raman scattering is amplified by many orders of magnitude. Despite its usefulness, one of the factors that has so far prevented SERS from moving out of the laboratory and into the marketplace is a lack of affordable and reliable nanostructured substrates.

Since the discovery of the SERS effect over 30 years ago, many different techniques have been developed for producing the necessary substrate structures. Common techniques used include mechanical surface roughening, colloidal metal solutions, metal island films and lithographic techniques. While all produce SERS capable surfaces they either rely on random processes (which limit sample-to-sample reproducibility) or expensive manufacturing equipment. Both of these issues prevent cost effective commercialisation.

A novel alternative, which is investigated in this thesis, is to use an optical fibre based system. The fibres presented in this work are based on highly modified medical imaging fibres. These fibres consist of a fused bundle of single-mode fibres ("pixels") drawn in such a way that each fibre maintains its position along the length of the bundle. Previous works have shown that a selective chemical etchant can be used to erode the cores of these fibres leaving an array of wells. The work presented in this thesis shows that, by drawing the imaging fibre until the spacing between the cores is

of the order of hundreds of nanometres, the structures formed after etching are of a suitable scale for SERS. The glass itself is incapable of producing surface plasmons, so in order to generate the SERS functionality, the structures are coated with a thin layer of metal.

Initial fibre SERS sensors were produced by manually drawing commercially available imaging fibres to smaller diameters. As a result of the draw process, the initial inter-core spacing (the distance between two adjacent pixels) was reduced from approximately 4 μm to 150 - 650 nm. The cleaved tips of the fibres were then etched using a modified buffered hydrofluoric acid solution which resulted in the formation of nanostructures. The structures were then coated with silver and the fibre immersed in a solution of thiophenol for SERS testing. Due to difficulties in determining exactly how many molecules contributed to the SERS signal, an accurate measure of the SERS enhancement factor cannot be made. However, by estimating the molecular coverage density, an enhancement figure of $10^{5.3}$ to $10^{5.5}$ can be produced.

Although the manual drawing technique proved successful, lack of reproducibility meant that it was not suitable for large-scale commercial manufacturing. Before an attempt at manufacturing could be conducted, the parameters for the draw process (in particular temperature) needed to be determined. As the fibre is drawn by heating it to a high temperature in a furnace, it was necessary to understand the effects of the resultant diffusion of dopants within the fibre structure. To do this, a computer simulation was performed. The simulation package models a unit cell within the fibre structure and calculates firstly how the temperature affects the distribution of dopants and secondly, what the structures produced after etching would look like. It was found that in order to produce suitable nanostructures on the tips of the fibres, the diffusion length of the dopants must be less than 25% of the inter-core spacing. Knowing the maximum allowed diffusion length, means the maximum temperatures and heating times for manufacturing can be calculated.

After determining the desirable manufacturing conditions, a number of production attempts using commercial fibre drawing towers were made. Ultimately, a short length of suitable fibre was produced allowing a full characterisation of the SERS capabilities of the fibre to be conducted. It was found that despite the high reproducibility of the structures, for an optimised sensor, the SERS signal counts still varied by approximately 40% from sample to sample. Careful investigations of the surfaces indicated this variability is most likely due to the nature of the metal coating applied

rather than the fibre structures themselves. As such, it was found that to use sensors such as this for quantitative analysis, a form of internal SERS calibration is required. This was accomplished by exposing the sensor to a molecule of known concentration and measuring the signal intensity. After calibration, it was found the sample to sample variability dropped to approximately 8%.

As a practical demonstration of the use of the SERS fibres, experiments on the detection of glucose, CEES (a simulant for the nerve agent HD mustard) and chlorsulphuron (a commonly used herbicide), were conducted. To test the procedures for gathering quantitative results, the sensors used in the experiment were calibrated by applying a monolayer of 1-decanethiol. In addition to providing the calibration spectrum, this molecule also aids in bringing the target analytes close to the active surface. Characteristic spectral lines could be easily identified from solutions of 5,000 ppm glucose, 549 ppm CEES and 10,000 ppm chlorsulfuron. Results of these experiments also indicate that the SERS fibres are reversible, that is, capable of tracking both increasing and decreasing concentrations. While the sensitivity is, at this stage, low when compared to other substrate formats, the speed and ease with which measurements can be taken and the potential for further optimisation of the fibre's surface both indicate the significant potential of this technique.

Acknowledgements

This project started in 2004 with only my two supervisors and myself. Over the years though, the team grew and grew and as such, I have a fair few people to thank:

My family - parents Shirley and Alan, my sister Rebecca, my grandparents and my extended family. Without your encouragement and support throughout all my years of education, none of this would have been possible.

Dr. Paul Stoddart and Dr. Alex Mazzolini - my supervisors. Despite my previously limited experience in physics research, they took me in, taught me the ropes and supported me financially.

The folks in the Applied Optics research group - the successor to the Centre for Imaging and Applied Optics (CIAO) and now a part of the Centre for Atom Optics and Ultrafast Spectroscopy (CAOUS). Special thanks to Prof. Peter Cadusch for his help with all things mathematical. Thanks also to the other members: Jack, Annelene, Keith, Elena, Sasani and Felix for their support.

The crew at CAOUS: Prof. Peter Hannaford, centre leader and Tatiana Tchernova and Sharon Jesson, administrative staff. Thanks also to Dr. James Wang for assistance with the chromium coating. Extra thanks to Mark Kivinen, our workshop supervisor for building all those special items.

Mircea Petre and Sorin Theodorescu at OptoTech for the laser systems. Over the course of the project we were fortunate enough to be there during the development of the lasers and as such, enjoyed the ability to design systems to our exact specifications.

Hans Brinkies at the Industrial Research Institute of Swinburne (IRIS) for the polishing units and the Zeiss electron microscope.

Phil Francis and Yuxun Cao at the Royal Melbourne Institute of Technology (RMIT) for their help with the Philips electron microscope and the polishing units.

Finlay Shanks at Monash University for assistance with the Renishaw RM2000 Raman microscope.

Dr. Colin Cook at the Department of Primary Industries for his support on the chemistry side of the project and the use of the Renishaw InVia Raman microscope.

Dr. Katja Digweed, Dr. Justin Digweed, Ron Bailey, Peter Henry, Prof. John Canning and all the staff at the OFTC in the University of Sydney for their help during the nanostructured optical fibre manufacturing attempts.

Hiroki Sekiya and all the engineers and staff at Fujikura Asia Ltd for the imaging fibre modifications and the successful production of nanostructured optical fibres.

David Henderson, Tom Szafranski and the staff at Diamond Australia for their assistance in designing, manufacturing and polishing the ferrules.

Kaushal Vora at Minifab for his help with the initial hydrofluoric acid work.

Dr. Stuart Rumble at Lastek for his help in setting up the Raman microscopes and spectrometers.

Dr. Narelle Brack at La Trobe University for the use of the TOF-SIMS.

Last be certainly not least: to all my fellow students at the Swinburne Optics and Laser Laboratories during the years I was there. Far too many to mention you all but particular thanks go to Dave, Jack, Annelene, Michael, Peter, Linda, Tra My, Chris and Brendan who were around at the end when things got really stressful. Thanks to these guys, I found there's nothing that can't be fixed by stopping work and going to the pub! On that topic, thanks also to the crew at Mario's Coffee and Haddon's Bar for all those drinks.

Daniel White
Melbourne, Australia
October 2, 2008

Declaration

I, Daniel Joshua White, declare that this thesis entitled:

"Nanostructured Optical Fibre for use as Miniature Surface-enhanced Raman Scattering Sensors"

is my own work and has not been submitted previously, in whole or in part, in respect of any other academic award.

Daniel Joshua White

Centre for Atom Optics and Ultrafast Spectroscopy
Faculty of Engineering and Industrial Sciences
Swinburne University of Technology
Melbourne, Australia

Dated this day, October 2, 2008

Contents

List of Figures

List of Tables

Glossary

AFM	Atomic Force Microscope
BHF	Buffered Hydrofluoric Acid
CCD	Charge Coupled Device
CEES	2-chloroethyl ethyl sulfide
cps/mW	Counts-per-second per milliwatt
D_L	Diffusion length
E	SERS Enhancement Factor
EM	Electromagnetic
EFL	Effective Focal Length
FON	Film-on-Nanosphere
GCMS	Gas Chromatography - Mass Spectroscopy
HCl	Hydrochloric Acid
HDPE	High Density Polyethylene
HF	Hydrofluoric Acid
HJY	Horiba Jobin-Yvon Modular Raman Microscope
FWHM	Full-width half-max
I_C	Inter-core spacing
$\overline{I_{tp}}$	Average intensity of thiophenol peaks
KJL	Kurt J. Lesker Coating Unit
LCMS	Liquid Chromatography - Mass Spectroscopy
LSPR	Localised Surface Plasmon Resonance
MCVD	Modified Chemical Vapor Deposition
n	Refractive Index
N.A.	Numerical Aperture
NRS	Normal Raman Spectroscopy
NSL	Nanosphere Lithography
OFTC	Optical Fibre Technology Centre

PP	Polypropylene
ppm	Parts-per-million
SAM	Self-assembled Monolayer
SEM	Scanning Electron Microscope
SERS	Surface Enhanced Raman Spectroscopy
TEC	Thermo-electric Cooler
TOF-SIMS	Time-of-flight Secondary Ion Mass Spectrometer
ξ_d	Smearing ratio (D_L to I_C ratio)

Chapter 1

Project Motivation

1.1 Vibrational Spectroscopy

The work presented in this thesis is based around Raman spectroscopy - one of the forms of vibrational spectroscopy. Before discussing Raman spectroscopy however, it is important to first introduce molecular vibrational states. When a photon is incident upon a molecule, it may excite the molecule to a different vibrational state. In almost all cases, the molecule will relax back to its original ground state. When this occurs, the molecule scatters a photon of the same energy that was absorbed. This is called Rayleigh scattering (Fig. 1.1 (a)). However, depending on the molecule and the energy of the incident photon, this may not always be the case.

Figure 1.1 (b) shows the process of infra-red (IR) absorption. When IR absorption occurs, the photon directly excites a vibrational level and is converted solely to vibrational energy. The condition for IR absorption to occur at a particular energy is a permissable change in the dipole moment of the molecule [Hof, 2003]. As the photon energy is completely absorbed, no scattering occurs. Thus to gather an IR spectra, the transmittance of the material over a range of IR frequencies is recorded. The energies of the bands that are absorbed by the material correlate to the energies of the vibrational states.

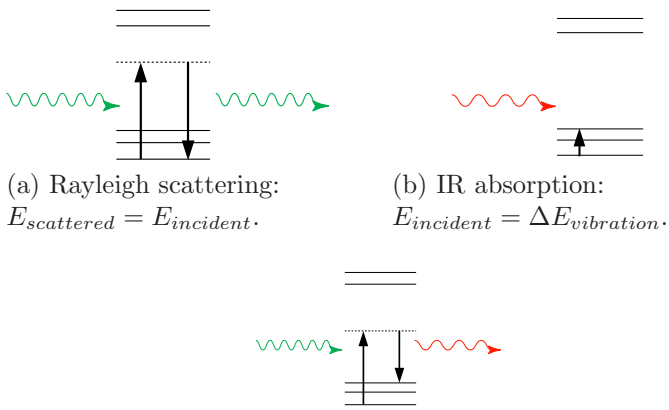

(a) Rayleigh scattering:
$E_{scattered} = E_{incident}$.

(b) IR absorption:
$E_{incident} = \Delta E_{vibration}$.

(c) Raman scattering:
$E_{scattered} = E_{incident} - \Delta E_{vibration}$.

Fig. 1.1: Vibrational processes: solid horizontal lines indicate possible vibrational modes, dotted lines indicate virtual modes.

Figure 1.1 (c) shows the Raman process. In this case, the incident photon energy is higher than the energy required for IR absorption. Instead, the molecule is excited to a virtual electronic level which spontaneously relaxes to an excited vibrational state. In the process, a new photon is emitted. However, because the molecule has now moved to an excited state and absorbed some energy, the energy of the scattered photon is lower than that of the incident photon [Nafie, 2001].

As opposed to IR absorption which relies on a direct change in the dipole moment of a molecule, the Raman transition instead involves a change in the polarizability. The net effect of this change is an *induced* dipole moment which, like IR absorption, then leads to a change in vibrational states [Hof, 2003]. However, because of the different processes involved, not all IR-active transitions are Raman-active and vice versa.

It should be noted that there can be two possible ways in which a Raman transition can occur (Fig. 1.2). In the case where a molecule starts in the ground state and moves to an excited state, it has absorbed energy ($\Delta E_{vibration}$) and so the photon scattered is of a lower energy and a longer wavelength ($E_{scattered} = E_{incident}$ - $\Delta E_{vibration}$). This process results in what is referred to as "Stokes" radiation (Fig. 1.2a). The opposite effect, where a molecule starts in an excited vibrational state and moves to the ground state is also possible ($E_{scattered} = E_{incident} + \Delta E_{vibration}$). In this instance, the scattered photon will have more energy and be of a shorter wavelength (Fig. 1.2b). However, this "anti-Stokes" radiation is usually considerably weaker than Stokes radiation due to

the relatively small excited state population at room temperature. As the vibrational states of a molecule are dependent on the atomic composition and arrangement, every Raman-active substance scatters its own unique "signature" spectrum.

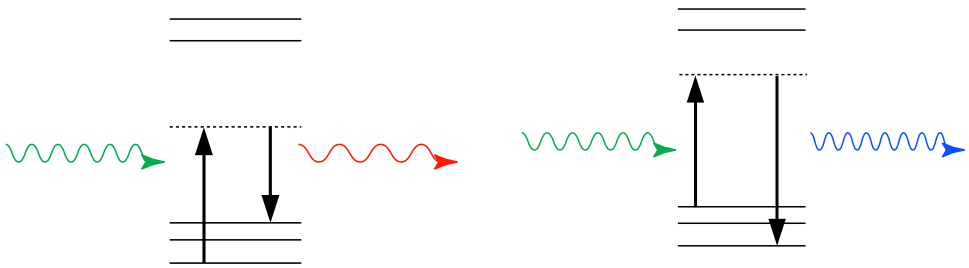

(a) Stokes radiation:
$E_{scattered} = E_{incident} - \Delta E_{vibration}$.

(b) Anti-stokes radiation:
$E_{scattered} = E_{incident} + \Delta E_{vibration}$.

Fig. 1.2: The two forms of Raman scattering: solid lines indicate possible vibrational modes, dotted lines indicate virtual modes.

As a spectroscopic technique, Raman scattering has attracted a great deal of interest as it provides rich spectral data with information on not only which atomic bonds are present but also what configuration they are in. However, one of the drawbacks of the technique is that Raman scattering is a very weak process. Typical scattering cross-sections are on the order of 10^{-29} to 10^{-32} cm^{-2} which is some 13 to 16 orders of magnitude lower than a typical fluorescence cross-section [Baker and Moore, 2005]. To make use of normal Raman scattering (NRS) therefore, requires high laser powers to generate a strong signal or alternatively, long spectral collection times. While these conditions can be met for certain bulk samples, applying them to trace-level detection remains difficult.

1.2 Surface-enhanced Raman Spectroscopy

Surface-enhanced Raman scattering (SERS) was first observed in 1974 by Fleishmann *et al.* who noted the increase in the Raman scattering from pyridine adsorbed on electrochemically roughened silver electrodes [Fleischmann et al., 1974]. A similar result was also noted by Albrecht [Albrecht and Creighton, 1977]. Later research showed that this increase was not due to the additional surface area of the electrode, as was first postulated, but to an interaction between the molecule under investigation and the electromagnetic field associated with the localised surface plasmon resonance generated by nanoscale metal particles when the two are in close contact [Jeanmaire and Van Duyne, 1977; Moskovits, 1978]. Today, the effect is largely understood to comprise both electromagnetic and chemical interactions between the molecule and the metal nanoparticles.

The electromagnetic effect can, in essence, be thought of as consisting of two complimentary conditions which both depend on the surface plasmon field formed around metal nanoparticles [Baker and Moore, 2005; Moskovits, 2005]. Firstly, the incident electromagnetic field that the molecule is exposed to is enhanced by the superposition of the localised plasmon field (generated by the nanoparticles) and the incident laser light. Secondly, the Raman photons emitted by the molecule are also enhanced by the field in the same manner. Thus it is the amplification of the Raman signal by the nanoparticles that results in the SERS spectrum (Fig. 1.3). Because the localised plasmon field is very short range (field strength drops as r^{-12}), the SERS effect only occurs for molecules either on the surface of the nanoparticle, or within a few nanometres of it [Baker and Moore, 2005]. However, some recent studies indicate interaction ranges of around 30 nm are possible [Liu et al., 2006].

The surface plasmon resonance of a particular metal depends on the electromagnetic properties of the material. Ideally, the peak surface plasmon absorption (the localised surface plasmon resonance - LSPR) should lie between the laser wavelength and the expected Raman bands [Haynes et al., 2005]. When using laser excitation in the visible spectrum, silver has been shown to provide the highest plasmon field strength of all metals [Schatz and Van Duyne, 2002]. Gold and copper have also shown plasmon resonances but have considerably lower field strengths. Despite the high field strength, issues such as film degradation, bio-compatibility and resonant enhancement can often override the choice of silver for a sensing application. Additionally, the size and shape

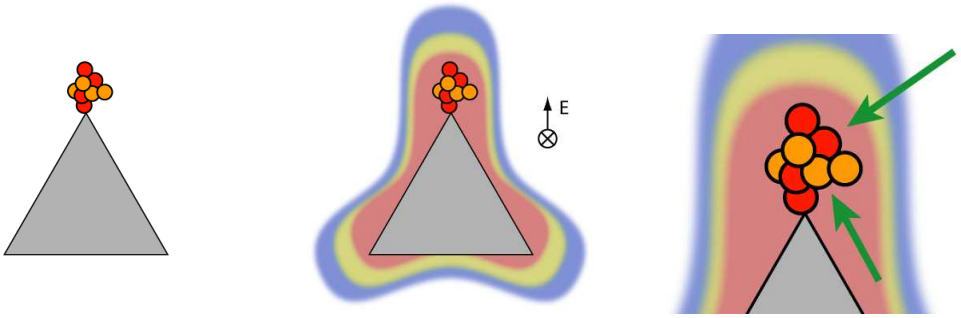

(a) A molecule is placed in close contact with a nanoparticle.

(b) The laser light generates a surface plasmon field around the nanoparticle (field pattern adapted from Hao and Schatz, 2004).

(c) The molecule is exposed to both the laser and the field energy.

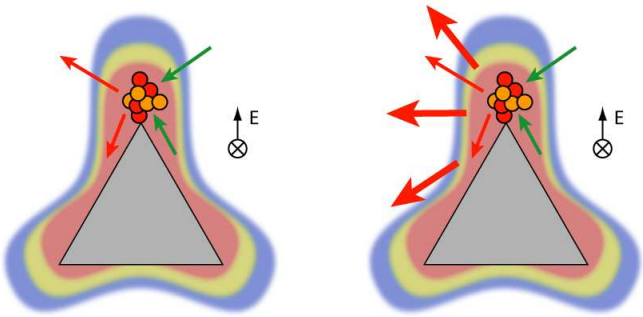

(d) Raman photons are scattered in all directions.

(e) The SERS signal is formed when the Raman photons outcouple energy from the plasmon field.

Fig. 1.3: Schematic representation of the electromagnetic SERS process.

of the metal nanoparticles also affect the LSPR and thus, to obtain the highest field strength for a given laser excitation, these parameters must also be tuned.

While the size, shape and EM properties of a metal particle are critical factors in generating an LSPR, it has also been shown that an additional gain in the surface plasmon strength may be generated by the long range interactions among an *array* of particles. Zou *et al.* published a report indicating that, in theory, an array of nanoparticle silver spheres in close contact produce a peak EM field approximately 70 times more intense than a single particle of the same dimensions [Zou and Schatz, 2005]. Thus, if a surface can produce arrays of nanoparticle sites, it may be possible to further increase the plasmon strength and increase the SERS enhancement factor.

As a side note, it is proposed that in addition to the EM process, there also exists a chemical process which can produce an additional enhancement factor. This enhancement is due to a charge-transfer between the metal surface and the Raman molecule [Otto, 2005; Smith and Rodger, 2002]. The process is still not fully understood but it is believed that molecules adsorbed on the metal surface experience an induced change in polarizability (ie. induced dipole moment) by the transfer of electrons from the metal's conduction band. As this effect can only occur for molecules forming a chemical bond with the surface, not all Raman molecules will experience this enhancement. Furthermore, due to the extremely short range of this effect (considerably less than that of the EM enhancement), only atomic bonds close to the surface will undergo enhancement.

The last critical aspect of SERS in relation to this work is the quenching of fluorescence. Typical SERS systems involve excitation using a laser in the visible wavelength band. However, such energies can lead to fluorescent emissions from the sample. As stated before, in the case of NRS, this fluorescence can easily overpower the weak Raman signal by many orders of magnitude. In the presence of the SERS surface however, it is believed that the fluorescence process is quenched by the decrease in the decay time of the molecule through interactions with the plasmon field [Le Ru and Etchegoin, 2005; Weitz et al., 1983]. As the decay time decreases and the molecule undergoes non-radiative energy transfer back to the plasmon field, the number of fluorescent photons emitted is reduced. Thus the combined increase in Raman photons and the decrease in fluorescence photons results in an improved ability to investigate the vibrational modes of fluorescent molecules using visible light.

1.2.1 Enhancement Factors

Typical quoted enhancements of the Raman signal are on the order of 10^6 but under exceptional circumstances can reach as high as 10^{14} for single molecule detection [Etchegoin et al., 2003; Kneipp et al., 2006]. These high values reduce the spectral collection times from minutes or hours that are typically required for NRS to seconds. Additionally, it also enables the gathering of Raman spectra with low laser powers (< 1 mW) thus reducing the likelihood of damaging the sample under investigation.

The enhancement factor, E, is determined by comparing both the NRS intensity and SERS intensity of the same sample taken under the same conditions:

$$E = \frac{\mathrm{I}_{SERS}}{\mathrm{I}_{NRS}} \times \frac{\mathrm{N}_{NRS}}{\mathrm{N}_{SERS}} \tag{1.1}$$

where I is the signal intensity and N is the number of molecules contributing to the signal.

While commonly used, this equation is difficult to implement as often the number of molecules contributing is not accurately known. Estimation of these values results in only order-of-magnitude answers. For completeness, an example of this equation is shown in Section 3.4.3.1 but for the remainder of the thesis, SERS signals are quoted in units of signal counts per second per unit of laser power (cps/mW). This value is preferred as regardless of the number of molecules contributing, it is the simple change in signal intensity that is recorded and is the useful quantity in practice.

1.3 Existing SERS Substrates

There has been much work conducted on the engineering of suitable nanostructured substrates for SERS use. Due to the numerous methods available, the discussion in this section is limited to the commonly employed techniques. Simple roughened surfaces such as those formed by electrochemical reactions or mechanical ablation (Fig. 1.4) can be easily manufactured [Fleischmann et al., 1974; Viets and Hill, 1998]. However, as the roughening process is fundamentally a random process, devices produced in this manner have little sample-to-sample reproducibility.

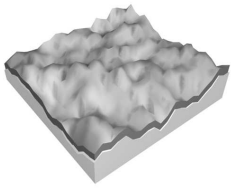

Fig. 1.4: Metal coated mechanically roughened surfaces.

Metal island films consist of an arrangement of nanoscale metal particles deposited onto a substrate. Such films can be easily manufactured using commonly available metal evaporation coating units (see Section 2.3 for examples). Once again, this technique relies on a random process and although particle size can, to a degree, be controlled, the spacing of the metal islands cannot. An alternative method of producing island films is to deposit colloidal solutions onto a substrate (Fig. 1.5). Silver colloidal solutions can be formed by citrate reduction of either $AgNO_3$ or Ag_2SO_4 and are popular as the size of the particles can be accurately maintained by careful control of the colloidal chemistry and by filtering the resultant particles [Aroca et al., 2005; Munro et al., 1995; Vosgrone et al., 2005].

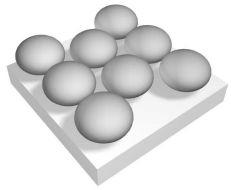

Fig. 1.5: Colloidal metal.

Although colloidal solutions can have high particle size reproducibility, they rely on the interaction between two or more metal particles (forming dimers, trimers, etc.) to generate high signal counts [Khan et al., 2006; Moskovits, 2005]. As there is no easy way to ensure if that interaction occurs, large differences in the SERS enhancement can result.

Lithographic techniques have also attracted considerable research efforts. Nanosphere lithography (NSL) occurs when a metal is deposited (typically by thermal evaporation) in the spaces formed between a monolayer of sub-micron sized latex spheres (Fig. 1.6a) [Deckman and Dunsmuir, 1982; Kosiorek et al., 2004]. These spaces result in arrays of pyramidal structures once the spheres are removed. Although not lithography, a similar technique to this is film-on-nanosphere (FON) coating where a thick layer of metal is deposited over the top of the spheres (Fig. 1.6b) [Dieringer et al., 2006; Haynes and Van Duyne, 2001].

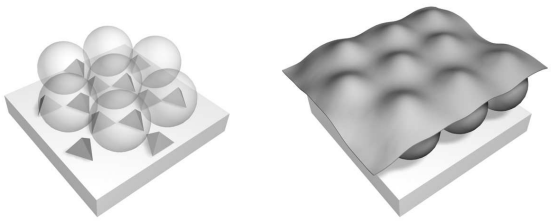

(a) (b)

Fig. 1.6: (a) Nanosphere lithography (NSL) and (b) film on nanosphere (FON).

The difficulty with NSL and FON techniques is that they rely on micro-spheres arranging themselves into a monolayer. While there are several methods available that can assist this process, gaps in the monolayer or multi-layer arrangements can still occur. Additionally it is difficult to produce large areas of these surfaces which places limitations on the potential for large scale manufacturing.

Electron-beam lithography has been shown to produce suitably structured nanoparticle arrays by patterning sites onto an appropriate substrate (Fig. 1.7) [Kahl et al., 1998; Sackmann et al., 2007]. This technique has the advantage of allowing precise control over the size, shape and spacing of nanoparticles. Furthermore, the metal coating can be controlled in terms of thickness as well as coating angle as shown in Figure 1.7 (a). More traditional UV lithographic techniques have also shown potential. Xia *et al.* demonstrated a technique where interfering UV beams could be used to produce nanoparticle arrays [Xia and Brueck, 2004]. Recently, arrays of inverted etched pyramids into silicon wafers (with their patterns defined by lithographic masks) have become commercially available under the "Klarite" brand name [Perney et al., 2006].

Lithographic techniques avoid the inherent randomness issues that are associated with other techniques such as roughening but come with high equipment costs. While allowing large numbers of samples to be produced simultaneously, from a commercial point of view, a correspondingly large number of sensors need to be sold to recoup this capital expense.

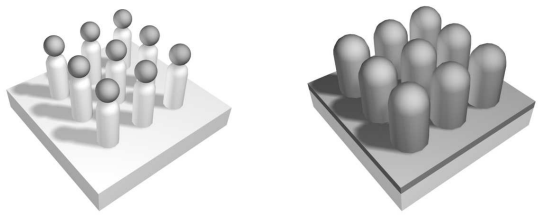

(a) (b)

Fig. 1.7: Metal coated lithographically prepared structures. (a) Extremities coated by tilting substrate and (b) blanket coating.

The goal for more widespread use of SERS, therefore, is to produce substrates that have high sensitivity / enhancement, a high sample-to-sample reproducibility, low set-up costs and a low per-sample cost. Additional desirable qualities include a small device footprint, easy maintenance, simple operation, and a robust system to minimise downtime. Optical fibre SERS substrates potentially offer an attractive solution to all of these issues.

1.4 Optical Fibre Probes

An optical fibre platform offers many advantages in sensor applications. Chief amongst these is the ability to easily separate the sensing component from the user. Remote sensing capability is considered highly desirable for situations where there is an imminent physical threat to the operator (eg. explosives, bio-warfare agents, toxic chemicals or radiation environments). To cater for these markets, a number of commercial NRS remote optical fibre probe systems are currently available. Such systems are either single-fibre, where the same fibre optic is used for both light delivery and collection, or multi-fibre systems where separate fibres are used (Fig. 1.8). In both cases the collection is via backscattering from the sample as in situations where the molecule of interest has unknown orientation (eg. in liquid or powder form), the backscatter collection is usually no more or less efficient than forward or side collection [Druger and McNulty, 1984; Nafie, 2001]. However, one of the main drawbacks of the current fibre based systems, is the high laser power required for NRS. The large laser intensity within the fibres creates an additional background Raman signal from the

glass which leads to decreased signal-to-noise sensitivity. This issue, in the case of multi-fibre systems, has largely been addressed by using appropriate filtering on the laser delivery and collection fibres (Fig. 1.8 (a)) [Buschman et al., 2001]. However, such an approach cannot be used in single fibre systems, in which case it is necessary to keep the length of fibre as short as possible [Mahadevan-Jansen, 2003].

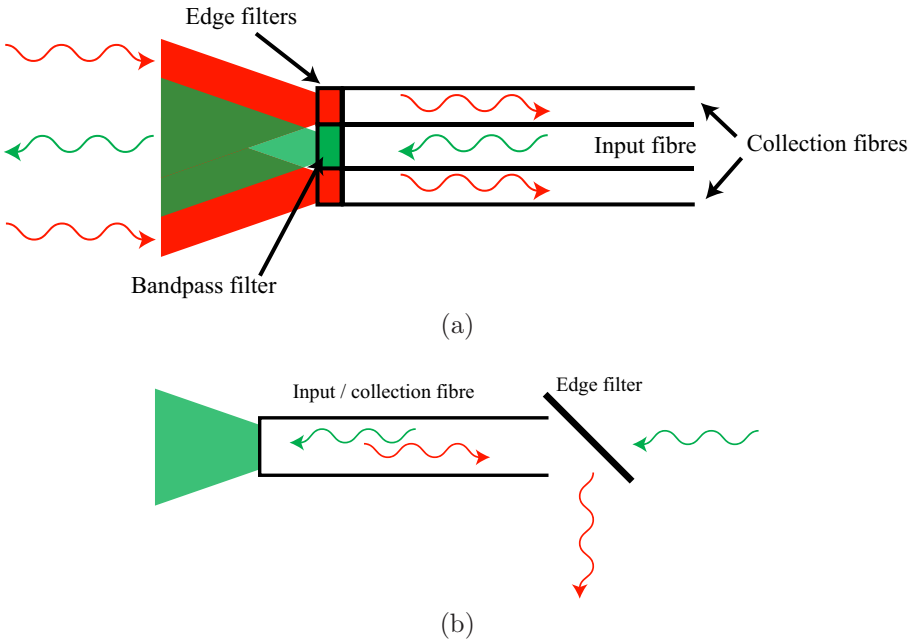

Fig. 1.8: (a) Multi-fibre and (b) single-fibre Raman probes.

An additional benefit of an optical fibre based platform is the ability to interface the probe with other optical fibre components. The availability of fibre-coupled lasers and spectrometers raises the possibility of a completely fibre-based system. Replacing discrete optical components with fibre components allows for more robust and potentially smaller devices. Several types of fibre couplers allow micron-level accuracy, removing the need for regular alignment required by free-space components. Furthermore, optical fibres only require the excitation laser to be focussed into the proximal end of the fibre rather than onto the sample itself. This offers the advantage of having a fixed focal system and removes the need for expensive objective lenses. Once again, for an on-line or fieldable commercial system, reduced down-time for maintenance and push-button operation are essential qualities.

There have been a number of previous attempts to build SERS capable optical fibres. Polwart *et al.* immobilised silver colloids on the tip of a commercial multimode optical fibre using an interfacial layer of 3-aminopropyltrimethoxysilane (ATPMS) [Polwart et al., 2000]. As stated earlier, when using a single fibre for both excitation and collection, the fibre length must be kept short to minimise extraneous Raman signal generated by the glass. In the Polwart SERS fibre, the length was kept to less than 100 mm.

A similar approach was reported by Lucotti and Zerbi who instead used a tapered optical fibre [Lucotti and Zerbi, 2007]. The tapered substrates in question were produced by slowly withdrawing an optical fibre that was immersed in a hydrofluoric acid solution. The narrowed fibre was then coated with silver nanoparticles again using an ATPMS interfacial layer. Tapering the distal end of the fibre results in an increased surface area to which metal can be deposited. A somewhat simpler approach using a tapered optical fibre with the metal film evaporated directly onto the surface was reported by Gessner *et al.* [Gessner et al., 2002].

Another technique involving immobilised particles was demonstrated by Stokes and Vo-Dinh [Stokes and Vo-Dinh, 1999]. In this example, a fibre was coated with a monolayer of alumina particles which were then functionalised with a layer of silver.

Viets and Hill also developed several SERS fibre designs based on roughened tips [Viets and Hill, 2001, 1998]. Surfaces were prepared in a number of ways including sand-blasting, etching and grinding at an angle. Fibres were then activated either by coating a continuous silver film over the roughened surfaces or by depositing particles to form metal islands.

Although the above examples all showed SERS activity, they rely on the same fundamentally random metal film formations as discussed earlier. As such, like their conventional planar surface counterparts, these sensors suffer from the same sample-to-sample reproducibility issues. By omission, the literature suggests that lithographic techniques may be difficult to apply to fibre end-faces.

1.4.1 Imaging Fibres

The work presented in this thesis is based on modified imaging fibres. Imaging fibres consists of thousands of individual single-mode fibres (called "pixels") drawn in a coherent bundle in such a way that each fibre maintains its position along the length of the bundle. These bundles are commonly used in medical endoscopes for transferring an image from one end of the fibre to the other [Dubaj et al., 2002]. The imaging fibres used in this work consist of three primary components: an array of single mode fibres, a "matrix" filler material and a silica outer tube (Fig. 1.9).

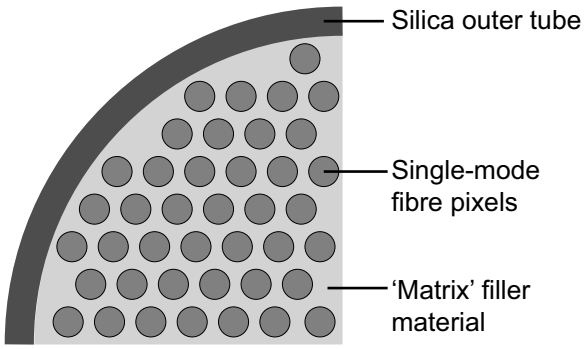

Fig. 1.9: Imaging fibre components.

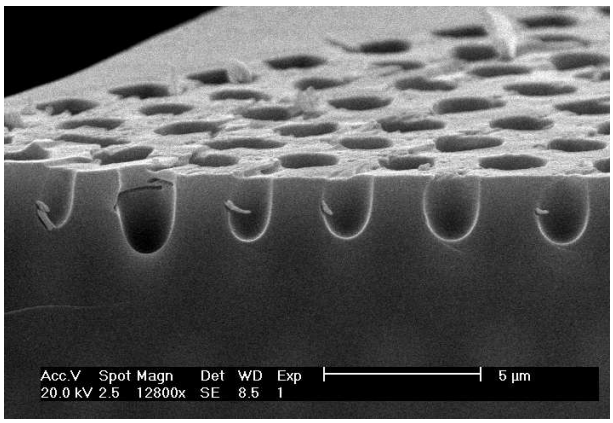

Fig. 1.10: Chemically etched imaging fibre showing the wells formed in the locations of the pixel cores.

Several publications have demonstrated that the cores of the imaging fibre can be preferentially eroded using a selective hydrofluoric acid based etchant to produce an array of micron-scale wells [Bernhard et al., 2001; Pantano and Walt, 1996]. These microwells have been utilised as supportive structures for functionalised microspheres, which have been used for the detection of various chemical substances, typically by fluorescence [Epstein et al., 2003; Song et al., 2006; Wygladacz et al., 2005].

At their native size, the structures produced by etching imaging fibres are too large to act as efficient SERS substrates (Fig. 1.10). However, the proposition presented in this work is that by reducing the scale of the features to sub-micron sizes (by drawing the fibre to a smaller diameter), the structures produced after etching can be of an appropriate size for use as a SERS substrate.

Subsequent to the initial results published for this work, a similar approach was utilised by Hankus *et al.* to produce a tapered fibre with SERS functionality at the drawn end [Hankus et al., 2004]. It was claimed that this structure allows SERS imaging with sub-micron resolution. Although tapered tips could also be used as chemical sensors, the tapering process is not amenable to scaling up to industrial levels in the same way that fibre drawing can potentially be. Therefore this work aims to investigate the potential for large scale manufacturing by fibre drawing.

1.5 SERS Applications

The many thousands of Raman-active molecules are promoting continual research into new applications of SERS. While a full review of current SERS uses is well beyond the scope of this thesis, there are a number of particularly interesting applications that require the development of novel SERS platforms for practical application.

The Van Duyne group have published several papers on the use of SERS for the monitoring of blood glucose [Haynes et al., 2005; Shefer-Peltier et al., 2002; Yonzon et al., 2004]. Vo-Dinh has also discussed SERS for the early detection of cancer cells [Vo-Dinh et al., 2002, 2005]. In these cases (and medical uses in general), having a small SERS probe provides the possibility of in-vivo detection of the molecules under investigation. Additionally, by having a small fibre diameter, such a probe can be considered minimally invasive.

There are also a number of scenarios where an optical fibre platform provides a distinct advantage due to the robustness and simple integration of the system. Identification of water contaminants, illicit drug detection and counter bio-warfare are all applications where inexpensive, portable and mechanically robust devices are highly desirable [Murphy et al., 2000; Schmidt et al., 2004; Sengupta et al., 2005; Stuart et al., 2006a].

The use of the SERS probe described in this thesis for a number of the above applications is presented in Chapter 7.

1.6 Thesis Structure

This thesis is based around the design, manufacture and characterisation of SERS capable surfaces generated by chemically etching drawn imaging optical fibres.

This chapter provides an introduction to the basic mechanisms of Raman and surface-enhanced Raman scattering. A literature review covering previous attempts and manufacturing suitable SERS surfaces as applicable to optical fibre probes is also presented.

Chapter 2 covers some of the fundamental experimental equipment that was employed during the experiment. The basic parameters for the chemical etching, metal film deposition, electron microscope characterisation and Raman spectral acquisition are presented. Detailed information is presented as appropriate in the following experimental chapters.

Chapter 3 presents the results gathered from the prototype drawn imaging fibre. These fibre probes were made from commercially available imaging fibres drawn by hand to smaller diameters. The fibres were then chemically etched and coated with silver to generate SERS activity. Despite the difficulties involved in the manufacturing and handling of the prototype fibres, the samples produced in the experiment showed good SERS enhancement factors.

Chapter 4 is a theoretical study of the etching process for the fibre. The chapter details a simulation program written to track the changes in surface topology as the fibre etches. Furthermore, the simulation also calculates dopant diffusion

within the fibre. Understanding how the dopants will diffuse at high temperatures provides guidelines to the upper temperature limits for large scale (ie. commercial) manufacturing of the drawn imaging fibres.

Chapter 5 details the attempts at producing SERS probes suitable for "large scale" commercialization. A number of different designs were trialled with the assistance of the Optical Fibre Technology Centre (OFTC) at the University of Sydney and with Fujukura Ltd. Also presented in the chapter are details of the handling methods employed.

A full characterisation of the fibre produced by the successful manufacturing attempt is presented in Chapter 6. Samples were etched for a range of times and coated with a range of metal thicknesses in order to determine optimal SERS conditions. Also shown are results for determining the location of the LSPR peaks and the SERS repeatability of the samples.

Chapter 7 presents preliminary results of tests using the SERS fibre for the detection of glucose, CEES and chlorsulphuron. The chapter also details investigations into the sensitivity and reversibility of the SERS fibre for these analytes.

Finally, Chapter 8 concludes the thesis and presents recommendations for further experiments using the SERS fibre.

Chapter 2

Experimental Methods

2.1 Introduction

This chapter outlines the main experimental apparatus and methods for the work presented in this thesis. Specific details of parameters used are presented as appropriate in the relevant sections of the following chapters. Described here, however, are basic details on the chemical etching of silica fibres, the coating of etched fibres with metal films, investigations of the structures produced using electron microscopes and finally the use of Raman microscopes for collecting spectral information.

2.2 Etching

The SERS active surfaces presented in this thesis were formed by chemically etching nanoscale silica optical fibres using a hydrofluoric acid (HF) based etchant. Both pure HF and buffered HF etchants were investigated.

The chemical reaction of SiO_2 and HF is shown in Equation 2.1 [Buhler et al., 1997].

$$SiO_2 + 6HF \rightleftharpoons 2H^+ + SiF_6^{2-} + 2H_2O \tag{2.1}$$

An alternative to pure HF, buffered hydrofluoric acid (BHF - also known as buffered oxide etchant or BOE) consists of both hydrofluoric acid and ammonium fluoride (NH_4F) in ratios of approximately 1:5 to 1:100. The chemical reaction of SiO_2 and BHF is shown in Equation 2.2 [Buhler et al., 1997].

$$SiO_2 + 4HF + 2NH_4F \rightleftharpoons 2NH_4^+ + SiF_6^{2-} + 2H_2O \tag{2.2}$$

In both cases the etching of SiO_2 is performed by a reaction with HF_2^- [Williams and Muller, 1996]. However, the two solutions vary in their dissociation into HF_2^- [Kikyuama et al., 1991]. The dissociation of HF is shown in Equation 2.3 and of BHF in Equation 2.4.

$$\begin{aligned} HF &\rightleftharpoons H^+ + F^- \\ HF + F^- &\rightleftharpoons HF_2^- \end{aligned} \tag{2.3}$$

$$\begin{aligned} NH_4F &\rightarrow NH_4^+ + F^- \\ HF + F^- &\rightleftharpoons HF_2^- \end{aligned} \tag{2.4}$$

HF itself is a very weak acid and as such does not produce many F^- ions. In contrast, NH_4F is a strong electrolyte and produces a large number of F^- ions [Kikyuama et al., 1991]. As such, a buffered HF solution has the ability to generate more active HF_2^- ions and hence BHF solutions etch considerably faster than HF solutions. Additionally, as the F^- ions are generated by the dissociation of NH_4F instead of HF, the pH of the solution remains constant during the etch thus providing a linear rate of material removal over time.

As HF is commonly used to etch silica, no glass equipment could be used in the laboratory. Instead polypropylene (PP) beakers, pipettes, funnels, etc. were used to conduct the experiments. The HF solutions and waste products were stored in high density polyethylene (HDPE) bottles. All bottles were stored in a locked HDPE acid safe cabinet.

2.2.1 Safety Procedures

Special note must be made regarding the use of HF in a research environment. HF is extremely dangerous and should only be handled with appropriate safety measures in place. Dermal (ie. skin) exposures of 1% area from $> 50\%$ concentration HF can lead to systemic effects. Exposure of greater than 2.5% at $> 50\%$ concentration can lead to death [Greco et al., 1998; NICNAS, 2001]. This is equivalent in area to the back of the hand. The primary cause of HF related deaths has been the absorption of fluorine ions which bond to calcium leading to hypocalcemia - an acute lack of calcium. This, in turn, can lead to ventricular fibrillation. At lower (ie. non-lethal) exposures, painful second and third degree burns ensue. Due to these issues, great care must be made to ensure lab workers are protected from spills of HF.

To ensure the safety of personnel, several items of personal protective equipment (PPEs) were used. Full body splash protection was provided by wearing DuPont® Tychem 'F' suits. These have a 40% HF breakthrough time of over 8 hours. Double gloving using nitrile rubber gloves (inside) and butyl gloves (outside) provided hand and forearm protection. Uvex® polycarbonate goggles were worn for eye protection and a long acetate visor was used as a face shield. Chemguard® rubber boots were used for foot protection.

To cater for accidental exposures, a supply of 2.5% calcium carbonate gel and tables was always on hand during experiments. HF releases fluorine ions in the body which react with calcium. To delay or prevent hypocalcemia, replenishment of calcium either by topical gel or intravenous infusion is the advised treatment. In case of spills, a supply of lime was also kept available.

HF based waste products were all disposed of in accordance with the university's Occupational Health and Safety procedures.

2.3 Metal Film Deposition

As stated previously, the SERS effect relies on the interaction between a molecule and a nanoscale metal particle. This thesis concentrates on the manufacture of structured glass substrates which must therefore be coated with metal to function as SERS devices. However, in addition to using metal for SERS, coatings were also required to prevent charging effects when using the SEMs and to aid in the adhesion of the active silver coatings to the sensors.

Three coating systems were used in the experiments presented here: an SPI Module plasma sputter coater, a Kurt J. Lesker (KJL) sputter coater and an Emitech K950X thermal evaporation coater.

2.3.1 SPI Module Sputter Coater

The SPI (Model ♯11430) sputter coater was used to deposit a thin layer of gold onto the samples to enable inspection using a Philips XL30 SEM. Sputter coaters work by initalising a gas discharge between two electrodes. In the case of this unit, a gold target acts as one electrode and the samples (which are grounded by the unit), the other. To coat a sample, the chamber is first pumped to vacuum and then filled with argon to a pressure of ≈ 0.5 mbar. When a current is applied between the electrodes, the argon ionises. These ions are then attracted to the gold target, sputtering off gold atoms. By carefully controlling the current and the amount of argon in the chamber, a thin and uniform coating can be applied to the sample. The deposition thickness is controlled by a timer system. For the experiments conducted, a coating time of 80 seconds was used which corresponds to a thickness of approximately 30 nm. Note that this coating was only applied to prevent charging effects for samples investigated using the XL30 SEM. Samples investigated using the Supra 40VP SEM required no such preparation as the lower acceleration voltage meant charging was not a problem.

2.3.2 Kurt J. Lesker Sputter Coater

The KJL (Model CMS-18) coater was used to apply a layer of chromium to the fibre surfaces in Chapters 6 and 7. The application of a thin layer of chromium has been

shown to aid the adhesion of silver films to glass surfaces [Vo-Dinh et al., 2005; Xu et al., 2004]. In this work, a 2 nm thick film was applied to the fibres to act as an adhesion layer before the deposition of silver using the Emitech coater. While a thicker layer would further improve adhesion, the layer had to be kept thin to avoid targeted molecules binding to the chromium instead of the silver [Haes et al., 2004].

As with the SPI coater, the KJL coater uses a plasma discharge in an argon environment to sputter chromium onto the sample. However, in this unit, the chamber pressure was much lower at approximately 5×10^{-3} mbar. Once again, the thickness of the coating is determined by the deposition time. As the unit deposits at a rate of 10 nm/minute, the deposition was timed to last 12 seconds.

2.3.3 Emitech K950X Thermal Evaporation Coater

The Emitech coater was used to deposit silver onto the structured surfaces to enable SERS functionality. Unlike the sputter coaters, this system uses a thin tungsten wire to heat a sample of the coating metal to melting point. Once this is achieved, the metal particles then evaporate in a uniform, isotropic manner from the source. The evaporation process inside the thermal coater requires a vacuum and the operational pressure recorded in the chamber was less than 1×10^{-3} mbar.

To enable thickness monitoring, this unit was fitted with an Emitech K150X quartz crystal oscillator. The monitor functions by measuring the change in oscillation frequency as the amount of material deposited onto the crystal face increases. The unit also has the facility to terminate the deposition process when the desired thickness is reached. However, due to the deposition being generated by a thermal source which cannot be stopped immediately, overshoots of up to 0.5 nm were common.

2.4 Electron Microscopy

Two scanning electron miscroscopes (SEMs) were used to investigate the devices produced in the work presented in this thesis - a Philips XL30 and later a Zeiss Supra 40VP.

2.4.1 Philips XL30

During the early stages of the experiment, a Philips XL30 SEM was employed. The outputs from this system are shown in Chapters 3 and 5. A maximum magnification of approximately 130,000× was used, although at this level, imaging was difficult and the results often blurry and indistinct. As such, most images were taken at 50,000 to 100,000× magnification. On this system an acceleration voltage of 20 kV was used, which required the samples to be coated with a conductive metal (gold) to prevent charging effects (refer to Section 2.3 for details). Despite the limitations of this system, the resolution was high enough to enable clear characterisation of the etched glass structures on the tip of the optical fibres. It could not, however, image the metal films deposited.

2.4.2 Zeiss Supra 40VP

For the later part of the work (Chapters 5 and 6) a Zeiss Supra 40VP SEM was utilised. This newer system had several important advantages over the XL30. Firstly, the maximum magnification achievable was approximately 900,000×. As such, when imaging at 100,000×, the images produced were much clearer than those obtained in the XL30. This increase allowed the metal deposition to be clearly imaged. Secondly, this system can function with an acceleration voltage of < 1 kV. Such a low voltage prevented charging effects from occurring and as such, no gold film was required on the samples. Finally, the 40VP produced images with three times the pixel resolution of the XL30 which once again, allowed more detailed investigation into the surface features.

2.5 Raman Systems

All the spectra presented in this thesis were collected using Raman microscopes: a Renishaw RM2000 (Chapter 3) and a Horiba Jobin-Yvon (HJY) Modular Raman Microscope (Chapters 6 and 7). While the two systems are manufactured by different companies, they both function in similar ways and have similar components as detailed below. Specific experimental parameters such as excitation wavelength and grating density used in these systems are presented as appropriate in the following chapters.

The basic operation of the systems is listed below:

1. Laser light is coupled into the microscope.
2. The light is filtered by a band-pass filter to remove unwanted wavelengths (eg. Raman from the input fibre or plasma lines from a gas laser source).
3. The collimated beam is reflected off the Raman filter and directed to the objective.
4. Between the Raman filter and the objective, beamsplitters for a white light source and video camera can be inserted as needed for sample inspection.
5. An infinity corrected lens focusses the laser onto the sample and collects the backscattered Raman signal.
6. The returning light passes through the Raman filter which removes the unwanted Rayleigh scatter but passes the Raman signal.
7. In the HJY system, the signal is then coupled into an optical fibre connected to a spectrometer. In the Renishaw system, the spectrometer is integral with the microscope.
8. In the spectrometer, the Raman signal is dispersed by a holographic grating and then imaged by a thermoelectrically-cooled (TEC) CCD .

2.5.1 Renishaw RM2000 Raman Microscope

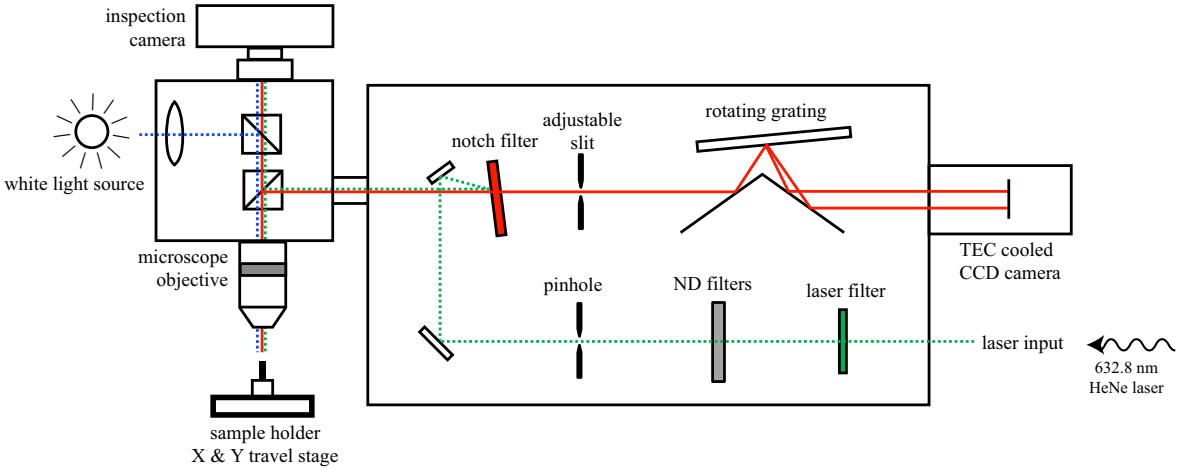

Fig. 2.1: Renishaw RM2000 system.

Figure 2.1 shows the layout of the major components in the RM2000 microscope. As can be seen, this system comprises of two units - the box on the right for laser input and filtering and the microscope unit on the left for directing the laser onto the sample and collecting the Raman signal. A connecting tube between the two allows light to pass from one unit to the other in a safe and stable manner. The spectrometer for dispersing the incoming Raman signal and the CCD for recording the spectrum is also encased in the main unit.

2.5.1.1 Laser Source

The Renishaw system was configured to use a 632.8 nm (HeNe) laser. The sources used were Spectra-Physics Model 127 and Coherent 40.6" helium neon lasers. The free-space laser input is directed into the RM2000 through the use of a series of mirrors. A laser line filter is included in the RM2000 to remove unwanted plasma lines from the HeNe source. The RM2000 system is also fitted with a series of ND filters to modulate the laser intensity.

2.5.2 Horiba Jobin-Yvon Modular Raman Microscope

The diagram and picture in Figures 2.2 and 2.3 shows the modular system produced by Horiba Jobin-Yvon.

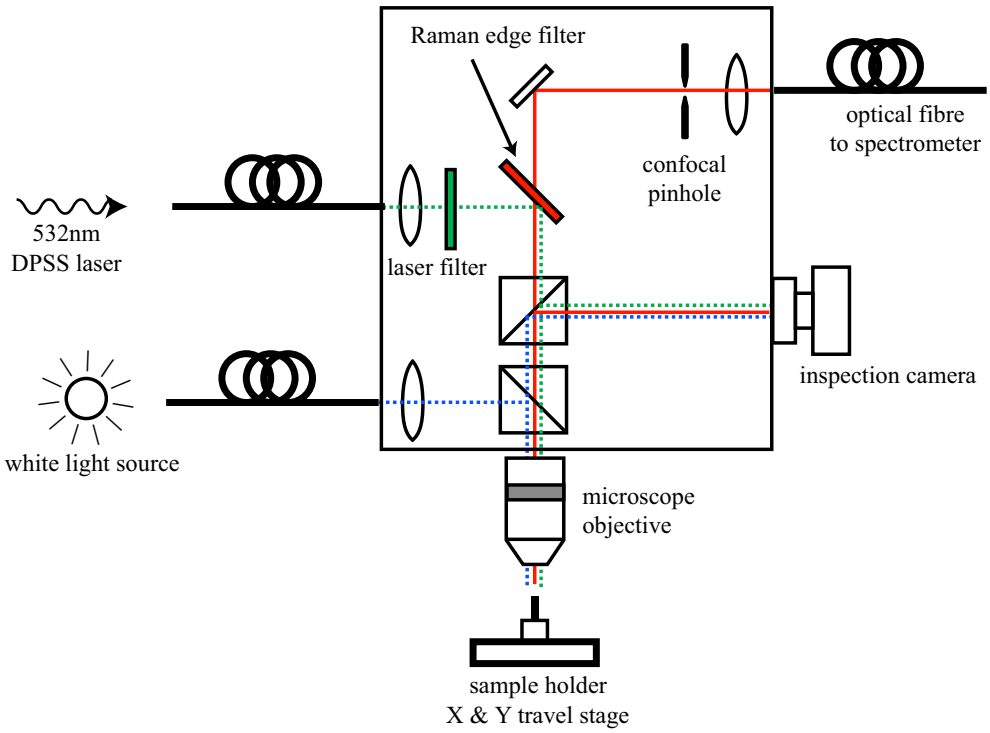

Fig. 2.2: HJY Modular Raman system schematic.

As can be seen, this system uses many of the components found in the RM2000, but arranges them in a different fashion. The main difference between the two units is that all of the inputs and outputs of the HJY microscope are fibre coupled whereas the RM2000 system uses free-space optics. This offers a number of advantages and disadvantages. By fibre coupling the input laser, a virtually infinite number of laser lines can be used as sources can be changed simply by plugging in a new optical fibre. Furthermore, the laser can be located away from the microscope unit. In the RM2000 system the lasers must be located directly next to the microscope as the light is coupled in using free-space mirrors. The disadvantage of a fibre based input is that the fibre itself can contribute unwanted Raman and fluorescence signals. As such, the input line is fitted with a laser band-pass filter with a full-width half-max (FWHM) of approximately 2 nm. Note that the contribution to the signal from the fibre is a

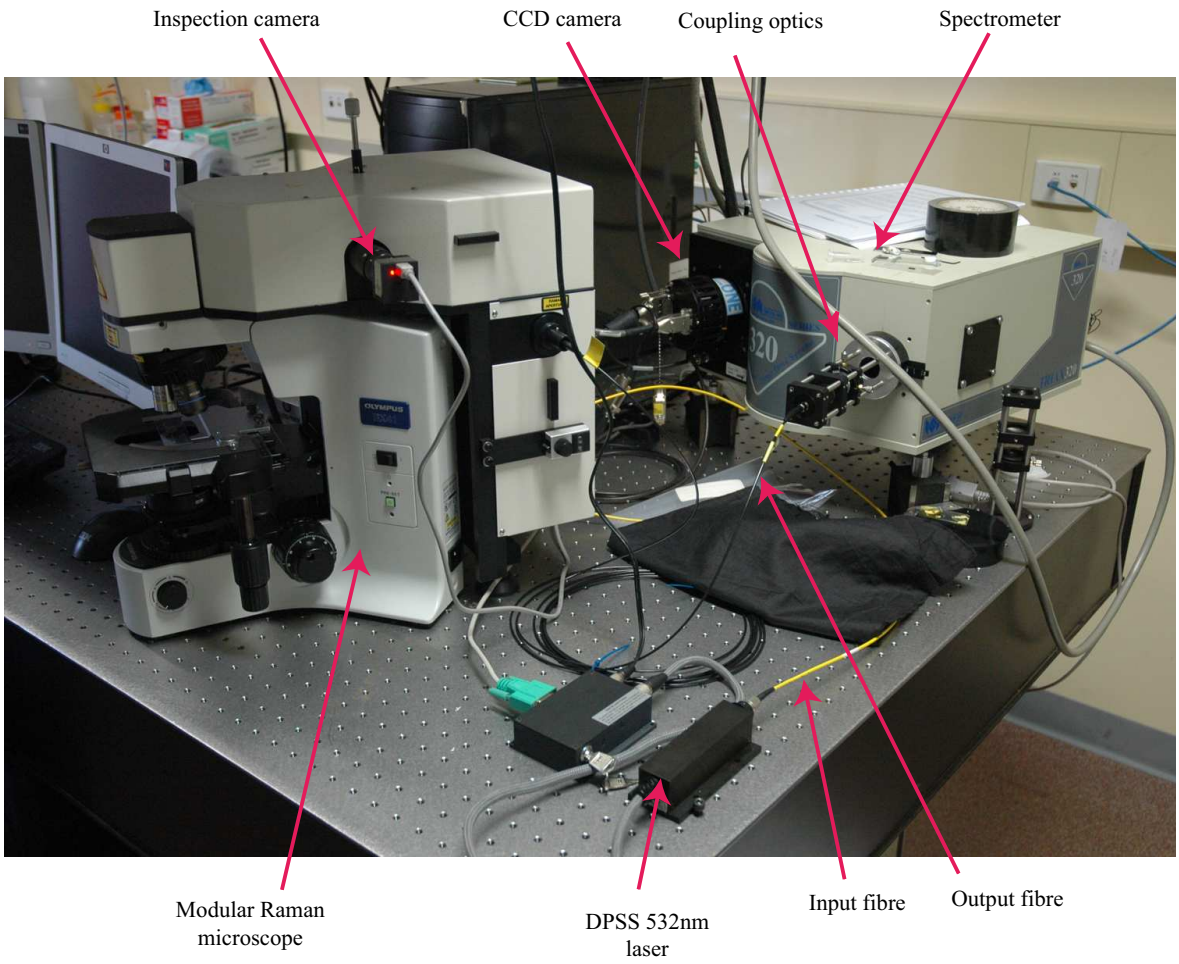

Fig. 2.3: HJY Modular Raman system. Note the black output fibre from the microscope to the spectrometer and the attached cage holding the input lenses. Under experimental conditions, the cage is covered by the black cloth underneath to prevent extraneous light entering the spectrometer.

function of the power being carried. The output fibre connecting the microscope to the spectrometer, on the other hand, carries very low powers and as such does not require such filtering.

2.5.2.1 Laser Source

The HJY system was configured for 532 nm excitation. This was provided by a diode-pumped solid state (DPSS) 532 nm laser from OptoTech P/L. The laser was coupled to a 5 μm core, single mode optical fibre for input into the microscope. A single mode fibre

produces a Gaussian output beam which allows easier collimation and focussing. Once again, details of the laser powers used are presented as appropriate in the following chapters. Note that unlike the RM2000 system, the HJY microscope does not provide space for ND filters. Instead, the power was modulated by the laser's operating current.

2.5.2.2 Triax 320 Spectrometer

In the Renishaw system, the spectrometer used to disperse the incoming Raman signal is integral with the microscope. However, in the HJY system, the spectrometer is a separate unit. A Horiba Jobin-Yvon Triax 320 spectrometer was employed (Fig. 2.4). This unit is a single pass, 320 mm path length spectrometer and uses a 1200 l/mm blazed grating to disperse the beam. As the HJY microscope offers an optical fibre output, a custom input module was built to couple the signal from the fibre into the spectrometer. The coupler consists of two 25 mm diameter achromat lenses: a 45 mm effective focal length (EFL) lens to collimate the output from the optical fibre and a 100 mm EFL lens to direct the beam into the spectrometer. The lens combination serves to match the fibre N.A. of 0.2 with the spectrometer N.A. of 0.11. To improve spectral resolution, the input path is also fitted with a 100 μm slit, which allows efficient coupling of signal from the 50 μm core of the input fibre. Fine positioning of the beam through the slit is done by fitting the 100 mm input lens in an X-Y adjustable mount. To collect the spectral data, the Triax is fitted with a Horiba Jobin-Yvon CCD 3000V cooled array detector.

2.5.3 Signal Acquisition

As stated above, the Raman signal is recorded by a cooled CCD detector. Cooling the detector lowers the dark current noise associated with the CCD device. Both systems were cooled by a multi-stage TEC coolers to < 240 K. In order to gather enough photons for a reliable signal, integration times of ten seconds were commonly used. To improve the signal to noise ratio, five accumulations were averaged together. For some spectra, a cosmic ray removal algorithm was employed. This algorithm works by first taking a reference spectrum against which subsequent spectra are then compared. Any sharply defined peaks (i.e. high intensities on a single CCD pixel only) are treated as cosmic noise and are hence removed. To further remove high frequency noise, in most

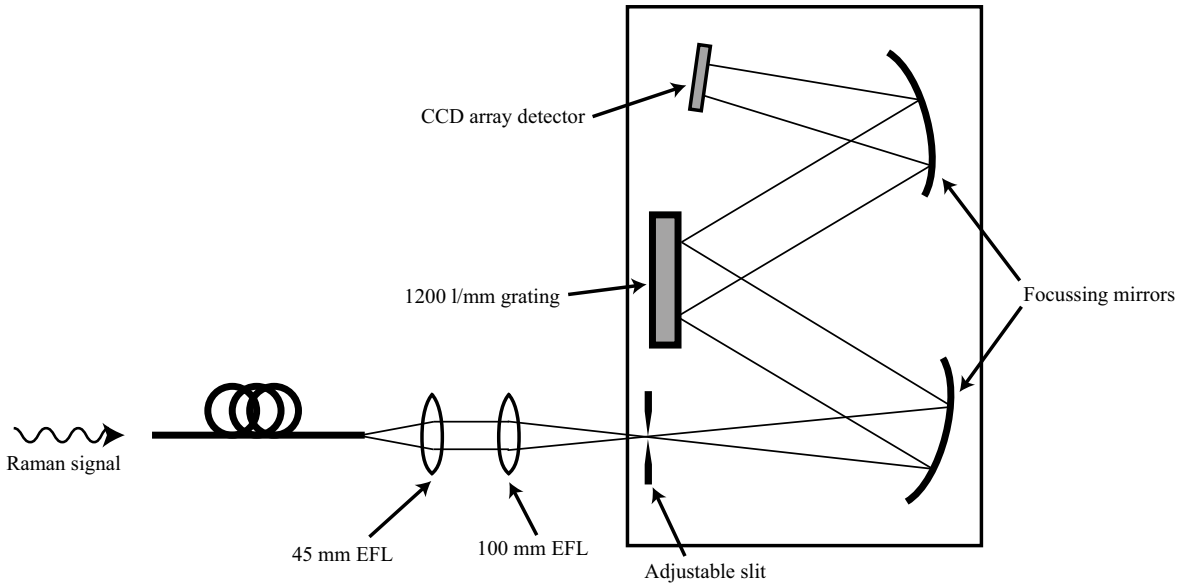

Fig. 2.4: HJY Triax 320 spectrometer.

cases a 3^{rd} order Savitzky-Golay smoothing filter was also applied. The low frequency background signal was removed either by a 4^{th} order polynomial or by a manually defined curve. All post-processing was done using MathWorks Matlab 7.

Chapter 3

Prototype Nanostructured Optical Fibres

3.1 Introduction

This chapter describes the initial attempts to produce a SERS capable surface on the tip of a drawn optical fibre. The fibres in this section were commercial imaging fibres drawn by hand to smaller diameters and etched using hydrofluoric acid based solutions.

Also presented in this chapter are the initial estimates of SERS enhancement factors using thiophenol as the Raman active molecule.

3.2 Imaging Fibres

The fibre used in this experiment was a Fujikura FIGH-10-350S imaging fibre. The as-received fibre has an outer diameter of 350 μm and a pixel count of 9,450 cores. The pixel diameter is approximately 2 μm and the inter-core (I_C) spacing (the centre-to-centre distance between two adjacent pixels) is approximately 4 μm. This fibre was chosen as at the time of the experiment, the FIGH series fibres had the smallest I_C available. Using a fibre with a larger I_C would have still been feasible but would have required drawing the fibre by a greater amount to reduce the I_C to sub-micron levels. The 350S was chosen as it only required drawing to approximately 10% of its original diameter. Additionally, after drawing, the dimensions of the fibre allowed relatively easy handling.

3.2.1 Structure

As illustrated in Chapter 1, Fujikura imaging fibres consist of three components: an array of single mode fibres, a "matrix" filler material and a silica outer tube. The precise composition is not be divulged by the manufacturer for commercial reasons, however identification of the dopants used can be made using a time-of-flight secondary ion mass spectrometer (TOF-SIMS).

TOF-SIMS works by bombarding the sample with high energy ions. When these collide with the atoms on the surface of the sample, secondary ionised particles are ejected. These particles are then accelerated to a potential such that all ions have the same kinetic energy. Lighter particles are thus accelerated to a higher velocity than heavier ones. The time then taken for the ions to strike the detector correlates with their mass. By using a pulsed ion source and rastering the beam over the surface of the sample, a map of the distribution of secondary ions can be gathered [Stoddart and Brack, 2007].

TOF-SIMS was conducted using a TOF-SIMS IV system manufactured by Ion-TOF Gmbh fitted with a Ga^+ source producing ions at an energy of 25keV. To prevent unwanted ion collisions with atmospheric particles, the sample, source and detector was placed in a vacuum chamber with a pressure $< 1.3 \times 10^{-8}$ mbar. A sample of the FIGH-10-350S fibre was cleaved and washed in methanol to remove surface contaminants before being placed into the chamber. The sample was held vertically so that the cross-section of the fibre was presented to the ion source. It must be noted that TOF-SIMS is a destructive technique in that the surface atoms are physically removed each time a scan is performed. This, however, did not impact on the results as the the structure of the imaging fibre is constant along its length (ie. varying only in cross-section).

Analysis of the TOF-SIMS data revealed the cores to be germanium doped; the surrounding matrix material was fluorine doped and the outer tube was pure silica glass (Fig. 3.1). The combination of the germanium and fluorine doping results in a raised refractive index in the cores and a depressed index in the matrix. This has the effect of increasing the numerical aperture (N.A.) of the pixels (recall: $\text{N.A.}_{fibre} = \sqrt{n_{core}^2 - n_{cladding}^2}$). According to the manufacturer, the N.A. of the fibre pixels is 0.41. This relatively high value (usual telecommunications fibre has an N.A. $\approx$ 0.2) allows for more light to enter the smaller than usual cores. Knowing

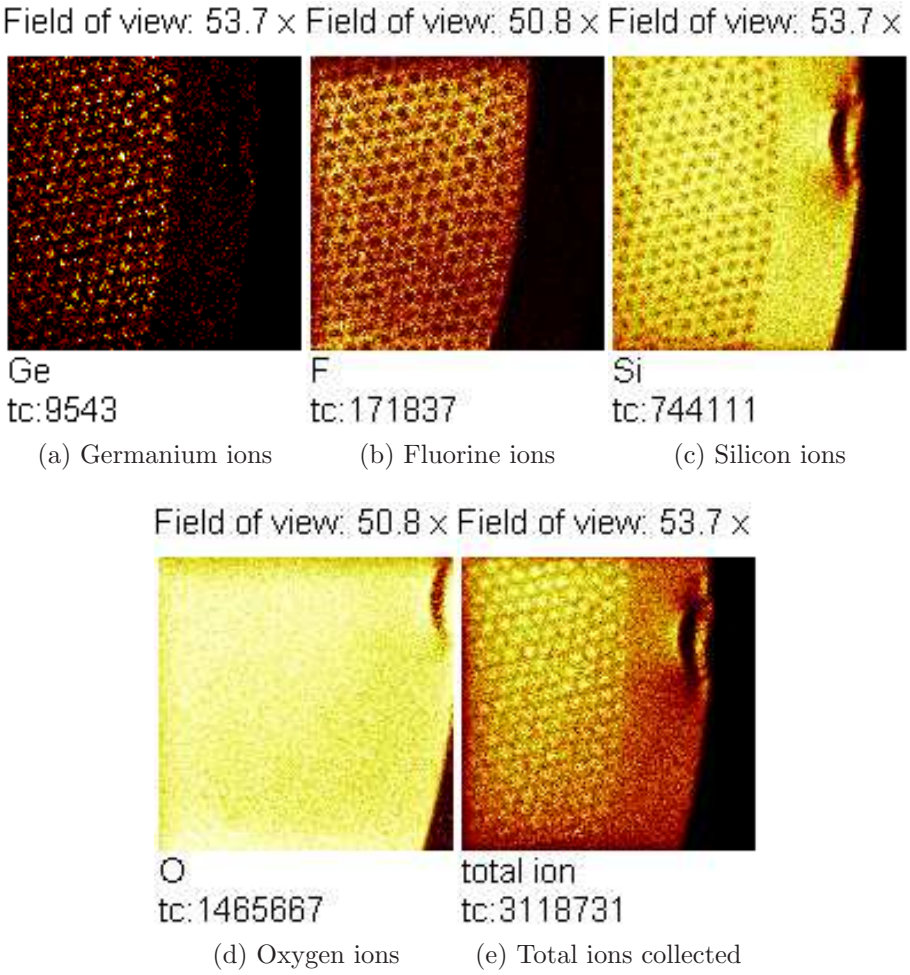

(a) Germanium ions (b) Fluorine ions (c) Silicon ions

(d) Oxygen ions (e) Total ions collected

Fig. 3.1: TOF-SIMS output images from a cleaved surface on the (as received) FIGH-10-350S fibre. The mark on the right side of the fibre is the nick made by the fibre cleaver.

that the fibre components each have a different dopant means a selective acid etchant can be used to preferentially erode only those parts of the imaging fibre chosen.

3.3 Fibre Etching

As described in the previous chapter, both HF and BHF can be used to etch silica optical fibres. The aim of the experiment shown here was to determine which of these would be most suitable for preferentially etching the germanium doped cores of the drawn optical fibre. If the cores can successfully be removed, the remaining fluorine

doped matrix material should form nanoscale structures.

Pure HF has been previously shown to erode germanium doped optical fibre cores [Pace et al., 2004; Williams et al., 2003]. However, other works have also shown the suitability of BHF as an etchant for imaging fibres [Bernhard et al., 2001; Pantano and Walt, 1996; Wygladacz et al., 2005]. It has also been shown that the unwanted additional surface roughness of the SiO_2 structures produced by etching using BHF can be reduced by addition of high concentrations of hydrochloric acid (HCl). The ratio chosen was based on that presented by Stjernström [Stjernström and Roeraade, 1998] and adjusted slightly to suit the chemical concentrations available.

3.3.1 Fibre Preparation

The FIGH-10-350S fibre comes sheathed with an outer silicone buffer (to prevent abrasion and embrittlement through the ingress of OH^- ions) which must be removed before experimentation to gain access to the glass. This is done by rubbing away the buffer using a lint-free tissue soaked in acetone. Initial attempts at drawing the fibre to smaller diameters were done using an oxy-acetylene torch. With the fibre held vertically, a 3 gram mass was attached to the end before heating the mid section of the fibre with the torch. Due to the high temperature, the glass softened quickly allowing the falling mass to draw the fibre. This method produced a sharp taper followed by a long length (typically > 15 cm) of sub 100 μm diameter fibre with a continuous taper to the point where the tapered section broke free from the remaining fibre.

After drawing the fibre, the sample was placed under a microscope fitted with a graticule in order to find the position where the fibre diameter was approximately 20 μm. A mark was made on the fibre as close to this point as possible. A small hand-held commercial fibre cleaver (FITEL S-311) was used to cleave the fibre. This cleaver works by creating a small nick in the side of the fibre using a diamond blade and then placing the fibre under tension. When the correct force is attained, a crack propagates across the fibre resulting in a clean break. Due to the inaccuracies in the marking of the location, a range of diameters between 20 μm and 30 μm were produced. This resulted in drawn fibres with a range of I_C between approximately 220 nm and 360 nm.

Unfortunately, the fibres drawn this way frequently broke due to the stresses of the

draw. Handling of the surviving fibres also proved problematic due to the relatively long length of the thin and fragile fibre. As a result of these difficulties, only eight samples were successfully produced. For future experiments, this technique was replaced with that shown in Section 3.5.1.

3.3.2 Etching

To test the suitability of using a pure HF solution, approximately 25 ml of 10% (by volume), hydrofluoric acid (Asia Pacific Specialty Chemicals) was poured into a PP beaker. Five fibre samples were mounted together (using adhesive tape) onto a small piece of cardboard cut to fit into the neck of the beaker holding the acid. The samples were etched for 10 minutes before rinsing in de-ionised water. The first sample was then removed and the remaining returned to the acid for a further five minutes. This process of rinsing, removing a sample and re-etching the remainders was repeated so that the sample set consisted of fibres etched for between 10 and 30 minutes in five minute increments.

The BHF solution used consisted of 1 part 49% HF (Asia Pacific Specialty Chemicals), 6 parts 40% ammonium fluoride (NH_4F) (Sigma) and 14 parts 38.7% hydrochloric acid (HCl) (Merck). The ratio of the active components NH_4F:HF:HCl can be expressed as approximately 5:1:11. The three remaining fibre samples were mounted on card and immersed in approximately 25 ml of the BHF/HCl solution. After one minute, the samples were rinsed in de-ionised water and the first fibre removed. The remaining two were placed into the acid together for another minute, rinsed and the second fibre removed. The last fibre was then placed into the acid for a further eight minutes and rinsed giving a sample set containing fibres etched for one, two and ten minutes.

Once etched, the fibres were mounted individually onto small brass rods using conductive SEM tape to allow inspection in an electron microscope. For storage, the samples were kept next to desiccant crystals inside a nitrogen cupboard.

3.3.3 Results and Analysis

To prevent charging of the samples in the electron microscope, the mounted fibres were exposed in a SPI-Module plasma sputter coater (Section 2.3) fitted with a gold target for 80 seconds resulting in a coating thickness of approximately 30 nm.

Investigation using a Philips XL30 SEM microscope indicated that the straight HF acid had preferentially etched the silica outer tube rather then the germanium doped cores (Fig. 3.2).

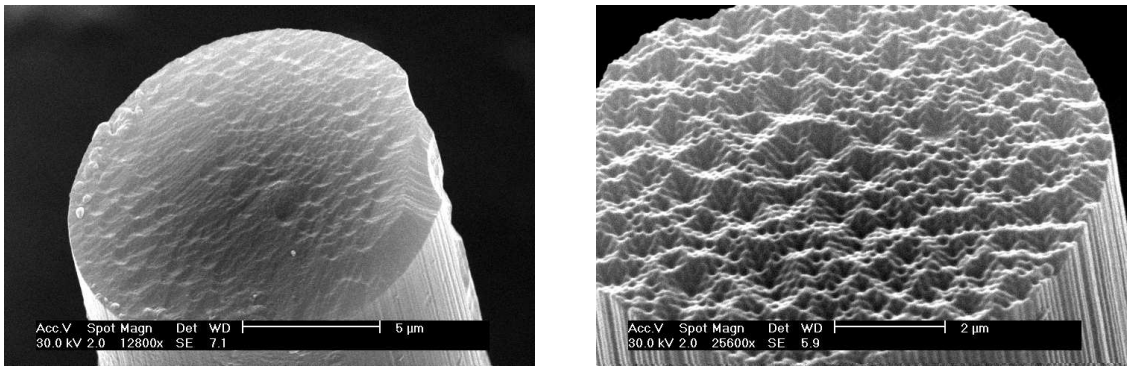

(a) (b)

Fig. 3.2: (a) Imaging fibre after 15 min etching using 10% HF solution and (b) after 30 min

In contrast to the results gained from the pure HF etchant, the fibres prepared using the BHF/HCl solution showed the cores being preferentially etched. This produces the desired result as seen in Figure 3.3 where the cores have formed wells and the silica outer tube is left largely intact. Between the wells, for the samples etched for one and two minutes ($I_C \approx 240$ nm and 340 nm), the remaining matrix material has formed structures resembling rounded pyramids with base lengths of approximately 140 nm and 230 nm respectively. The samples etched for one and two minutes were of satisfactory quality but the last sample etched for ten minutes was found to be severely over-etched.

3.3.3.1 Selectivity

The selectivity of an etchant is determined by comparing how much of the target material was removed to how much non-targeted material was removed. It is quite clear from Figure 3.2 that a pure HF etchant has little to no selectivity for the germanium

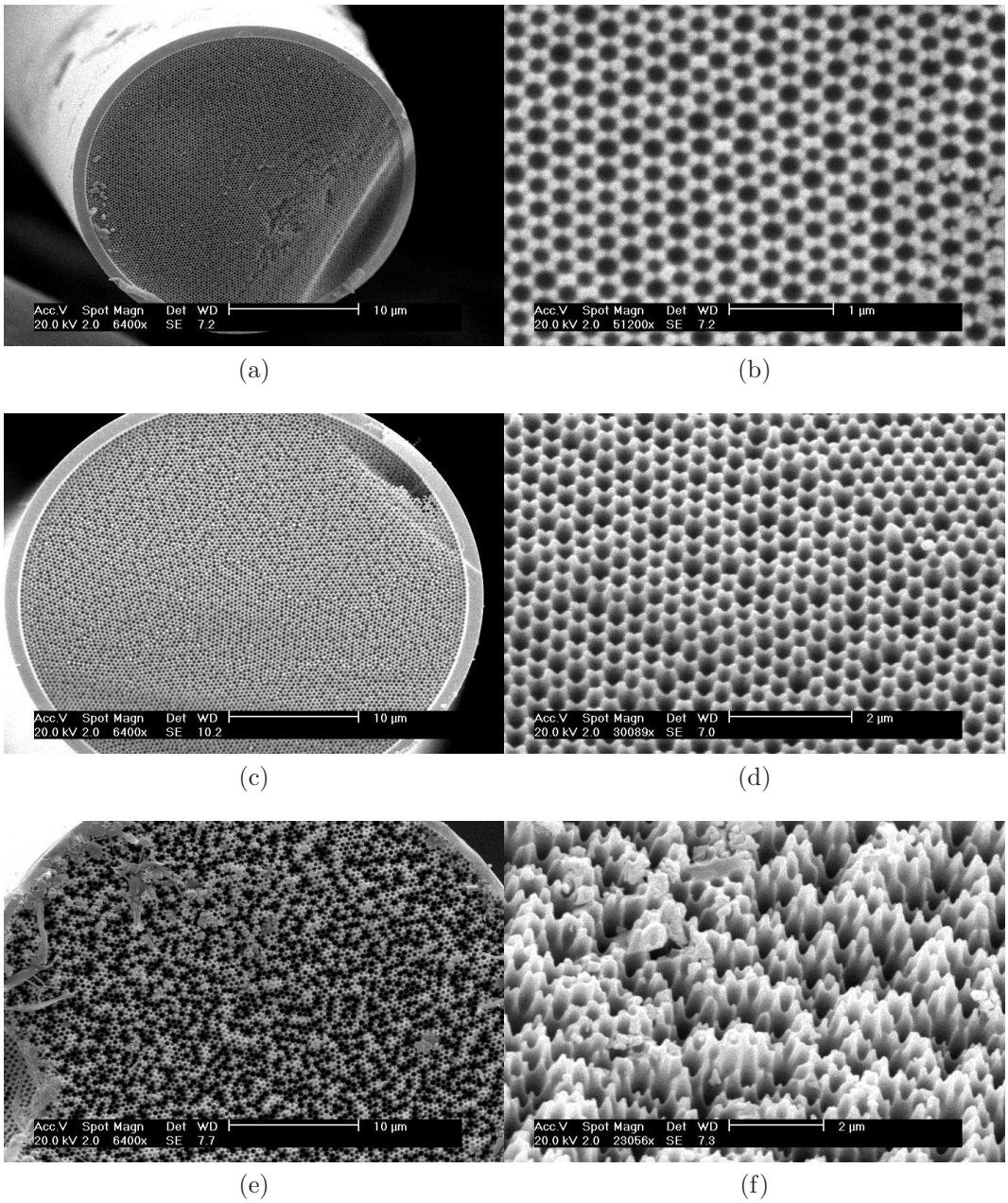

Fig. 3.3: Drawn imaging fibre after etching using the BHF/HCl solution for (a and b) 1 minute ($I_C \approx 240$ nm), (c and d) 2 minutes ($I_C \approx 340$ nm) and (e and f) 10 minutes ($I_C \approx 360$ nm). Images (a), (b), (c) and (e) are taken looking straight down on the fibre tip. Images (d) and (f) are taken at an angle of 30° to the fibre axis.

doped cores. Figure 3.3 on the other hand, shows that the buffered HF solution has a high selectivity.

A possible explanation for the difference may be due to the differences in binding energies between Si-O and Ge-O in the glass matrix (4.7 eV and 3.7 eV respectively) [Rudder et al., 1993]. The lower binding energy of the germanium bond makes it more likely than the silicon bond to break in the presence of an active F^- ion (and form a Ge-F bond). This is similar, in principle, to the F^- etching selectivity noted in pure Si_xGe_{1-x} materials where Ge-Si bonds break more easily than Si-Si bonds [Borel et al., 2004]. As was shown in Section 2.2, a BHF solution generates more F^- by the dissociation of NH_4F than a pure HF solution. Hence it is possible that the relative increase in active F^- ions provides the observed selectivity to germanium.

3.4 SERS

3.4.1 Experimental Setup

The samples etched for one and two minutes in the BHF/HCl solution formed the desired structures and were chosen for further experimentation. The two fibres were coated together with 100 nm of high purity silver (99.99% ProSciTech) using an Emitech K950X vacuum coater with the deposition controlled by a quartz crystal microbalance (Section 2.3). Although several metals exhibit SERS behaviour, silver was chosen as it provides the greatest electric surface plasmon field when excited by light in the visible spectrum (632.8 nm in this case).

Thiophenol (C_6H_6S) (99%+, Sigma-Aldrich) (Fig. 3.4) was chosen as the reference SERS molecule because it has a well know Raman signature and is a strong scatterer. Thiol (sulfur-hydrogen group) tipped molecules are known to bond to noble metal (e.g. silver, gold and copper) surfaces via the sulfur bond [Carron and Hurley, 1991]. The mechanism by which the molecule adsorbs to the surface is believed to be cleaving of the S-H bond to form a S-Ag bond [Bryant and Pemberton, 1991]. Additionally, thiol molecules also form stable self-assembled monolayers (SAMs) on noble metals [Bryant and Pemberton, 1991; Schreiber, 2000; Yang and Liu, 2003]. The SAM formation helps to ensure a consistent molecular coating of the SERS probes from one experiment to another thus ensuring changes in Raman signal counts are due solely to the probes'

performance and not caused by differences in molecular concentration.

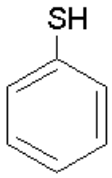

Fig. 3.4: Thiophenol molecule. [Sigma-Alrich-Thiophenol, 2008]

The samples were allowed to soak in a 10 mM solution of thiophenol diluted in ethanol (>99.7%, Merck) for ten minutes. *Note: thiophenol is a dangerous substance that can cause respiratory distress if inhaled and can also attack the central nervous system. Thiophenol should only be handled in an appropriately vented fume hood or with proper breathing apparatus.* The exact adsorption rate of thiophenol onto silver is unknown, however, measurements of thiols adsorbing onto gold indicate a coverage of over 90% is achieved after at most five minutes [Schreiber, 2000; Whelan et al., 1999]. The rate for silver is believed to be similar. The soaking was followed by a rinse in ethanol for two minutes in order to remove any free thiophenol that was not part of the SAM.

Spectra were collected using a Renishaw RM2000 microscope fitted with a 20× lens (0.4 N.A.). In all cases, the spectra are collected by focussing the laser onto the SERS active tip of the fibre and collecting the backscattered signal. Measurements through the fibre were attempted but were found to give no useful data. This is attributed to the losses induced by the sharp taper in the fibre, the lack of a suitable cladding layer and the internal scattering caused by the nanostructured core.

A 632.8 nm HeNe laser (Spectra-Physics Model 127) was used to excite the spectra and a holographic notch filter to reject the laser line from the scattered light. A 1200 l/mm grating was used to disperse the returning beam and the spectra were recorded using a TEC cooled silicon array detector. Five scans of ten seconds each were summed to increase the S/N ratio and a cosmic ray removal algorithm was employed. Power at the sample was approximately 36 μW.

3.4.2 Results and Analysis

Figure 3.5 shows the spectra collected for the samples etched for one and two minutes. All spectra have had the slowly varying background removed by subtracting a 4th order polynomial from the data. High frequency noise was removed by a 3rd order Savitzky-Golay filter with a window size of 11. Spectra are presented as counts per second per milliwatt of incident power at the sample. The high signal counts seen in both spectra are a clear indication the SERS effect is occurring.

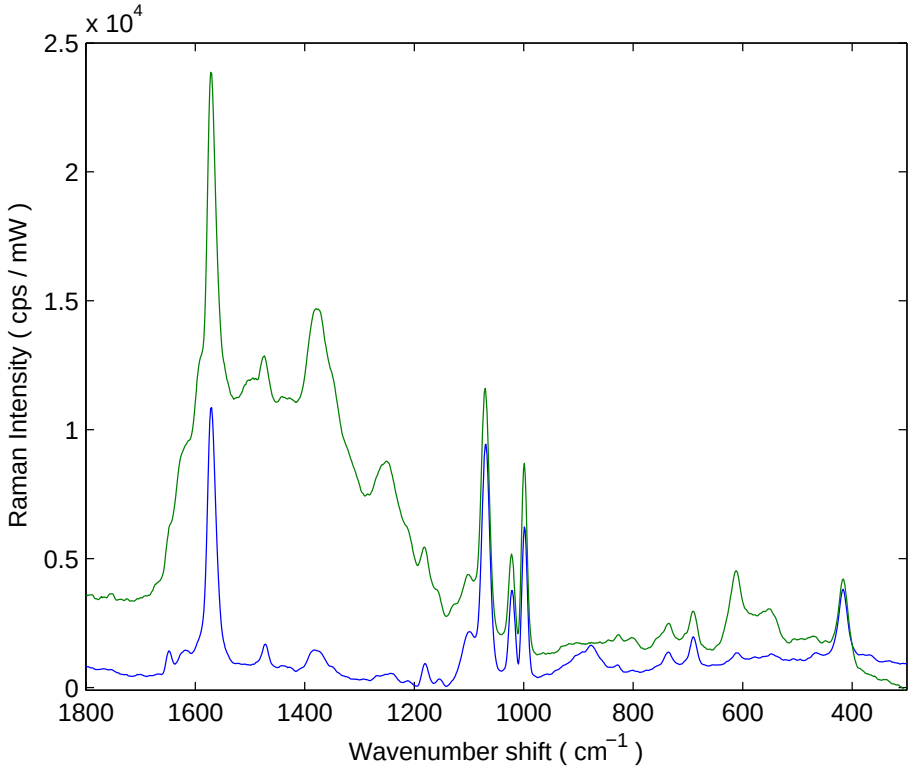

Fig. 3.5: Stokes SERS spetrum of thiophenol from fibres etched for one minute (blue) and two minutes (green) after background subtraction.

The source of the large background signal in the green trace from 1000 cm^{-1} to 1700 cm^{-1} in Figure 3.5 is unknown but may be attributed to excess ethanol (which has a large number of C-H vibrational modes between 1200 cm^{-1} and 1600 cm^{-1}) remaining on the surface.

3.4.3 Enhancement

The calculation of SERS enhancement of thiophenol requires a normal Raman spectrum of the molecule to be taken. A few mililitres of pure thiophenol were placed into a thin glass vial. A 50× ULWD lens (0.55 N.A.) was used to collect the spectra of both the glass cell and the thiophenol within. Once again, five scans of ten seconds each were summed to increase the S/N ratio. Measuring the relatively low NRS of thiophenol required the laser power be increased to 2 mW. Even so, the signal count for the main peak at 1000 cm^{-1} was still quite low producing approximately 40 counts/second/mW. Subtracting the spectrum of the glass vial results in the lower spectrum shown in Figure 3.6. Note that in the thiophenol spectrum, the peaks associated with the vial (1600 to 1800 cm^{-1}) are of a lower intensity. This is a result of the confocal nature of the microscope. For the vial spectrum, the objective was focussed onto the surface whereas for the thiophenol spectrum, the focus was moved into the vial. As such, the spectral intensity from the now out-of-focus vial is considerably lower. This results in the negative spectral counts seen in the lower graph.

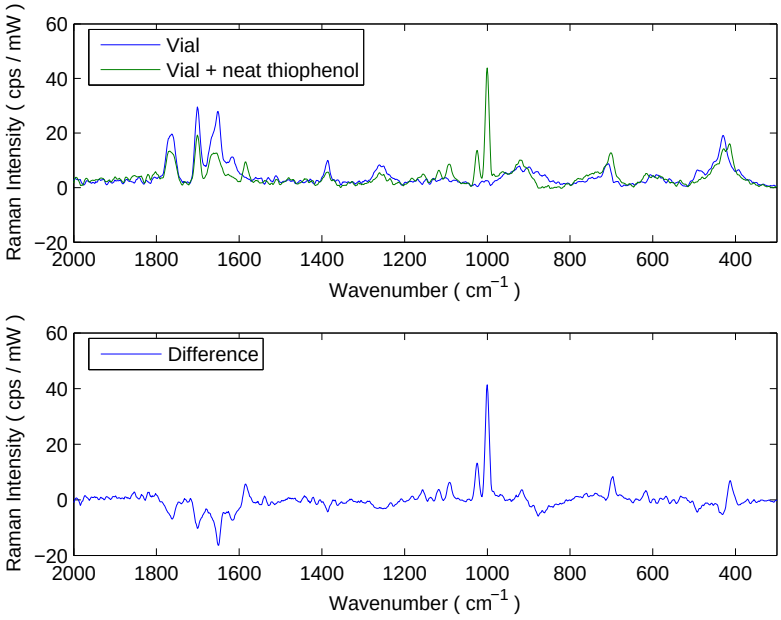

Fig. 3.6: NRS spectrum of thiophenol after background subtraction taken with the Spectra-Physics Model 127 623.8 nm laser. Power at the sample was approximately 2 mW.

3.4.3.1 Calculation

To determine the enhancement factor, the spectra in Figures 3.5 and 3.6 are normalised to the estimated number of molecules contributing in each case. For these calculations, the Raman peak at 1000 cm^{-1} is used as it is clearly visible on both the NRS and SERS spectra. Once normalised, Equation 1.1 is simplified to:

$$E = \frac{\text{SERS peak height at 1000 } cm^{-1}}{\text{NRS peak height at 1000 } cm^{-1}} \tag{3.1}$$

For the NRS measurement, the number of contributing molecules was calculated by determining the number of molecules situated in the focal volume. For the SERS measurement, the number of molecules contributing was calculated by estimating the number of molecules in the planar focal spot. This equation is used as it gives a simple *in* or *out* comparison (ie. for the same system, what are the counts with the SERS fibre present: *in*, or not present: *out*). This is useful as it gives a very practical result.

A simple example of the calculation of this term is presented in Table 3.1. A thorough breakdown of this calculation is presented in Appendix A.

Sample	Signal (cps/mW)	No. molecules contributing	Ratio (cps/mW/molecule)
Bulk	40	4.7×10^9	
1 min etch	5673	3.4×10^6	200×10^3 ($\approx 10^{5.3}$)

Table 3.1: Variables for signal intensity enhancement calculation.

Applying these equations to the spectra gained from the fibres etched for 1 and 2 minutes gives the values presented in Table 3.2.

I_C (nm)	Etch time (min)	Signal intensity enhancement ($log_{10}E$)
240	1	5.3
340	2	5.5

Table 3.2: Signal intensity enhancements.

The above equation is not however, a true measure of enhancement. In order to

calculate the real figure, the *exact* number of molecules in a saturated monolayer in the focal volume on the surface of the fibre needs to be known. In other words, the number of molecules that may be on the walls of the structures need to be known. The calculation here, however, is made on the basis of a monolayer coverage of thiophenol in the *planar* surface area covered by the laser focus. This approximation is based on the assumption that the surface regions that are oriented parallel (i.e. the walls) to the evaporated metal flux would not be coated. This scenario is unlikely as the samples were positioned by eye and hence would almost certainly not be perfectly parallel to the flux.

Unfortunately, there is no easy way to determine the degree of metal coating in the wells and hence the number of extra molecules present. A traditional technique for measuring the coverage of thin films is electrolysis (coulometry) [Kenzin et al., 1996]. In essence, this method requires measuring the amount of current needed to dissolve a known area of film of a known thickness. The method, however, cannot be used on the coated fibres for a number of reasons. Firstly, electrolysis requires attaching an electrical supply to the coated surface. The minute surface area and the fragility of the fibres make this a very difficult task. Secondly, this method can only work on continuous films. Given the surfaces of the well walls are almost parallel to the coating source, the probability of a continuous film being present over these surfaces is low.

Because of this uncertainty, the simplified equation above is used. The net result of this simplification is an overestimation of the enhancement as there is likely an underestimation of the number of molecules contributing to the total SERS signal.

It is also important to note that the SERS effect seen is averaged over the focal spot size. In regions where metal nanoparticles are at an optimal separation, the enhancement may be very high. Conversely, in other regions, the enhancement may be very low. As the focal spot of the laser is larger than any of these individual features, regions with a wide range of enhancement may be averaged together. Without the ability to select a single nanoparticle site, this makes the calculation of a true single enhancement factor difficult. As an aside, previous works have used near-field scanning probe techniques to study individual SERS sites [Prikulis et al., 2003]. This, however, is beyond the scope of the project.

Both of the above issues prevent an accurate measure of the enhancement factor. The enhancement therefore, should only be expressed in terms of orders of magnitude.

For the remainder of this thesis, the more mathematically precise term of "counts per second per milliwatt (cps/mW)" is substituted as it is the number of signal counts per second that is the observable quantity of practical interest.

This value is also dependent on the system on which the spectrum was recorded as it is directly related to the type of objective lens used, the efficiency of the grating and the efficiency of the detector. It is for these reasons that the spectra shown in the following chapters can only be compared against those in the same experimental set and not others.

Ultimately, the exact SERS enhancement value is not important. The data shown here demonstrate that the SERS effect is occurring. What is of more interest is how the different structures and fibre types vary this behaviour.

3.5 Dependence on Surface Features

When varying the diameter of the drawn fibre, the internal structure is scaled proportionally. To help illustrate how this affects the etching behavior consider the two fibres shown in Figure 3.7. The fibre on the left has cores with a diameter of two units spaced four units apart. The one on the right has cores with a diameter of one unit spaced two units apart. If they are both etched for the same period of time, the diameters of the cores will increase by the same amount regardless of the initial diameter. If we say that the etch increases the core diameter by one unit, the fibre on the left now has cores with a diameter of three units and the one on the right, two units. So, after etching, the fibre on the left has cores of three units spaced four units apart. Clearly, the matrix between them remains intact. However, the fibre on the right has cores of two units spaced two units apart - and they now overlap. The matrix is no longer intact and instead, triangular islands remain between the cores. Given that the matrix etches down from the top at the same time it's etching out from the cores, this transition to separated islands occurs first at the surface of the fibre.

To determine how the SERS signal counts vary with changing inter-core spacing and etch time, 12 new fibre samples were prepared.

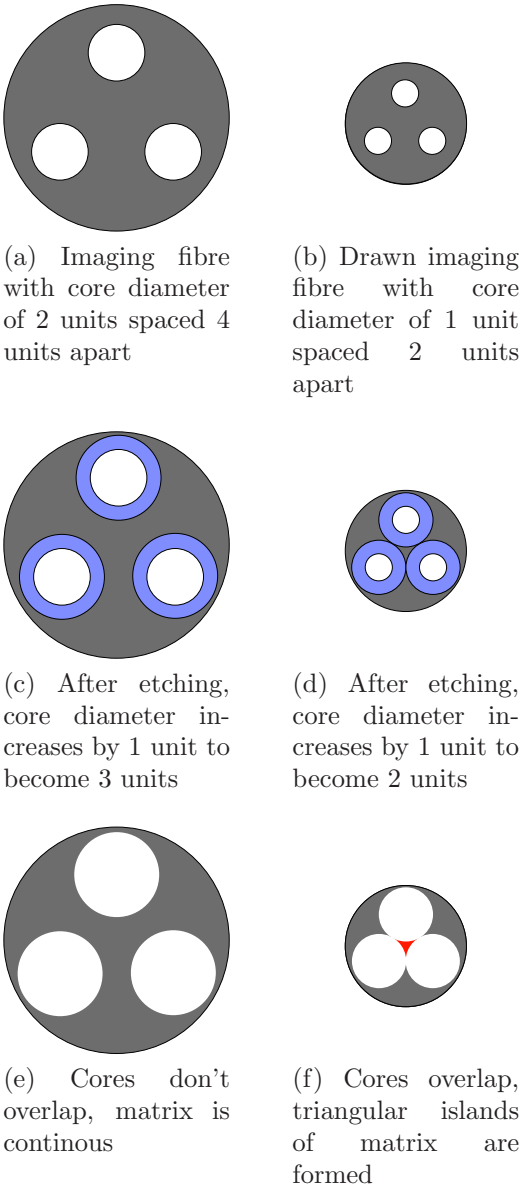

(a) Imaging fibre with core diameter of 2 units spaced 4 units apart

(b) Drawn imaging fibre with core diameter of 1 unit spaced 2 units apart

(c) After etching, core diameter increases by 1 unit to become 3 units

(d) After etching, core diameter increases by 1 unit to become 2 units

(e) Cores don't overlap, matrix is continous

(f) Cores overlap, triangular islands of matrix are formed

Fig. 3.7: Structure dependence on fibre size given a fixed etch duration.

3.5.1 Experimental Setup

Due to the problems encountered in drawing the fibre discussed in Section 3.3.1, an alternate method was employed to prepare a second set of samples. For these samples a small butane torch was used as the heat source and the fibre drawn by hand. The lower flame temperature results in the fibre taking longer to reach the softening temperature but once that temperature is reached, a slow and gentle application of tension by hand resulted in a more controlled taper with less breakage. Although the exact temperature of the flame is not know, it is estimated to be between 1000 and 1200 °C.

A microscope with a graticule was again used to locate the positions of the desired diameters (15 μm to 70 μm) along the taper of the fibre. For the larger fibres (>40 μm) the FITEL S-311 cleaver was used to cleave the fibres at the desired point.

The smaller fibres (<40 μm) proved too fragile for the above method. Instead, advantage was taken of the micro-cracks already present in the fibre. When the fibre is drawn under the above conditions, many micro-cracks are believed to form as a result of the stresses of the draw. By simply clamping the fibre at the desired point and applying tension, the fibre cleaved usually within 2-3 mm of the desired point. Two sets of fibre samples were produce using this method, one with a range of I_C of between 150 nm and 650 nm to test the surface structure dependence on spacing and the other set all having I_C of approximately 250 nm for testing the structure dependence on etch time. Although it would be preferable to use the same samples to study both spacing and etch time dependence, the need for metal coating to activate the surface made this unfeasible.

To test the dependence on inter-core spacing, the seven samples forming the first set were etched together in the buffered hydrofluoric acid solution prepared in the same manner as Section 3.3.2 for 30 seconds, rinsed twice in de-ionised water and mounted for inspection in the XL30 as described in Section 3.3.3. A selection of the fibres is shown in Figure 3.8. Note that depending on the inter-core spacing, the structures formed are either rod-like, triangular or planar.

To determine the dependence on etch time, the fibres of the second set were etched individually in the same manner as above for 10, 15, 20 and 30 seconds respectively. After etching, all samples were rinsed twice in de-ionised water and mounted for inspection. As before, samples were stored in a nitrogen cupboard when not in use.

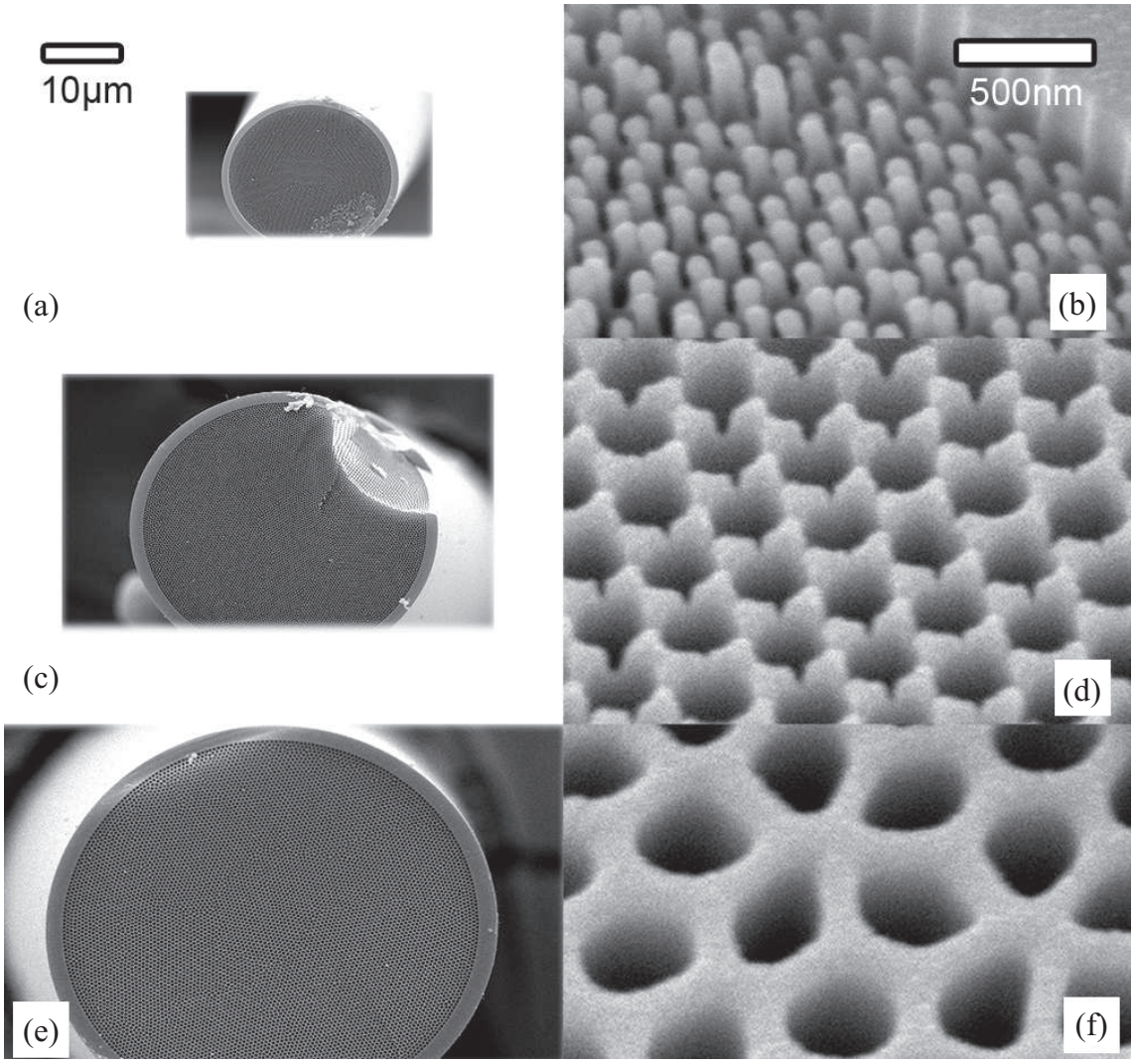

Fig. 3.8: Whole fibre tip and surface detail images of fibres with an inter-core spacings of (a and b) 250 nm, (c and d) 420 nm and (e and f) 650 nm after 30 seconds etching using BHF solution. Note the slight contamination of the samples on (a) the lower right and (c) the top. These are believed to be caused by contact with the adhesive on the conductive tape and dust respectively. Care was taken to ensure spectra were only gathered from the uncontaminated areas.

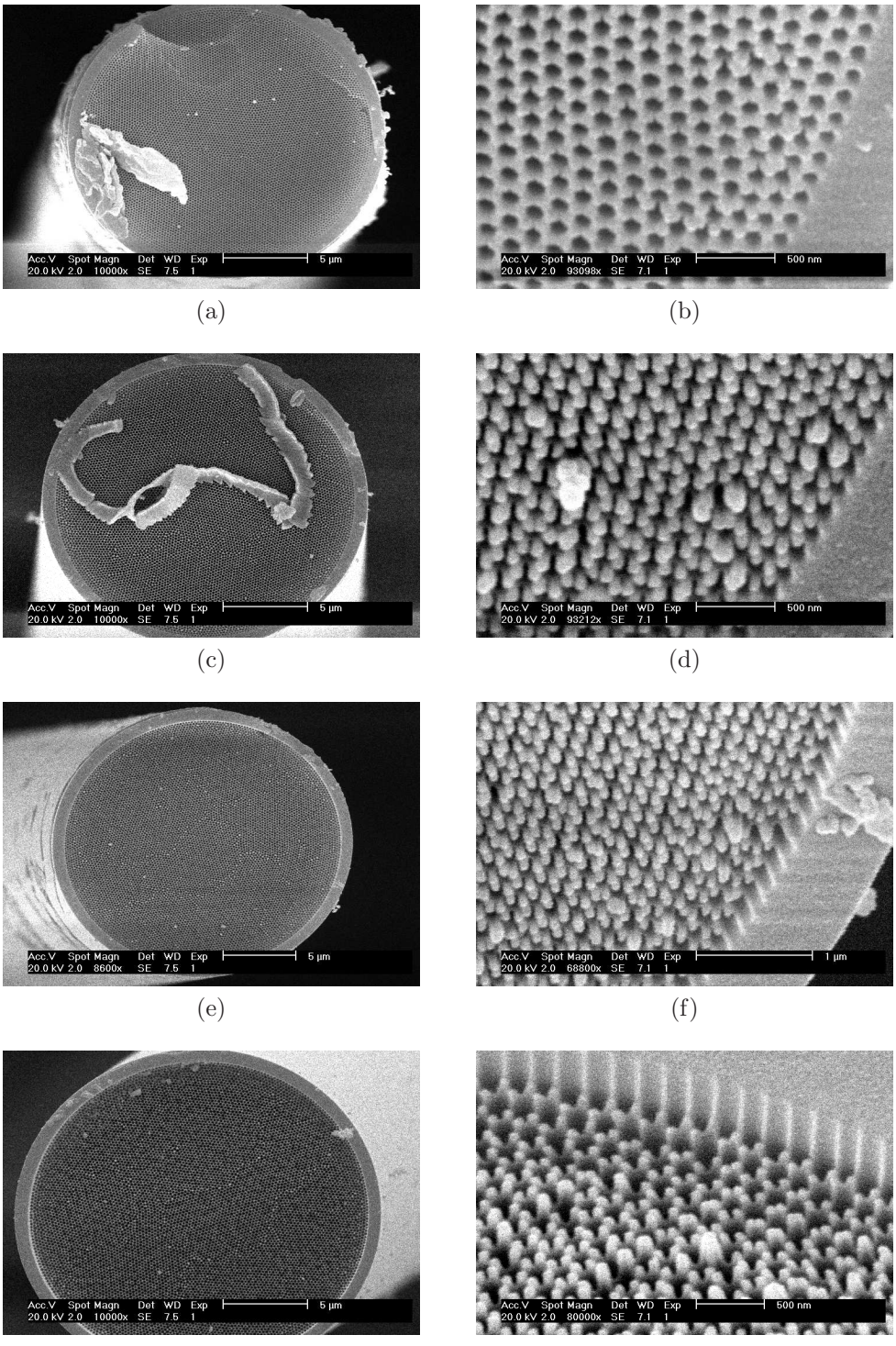

Fig. 3.9: Fibres with $I_C \approx 250$ nm etched for 10 seconds (a and b), 15 seconds (c and d), 20 seconds (e and f) and 30 seconds (g and h). Note the sample contamination by dust particles on (a) and (c) and to a lesser extent (f).

As in Section 3.4.1 all samples were coated with 100 nm of silver using the Emitech coater and soaked in thiophenol for ten minutes followed by a rinse in ethanol for an additional two minutes. The RM2000 system, this time fitted with a 50× ULWD lens was again employed to gather the spectra. In each case, five accumulations of ten seconds each were summed together. For the inter-core spacing test, power at the sample was approximately 20 μW (except for the $I_C = 150$ nm sample where power was increased to 40 μW). However, for the etch time test, a 632.8 nm Coherent 40.6" HeNe was employed in lieu of the Spectra-Physics Model 127. For this test, power at the sample was approximately 40 μW. All spectra are presented in units of cps/mW.

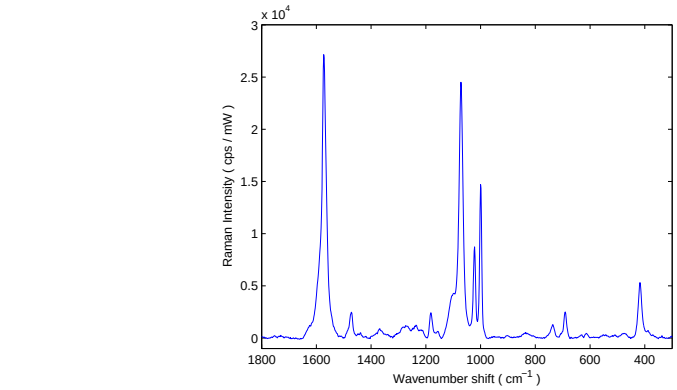

(a)

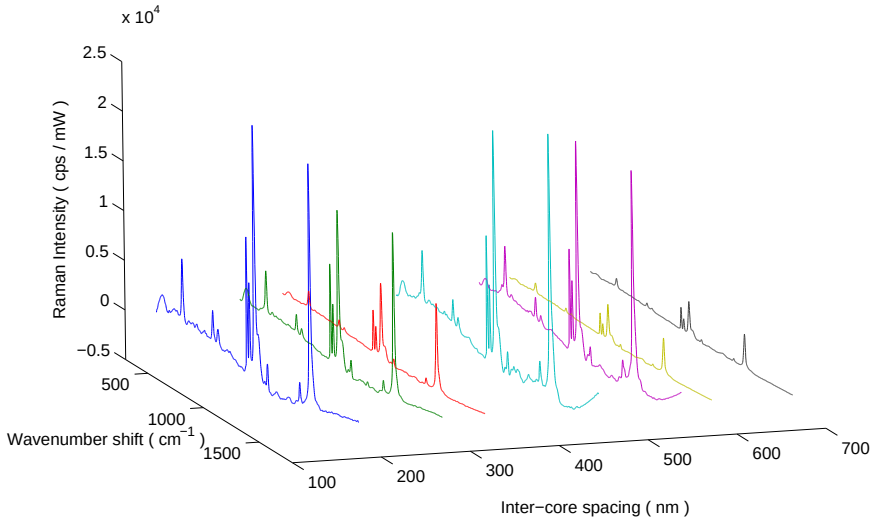

(b)

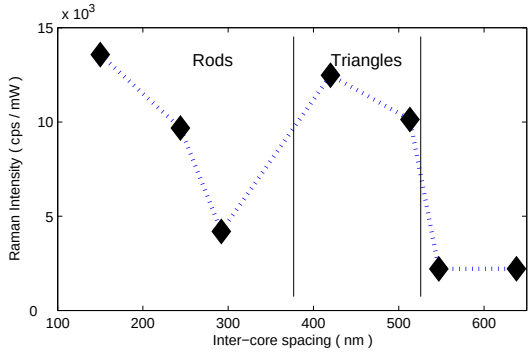

(c)

Fig. 3.10: (a) SERS spectrum of thiophenol taken on a fibre with an I_C of 420 nm after background subtraction; (b) SERS spectra for the fibres of varying inter-core spacing after background subtraction and (c) Raman intensity of the 1000 cm^{-1} peak plotted against the inter-core spacing and structure regime. Diamonds represent collected data points - the dotted line is included as an aid to the eye.

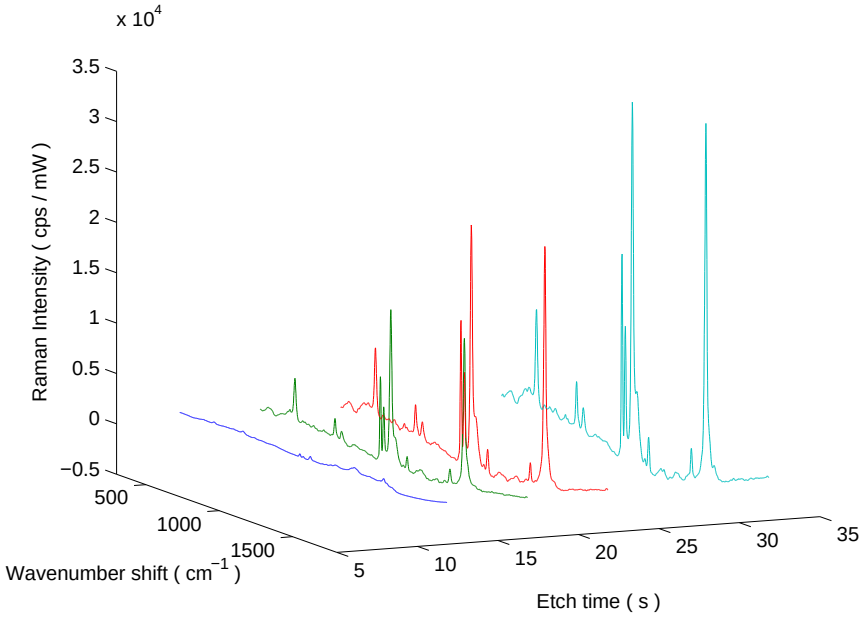

(a)

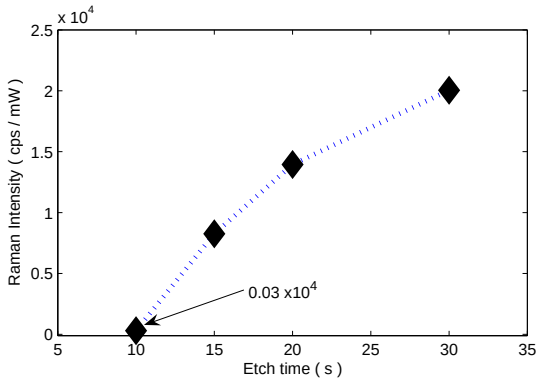

(b)

Fig. 3.11: (a) Background corrected SERS spectra for the fibres with $I_C \approx 250$ nm after varying etch durations; (b) Raman intensity of the 1000 cm^{-1} peak plotted against the etch time. Diamonds represent collected data points - the dotted line is included as an aid to the eye.

3.5.2 Results and Analysis

3.5.2.1 Dependence on Inter-core Spacing

Figure 3.10 (a) shows the SERS spectrum of thiophenol taken from the fibre with an I_C of 420 nm. Figure 3.10 (b) shows all the spectra collected for fibres with I_C of 150 nm to 650 nm. Figure 3.10 (c) shows the height of the 1000 cm^{-1} peak as a function of this inter-core spacing. The figure is divided according to the feature regimes produced, namely rods, triangles and continuous flat surfaces. As can be seen from the graph, both the rods and triangles produce higher signal counts than the planar surface. Additionally, smaller rods and triangles produced higher counts than larger rods and triangles respectively. It is interesting to note that the highest enhancement factor is generated by the surface with the triangular structures pointing at each other. This is in keeping with the high field intensity predicted for such a geometric configuration [Hao and Schatz, 2004].

3.5.2.2 Dependence on Etch Time

Figure 3.9 shows the fibres with an I_C of approximately 250 nm after etching for 10, 15, 20 and 30 seconds. Increasing the etch time produces samples with increasing SERS signal counts (Fig. 3.11). A preliminary explanation for this is that as the etch progresses, the surface area available increases. This increase however, does not fully explain the increase in Raman activity observed. The initial increase seen after the 10 second etch is most likely due to the fibre tip now having nanostructure (Fig. 3.9 (d)). Figures 3.9 (d), (f) and (h) indicate that the structure (arrays of rods) does not appreciably vary from this point. Rather, it appears the structures simply progress deeper into the fibre. Thus the observed signal increases beyond this point may be partially due to the increase in surface area and not change in structure. There cannot be a direct relationship to surface area as the metal coating applied does not produce a complete coverage of the well walls and hence the number of molecules contributing to the signal will not increase at the same rate as the surface area.

3.6 Conclusions

The results presented in this chapter demonstrate the potential of using tapered imaging fibres etched in a buffered hydrofluoric acid solution and coated with silver as SERS-capable substrates. An estimate of the signal enhancement can be made, but is not accurate as the exact number of molecules contributing to the Raman signal cannot be determined and is most likely underestimated. Because of this, the values presented are likely to be an overestimation.

When investigating the dependence of SERS activity on structure, the limited number of samples available (and the contaminants such as dust, glue, etc. found of them) require that caution be applied when drawing conclusions from the data. What can be stated, is that the different structure regimes do appear to produce different enhancement factors and the highest enhancements are associated with structures known to exhibit large plasmon field strengths.

It is clear that a simple silver covered surface can produce an enhancement factor on its own. This can be attributed to the rough "island" nature of the silver deposition. It is likely that several "hot spots" are produced between neighbouring silver particles leading to a SERS ability. However, it is also clear that when nanoscale structures are present, the enhancement can increase by approximately an order of magnitude. Thus there are likely to be two structure regimes present - each contributing to the overall enhancement. The variability in enhancement seen across the surface of a sample may also be a function of the deposition roughness. The limited resolution of the XL30 SEM prevents images of this sub-structure being taken and hence no data is available to describe it. However, experiments on different fibre samples conducted using the Supra 40VP microscope as discussed in Chapter 6 do show the nature of this roughness.

The variation of Raman activity as a result of the etch time can be possibly attributed to two different mechanisms. Initially, the transition from a continuous surface to discrete structure produces a large increase in intensity. A component of the extra signal counts seen after this transition may be attributed to the increased surface area of the wells allowing more molecules to attach to the surface. The increase is not directly proportional to the change in surface area as the metal coating does not cover the entire surface area of the well walls. Once again, the limited number of samples available for this experiment and the difficulty of measuring the precise shape of the

wells prevents further analysis of these mechanisms.

The small number of good quality samples generated by the manual production methods shown here prompted investigation into large scale manufacturing of nanostructured optical fibres. Before this can happen, however, a greater understanding of the fibre etching process as well as the effects of dopant diffusion as a function of the draw temperature is required. These are both needed in order to identify ideal manufacturing parameters.

Chapter 4

Simulation of Etching Progression and Dopant Diffusion in Nanostructured Optical Fibres

4.1 Introduction

In order to develop an understanding of the progression of structures found in the previous chapter, a simulation program was written. The aim of the software was to visualise the transition from a planar surface to one with etched wells and then to one with nanostructures. Furthermore, the program also simulates how a fibre produced using an industrial scale system with comparatively high temperatures would react to the acid etchant.

The transition from using the manual methods of fibre production shown in the previous chapter to using industrial-scale systems requires several changes to the manufacturing technique. Principal among these is the softening of the fibre bundle using an annular furnace in lieu of a small butane torch. Whereas in the torch flame, the fibre was held in the "hot zone" for only a second or two, in the furnace the fibre is likely to be held at a high temperature for much longer. This increase raises the importance of understanding dopant diffusion within the glass. The simulation program written can take into account this dopant diffusion when modeling the progression of the etch.

4.2 Computer simulation

The purpose of the simulation program is to visualise the progression of the acid etchant into an imaging fibre and the resulting progression of structures on the surface. The program was written using Microsoft Visual C++. Simulating the 10,000 cores comprising the FIGH-10-350S fibre is obviously not a feasible option but given the general structure of the fibre, this is not necessary. A repetitive honeycomb structure like the fibre cores can be broken up into a unit cell as shown in Figure 4.1. Furthermore, the simulation takes advantage of two axes of symmetry within this cell (also shown in Fig. 4.1). Doing so reduces the required calculations to a quarter of the entire cell.

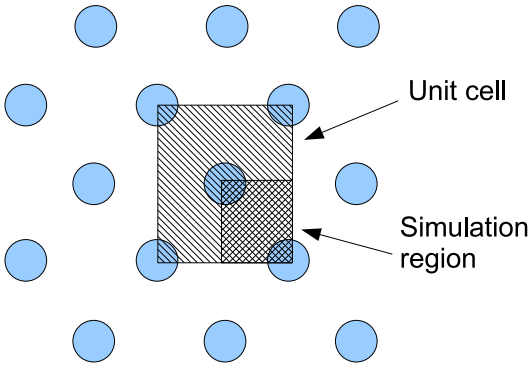

Fig. 4.1: Rectangular unit cell and simulation region in a hexagonal lattice.

4.2.1 Initial Conditions

A number of initial assumptions must be made in the simulation:

1. Imaging pixels have a diameter of 200 nm
2. $I_C = 400$ nm
3. Etch rate of core is 4,400 nm/min
4. Etch rate of matrix structure is 200 nm/min

The spacings above correspond to a FIGH-10-350S fibre drawn to approximately 10% of its original size. The initial etch rates were estimated by measuring the well

dimensions of an etched FIGH-10-350S fibre (Fig. 1.10). Note: the experimental values have an error of approximately 10% as a result of resolution the limit of the XL30. However, the values shown above are the exact figures used in the simulation. As a result, the accuracy of the simulation output must be considered with this error in mind. Using these values, the initial distribution of etch rates for a unit cell is shown in Figure 4.2. It is assumed that the etch rates inferred from the as-received image fibre allow for diffusion of etchant and reactants in the liquid above the glass surface.

As stated previously, the simulation only considers 1/4 of the unit cell and as such simulates a volume measuring 200 nm wide, 344 nm long and 2,048 nm deep broken into cubic elements measuring 4 nm on edge.

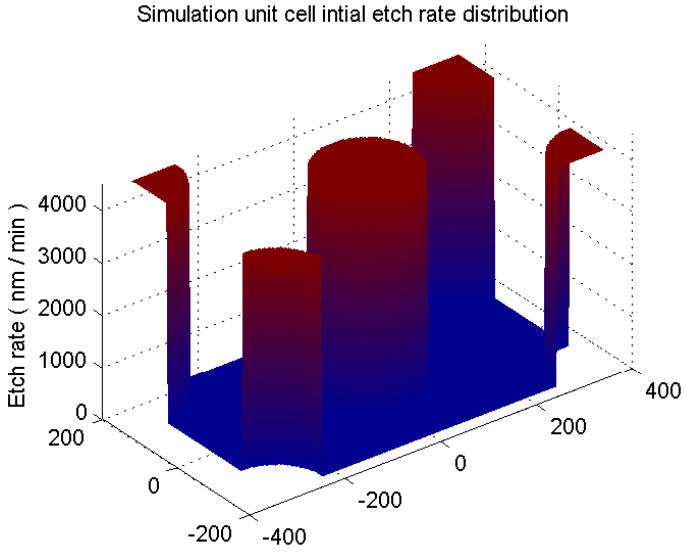

Fig. 4.2: Initial etch rate distribution.

4.2.2 Program Structure

The program holds a 3 dimensional array of elements representing the 1/4 unit cell where each point holds two values: the rate at which it etches and the percentage eroded away. The program accepts inputs for the etch rates in the x and y dimensions as the rates are assumed to be dependent on the cross section of the fibre (the z dimension along the length of the fibre is considered constant). The basic simulation outline is shown below:

```
(1) calculate possible exposures

loop
{
(2) for every element
    {
    if not acid
        {
            determine exposure and erode element
        }
    }
(3) for every element
    {
        if amount remaining <= 0
        {
            element becomes acid;
        }
    }

(4) find surface
}
```

Functions (1)-(4) are shown in detail in Appendix B.

The exposure parameter is determined using a nearest neighbour principle. For each element in the simulation, the program first determines how many of its neighbours (up to 26: 3 x 3 x 3 - 1) are acid. The particle is then eroded by a percentage depending on this quantity. Figure 4.3 illustrates three of these scenarios. As can be seen, when 3 of the neighbours are acid, the central particle is 25% exposed. When 9 neighbours

are acid, it is 50% exposed and when 15 are acid, 75% exposed. When plotted, these (and other predetermined) values approximate a sine curve (Fig. 4.4).

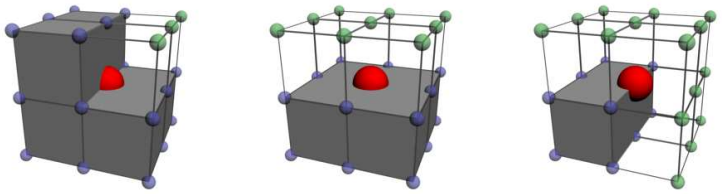

(a) (b) (c)

Fig. 4.3: (a) 3 points are acid = 25% exposed, (b) 9 points are acid = 50% exposed and (c) 15 points are acid = 75% exposed

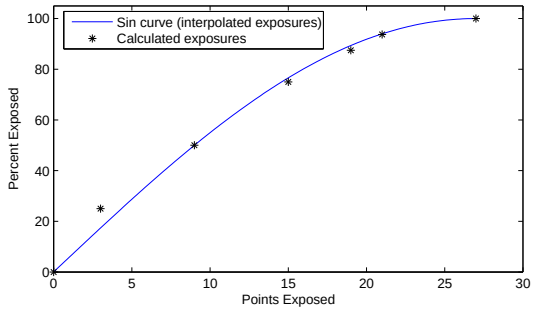

Fig. 4.4: Particle exposures curve.

In practice, the exposures are doubled such that with 9 neighbours acidic (ie. half exposed) the particle will erode at 100% of the specified rate (eg. 4,400 nm/min for the cores). This ensures the cores etch down at the required speed.

In order to reduce the quantisation errors associated with any finite time system such as this, the program calculates 2000 steps for every second of simulation time. As the maximum possible etch rate of a particle is 4,400 nm/min (73.3 nm/s), and each element measures 4 nm across, the particle will undergo the above operations 109 times before complete erosion at this rate (ie. 27 steps per nm). This implies a maximum quantisation error (on the z axis) of 0.9%. Although this error compounds as the simulation runs, it must be remembered that this is the absolute worst case. As another example, for a particle etching at 600 nm/min (as encountered later in Section 4.3), this error drops to approximately 0.1%.

4.2.3 Visualisation and Results

In order to visualise the output of the simulation, the data produced by the program (the "surface" value found in function (4) above) was first saved as a 16-bit data file. This information was converted to a height map which was then imported into Autodesk's 3D Studio Max 5 - an animation package. In Max, the data was then mirrored and replicated to produce the output shown in Figure 4.5. It must be remembered when comparing these images to those in the previous chapter that the prototype fibres had a layer of gold approximately 30 nm thick deposited over the nanostructures. As such, it is likely the rod-like structures seen in Figures 3.8 and 3.9 are sharply tapered pyramids capped with metal. Higher resolution images taken later using the 40VP SEM on subsequent fibres agree with this interpretation.

The matrix breakthrough occurs after a simulated etch time of approximately 28 seconds (Fig. 4.6). This is consistent with the results shown in Figure 3.8 (d). This picture shows a fibre etched for 30 seconds and clearly shows the recent matrix breakthrough. Matching the results gathered in the previous chapter indicates the simulation is producing an accurately model of the etch process.

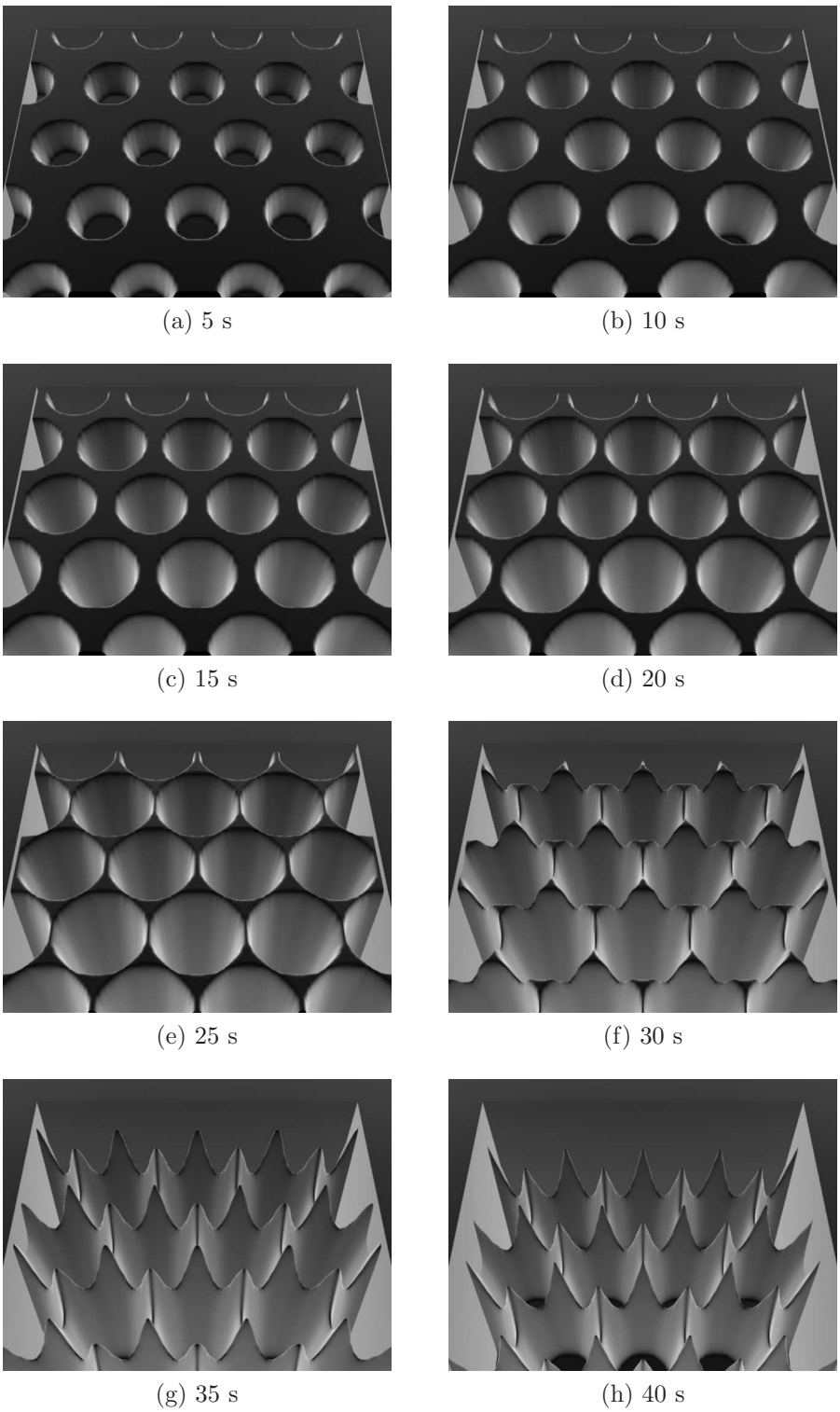

(a) 5 s (b) 10 s

(c) 15 s (d) 20 s

(e) 25 s (f) 30 s

(g) 35 s (h) 40 s

Fig. 4.5: Simulation output for fibre based on initial conditions.

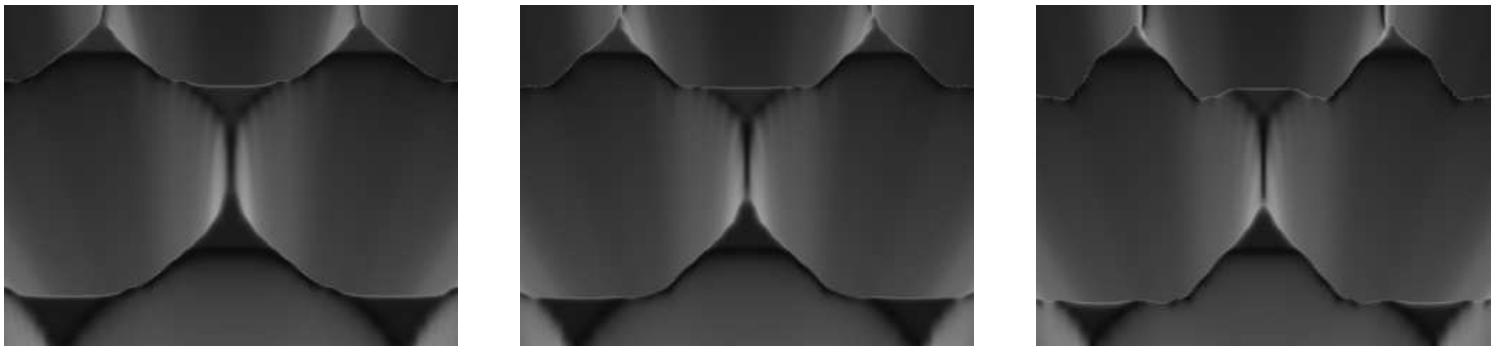

(a) 27 s (b) 28 s (c) 29 s

Fig. 4.6: Simulation output for fibre based on initial conditions at 27, 28 and 29 seconds showing matrix breakthrough and triangular structures.

4.3 Diffusion

4.3.1 Theory

The aim of this theoretical exercise is to create a 2-dimensional convolution mask that can be applied to the 2-dimensional cross-section distribution of dopants within an imaging fibre in order to determine the diffusion of atoms at certain temperatures and times. The output of this convolution operation is then imported into the simulation program that models the resultant development of structure on the fibre axis during etching.

The diffusion of a particle can be described using the Arrhenius equation [Carslaw and Jaeger, 1959; Laidler, 1984]:

$$D = D_0 \exp^{-\left(\frac{E}{RT}\right)} \tag{4.1}$$

where D_0 is the pre-exponential term $[m^2/s]$, E is the activation energy $[J/mole]$, R is the gas constant $[8.314\ J/(K \cdot mole)]$ and T is the temperature in Kelvin.

In this case, we are only considering the diffusion of dopant atoms radially 'out' of the pixel cores and as such can treat the diffusion range as one dimensional, giving:

$$\langle r^2 \rangle = 2D \cdot t \tag{4.2}$$

where t is the time $[seconds]$. This produces the radial diffusion length (D_L) of:

$$D_L = \sqrt{2D \cdot t} \tag{4.3}$$

The diffusing atoms travel according to Brownian motion and, as such, have a Gaussian shaped concentration curve, which in 2 dimensions can be expressed as:

$$f(x, y) = \exp^{-\left(\frac{x^2 + y^2}{\sigma^2}\right)} \tag{4.4}$$

where $\sigma^2 = \langle r^2 \rangle = 2D \cdot t$.

Brownian motion also has the condition such that at any time t, the curve conforms to the probability distribution function:

$$\int_{-\infty}^{\infty}\int_{-\infty}^{\infty} f(x,y)dxdy = 1 \tag{4.5}$$

which expresses conservation of mass in the system.

Replacing σ in Equation 4.4 and normalising the area to unity as per Equation 4.5 now gives:

$$f(x_i, y_i) = \frac{\exp^{-\left(\frac{x_i^2+y_i^2}{2D\cdot t}\right)}}{\sum_{i,j}\exp^{-\left(\frac{x_i^2+y_i^2}{2D\cdot t}\right)}} \tag{4.6}$$

Equation 4.6 is now be used to generate a filter which can be convolved with a matrix containing the estimated etch rates of the glass dopants.

4.3.2 Analysis

Lyytikkainen *et al.* quote the following experimental values for the diffusion of germanium in a drawn silica optical fibre:

$$\begin{aligned} D_0 &= 2.4 \times 10^{-6}\ m^2/s \\ E &= 310 \times 10^3\ J/mol \end{aligned}$$

Table 4.1: Diffusion parameters. [Lyytikainen et al., 2004]

Figure 4.7 (a) shows the diffusion coefficient D (expressed as nm^2/s) for the values quoted in Table 4.1. Figure 4.7 (b) shows the diffusion length (D_L) for temperatures of 1000 to 2000K and times up to one minute. Figure 4.8 shows four values from Figure 4.7 (b) illustrating the dramatic increase in D_L with increasing temperatures.

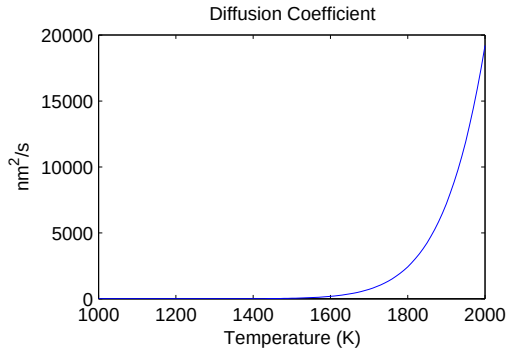

(a)

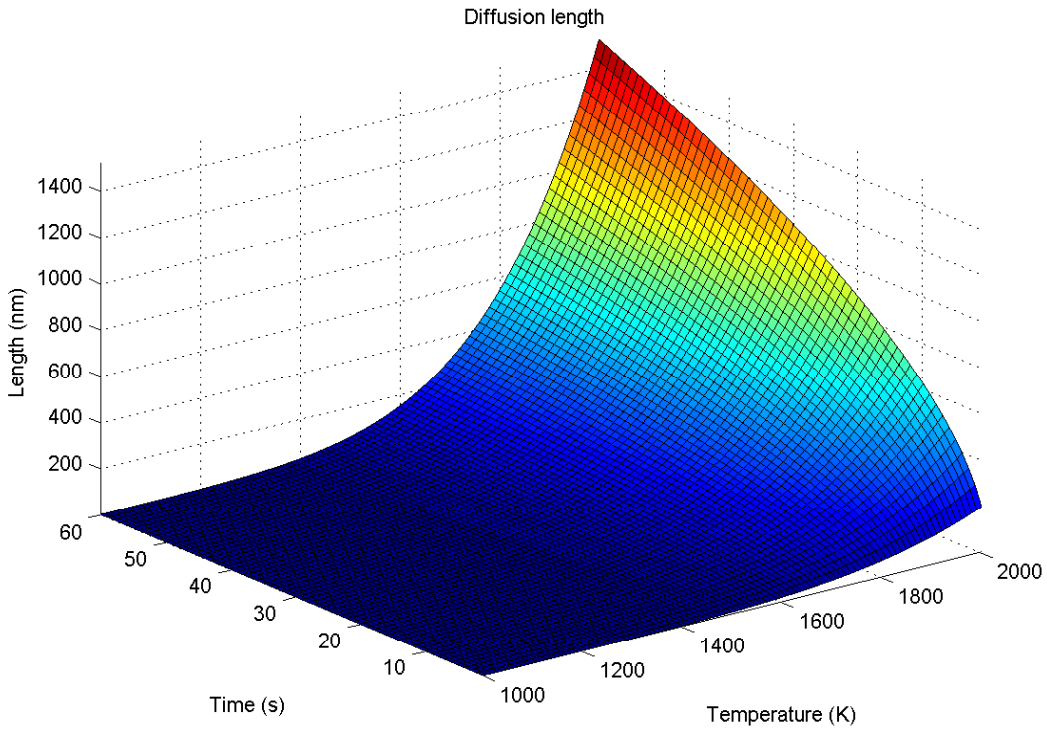

(b)

Fig. 4.7: (a) Diffusion coefficient D as a function of temperature and, (b) D_L as a function of temperature and time.

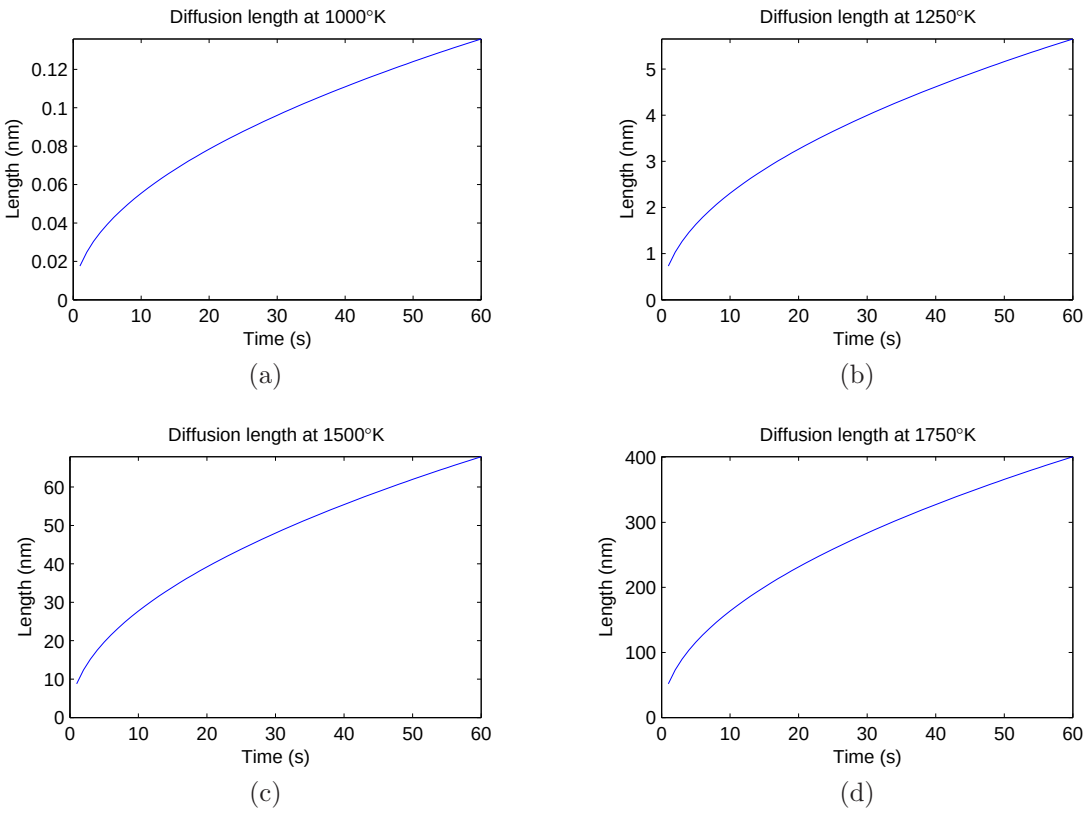

Fig. 4.8: D_L at (a) 1000°K, (b) 1250°K, (c) 1500°K and (d) 1750°K.

4.3.3 Etch Rate Distribution with Diffusion

For the purposes of the simulation, D_L ranges of 20 nm to 180 nm (in 20 nm steps) were simulated. This equates to D_L / I_C ratios of 5% to 45% for an I_C of 400 nm. This ratio is hereafter referred to as the 'smearing ratio', ξ_d. It should be noted that structures produced from fibres with the same ξ_d will look identical regardless of the I_C. What does vary with I_C, however, is the amount of time needed to generate such structures (smaller I_C will produce structures faster than larger I_C for a given etchant). Additionally, as the etch rate is dependent on the concentration of acid, the time values can also be scaled accordingly for different etching solutions. The time / temperature correlations for these lengths can be determined by inverting the Arrhenius equation (derivation shown in Eq. 4.7) and is shown in Figure 4.9. Note that although the graph shows the diffusion length expressed in nanometres, these values are calculated in the S.I. units of metres.

$$
\begin{aligned}
D &= \frac{(D_L)^2}{2t} \\
T &= \frac{-E}{Rlog(\frac{D}{D_0})}
\end{aligned}
\tag{4.7}
$$

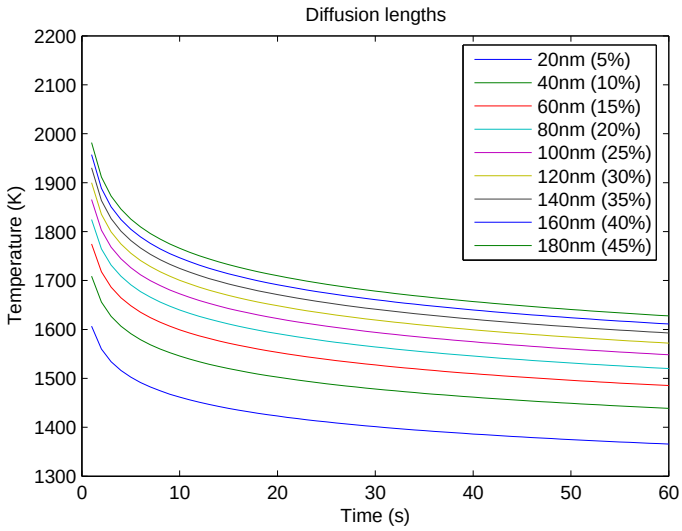

Fig. 4.9: Time / temperature curves for various D_L. Corresponding ξ_d values for a fibre with an I_C of 400 nm are shown in brackets.

A selection of the convolution templates and corresponding etch rate distributions are shown in Figure 4.10.

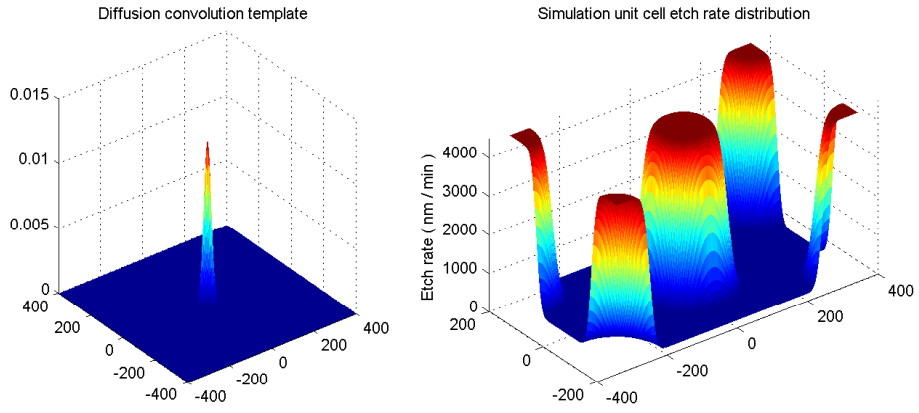

(a)

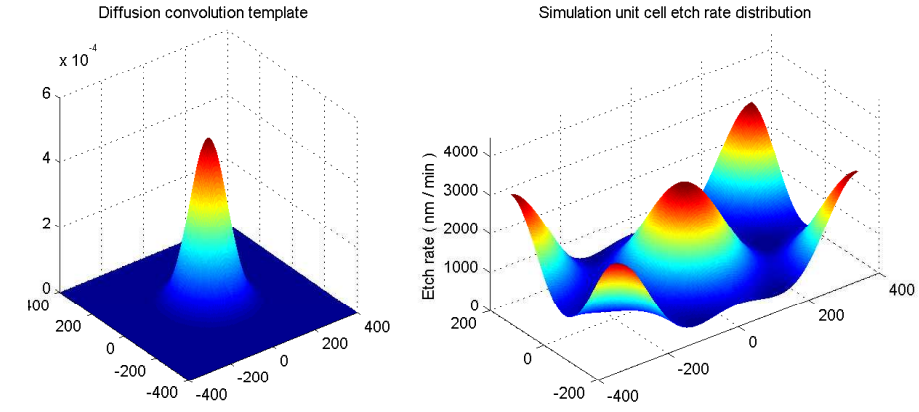

(b)

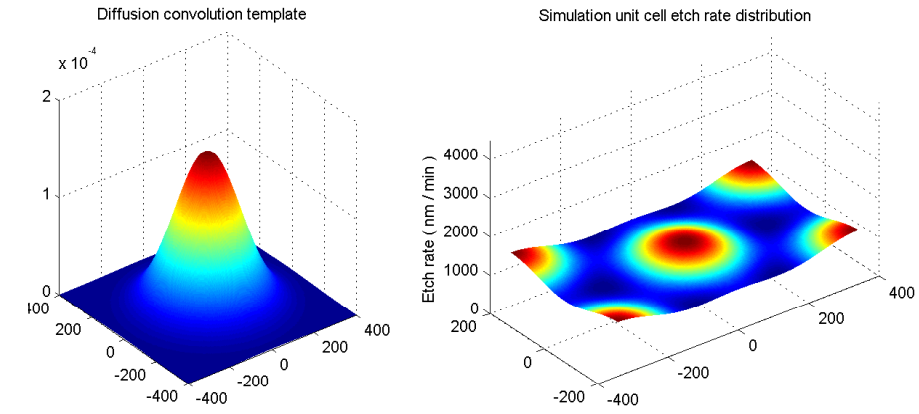

(c)

Fig. 4.10: Convolution template and corresponding unit cell etch rate distributions for D_L of (a) 20 nm ($\xi_d = 5\%$), (b) 100 nm ($\xi_d = 25\%$) and (c) 180 nm ($\xi_d = 45\%$).

4.3.4 Results and Analysis

These etch rate distributions above were loaded into the simulation program for analysis and visualisation. Figures 4.12 to 4.14 show the output of the simulation at 10, 20 and 30 seconds for D_L of 0 to 180 nm in 20 nm steps (ξ_d of 0 to 45% for an $I_C = 400$ nm). Additional images of the simulation output are presented in Appendix B. Videos of the simulation output are provided on the attached disk.

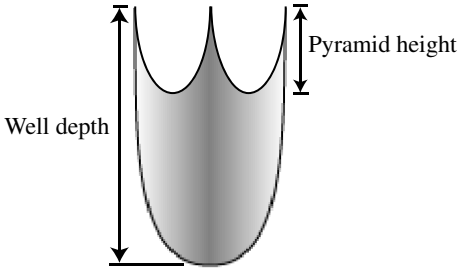

Fig. 4.11: Illustrated cross section of simulation data showing definitions of well depth and pyramid height.

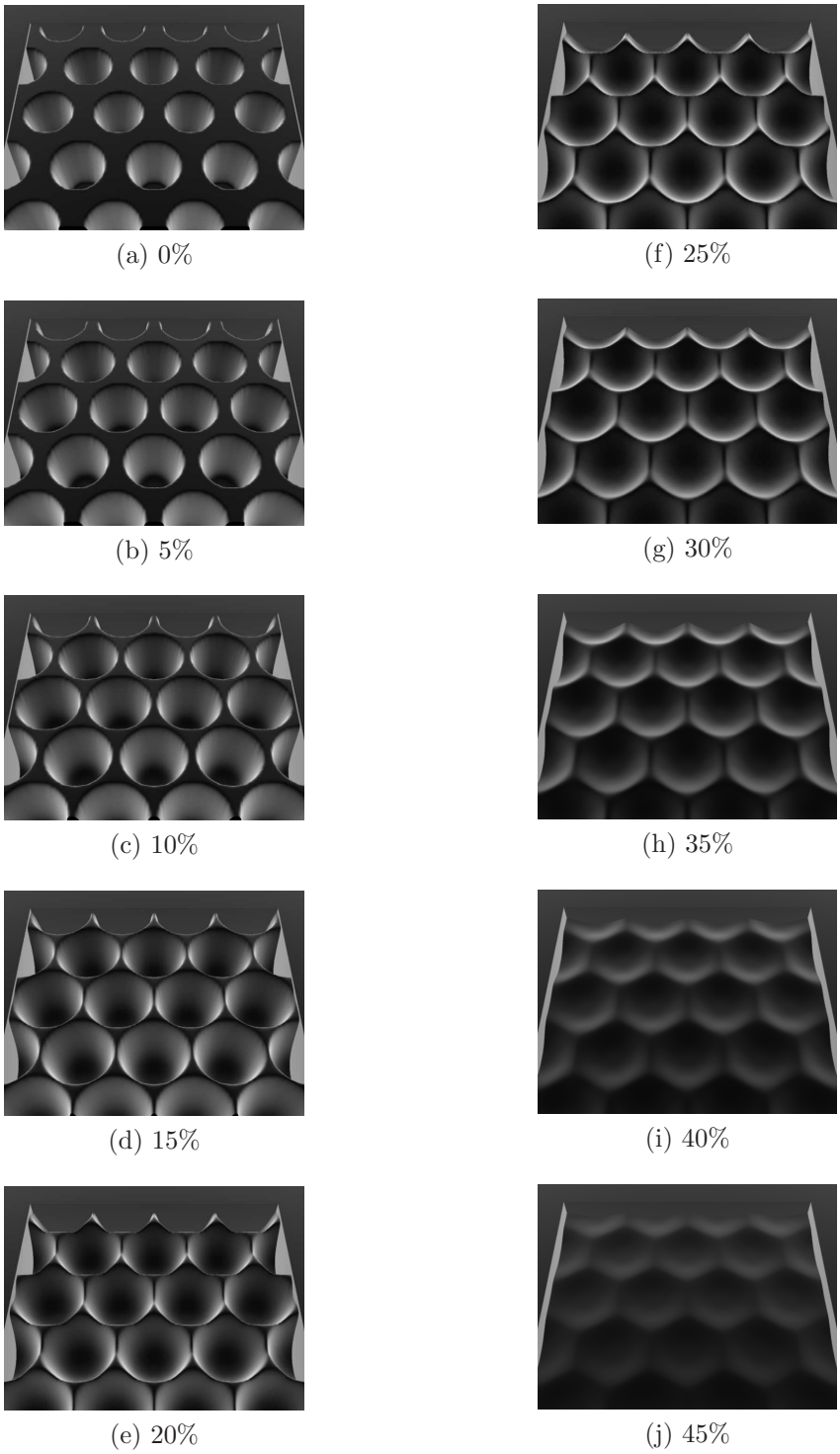

(a) 0% (f) 25%

(b) 5% (g) 30%

(c) 10% (h) 35%

(d) 15% (i) 40%

(e) 20% (j) 45%

Fig. 4.12: Simulation output for various ξ_d ratios after a simulation etch time of 10 s (I_C = 400 nm). Addition intermediary images are presented in Appendix B. Details on the dimensions of structures produced are presented in figures 4.15, 4.17 and 4.21.

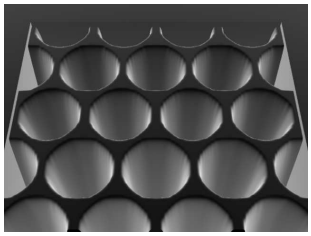

(a) 0%

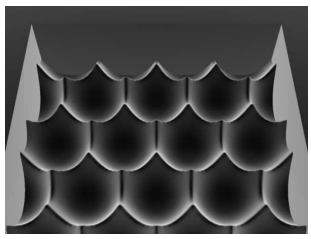

(f) 25%

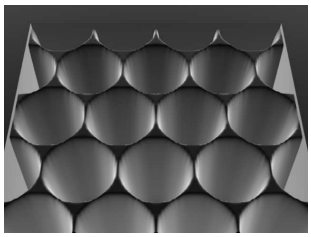

(b) 5%

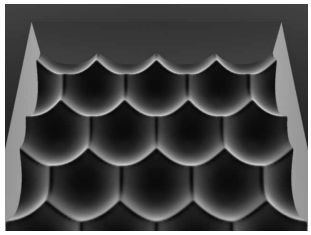

(g) 30%

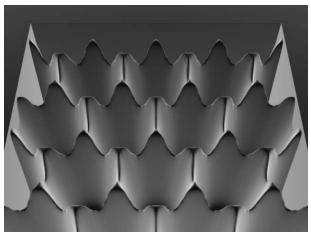

(c) 10%

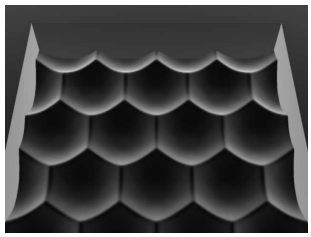

(h) 35%

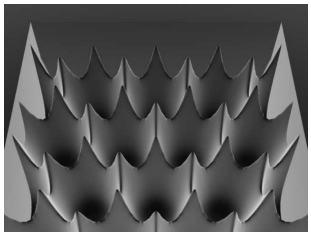

(d) 15%

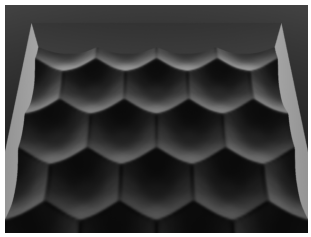

(i) 40%

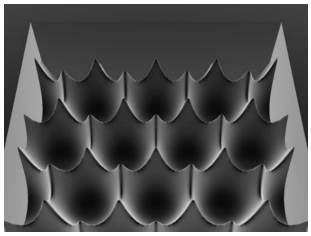

(e) 20%

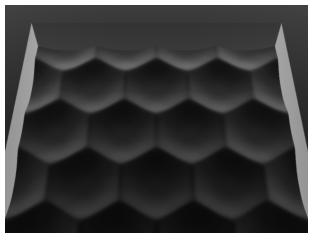

(j) 45%

Fig. 4.13: Simulation output for various ξ_d ratios after a simulation etch time of 20 s (I_C = 400 nm)

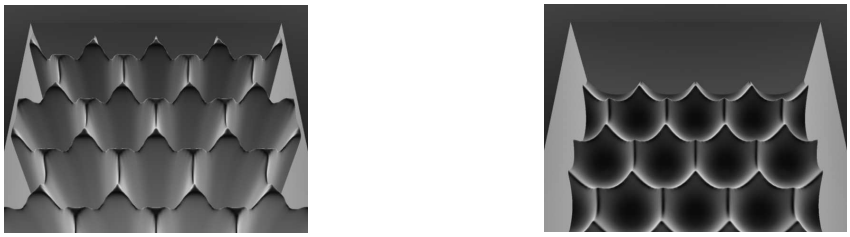

(a) 0%

(f) 25%

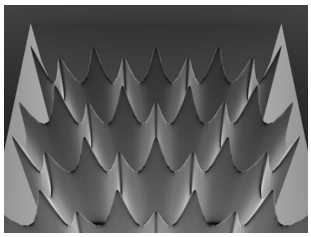

(b) 5%

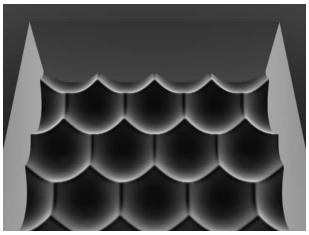

(g) 30%

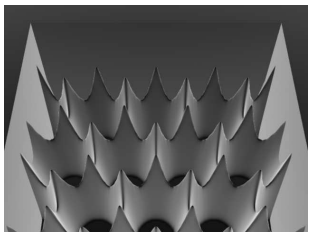

(c) 10%

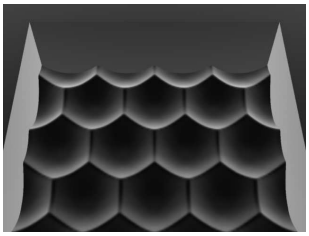

(h) 35%

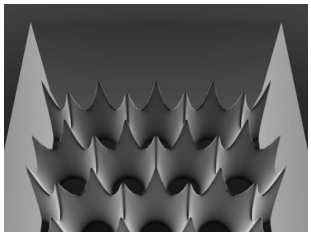

(d) 15%

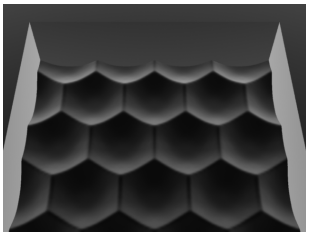

(i) 40%

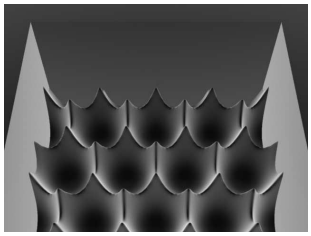

(e) 20%

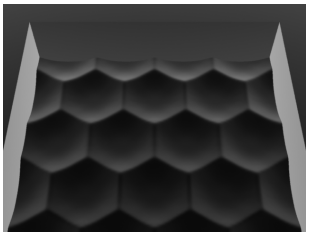

(j) 45%

Fig. 4.14: Simulation output for various ξ_d ratios after a simulation etch time of 30 s (I_C = 400 nm)

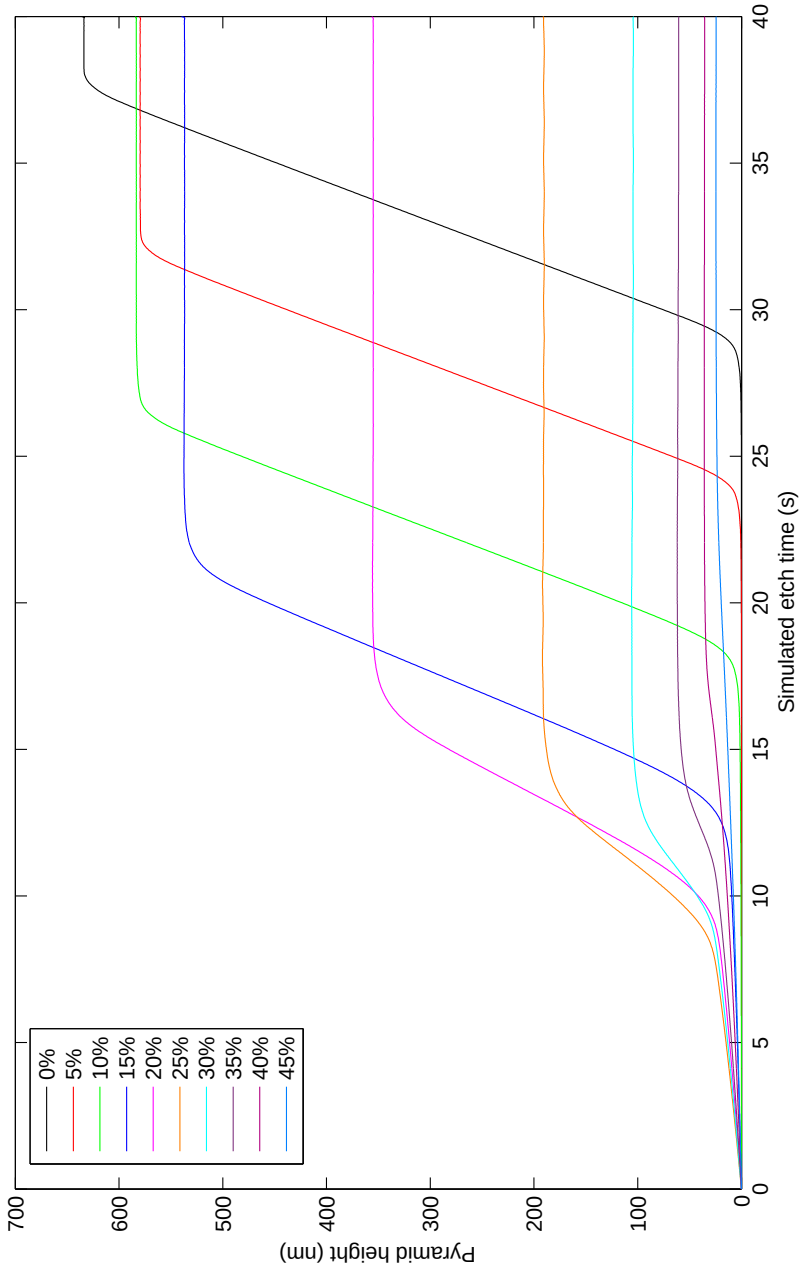

Fig. 4.15: Simulated pyramids heights of various ξ_d for a fibre with $I_C = 400$ nm.

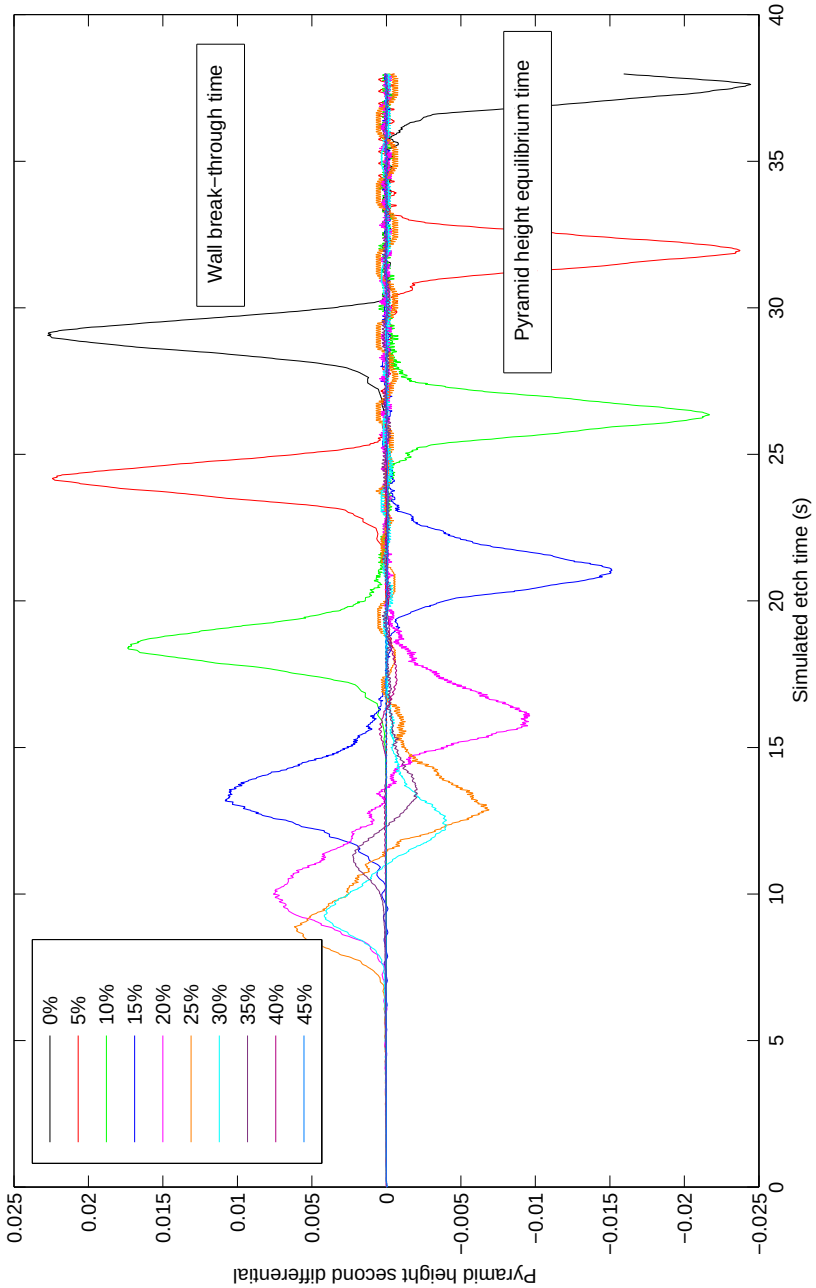

Fig. 4.16: Second differential of the pyramid heights of various ξ_d for a fibre with $I_C = 400$ nm. Positive values occur when the matrix wall break-though occurs. Negative values occur when the pyramid stops growing. Note that curves have been smoothed to remove quantisation noise generated by the simulation steps.

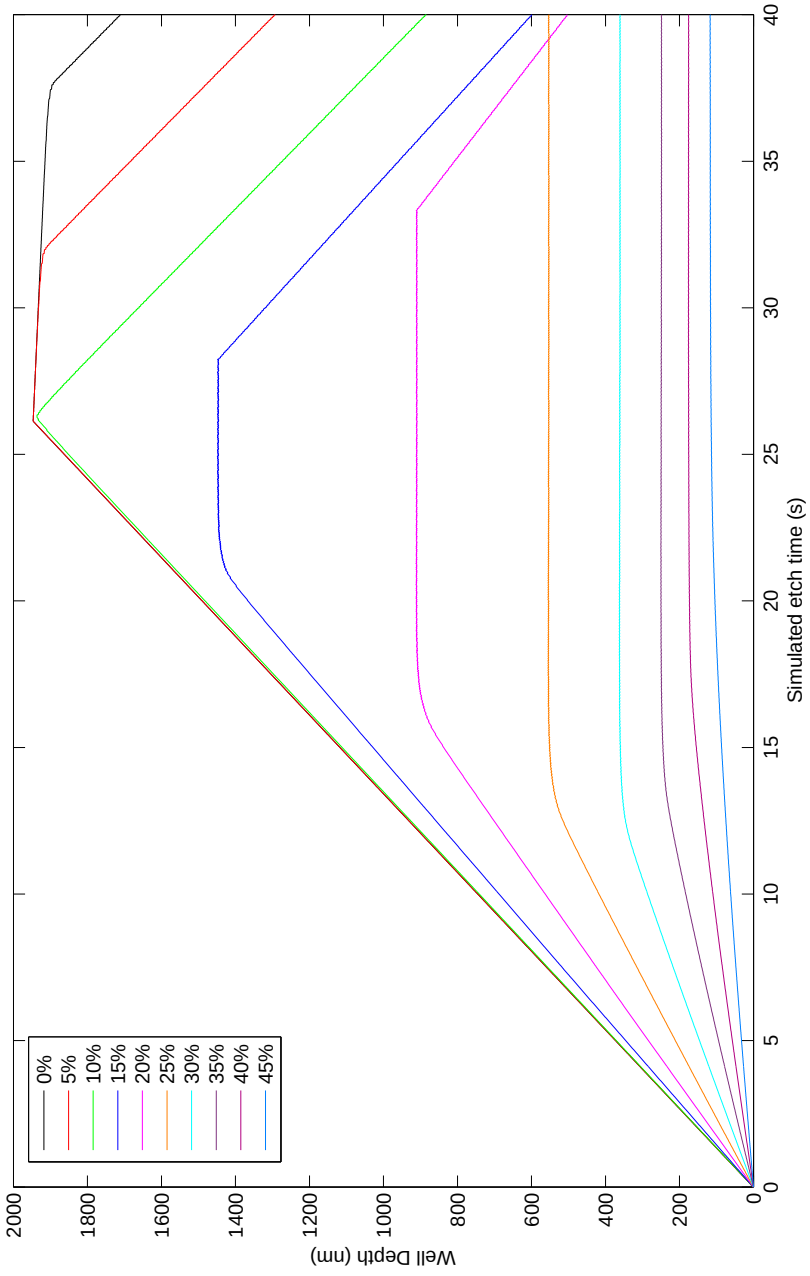

Fig. 4.17: Simulated well depths of various ξ_d for a fibre with $I_C = 400$ nm. Note that the peak values shown for ξ_d of 0%, 5% and 10% are invalid due to the limited z axis depth of the simulation. The tapering seen after equilibrium for ξ_d of 15% and 20% is due to the same limitation. Data is included for completeness only and is not used for analysis.

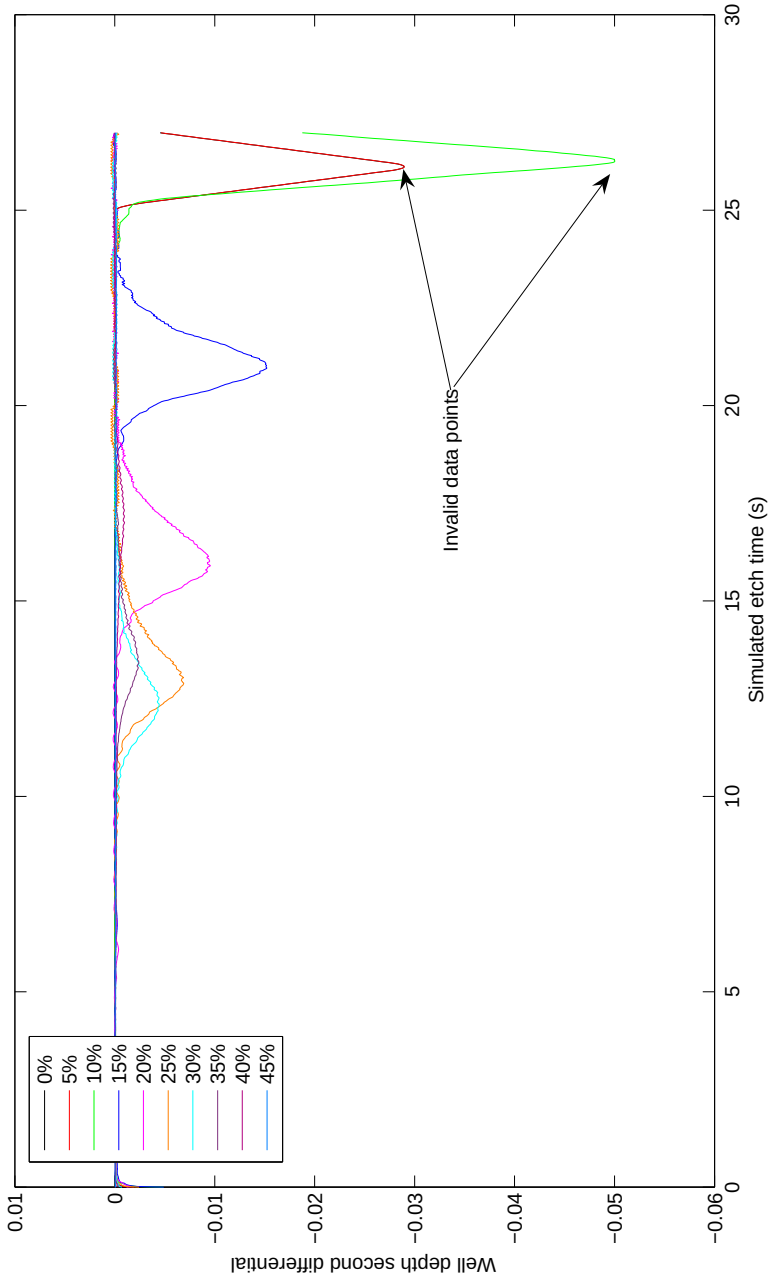

Fig. 4.18: Second differential of the well depths of various ξ_d for a fibre with $I_C = 400$ nm. Note that the values shown for ξ_d of 0%, 5% and 10% are invalid due to the limited z axis depth of the simulation. Data is included for completeness only and is not used for analysis.

Figure 4.15 shows the growth of the nanoscale pyramids for simulated fibres with varying degrees of diffusion. Figure 4.17 shows the well depths for simulated fibres for the same degrees of diffusion. A number of interesting features can be seen from these figures. Firstly, an increase in diffusion length results in the well wall breakthrough (to form the structures) occurring faster. Secondly, the increase also results in pyramids of lower heights. Another interesting structural effect is what happens to the fibres when the ξ_d is $> 25\%$. From this ξ_d onwards, the fibres no longer produce sharply defined 3-dimensional nanostructures but instead form shallow, predominantly 2-dimensional structures.

What can also be seen is that in each case, an equilibrium is reached for the pyramid height and the well depth (Fig. 4.16 and 4.18). In other words, at some point during the simulation, the rate at which the peak of the pyramid is eroded (which is a function of both the molecule's pre-determined etch rate *and* the amount the molecule is exposed to acid) matches that of the well centres. The times at which this occur are presented in Table 4.2 and Figure 4.19. Note that the limited simulation z depth of 2,048 nm was not enough to determine if or when well depth equilibrium is reached for ξ_d of 0%, 5% and 10%. However, when an equilibrium was recorded ($\xi_d > 10\%$), the time taken to reach this point matches closely with that of the pyramid equilibrium time.

D_L (nm)	ξ_d	Wall break-though (s)	Pyramid height equilibrium (s)	Well depth equilibrium (s)
0	0%	29.1	37.6	*
20	5%	24.2	32.0	*
40	10%	18.4	26.4	*
60	15%	13.4	21.1	21.0
80	20%	10.0	16.1	15.9
100	25%	8.9	12.9	12.9
120	30%	9.3	12.4	12.4
140	35%	11.3	13.4	13.4
160	40%	15.6	17.3	17.0
180	45%	33.3	22.9	22.9

Table 4.2: Wall break-through, pyramid equilibrium and well depth equilibrium times for a fibre with $I_C = 400$ nm. Asterisks indicate invalid data points due to the limited z axis depth of the simulation.

Note that the breakthrough and equilibrium times are recorded at the maximum or minimum second differential (turning point) of the pyramid growth. The actual moments of wall breakthrough and pyramid equilibrium occur just before and after

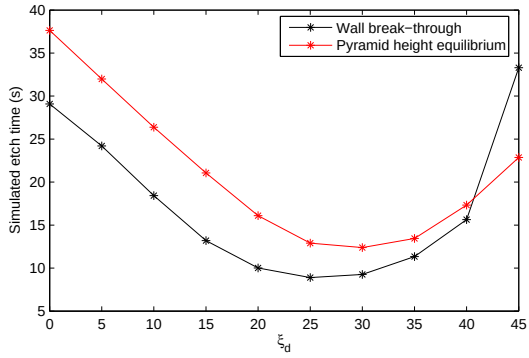

Fig. 4.19: Wall break-through and pyramid equilibrium times for a fibre with $I_C = 400$ nm.

these points respectively. As shown in Section 4.2.3, for a fibre of $\xi_d = 0\%$, the first indication of breakthrough occurs at 28 seconds but the turning point is at 29.1 seconds. However, the turning point is useful for analysis as it is a clearly identifiable location on the time scale.

Table 4.3 shows the equilibrium pyramid heights and well depths for the various ξ_d. Also shown is an estimation of the surface area of the unit cell once equilibrium is reached. $\Delta A/A$ is the ratio of the equilibrium surface area to the initial (ie. before etching) planar area. Recall that in this simulation, a unit cell is 400 nm wide and 688 nm long (275 $\times 10^3$ nm^2). The surface area is estimated by faceting the simulation surface data into a series of planar triangles and summing all their areas (Fig. 4.20). Note that in cases like this where a quadrilateral or grid scheme is broken into triangles, there can be two different ways (ie. diagonals) that can be used (Fig. 4.20 (a) and (b)). For this data, both forms of faceting were calculated but were found to differ in their final answers by $< 0.1\%$. Thus the average surface area calculated from both schemes as a function of etch time are presented in Figure 4.21.

Figure 4.22 highlights this point by plotting the cross section of the well for a fibre with $\xi_d = 25\%$. In this figure, the top of the pyramid has been normalised to zero for every time step. Once again it can be seen that both the pyramid height and well depth reach an equilibrium after which they no longer increase.

The implications of this are clear - a fibre with little diffusion will have a far greater surface area (which can be coated with metal to generate a SERS substrate) than one with high levels of diffusion. Note however, that the increase in surface area with etch

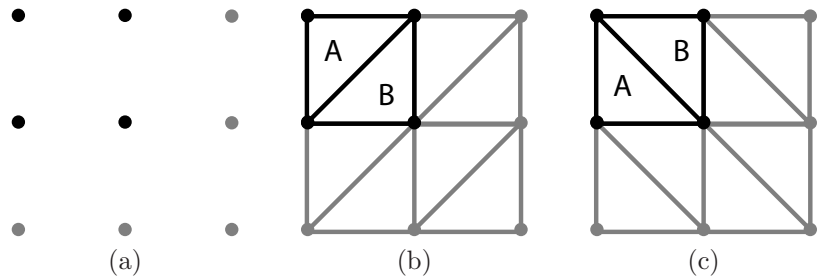

Fig. 4.20: Faceting to find the surface area. (a) Initial height grid; (b) triangulation scheme 1 and (c) triangulation scheme 2.

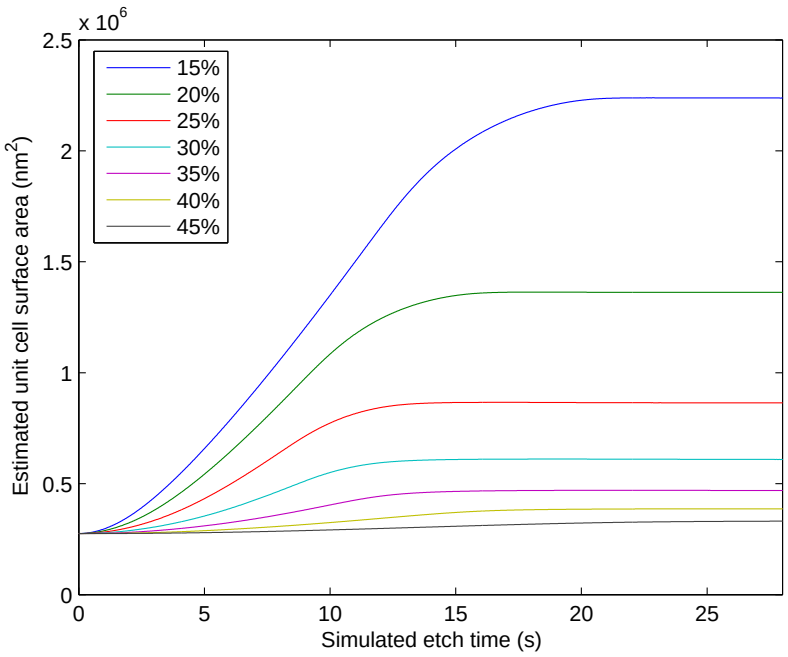

Fig. 4.21: Estimated unit cell surface area for ξ_d from 15% to 45%.

ξ_d	Pyramid height equilibrium (nm)	Well depth equilibrium (nm)	Estimated unit cell surface area (nm^2)	$\Delta A/A$ (%)
0%	636	*	*	*
5%	580	*	*	*
10%	584	*	*	*
15%	540	1450	2.24×10^6	814
20%	356	911	1.36×10^6	496
25%	192	555	0.87×10^6	315
30%	106	362	0.61×10^6	222
35%	62	250	0.47×10^6	171
40%	36	176	0.39×10^6	141
45%	26	117	0.33×10^6	121

Table 4.3: Equilibrium pyramid heights, well depths and estimated unit cell surface areas for a fibre with $I_C = 400$ nm. $\Delta A/A$ is the ratio of the surface area to the initial planar area. Asterisks indicate invalid data points due to the limited z axis depth of the simulation.

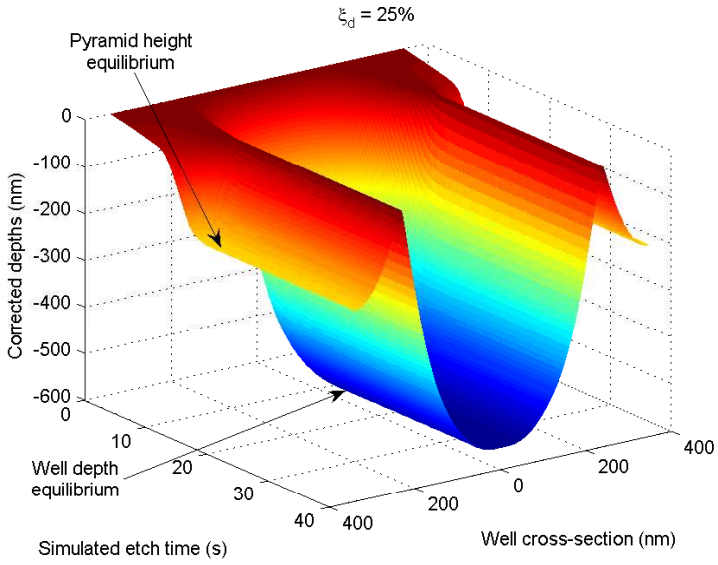

Fig. 4.22: Cross-section of a simulated well for a fibre with $\xi_d = 25\%$ showing the pyramid height and well depth equilibriums. Depths have been corrected so that the pyramid top is constant.

time is not sufficient to explain the observed increase in Raman signal in Figure 3.9, where plasmonic effects must also be playing a role.

4.4 Conclusions

According to the equations of diffusion, the diffusion length of a germanium dopant increases exponentially with temperature or dwell time in the furnace. When dealing with dopant distributions of nanometer size, this can result in dramatic variations in the structure produced after etching.

The output of the simulations indicate that in order to produce the triangular pyramidal structures (as seen in Fig. 3.8 (d)) diffusion must be kept to an absolute minimum. Using the technique described in the previous chapter where a fibre was hand drawn in less than one second, this is achievable. However, such a fast draw is unlikely to be possible using a commercial drawing system.

To produce more 3-dimensional tapered pyramids or rod-like structures, a higher level of diffusion is acceptable. The simulation predicts that a ξ_d up to 25% will result in such structures. The time / temperature curve for this condition for a fibre with I_C of 400 nm is shown in Figure 4.23 (a). Figure 4.23 (b) shows the $\xi_d = 25\%$ curve for a range of I_C from 150 nm to 650 nm. By setting conditions below this curve, the fibre produced should contain nanostructures.

ξ_d beyond 25% however, result in so much diffusion that the original structure is virtually lost. While the output of the simulation shows that the characteristic honeycomb pattern is retained, the surface does not produce sharply defined 3-dimensional nanostructures. Rather the surface simply consists of regular undulations. For a given diffusion length therefore, this condition determines the minimum feature size that can accurately be maintained through the fibre drawing.

The simulation suggests that there is only a limited range of desirable heating conditions for the industrial scale production of the nanostructured optical fibre.

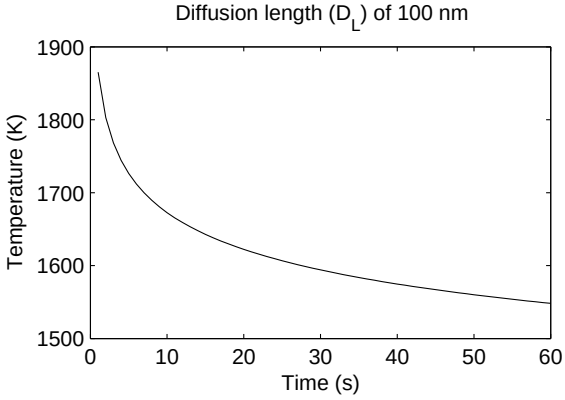

(a)

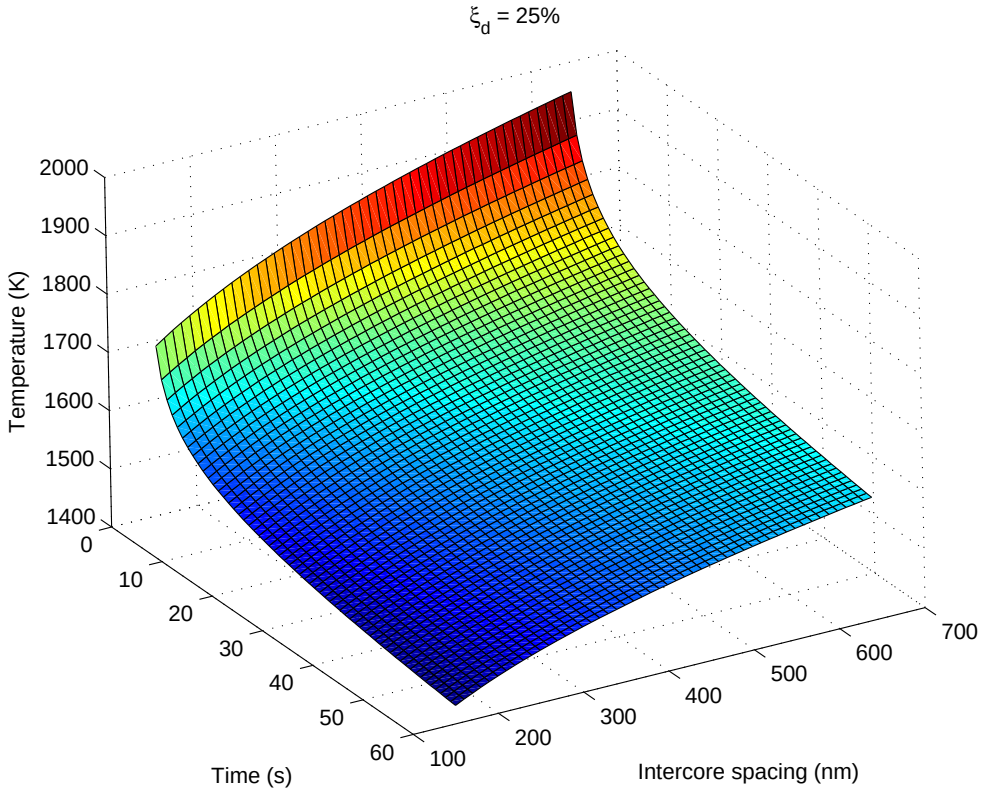

(b)

Fig. 4.23: Temperature versus time graphs for ξ_d of 25% for (a) a fibre with I_C of 400 nm and (b) a range of I_C from 150 nm to 650 nm. Setting manufacturing parameters to lie under the curves will produce acceptable results.

Chapter 5

Production of Nanostructured Optical Fibre SERS Probes

5.1 Introduction

In Chapter 3, nanostructured fibres were formed by drawing commercial imaging fibres to smaller diameters by hand. This technique, although successful, is not suitable for large scale production. The data generated by the computer simulation in Chapter 4 provide a guide to the temperatures and times required to maintain the fibre structure during the draw. However, as shown in the data presented in this chapter, what is theoretically desirable and what is physically possible using an industrial fibre production system are not necessarily compatible.

Initial attempts at an industrial scale production were conducted at the Optical Fibre Technology Centre (OFTC), a part of the University of Sydney. This facility has a highly configurable fibre drawing tower capable of producing specialty fibres for research purposes.

Based on the results achieved at the OFTC, subsequent manufacturing attempts were conducted in conjunction with Fujikura Ltd. Fujikura, as the manufacturer of the conventional imaging fibres, was uniquely positioned to use a modified production method to produce nanoscale fibres. One of the fibres produced by Fujikura was deemed successful and characterisation of this is presented in the following chapter.

Also presented in this chapter are the details of the processing methods designed to aid in the handling of the fragile fibres.

5.2 OFTC Fibre Production

Two fibre designs were attempted at the OFTC. Both of these were based around a 70,000 pixel imaging fibre (Fujikura Ltd, FIGH-70-1300N) which has an initial outer diameter of 1.3 mm.

The first design was to have the FIGH-70-1300N image fibre fixed inside a fluorine doped silica outer tube and drawn such that the diameter of the active area (the pixels) was reduced from 1.3 mm to 50 μm. The final outer diameter was to be 125 μm allowing this fibre to be handled with standard 50/125 fibre tools. A fluorine doped tube was used as the lower refractive index (compared to the core) would aid in guiding light down the fibre by total internal reflection.

The second design was to simply draw the FIGH-70-1300N image fibre by itself to a smaller diameter and coat the result with a polymer jacket.

5.2.1 First Design

The outer tube was made from high-purity silica glass approximately 25 mm in diameter. In order to apply the fluorine layer, the tube was mounted in a Heathway modified chemical vapour deposition (MCVD) machine. This device allows various gases to be passed through the tube whilst simultaneously heating it from the outside with a gas burner. This results in the chemicals being deposited uniformly on the inner surface of the tube [MacChesney et al., 1974]. During deposition, the heater is mounted on a movable stage that travels along the length of the tube. As such, the deposition is described in terms of a number of "passes", each of which is a single traverse of the heater. The series of passes is described in Table 5.1.

Some notes on Table 5.1: the high concentration of SF in passes 2-5 was used to clean the inner surface of the tube. For the deposition passes 6-24, phosphorus gas (POCl) was added as the presence of phosphorus facilitates the sintering of the deposited fluorine [Paul et al., 1997]. Phosphorus also increases the refractive index

Pass #	Chemicals (cc/min) SiCl	POCl	SF	O_2	Temp (°C)	Speed (mm/min)	Comments
1				1000	1800	100	Warm up
2-5			200	1000	2000	100	Etch inner surface
6-24	500	20	50	600	2050	100	Cladding deposition
25-32				600	2200	60	Collapse tube to 17.25 mm O.D.

Table 5.1: MCVD parameters for the first design.

slightly but this is more than offset by the reduction accomplished by the increased amount of fluorine. The speed measurements quoted above are the traverse speed of the heater along the tube.

After the deposition, the tube was drawn to have an outer diameter of 4.61 mm and an inner diameter of 1.4 mm. The inner core (FIGH-70-1300N) was then inserted. A short length (approx 100 mm) of silica rod was attached to the lower end of the preform to act as the sacrificial glass needed for the first "drop". Whilst attaching this rod, the lower end of the core was simultaneously fused to the inside of the tube. At the upper end of the tube, a 25 mm O.D. silica tube was tapered down around the preform. This second tube was required as the 4.61 mm O.D. of the preform was too small to be mounted in the draw tower. The larger mounting tube had several holes cut into the side to allow the air between the core and the inside of the preform tube to escape as the fibre is drawn.

The ratio of the core and the preform tube O.D. allowed for the following core/total size regimes:

Core (μm)	Cladding (μm)	Estimated I_C (nm)
34	125	130
55	200	210
68	250	260

Table 5.2: Fibre size regimes for the first design.

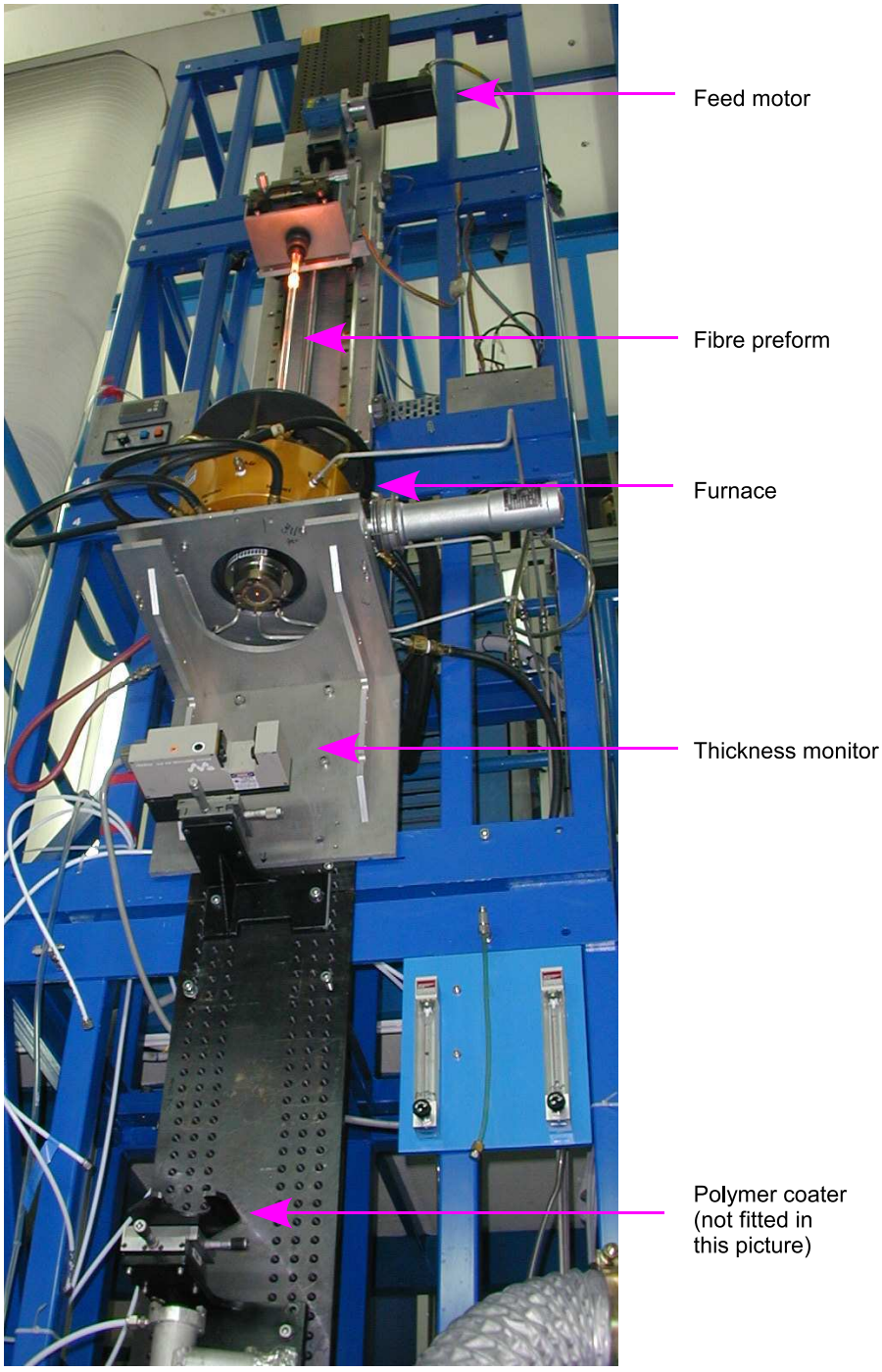

Fig. 5.1: OFTC fibre production tower.

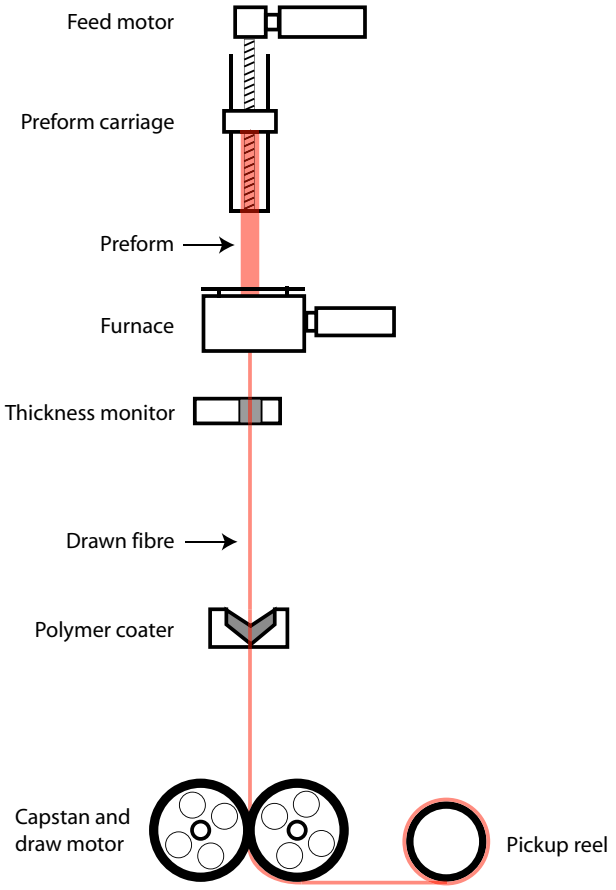

Fig. 5.2: Schematic of the OFTC fibre production tower.

Figure 5.1 shows the main components of the upper half of the fibre drawing tower used at the OFTC. The preform (glowing red from the heat) can be seen being lowered into the furnace by the feed motor at the top. Not shown in this view is the capstan at the base of the tower which is used to pull the drawn fibre out. A schematic diagram showing the main components of the OFTC drawing tower is presented in Figure 5.2.

To start the production, the finished preform was mounted in the draw tower with only the sacrificial silica glass rod at the lower end inserted into the furnace. The temperature of the furnace was initially set to 1000°C and then stepped up to 1500°C in 100°C steps. At each point, the temperature was allowed to stabilise for 1-2 minutes before a final increase to 1570°C (1843 K) was made. At this temperature, the preform had softened enough to "drop" - that is, to start flowing from the furnace. These temperature values are not an accurate measure of the temperature of the glass as they are taken at the surface of the furnace rather than at the preform itself. Given that the preform sits in the "hot zone" of the furnace, it is possible that the quoted temperature is actually lower than that of the preform. The true temperature at some points on the preform surface may be as high as 1900°C according to the experience of the OFTC staff. Once the preform has started flowing from the furnace, it was quickly drawn by hand down the tower and wound onto the capstan/draw motor which then pulled the remaining preform at a defined rate.

Fibre diameter (μm)	Feed speed (mm/min)	Draw speed (m/min)	Temp (°C)	Length produced (m)
125	2.3	3.1	1560	110
200	2.95	1.6	1560	100
250	4.52	1.5	1566	20

Table 5.3: Draw parameters for the first design.

After being drawn from the furnace, the drawn fibre first passes through a thickness monitor. The monitor measures the diameter of the drawn fibre and is connected via a closed-loop system with the draw motor controller. If the measured thickness is too low, the motor is slowed and vice versa. Once its diameter was measured, the fibre was then passed through the polymer coating unit where a protective layer of DeSolite 950-108 polymer was added. This is a UV cured polymer specifically designed for optical fibre use and provides structural strength to the glass. A 350 μm die was used for all fibre samples - this size dictating the final outer diameter of the polymer coating.

5.2.2 Results

In order to reveal the nanostructure, a modified version of the BHF/HCl etchant (see Section 3.3.2) was used. This new etch consisted of 25 ml of commercial BHF solution containing 6.5% HF and 34.94% NH_4F (Riedel-de Haën), 50 ml of HCl (37%, Sigma) and 675 ml of high purity water thereby creating a 750ml solution containing 75ml of active acid and is hereafter referred to as the 10% BHF/HCl etchant. The rationale for the addition of the water is that by slowing the etch process, the timing becomes less critical.

Figure 5.3 shows a sample of the 125 μm fibre from the first design. The fibre was stripped of its buffer, cleaved, etched in the 10% BHF/HCl solution for 20 minutes and rinsed in water. The sample was coated with a thin layer of gold in the SPI plasma coater for inspection in the XL30 SEM. As can be seen from Figure 5.3, the fibre has no detectable internal nanostructure. The results are the same for the larger 200 μm and 250 μm fibres.

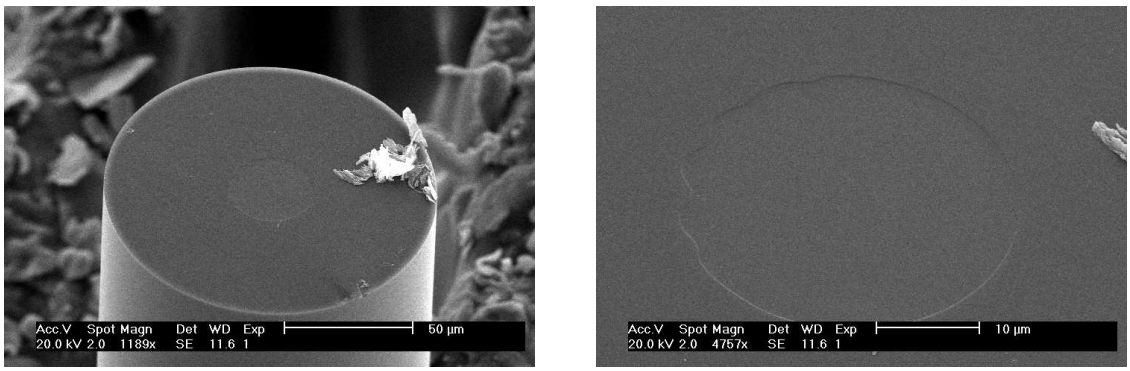

(a) (b)

Fig. 5.3: OFTC drawn imaging fibre (design 1) after etching using BHF solution. The germanium doped core region can just be discerned as an approximately circular depression in (b). Images are taken at an angle of 30° to the fibre axis.

The lack of nanostructures on the tip of the fibre indicates excessive diffusion during the fibre drawing phase and prompted a second attempt using different parameters.

5.2.3 Second Design

In the second design, no outer tube was used with the aim of simply drawing the imaging fibre by itself. The advantage of this version is that the fibre can be drawn at a much lower temperature and at a much faster rate. Both of these factors reduce the amount of dopant diffusion with the fibre.

As in the previous attempt, a thicker silica tube (approx 25 mm diameter) was tapered and fused onto the fibre to enable it to be mounted in the tower. The joint between the two glass sections proved to be a very fragile and broke several times before being successfully mounted. As in the previous attempt, the temperature was initially set at 1000°C, stepped up in 100°C increments up to a maximum nominal temperature of 1400°C (1673 K). At each step, the furnace was allowed to stabilise for 1-2 minutes. As before, once flowing from the furnace, the drawn fibre was quickly pulled onto the capstan. However, due to the relatively high tension encountered during this attempt, the drawn fibre broke many times during this procedure. Additionally, the draw speed required was the maximum the motor was rated for and as such, the motor had some difficulty maintaining the speed. The following parameters were used for the draw:

Fibre diameter (attempted) (μm)	Feed speed (mm/min)	Draw speed (attempted) (m/min)	Temp (°C)	Length produced (m)
≈ 100	20.88	≈ 5	1400	≈ 5

Table 5.4: Draw parameters for design 2.

5.2.4 Results

A sample of the drawn fibre from the second design was etched using the 10% BHF/HCl etchant in the same manner as Section 5.2.2. Figure 5.4 shows a sample from the second design after etching using the above conditions. As can be seen, in this design, the nanostructure is still present. Due to the difficulties encountered during the draw process, it was found that the fibre diameter (and hence I_C) varied by approximately 20% over the length of the drawn fibre. However, approximately 1 m of fibre was found to have a consistent diameter. For this section, the I_C is found to be approximately 400 nm.

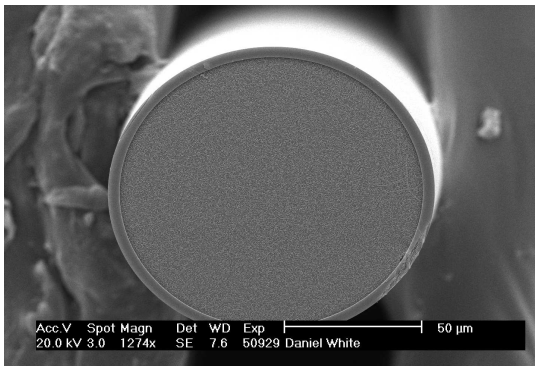

(a)

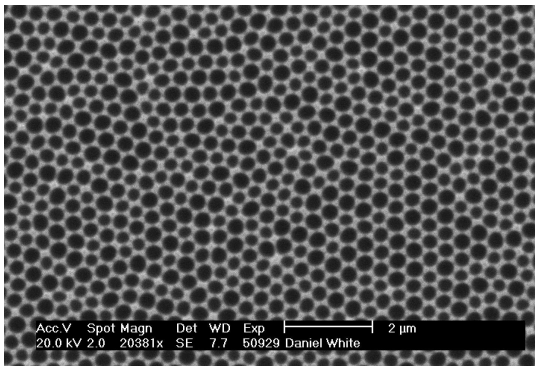

(b)

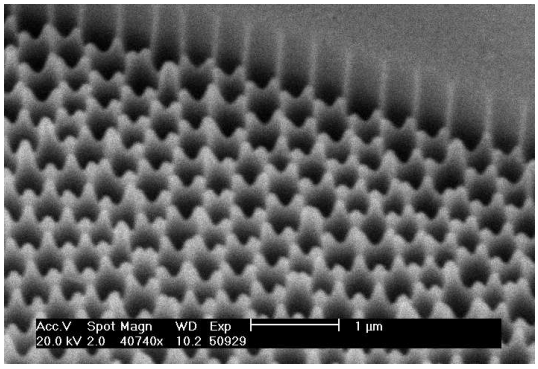

(c)

Fig. 5.4: (a) OFTC fibre with a diameter of 110 μm, (b) pixel spacing, (c) detail of structure (taken at an angle of 30° to the fibre axis).

5.2.5 Analysis

Figure 5.5 shows the D_L for the temperatures encountered in both the fibre designs.

Some rudimentary equations can be used to determine the amount of time the fibre spends in the furnace. If the acceleration is considered constant, knowing both the initial velocity (the feed speed u), the final velocity (the draw speed v) and an estimation of the furnace length ($s = 0.3$ m), the following equation can be used to determine the amount of time spent inside the furnace:

$$t = \frac{2s}{v + u} \tag{5.1}$$

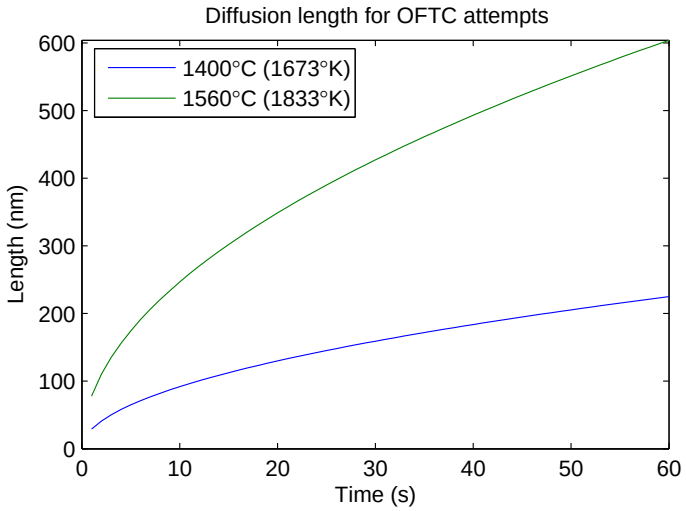

Fig. 5.5: D_L for the temperatures encountered during the draw attempts.

Applying the known values for the feed and draw speeds of the fibres to Equation 5.1 gives the results shown in Table 5.5.

Design	Diameter (μm)	I_C (nm)	Feed speed (mm/min)	Draw speed (m/min)	Temp (°C)	Time (s)	D_L (nm)	ξ_d (%)
1	125	130	2.3	3.1	1560	11.6	285	219
	200	210	2.95	1.6	1560	22.5	397	189
	250	260	4.52	1.5	1566	23.9	424	163
2	110	400	20.88	5	1400	7.1	84.8	21.2

Table 5.5: D_L and ξ_d ratios for both designs taking into account estimated temperatures and times inside the furnace.

The data generated in the previous chapter suggests that in order to maintain the fibre structure (to a reasonable degree), the desirable ξ_d should be $< 25\%$. As can be seen from Figure 5.5, for the first attempt, the critical D_L upper limits of 32.5, 52.5 and 65 nm (for the 125, 200 and 250 μm diameter fibres) are reached in less than one second. Given the fibres spent an estimated 11 to 23 seconds in the furnace, it is not surprising the D_L is found to be greater than the I_C and hence cores are completely diffused away.

For the second design, however, where $I_C = 400$ nm the desirable maximum diffusion length is 100 nm. This value is reached after 12 seconds at 1400°C. As shown in Table 5.5, it is estimated that in this design, the fibre spent approximately 7 seconds in the

furnace. This produces a ξ_d ratio of approximately 20% which should (and does) result in the nanostructure being maintained.

Although the fibre produced in the second attempt had an acceptable amount of diffusion and produced nanostructured surfaces, less than 5 m of drawn fibre could be produced. Additionally, due to difficulties encountered maintaining a steady draw speed during production, the fibre diameter and I_C were found to vary as much as 20% over the length of the draw. Also, due to the lower draw temperature, the fibre was drawn under relatively high tension during production and as such, broke many times. Working with such a fragile fibre proved to be very difficult and therefore, an alternative production technique involving Fujikura Ltd was attempted.

5.3 Fujikura

Due to commercial sensitivity, certain details of the production of the nanostructured optical fibre are not available at this time.

The Fujikura produced fibre contains 30,000 cores in a 80 μm diameter active region (total outer diameter is 110 μm). The I_C is found to be approximately 420 nm. The fibre was also produced with an outer silicone buffer which greatly improves structural strength. For the remainder of this thesis, the fibre is referred to by its production code: FIGH-30-100X.

Figure 5.6 shows a sample of the FIGH-30-100X fibre after being etched for 20 minutes in the 10% BHF/HCl solution as per Section 5.2.2. As can be seen, the fibre has clearly maintained its original structure after drawing.

Once again, commercial sensitivity prevents discussing the specific details of the draw. However, by comparing the images of the fibre after etching to the simulation results in Chapter 4, it can be estimated that the ξ_d ratio is 20% (Fig. 5.6). This corresponds to an approximate diffusion length of 85 nm. Given this length, the following temperature / dwell time graph can produced (Fig. 5.7) which shows both the $\xi_d = 20\%$ curve and the critical upper limit $\xi_d = 25\%$ curve.

Approximately 2 m of FIGH-30-100X fibre was produced by Fujikura. This fibre was used for the experiments in the remainder of the thesis (Chapters 6 and 7).

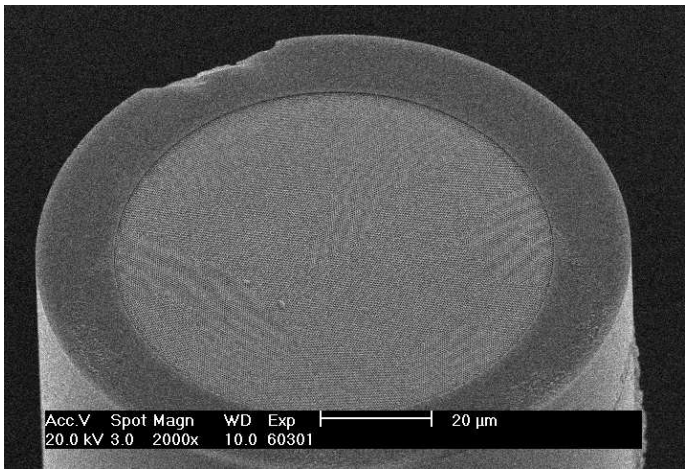

(a)

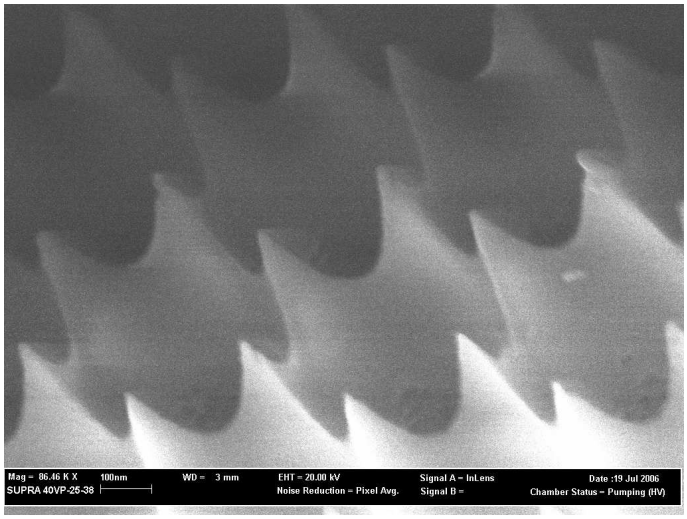

(b)

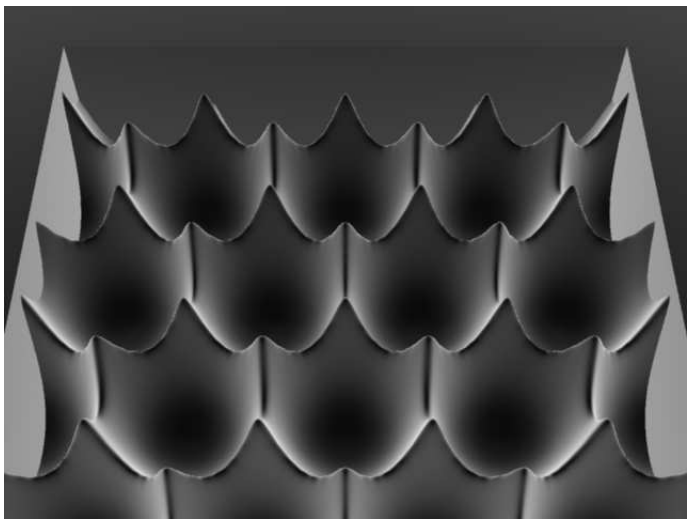

(c)

Fig. 5.6: (a) Etched FIGH-30-100X fibre, (b) detail of the surface and (c) simulated fibre with $\xi_d = 20\%$. Images were taken at an angle of 30° to the fibre axis.

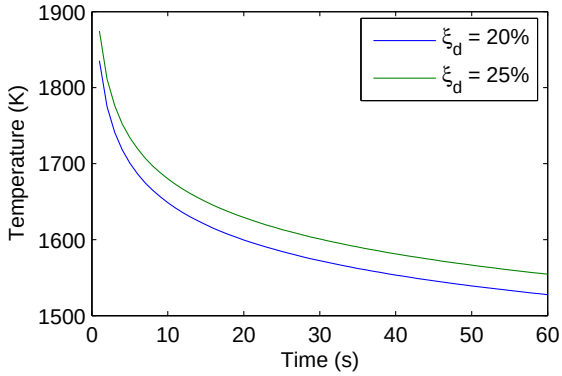

Fig. 5.7: Temperature versus time graph for $\xi_d = 20\%$ for a fibre with an I_C of 420 nm. This is the estimated smearing ratio for the Fujikura fibre. Also shown is the critical $\xi_d = 25\%$ curve which represents the upper limit of heating time and temperature allowable to maintain nanostructures.

5.3.1 Additional Manufacturing Attempts

After the success of the FIGH-30-100X fibre, nine additional designs were attempted with Fujikura. These are summarised in Table 5.6. The first four (codes FIGH-50-1000X, FIGH-50-2000X, FIGH-30-2400X and FIGH-30-1600X) were designed to have rather large total diameters. The rationale for this was that the thick fibre would provide greater structural integrity and remove the need for addition support (see Section 5.4.2). However, to draw such a thick fibre preform required a relatively hot furnace and as such, the fibres produced were found to have excessive diffusion.

The second series of fibres (codes FIGH-30-90X, FIGH-30-80X, FIGH-30-400X, FIGH-30-300X and FIGH-30-200X) were designed as variations of the successful FIGH-30-100X fibre. After etching, the nanostructures produced were found to be shallow bowls similar to those produced by the simulation for $\xi_d \approx 40\%$ (Fig. 5.8). This is significantly greater than that seen in the FIGH-30-100X fibre. Given that the I_C of these fibres is around half that of the FIGH-30-100X fibre and the ξ_d approximately twice, it can be estimated that the diffusion lengths of both designs are of the same order. This indicates that the fibres were drawn at approximately the same temperature. As such, the higher ξ_d is most likely due to the smaller I_C rather than an increase in drawn temperature thus indicating that if low I_C and low ξ_d are desired, the draw temperature must be very low. Ultimately, as these samples were delivered close to the end of the project, they could not be used for any experiments.

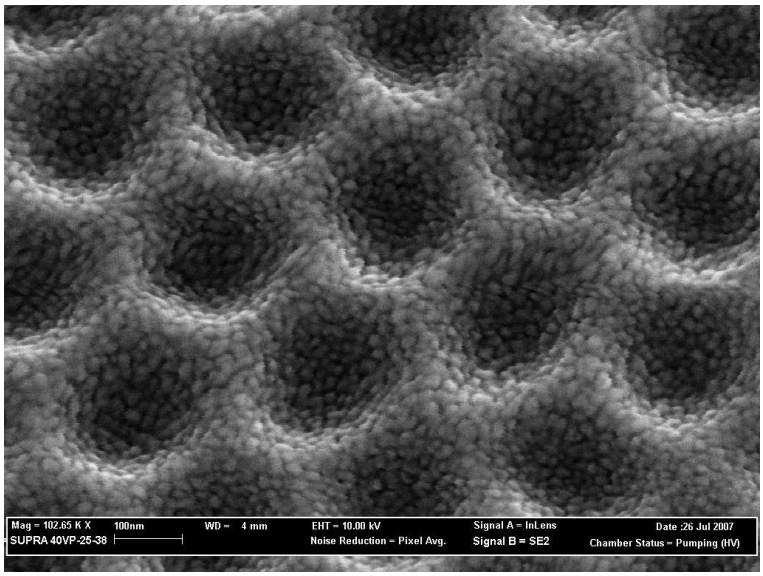

Fig. 5.8: FIGH-30-400X fibre etched for 20 minutes in the 10% BHF/HCl solution and coated with 60 nm silver. Note the structure has formed shallow bowls as predicted in Chapter 4 for a fibre with a high ξ_d.

Sample ID	Date	No. cores	Active diam. (μm)	Fibre diam. (μm)	I_C (μm)	Nano-structures?	SERS active?	Comments
OFTC1a	Jun, 2005	70,000	34	125	est. 130	No	No	Excessive diffusion.
OFTC1b	Jun, 2005	70,000	55	200	est. 210	No	No	As above.
OFTC1c	Jun, 2005	70,000	68	250	est. 260	No	No	As above.
OFTC2	Sep, 2005	70,000	$\approx$100	$\approx$110	$\approx$400	Yes	Yes	Only short length. Variable I_C
FIGH-30-100X	Mar, 2006	30,000	80	110	420	Yes	Yes	Successful attempt. 2 m length produced.
FIGH-50-1000X	Dec, 2006	50,000	50	1000	est. 200	No	No	Excessive diffusion.
FIGH-50-2000X	Jan, 2007	50,000	50	2000	est. 200	No	No	As above.
FIGH-30-2400X	May, 2007	30,000	80	2400	est. 400	No	No	As above.
FIGH-30-1600X	May, 2007	30,000	50	1590	est. 400	No	No	As above.
FIGH-30-90X	Jun, 2007	30,000	84	98	430	Yes	No	Moderate diffusion. Shallow nanostructures.
FIGH-30-80X	Jun, 2007	30,000	63	80	345	Yes	No	As above.
FIGH-30-400X	Jul, 2007	30,000	53	410	250	Yes	No	As above.
FIGH-30-300X	Jul, 2007	30,000	36	280	180	Yes	No	As above.
FIGH-30-200X	Jul, 2007	30,000	26	200	130	Yes	No	As above.

Table 5.6: Summary of nanostructured optical fibre industrial scale manufacturing attempts. Highlighted fibres were used for further experiments.

5.4 Handling Methods

Similar to the prototype drawn imaging fibres (Chapter 3), the FIGH-30-100X fibre (once stripped of its protective silicone outer buffer) was found to be quite fragile. Initial investigations were conducted by simply cleaving the fibre (Fig. 5.6 (a)). Cleaving resulted in a smooth surface suitable for immediate etching but in order to avoid breakage, the fibre had to be taped onto a solid aluminium block for support. Furthermore, cleaving could only be done on one fibre at a time which limited its usefulness for large scale sensor production. As such, a number of alternate techniques were trialled. Due to the limited supply of FIGH-30-100X fibre, initial attempts were conducted using the draw fibre from the second design produced at the OFTC.

5.4.1 Mass Polishing

The first alternative to cleaving was to mount a number of fibre sensor samples in a small glass block and polish them all simultaneously. A 1 mm hole was drilled through a 25 mm diameter glass blank. Thirty samples of the second OFTC fibre were placed into the hole. In addition to these, four generic optical fibres were inserted as packing pieces. The fibres were then glued into the hole using cyanoacrylate glue. Cyanoacrylate was chosen as once the samples were polished, the glue could easily be dissolved and the samples removed. The completed block is shown in Figure 5.9.

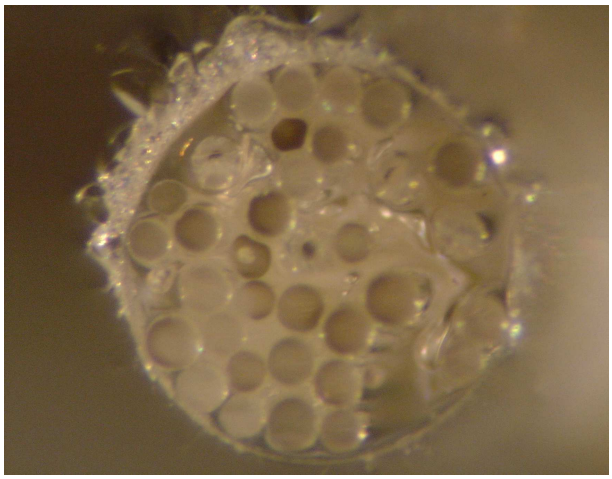

Fig. 5.9: Block mounted fibres.

The glass block was then mounted into a brass holder for polishing. To remove excess glue and any protruding fibres, the mounted block was first ground with 600 grit wet/dry sandpaper with water for 10 minutes. Rough polishing was then conducted using a Leco GP-25 machine, first with 15 μm then 10 μm diamond polishing paste for 15 and 10 minutes respectively. Fine polishing was conducted using a Leco GP-25 machine with 1 μm diamond polishing paste for 20 minutes and then a Buehler Vibromet vibrating polisher with a 0.05 μm aluminium oxide suspension (Gamma Micropolish) for approximately five hours.

Once polished, the block mounted fibres were then etched using the 10% BHF/HCl solution for 10 minutes followed by a rinse in pure water. The sample block was then coated with gold to prevent charging in the SEM. The results are shown in Figure 5.10. As can be seen from Figure 5.10 (a), the cyanoacrylate glue has shrunk during curing leaving small lengths of the fibres unprotected. During polishing, pieces of the fibres broke loose and were dragged across the surfaces causing a large number of scratches (Fig. 5.10 (b)).

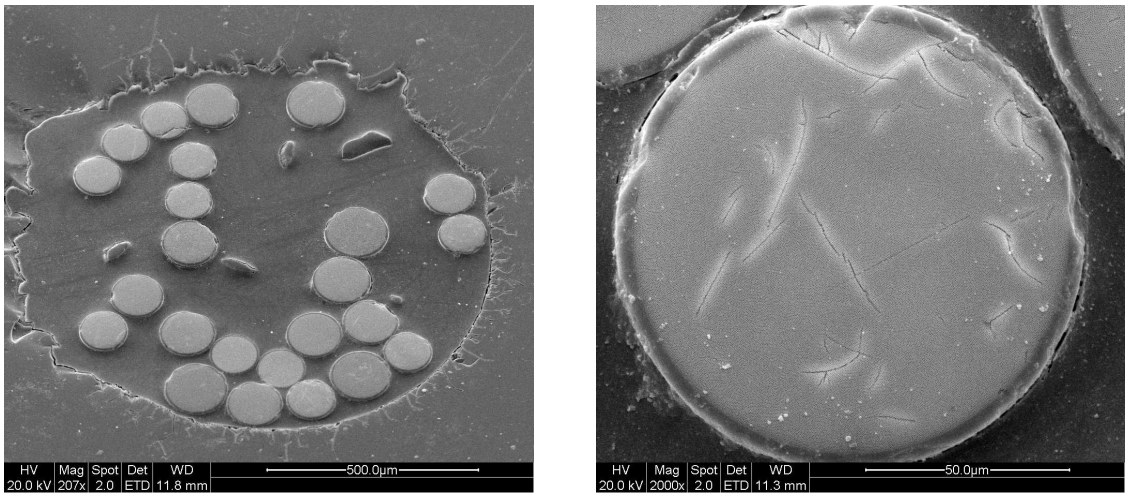

(a) (b)

Fig. 5.10: (a) Block mounted OFTC drawn fibres after the first attempt at polishing. Note the variation in drawn fibre diameters. This is due to the difficulties encountered in maintaining the draw speed. The image was taken at an angle of 30° to the fibre axis. (b) Detail of the scratches seen on the surfaces of the fibres.

The above method was found to be unsatisfactory and so a second attempt was made. To account for the cyanoacrylate shrinkage seen in Figure 5.10, additional glue

was poured over the surface. This time, rough polishing was done using a Logitech PM5 polishing unit fitted with a griding disk. To ensure all artefacts from the previous attempt were removed, approximately 0.3 mm was ground from the surface. Fine polishing was accomplished by fitting the PM5 with a lapping disk and Logitech SF1 polishing fluid. This step lasted approximately four hours.

As before, the samples were etched and coated with gold to enable inspection in the SEM. The results are shown in Figure 5.11. In this instance, no observable shrinkage of the glue has occurred. However, is it clear from the images that once again, pieces of glass have come loose and have caused severe scratches over the tips of the fibres.

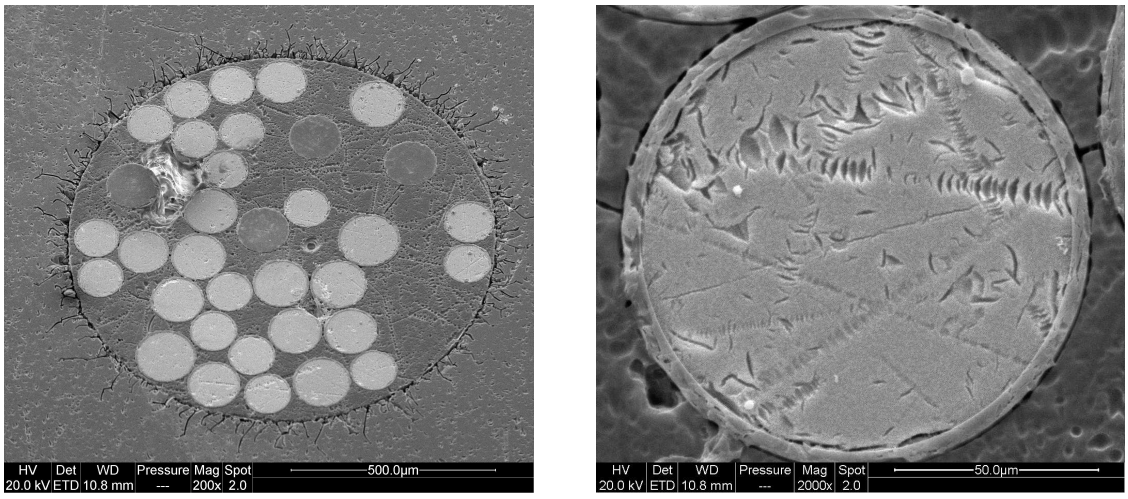

(a) (b)

Fig. 5.11: (a) Block mounted OFTC drawn fibres after the second attempt at polishing. Image was taken at an angle of 30° to the fibre axis. (b) Detail of the scratches seen on the surfaces of the fibres.

Ultimately, it was concluded that block mounting a number of fibre samples and polishing them in this manner was not a suitable technique.

5.4.2 Ferrule Mounting

Having found block mounted mass polishing unsuitable, a second mounting method was trialled. Standard telecommunications fibres are typically mounted in ferrules for connectivity. Such ferrules are not only mass produced but can also be mass polished so although each fibre sample would need to be mounted individually, once a set had been

prepared, they could theoretically all be polished simultaneously. Unfortunately, the outer diameter of the FIGH-30-100X fibre was too small to be placed inside any typical commercially available ferrule. Hence, a custom designed unit was commissioned. The ferrule designed had a 2.5 mm diameter and was 10 mm long. The dimensions chosen allow the ferrule to be integrated into any device fitted with an 'FC' style fibre connector port. The ferrule was designed in conjunction with Diamond FO - a company with a long history of producing fibre connectors. The ferrule consists of a zirconia sleeve (which holds the fibre) inside a nickel-plated brass tube (Fig. 5.12). The copper-nickel cap is specifically designed to match the hardness of the silica based optical fibre. When polishing, chipping usually occurs when the polisher encounters a change in material hardness. As such by maintaining the same hardness across the surface, chipping is dramatically reduced.

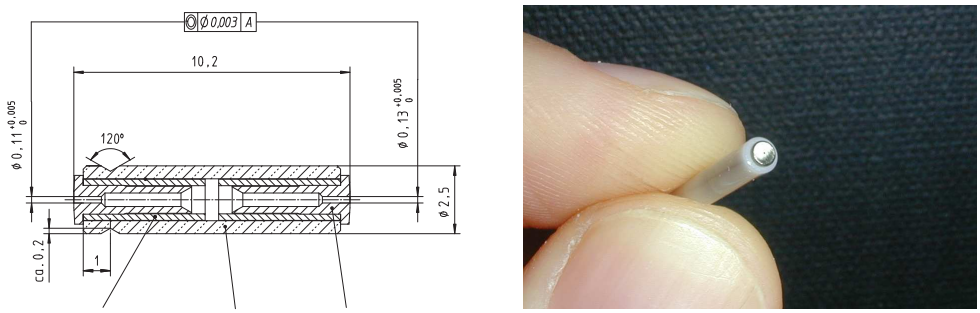

(a) (b)

Fig. 5.12: (a) Ferrule design manufactured by Diamond FO (all dimensions are in mm) and (b) assembled ferrule.

The fibre is glued into the ferrule using Epotek 377 glue. To speed the curing of the glue, the assembly is heated to 100° C for two hours. Once cooled, excess fibre is cut from the tip using a diamond blade saw. Initial polishing is performed using a 1 μm pad. Final polishing was accomplished using diamond paste ($<$ 100 nm particle size) and a soft felt polishing pad. The polishing pad was selected to minimise curvature over the polished area. Both steps were performed by a custom built mechanical polisher and lasted approximately one minute each. Between the two steps, the sample is sonicated to remove polishing debris. Figure 5.13 shows the polished tip and the fibre contained within after etching for 20 minutes in the 10% BHF/HCl etchant as per Section 5.2.2. As can be seen, the acid has no noticeable effect on the ferrule. Repeated polishing and etching of the same sample also produced no noticeable effects on the ferrule after five iterations.

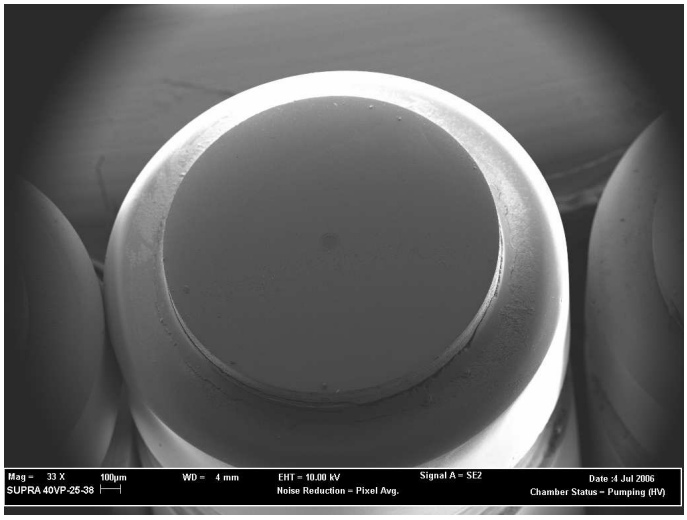

(a)

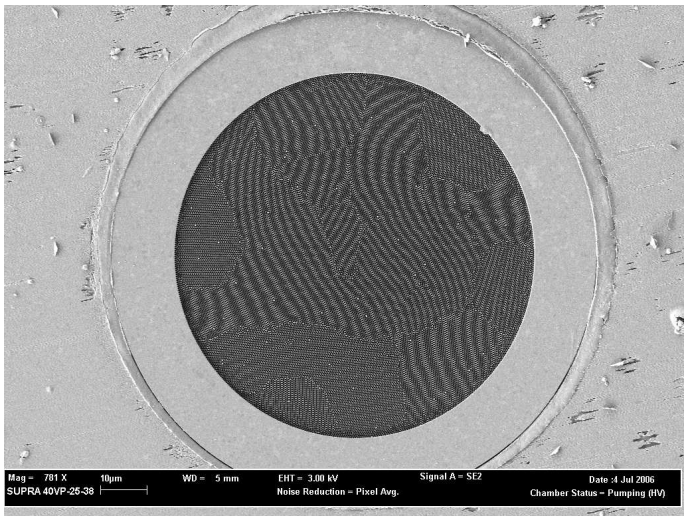

(b)

Fig. 5.13: (a) Ferrule tip. Note the copper-nickel cap standing proud of the ceramic casing. Image was taken at an angle of 30° to the fibre axis. (b) Fibre mounted in ferrule. The thin ring of glue holding the fibre in place is visible around the edges of the fibre's silica outer tube.

Using this method, a small number of samples still became scratched during the polishing process (Fig. 5.14). However, in comparison with the results shown in Figures 5.10 and 5.11, the size and frequency of the scratches was greatly reduced. Furthermore, examples such as that shown in Figure 5.14 were quite rare, typically appearing only once or twice in a batch of 20 samples.

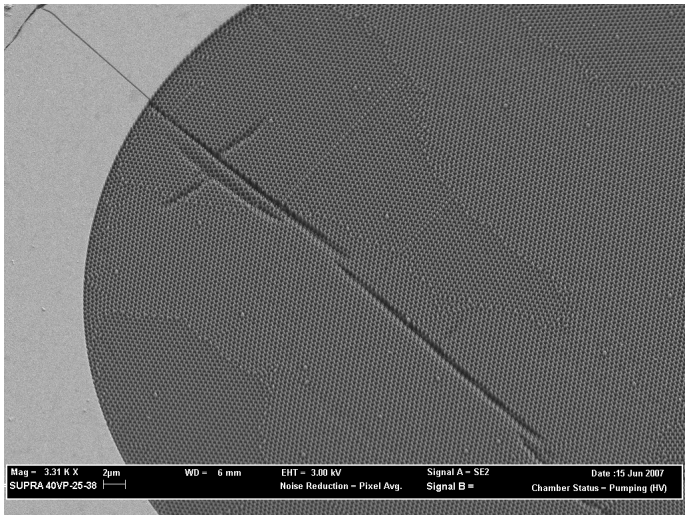

Fig. 5.14: Scratched ferrule mounted fibre after etching.

5.5 Conclusions

The draw temperature encountered during the production of a nanostructured optical fibre is found to be the critical factor in determining success. While a high temperature draw (> 1550 °C) produces a fibre with low internal stress, the large diffusion length diffuses the imaging fibre dopants to the point where the well structure disappears. Conversely, a low temperature (< 1400 °C) allows the dopant distribution to be maintained but results in a fragile fibre with numerous cracks. At the time of writing, there is no known process that can produce a low diffusion fibre without inducing high strain. As such, the issues of diffusion and fibre strength must be balanced.

Unfortunately these conditions could not be met using the OFTC facility. Fujikura had more success with their setup and have produced approximately 2 m of useful fibre. However, to date, it has not been possible to reproduce the fibre. Although the

temperature and drawing rate applied are not available, it can be estimated that the D_L of this fibre is approximately 85 nm. This is below the critical 25% ξ_d ratio required to maintain the nanoscale features.

The FIGH-30-100X when used with the Diamond FO ferrule is a mechanically stable, topologically repeatable substrate for use as a small SERS sensor. Repeated etching of the ferrule results in no visible degradation of the surfaces.

Chapter 6

Characterisation of the Nanostructured Optical Fibre SERS Probe

6.1 Introduction

The manufacturing of a large uniform length of SERS fibre allows a full characterisation experiment to be conducted. The work presented in this chapter illustrates the different structures that can be achieved when etching for different times and how the SERS signal count varies with both this change and the deposition of different silver film thicknesses. Additional investigations into annealing the SERS surface and the localised surface plasmon resonance (LSPR) of the sensors are also presented.

6.2 Etching Characterisation

6.2.1 Experimental Setup

Twenty lengths of FIGH-30-100X fibre (each approx 5 mm long) were stripped of their silicone buffer layer and glued into 10 mm long ferrules (see Section 5.4.2) using Epotek 377 glue. Samples were heated for 2 hours at 100° C to accelerate the curing of the glue. Once finished, excess fibre extruding from the ferrule cap was cut using a diamond blade saw and the samples were polished using a 1 μm pad. Final polishing

was accomplished using diamond paste and a soft polishing pad.

The 10% BHF/HCl solution from Section 5.2.2 was used to reveal the nanostructure. The 20 samples were placed together in a plastic basket and allowed to soak in approximately 25 mL of the 10% BHF/HCl etchant solution. Samples were removed at one minute intervals and triple rinsed in water giving a sample set of 1 to 20 minute etchings. To aid handling, all samples were mounted together in a small perspex block for the remainder of the experiment. Imaging of the surface features was conducted using a Zeiss Supra 40VP SEM. After the SEM investigations, a 2 nm layer of chromium was deposited onto the etched tips using a KJL coating unit to improve the adhesion of the silver particles to the surface (Section 2.3). Silver coating was performed using the Emitech coater also described in Section 2.3. To preserve sample integrity, when not used in experiments, samples were stored in a small container filled with ethanol.

6.2.2 Results and Analysis

Figure 6.1 shows the 20 samples after etching but before coating with metal. The progression of images show the fibres forming bowls (1 to 3 minutes), deep wells (4 to 7 minutes) and then pyramidal structures ($>$ 8 minutes). Note that the planar surface triangular structures seen in Section 3.8 do not appear. As was discussed in Chapter 4 this is attributed to the increased temperatures encountered during the production of this particular fibre. Visually, these figures correspond well to those generated by the simulation in the previous chapter for a fibre with a ξ_d of 20% (refer to Appendix B, Fig. B.5).

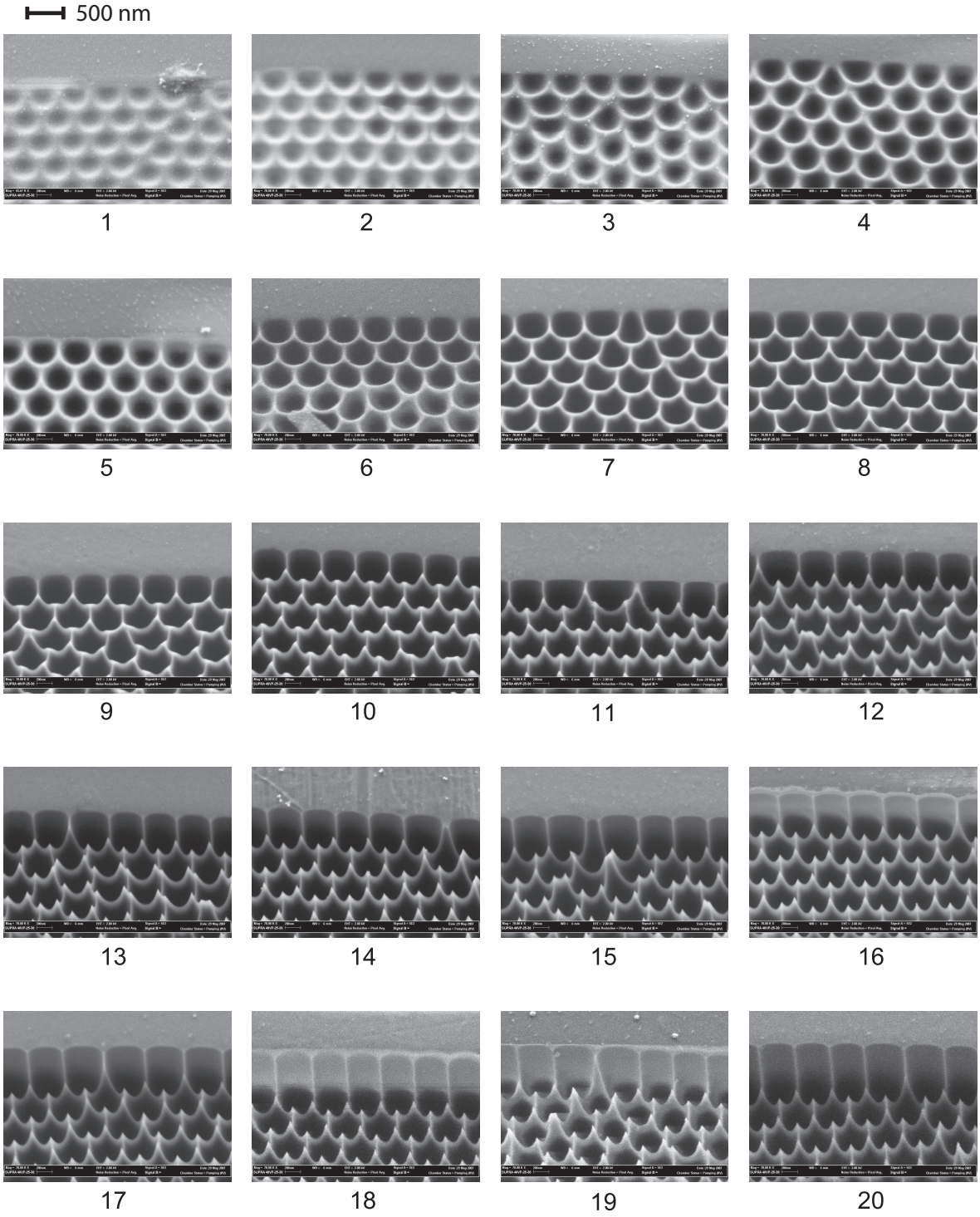

Fig. 6.1: Etched surfaces (uncoated) after 1 to 20 minutes etching. Images show the region where the active area meets the outer silica tube. All images were taken at a 30° angle to the fibre normal and have a magnification of 70,000×. A scale bar of 500 nm is included at the top left of the figure for reference.

6.3 SERS Characterisation

6.3.1 Experimental Setup

Samples were initially coated with 20.4 nm of high purity silver (ProSciTech, Australia) using the Emitech K950X thermal coating unit. After SEM inspection, samples were immersed together in 25 ml of a 10 mM solution of thiophenol in ethanol for 20 minutes (Section 3.4.1) followed by a rinse in pure ethanol for a further 2 minutes.

Spectra were collected using a Horiba Jobin-Yvon Modular Confocal Raman system. Details of the setup are provided in Section 2.5.

Laser excitation was provided by a single spatial mode fibre-coupled 532 mn DPSS laser using a 5 μm core optical fibre (OptoTech P/L, Melbourne). A laser line filter was used to remove the Raman background from the input fibre and a 50$\times$ ULWD lens (0.5 N.A.) was used to focus the laser onto the active fibre tip. Power at the sample was approximately 0.7 mW. Spectra were collected in back-scattering configuration from the free space end (ie. not through the fibre). An edge filter with a cutoff at 150 cm^{-1} was used to remove the laser line from the returning signal before passing it through a 0.4 mm confocal pinhole. The output signal was then coupled into a 50 μm core optical fibre which was connected to a Jobin-Yvon Triax 320 spectrometer (also Section 2.5). The spectrometer was fitted with a 1200 l/mm grating to disperse the beam.

Spectral data was collected using a TEC cooled CCD (Jobin-Yvon CCD3000V). Each spectrum comprised five accumulations of ten seconds exposure. No cosmic ray filtering was employed during collection as filtering was done during analysis. Five spectra were collected from different locations on each sample giving 100 spectra for each sample set. The background signal was manually subtracted from each spectrum. Spectra have the high frequency noise removed by employing a 3rd order Savitzky-Golay filter.

After collecting spectra from all the samples, the surfaces were annealed using a vacuum oven set to 80° C for 1 hr (excluding warm up and cool down time). Previous works have indicated temperatures up to 300° C are required to anneal silver films [Van Duyne et al., 1993; Vogel et al., 1998]. The temperature chosen, however, was the maximum achievable by the available oven. Investigations in the SEM indicated that despite the relatively low temperature, annealing still occurred. After heating, samples

were then re-soaked in the thiophenol solution for 20 minutes followed by another rinse in ethanol. Spectra were collected using the same arrangement as before.

After the second set of spectra had been collected, the samples were re-polished using the 1 μm pad and the diamond paste (Section 5.4.2). The entire process was then repeated using silver thicknesses of 40.5, 60.2, 80.5 and 100.0 nm.

6.3.2 Results and Analysis

Figures 6.2 to 6.6 show the fibre surfaces after coating with the various thicknesses of silver.

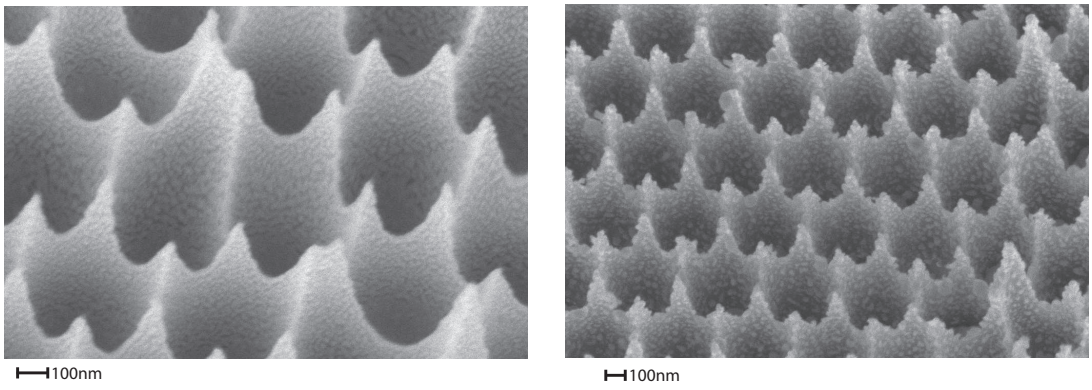

(a) (b)

Fig. 6.2: 18 minute etched sample with (a) 20.4 nm silver coating before annealing and (b) after annealing. Note that due to microscope malfunctions, high resolution images were unattainable for (b).

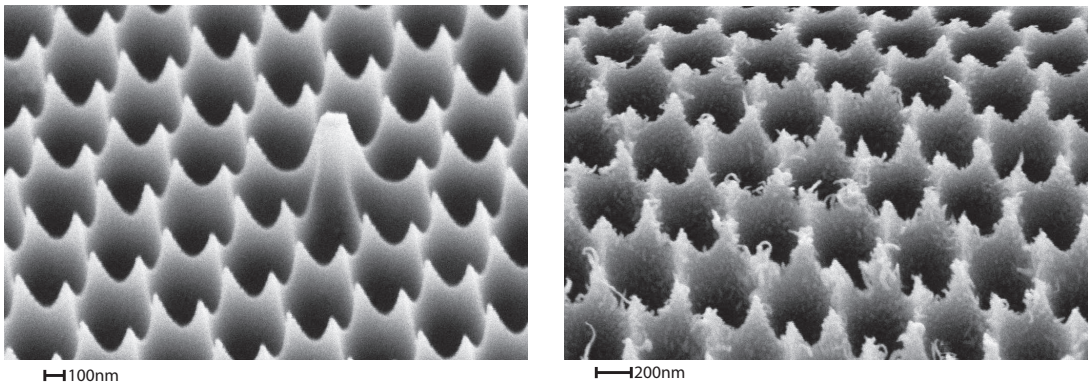

(a) (b)

Fig. 6.3: 20 minute etched sample with (a) 40.5 nm silver coating and (b) after annealing. Note that due to microscope malfunctions, high resolution images were unattainable. Also note the unknown contamination apparent after annealing. All annealed samples showed similar contamination features.

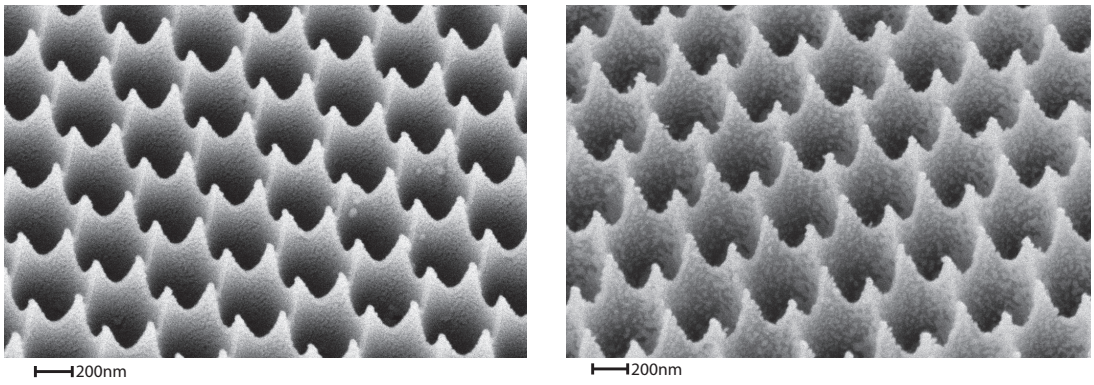

(a) (b)

Fig. 6.4: 20 minute etched sample with (a) 60.2 nm silver coating and (b) after annealing. Note that due to microscope malfunctions, high resolution images were unattainable.

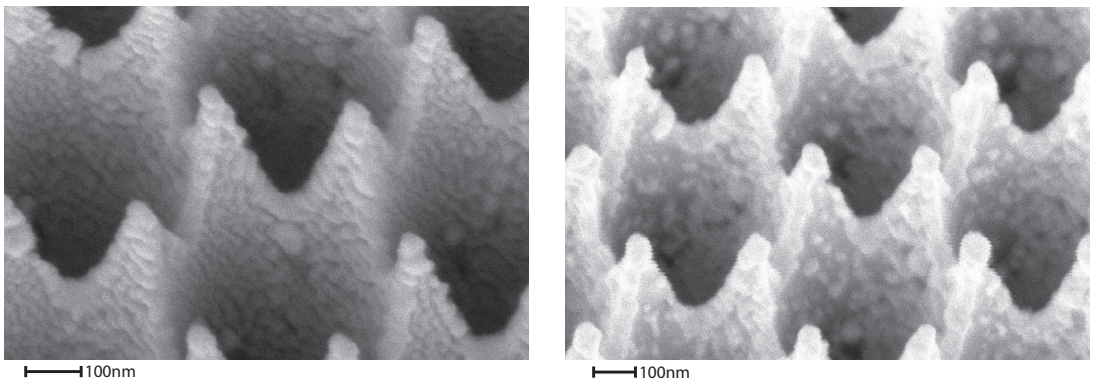

(a) (b)

Fig. 6.5: 20 minute etched sample with (a) 80.5 nm silver coating and (b) after annealing.

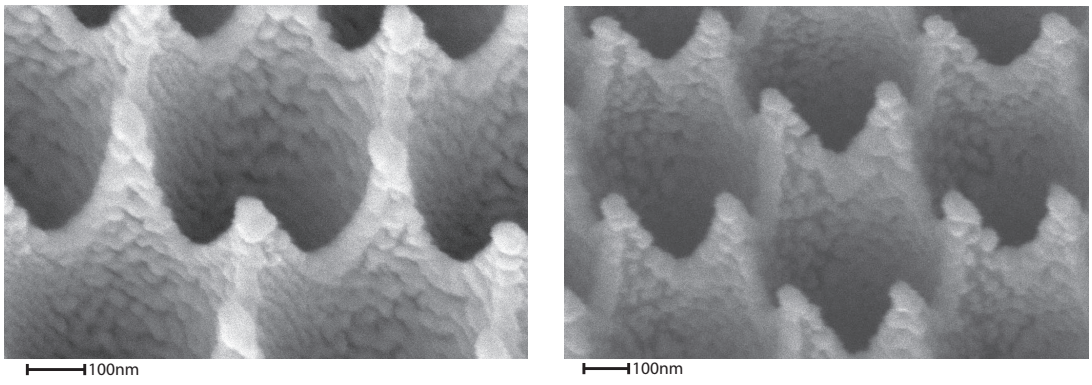

(a) (b)

Fig. 6.6: 20 minute etched sample with (a) 100.0 nm silver coating and (b) after annealing.

An example of one of the spectra collected is shown in Figure 6.7. This graph shows the thiophenol SERS signal for both the as-deposited silver and annealed silver (60.5 nm) surfaces from a sample etched for 14 minutes. Spectra have been background subtracted and smoothed using a Savitzky-Golay filter. To analyse the data, the signal counts for the peaks at 1000 cm^{-1}, 1021 cm^{-1}, 1072 cm^{-1} and 1573 cm^{-1} were averaged to form a new value $\overline{I_{tp}}$ (ie. the average intensity of the main thiophenol peaks). Figures 6.8 to 6.12 show the variation of this value as a function of the sample etch time.

The green trace in the following figures is for the data collected before annealing, the red for that collected after annealing. An asterisk over a data point indicates that sample had some form of contamination (eg. dust) on the surface. As there were only five spectra taken from each sample, error bars represent the maximum and minimum values rather than standard deviation. The dotted line traces through the average $\overline{I_{tp}}$ value.

Note that in Figure 6.9, the blue trace represents the data collected after annealing. As shown in Figure 6.3 (b), these samples suffered from an unidentified contaminant. Attempts at cleaning these samples were unsuccessful. The data collected does not follow the trends of the other samples and is included for completeness only.

Figure 6.13 shows all of the data collected using the same Y-axis scale.

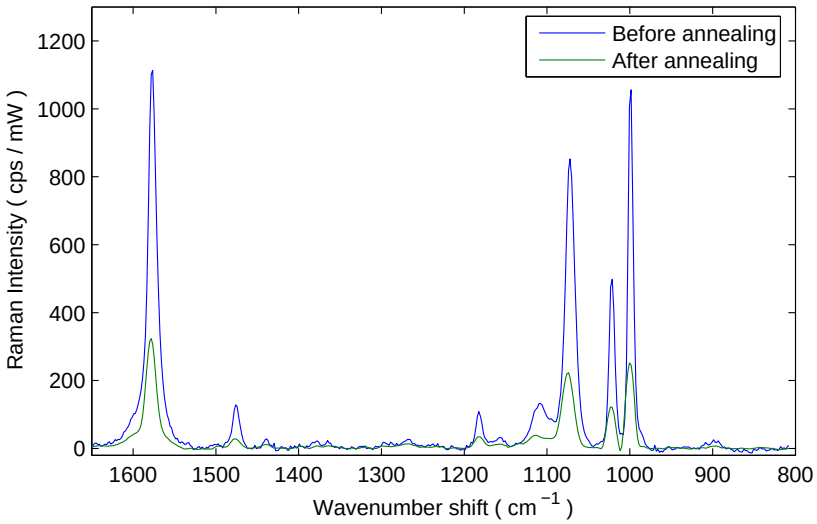

Fig. 6.7: Example spectra for a sample etched for 14 minutes with 60.5nm coating, before and after annealing and after background subtraction. Intensities of the 1000 cm^{-1}, 1021 cm^{-1}, 1072 cm^{-1} and 1573 cm^{-1} peaks are averaged to form the $\overline{I_{tp}}$ value.

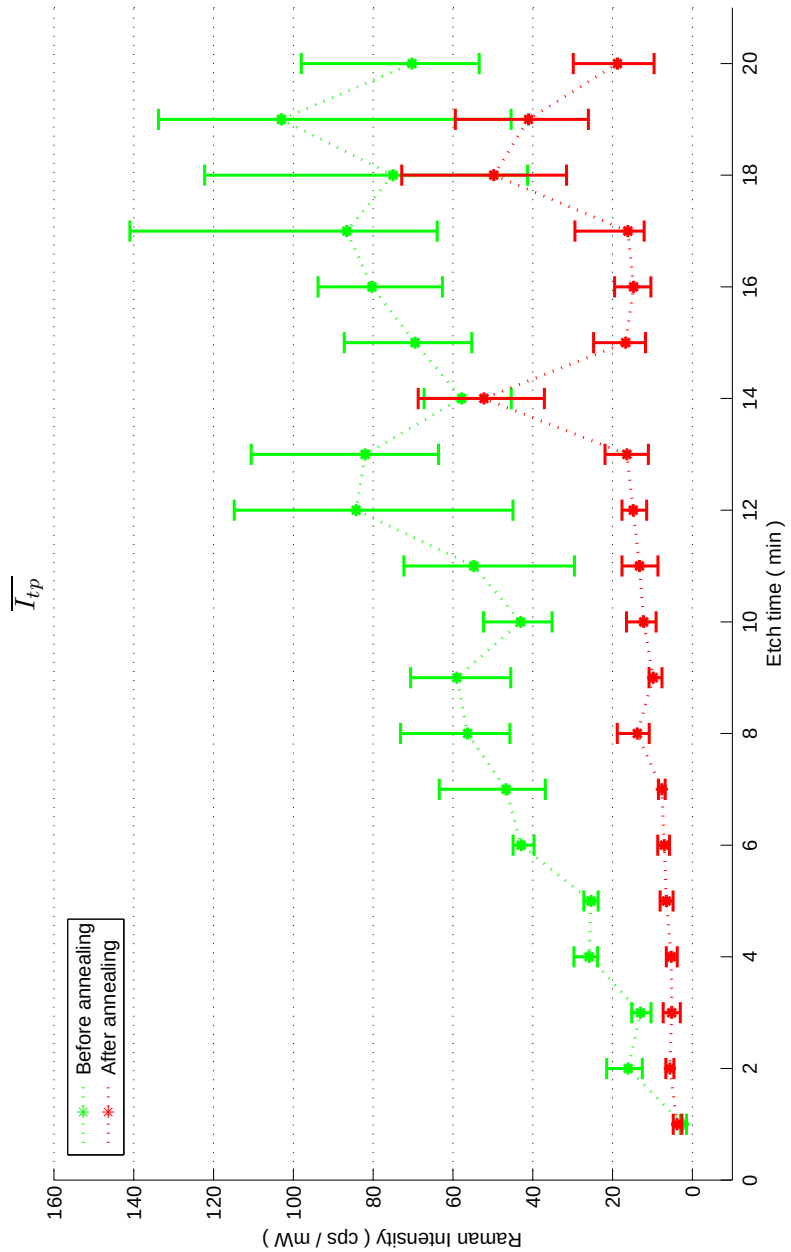

Fig. 6.8: Average thiophenol peak intensity ($\overline{I_{tp}}$) for samples coated with 20.5 nm silver.

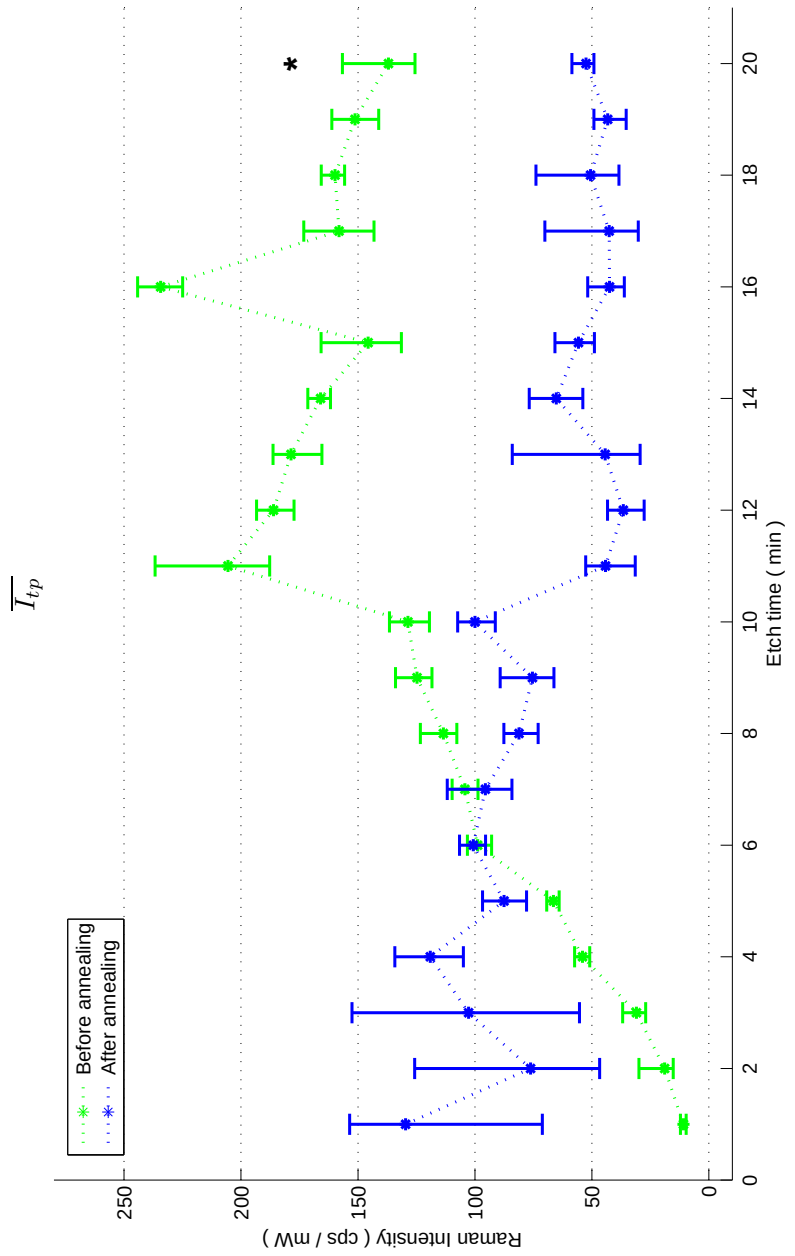

Fig. 6.9: Average thiophenol peak intensity ($\overline{I_{tp}}$) for samples coated with 40.5 nm silver. As all of the annealed samples (blue trace) showed significant contamination, the data is included for completeness but was not used in any further analysis. Asterisks indicate contaminated sample with reduced area due to surface contamination by particulates.

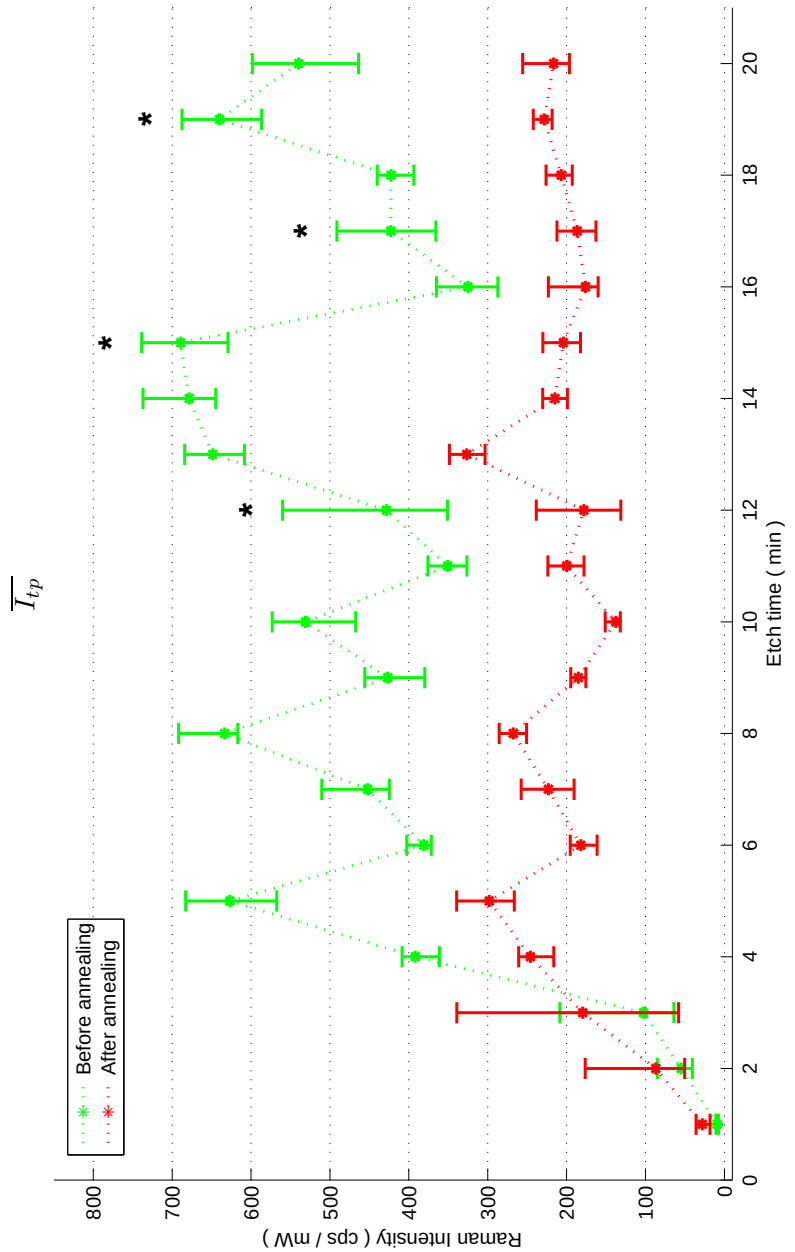

Fig. 6.10: Average thiophenol peak intensity ($\overline{I_{tp}}$) for samples coated with 60.2 nm silver. Asterisks indicate contaminated samples with reduced area due to surface contamination by particulates.

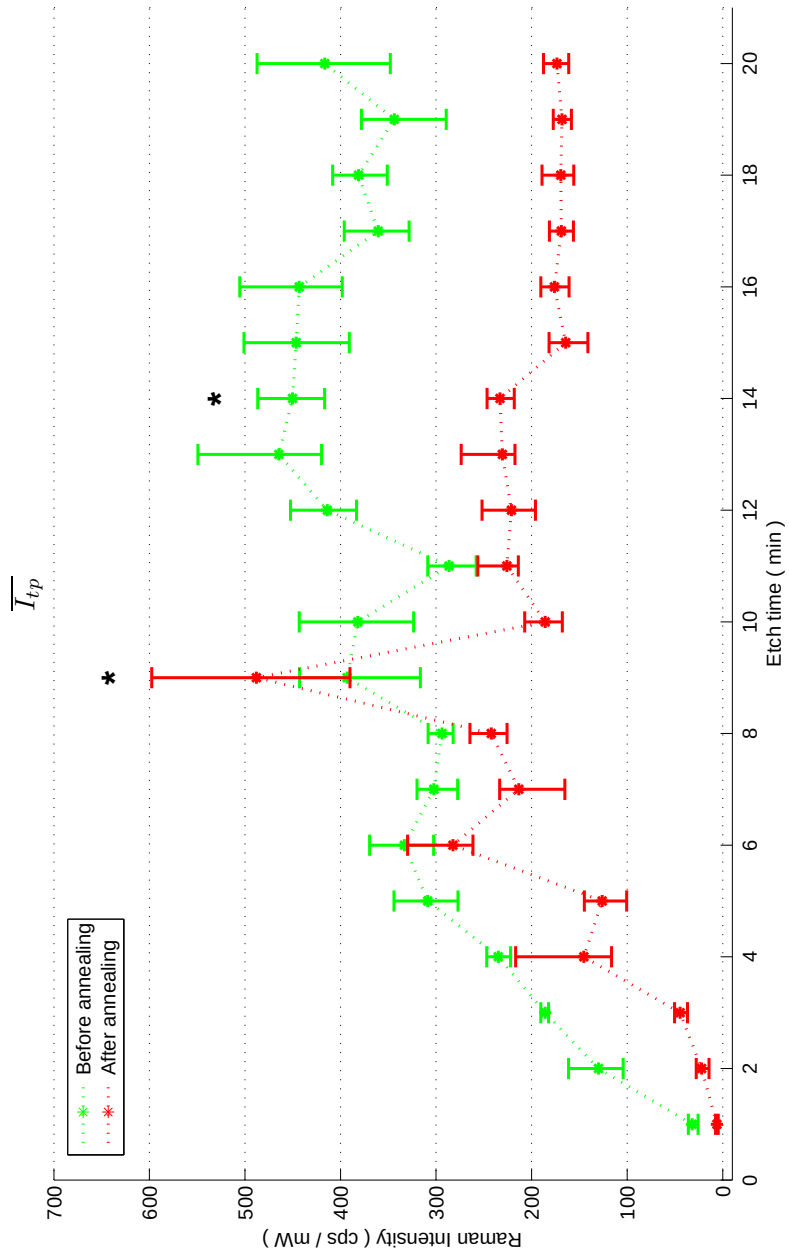

Fig. 6.11: Average thiophenol peak intensity ($\overline{I_{tp}}$) for samples coated with 80.5 nm silver. Asterisks indicate contaminated samples with reduced area due to surface contamination by particulates.

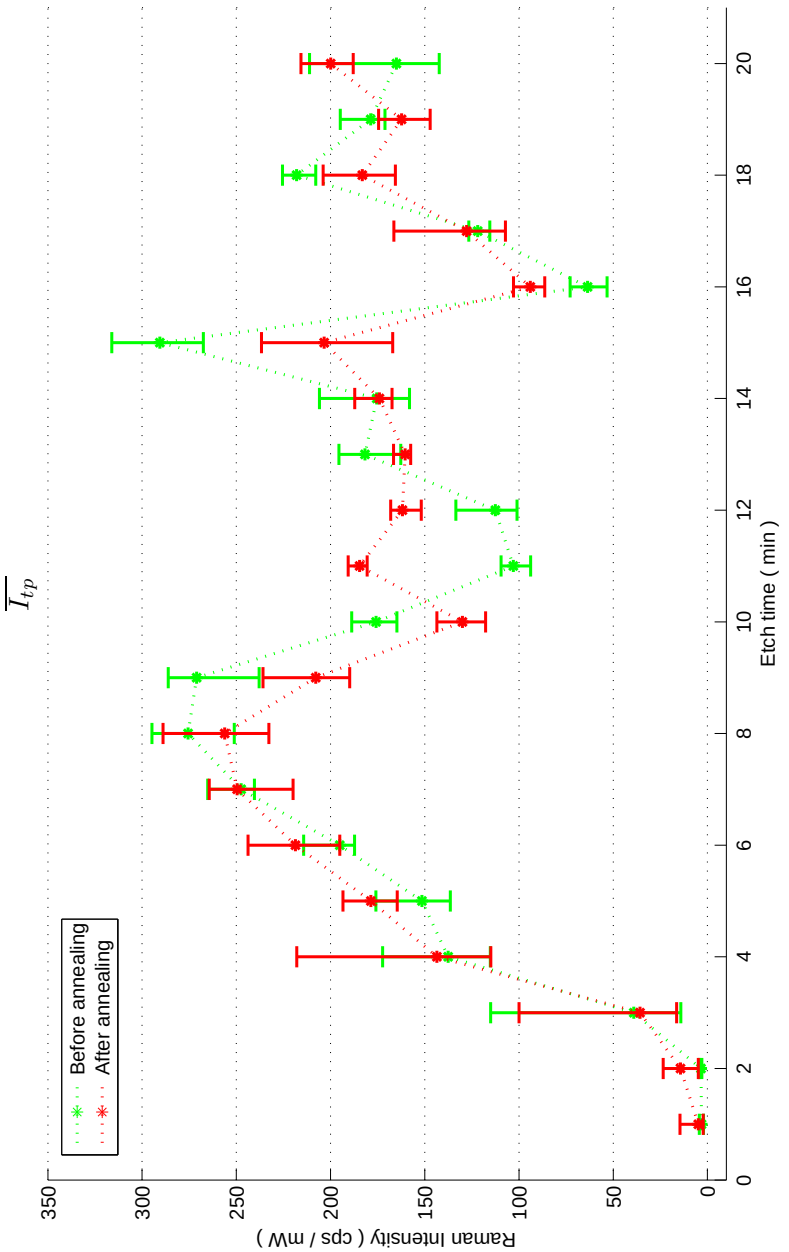

Fig. 6.12: Average thiophenol peak intensity ($\overline{I_{tp}}$) for samples coated with 100.0 nm silver.

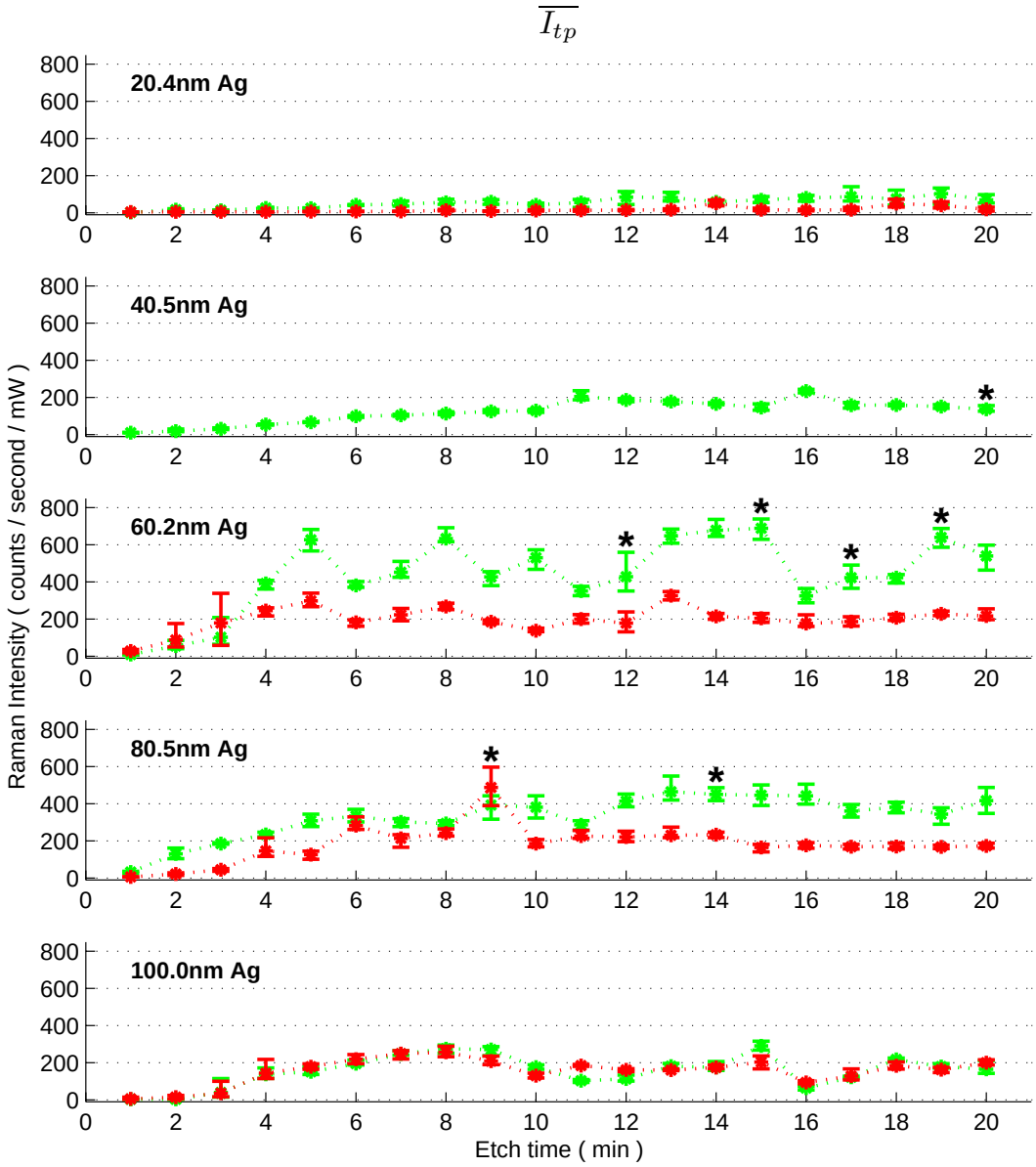

Fig. 6.13: $\overline{I_{tp}}$ counts for all samples. Asterisks indicate contaminated samples.

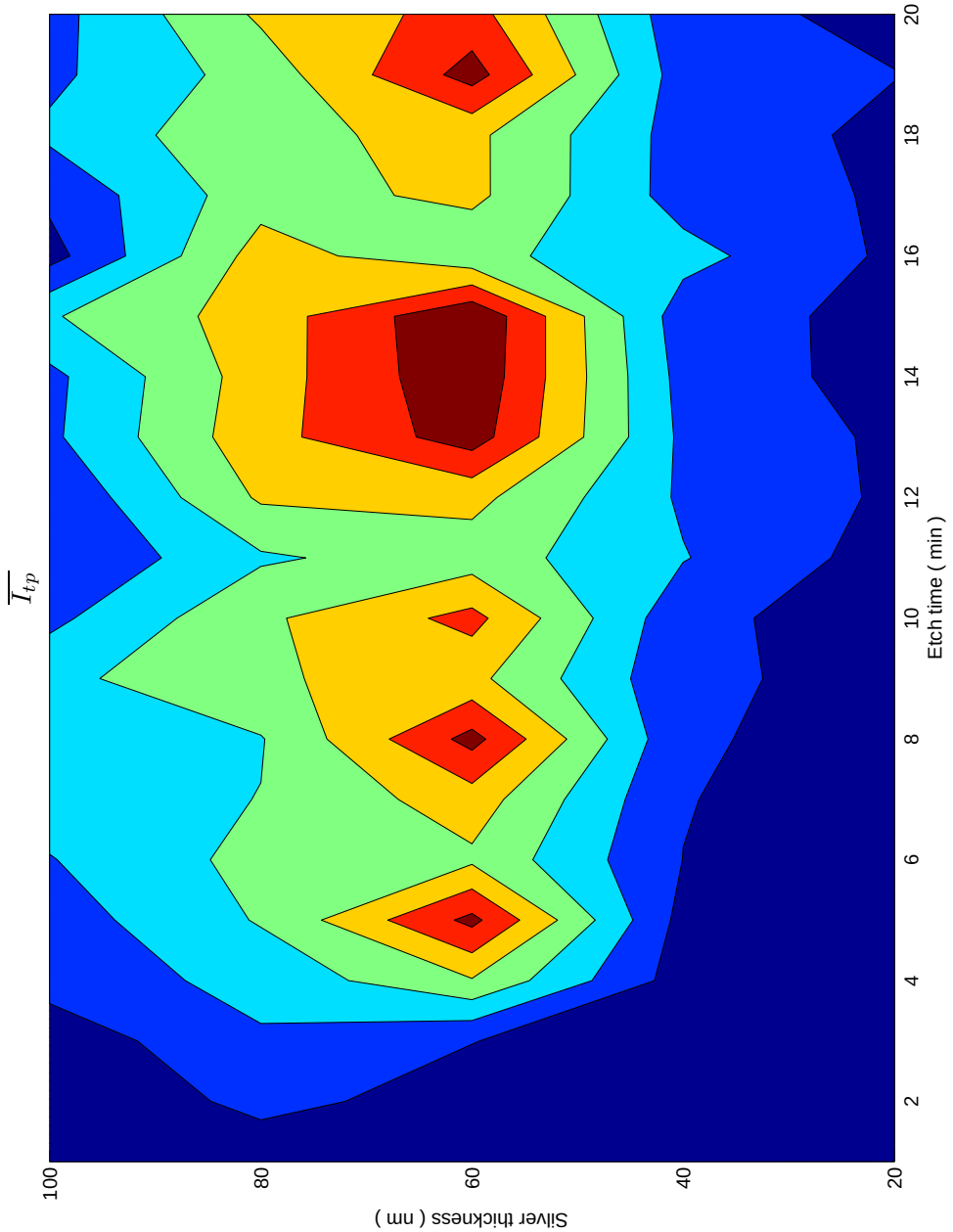

Fig. 6.14: Contour plot of $\overline{I_{tp}}$.

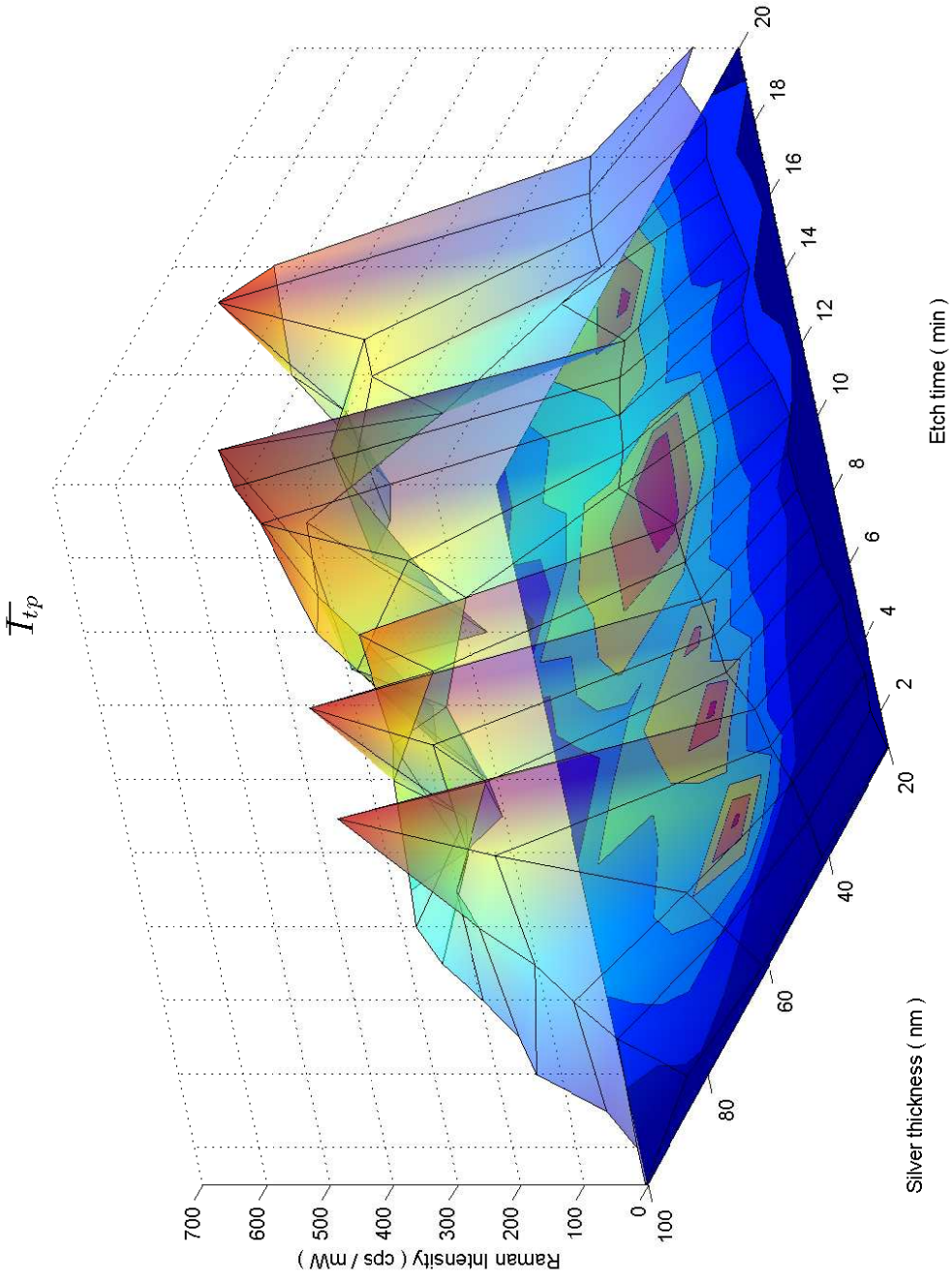

Fig. 6.15: Surface plot of $\overline{I_{tp}}$.

Figure 6.14 shows the data for $\overline{I_{tp}}$ from the pre-annealed samples in the form of a contour plot. Figure 6.15 shows the same data with the addition of a surface mesh. A number of interesting aspects can be seen in this data.

Firstly, the samples coated with 60.5 nm of silver generally achieve the greatest SERS signal counts. From these peaks, the counts drop with both increasing and decreasing coating thickness.

There is a clear step around the 3 minute etch mark in the samples coated with $\geq$ 40 nm of silver. At this point, the SERS effect appears to "switch on". From here to the 6 / 7 minute etch samples, the SERS signal intensity increases. However, after approximately 8 minutes of etching, the SERS counts plateau. There exists an amount of variability in the SERS signal level from this point (especially for the 60.5 nm coating) but there is no clear trend of increasing counts after this point. This observation matches the results of the simulation in Chapter 4 which indicate that at some point in time, an equilibrium is reached in the rates at which the surface pyramids and the wells etch. When this point is reached, the the structure type (ie. pyramid dimensions) and the surface area of the etched fibre no longer change with increased exposure to the acid.

It is estimated that the ξ_d of these fibres is approximately 20%. According to the simulation in Chapter 4, at equilibrium, the etched surface area would be approximately five times greater than the original planar area. It is clear from Figure 6.13, however, that the SERS intensity recorded at equilibrium is much greater than five times that of the planar samples. Thus the increase in SERS enhancement is not solely due to the increase in available surface area but rather must be a function of both the increased area and the surface structure characteristics.

The variability in the SERS count rate for the samples etched for $>$ 8 minutes is a very interesting result. The logical explanation for this is that the majority of the SERS signal is not from the pyramidal structures themselves but from the interaction between silver particles on the sides of the wells. Variations in the coating conditions (eg. slight changes in angle and distance from the coating flux source) would therefore contribute to variations in the signal counts.

Figure 6.16 (a) is a high resolution image of the well walls for a sample etched for 20 minutes and coated with 100.0 nm of silver. The discrete particles can easily be seen. Current theory suggests that the interaction between metal particles when

spaced only a few nanometres apart can generate a large SERS effect [Zou and Schatz, 2005]. As such, it is postulated that the enhancement seen in this experiment is due more to these interactions than the field produced by the pyramidal shaped "macro" structures.

Figure 6.16 (b) shows the same sample after annealing. In this image, the change in surface coverage is obvious. Regularly spaced nanoparticles of silver are now replaced with either areas of continuous film or smaller, further spaced particles. Both of these changes lead to a reduction in the number of particles with similar spacings to those seen in the pre-annealed sample. If the SERS effect is indeed reliant on these closely spaced particles, the reduction in their count rate as seen in all of the annealed samples, should (and is found to) produce lower SERS intensities (Fig. 6.13). This result correlates well with other studies, which indicate that an ensemble of a large number of small particles produce higher enhancements than those comprising a small number [Khan et al., 2006].

It must be noted that when dealing with particles on the walls of the wells, the thickness recorded by the coating unit does not relate to the height of the particles. The film thickness monitor (Emitech K150X) is recording a *planar* thickness. As can be seen in the Figures 6.2 to 6.6 and 6.16, the particles on the walls do not form a continuous film. Rather, the thickness recorded can only be related to a *growth time* for the particles (ie. the thicker the film recorded, the longer the time available for the particles to grow). This in turn relates to the ultimate size of the particles. Typically, a metal island formation such as this can be characterised by the use of an atomic force microscope (AFM). Although several attempts were made, the aspect ratios of the wells prevent the AFM probe tip from following the surfaces and as such, no quantitative data on the dimensions of the particles is available. It is know that highly enhancing metal island films can be obtained by oblique angle deposition but comparisons with this technique are beyond the scope of this thesis [Chaney et al., 2005].

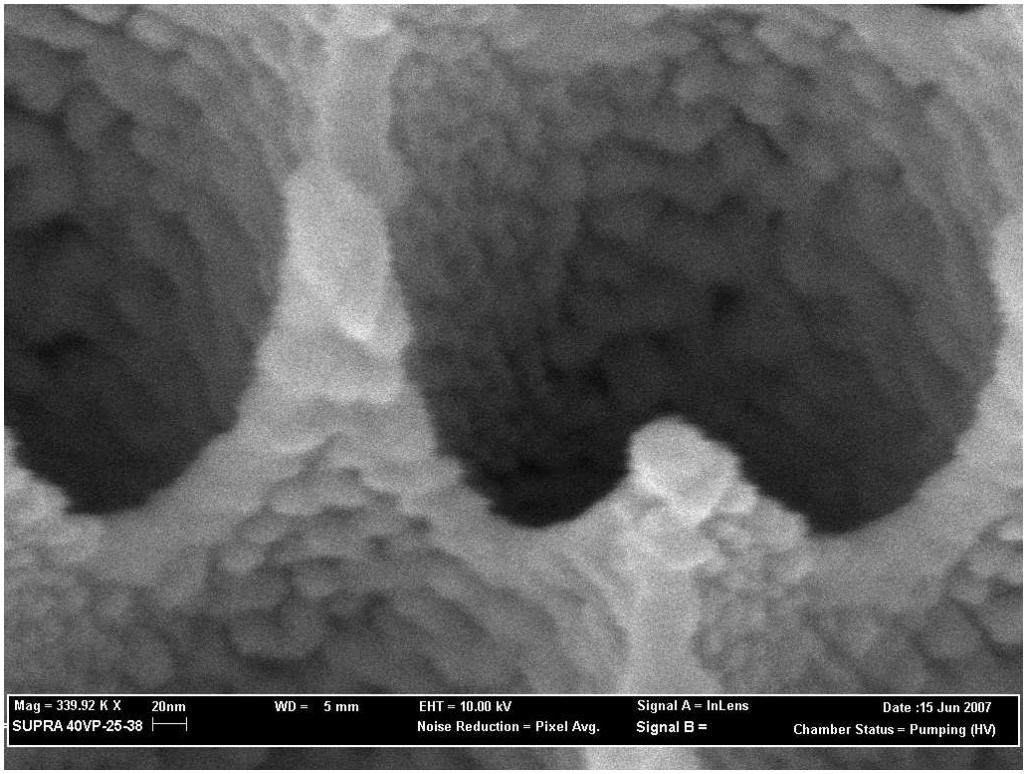

(a)

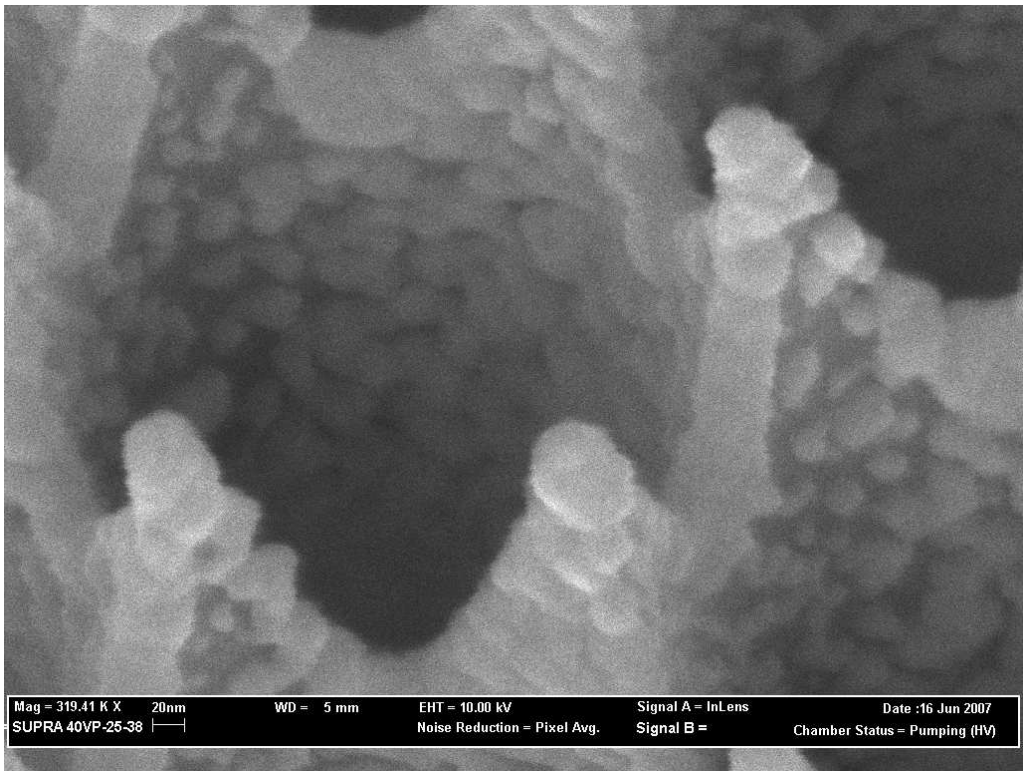

(b)

Fig. 6.16: Silver particles on the walls of the wells (a) before annealing and (b) after annealing for a 100.0 nm coating thickness.

6.4 LSPR Characterisation

6.4.1 Experimental Setup

When characterising a SERS substrate, it is important to find the peak plasmon resonance wavelength (LSPR peak). It has been suggested that the highest SERS enhancements can be found when the LSPR peak is between the laser excitation wavelength and the expected Raman wavelengths [Haynes et al., 2005]. To investigate the changes in the LSPR with different thicknesses of silver, an additional set of ten samples were prepared in the same manner as Section 6.2.1. However, in these samples, a 10 mm length of fibre was used, thus filling the ferrule and allowing transmission spectra to be gathered. Both ends were polished in the manner described in Section 6.2.1.

All ten samples were etched together in the same fashion as Section 6.2.1 for 15 minutes before being triple rinsed in de-ionised water. Before continuing, a reference transmission spectrum was taken from one of the etched fibres. On one end only, samples were then coated with 2 nm chromium (KJL unit). The samples were divided into five sets of two fibre each with each set then coated with the following silver thicknesses using the Emitech unit: 20.1 nm, 40.0 nm, 60.6 nm, 80.2 nm and 100 nm.

A purpose built micro-spectrophotometer (Fig. 6.17) was used to measure the LSPR absorption through the fibre. The system was fitted with a stabilised white light source (Newport Oriel Apex) focussed by a 6.3× lens (0.2 N.A.) onto the tip of the fibre. A 10× lens (0.3 N.A.) was used to collect the light from the opposite end of the ferrule. The collected light was then sent to a 300 mm spectrometer (Acton Research Spectra Pro) fitted with a TEC-cooled CCD detector (Pixis 100F).

After collecting both a reference spectrum from an uncoated sample and transmission spectra from the samples above, the ten fibres were annealed at 80° C for 1 hr and re-tested.

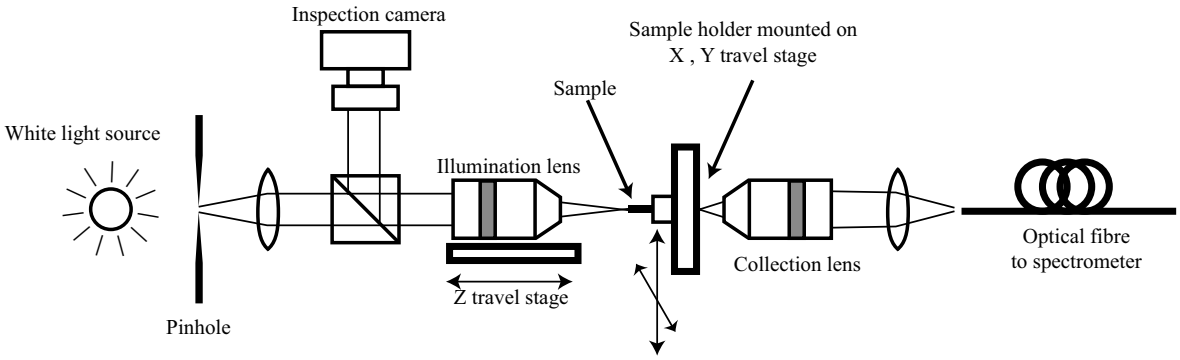

Fig. 6.17: Micro-spectrophotometer schematic.

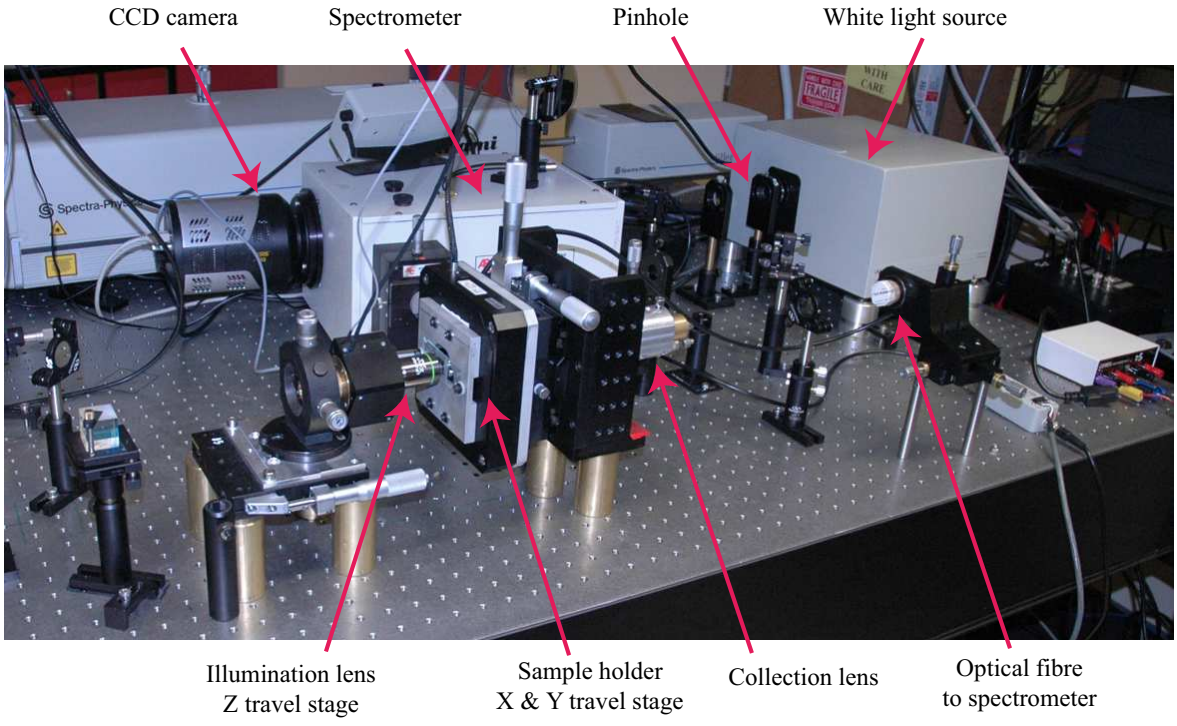

Fig. 6.18: Micro-spectrophotometer. Not identified are the steering optics used to bring the white light to the illumination objective.

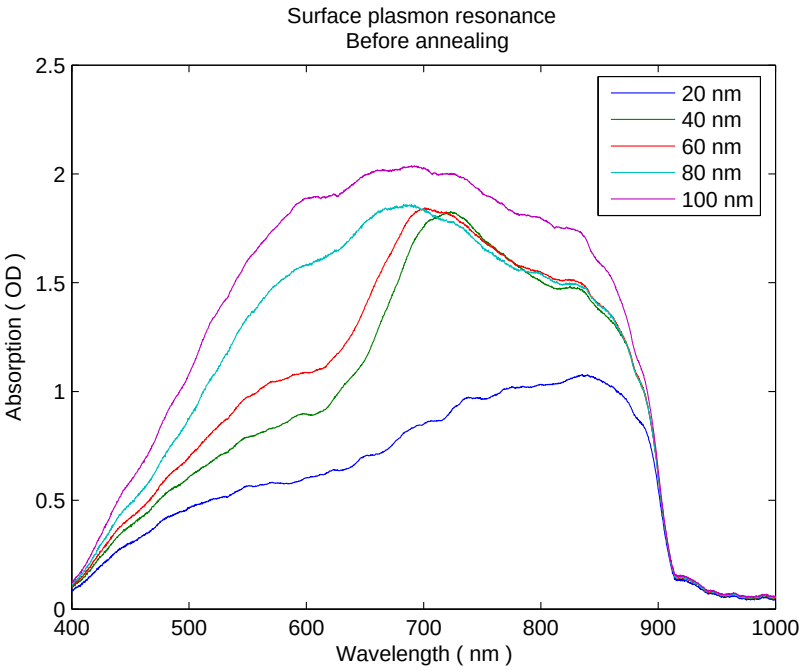

(a)

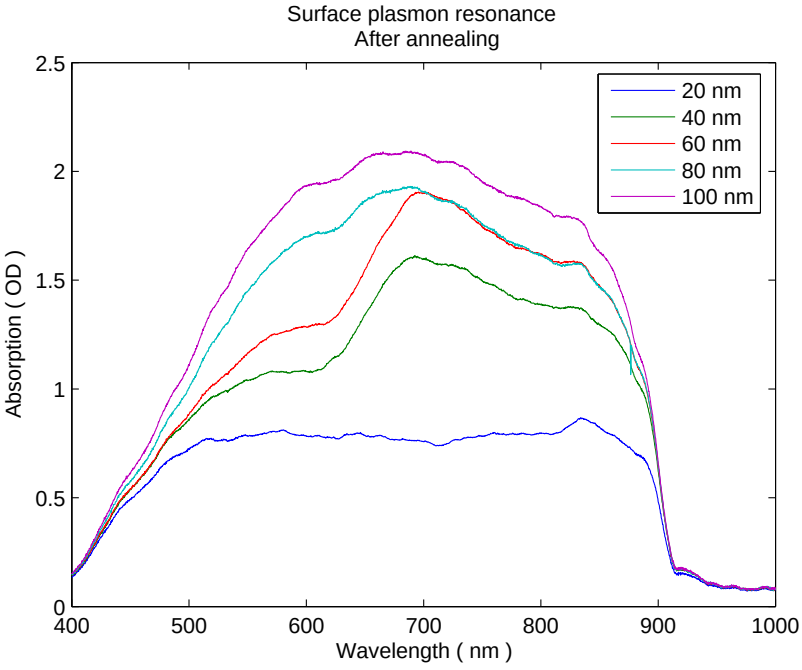

(b)

Fig. 6.19: Localised surface plasmon resonances (a) before annealing and (b) after annealing. Note that the Y axis (optical density) is a logarithmic scale. The cutoff at 900 nm is due to limitations of the experimental apparatus.

6.4.2 Results and Analysis

Five sets of two samples were prepared for this test. Figure 6.19 shows the averaged data from the two samples in each set in terms of their absorption (optical density). Plotting in this fashion makes the identification of any LSPR peaks straightforward as by definition, a resonance occurs when the surface absorbs light at the appropriate wavelength. Note that absorption (optical density) is defined by

$$OD = log_{10}\left(\frac{reference}{sample}\right) \tag{6.1}$$

Figure 6.19 shows a broad band of reduced transmission due to reflection for all samples with the optical density increasing, with film thickness, as expected [Sun et al., 2007; Xu et al., 2005]. However, there is also visible a narrower LSPR absorption peak for the samples coated with 40 nm and 60 nm and to a lesser extent 80 nm of silver (previous works have shown that typical SERS applicable LSPR absorption widths are on the scale of 200 nm FWHM [Yonzon et al., 2005]). The location of this peak at around 700 nm corresponds to the known peak absorption for a hexagonal array of triangular silver nanoparticles having a period of 400 nm [Haynes et al., 2003]. For the samples coated with 20 nm and 100 nm, however, no clear narrow LSPR peak can be identified. The implications of this are two-fold. Firstly, the relatively small amplitude of the LSPR peaks implies that the plasmon field strength is quite low, which in turn results in low SERS enhancement factors. On the other hand, this also means that the field resonates over a relatively large range of wavelengths thus making the sensor useful for a range of excitation wavelengths.

As stated earlier, it has been suggested that the highest SERS enhancements can be found when the LSPR peak is between the laser excitation wavelength and the expected Raman wavelengths [Haynes et al., 2005]. The data collected indicates an excitation around 700 nm would be best. The SERS spectra collected in this chapter were excited with a 532 nm source. Therefore, using a longer excitation wavelength close to the LSPR peak may help to improve the SERS enhancement factor. However, as the Raman intensity scales with ω^4, a move to a longer wavelength will significantly reduce the native Raman scattering intensity. As an example, using a 785 nm excitation reduces the signal by a factor of approximately 4.7, while using 632.8 nm reduces the signal by a factor of 2. The potential increase in enhancement factor must be balanced against this reduction.

6.5 Repeatability Characterisation

6.5.1 Experimental Setup

Before a study on the repeatability characteristics of the SERS fibres can be conducted, a measure of the repeatability of the experimental setup must be determined. This is necessary in order to account for such things as fluctuations in the laser power and errors in focussing. To do this, an experiment measuring the NRS signal of a silicon wafer was conducted. The experimental conditions were the same as presented in Section 6.3 with the exceptions of the laser power being 1.1 mW and the integration time reduced to three seconds. Ten measurements were taken and after each recording, the sample was moved and refocussed. All spectra have undergone background subtraction. Figure 6.20 (a) shows one of the NRS spectra recorded and (b) plots the height of the main 520 cm^{-1} peak.

A convenient measure of the repeatability of spectral features is the relative standard deviation (RSD) of the peak heights. The RSD is found simply by dividing the standard deviation of the peak height by the average value. For the data presented in Figure 6.20 (b), the RSD is found to be 4.5%.

Having determined the repeatability of the experimental setup, a measure of the repeatability of the fibres can now be made. To test this, ten samples were prepared in the same manner as Section 6.3 and etched together for 15 minutes in the 10% BHF/HCl etchant. All samples were coated with 2 nm chromium (KJL unit) and approximately 65 nm high purity silver (Emitech unit). An exact measure of the amount of silver deposited is not available as the film thickness monitor installed in the coating unit failed during deposition. The deposition thickness is instead determined by scratching the film off a planar area of the sample and measuring the the resulting valley depth using an AFM (Solver, NT-MDT).

Samples were soaked together in 25 ml of a 10 mM solution of thiophenol in ethanol for 20 minutes (Section 3.4.1) followed by a rinse in pure ethanol for a further two minutes.

Spectra were collected using the same experimental setup used in Section 6.3 but using a 10× lens (0.25 N.A.). In the previous section, five spectra were taken from different locations across the surface to determine the intra-sample repeatability.

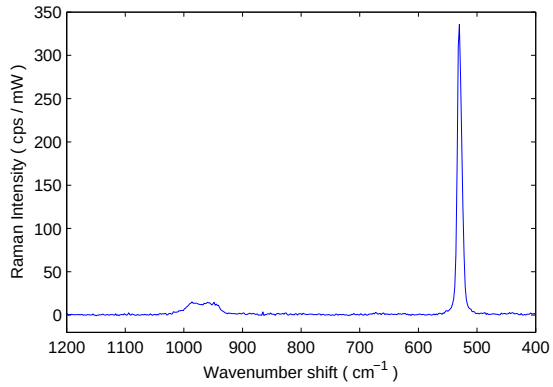

(a)

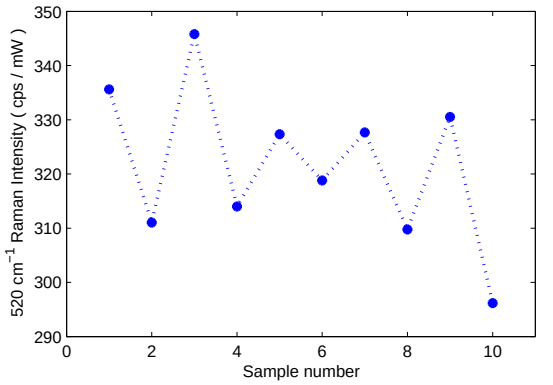

(b)

Fig. 6.20: (a) NRS spectrum of the silicon wafer and (b) plot of the peak heights at 520 cm^{-1}.

As this portion of the experiment is trying to determine the inter-sample SERS repeatability, a lower N.A. lens is used, in effect, to average over a larger number of nanoparticle sites. Doing so reduces the effect of intra-sample repeatability. Due to this lens being less efficient than the 50× lens, power at the sample was increased to 1.9 mW.

6.5.2 Results and Analysis

Figure 6.21 shows the 10 spectra collected for the repeatability study. Spectra are presented in no particular order. As can be seen, there is a significant amount of variability in the cps/mW across the samples. Using the data shown in Figure 6.21, the RSD for the $\overline{I_{tp}}$ is found to be 40%.

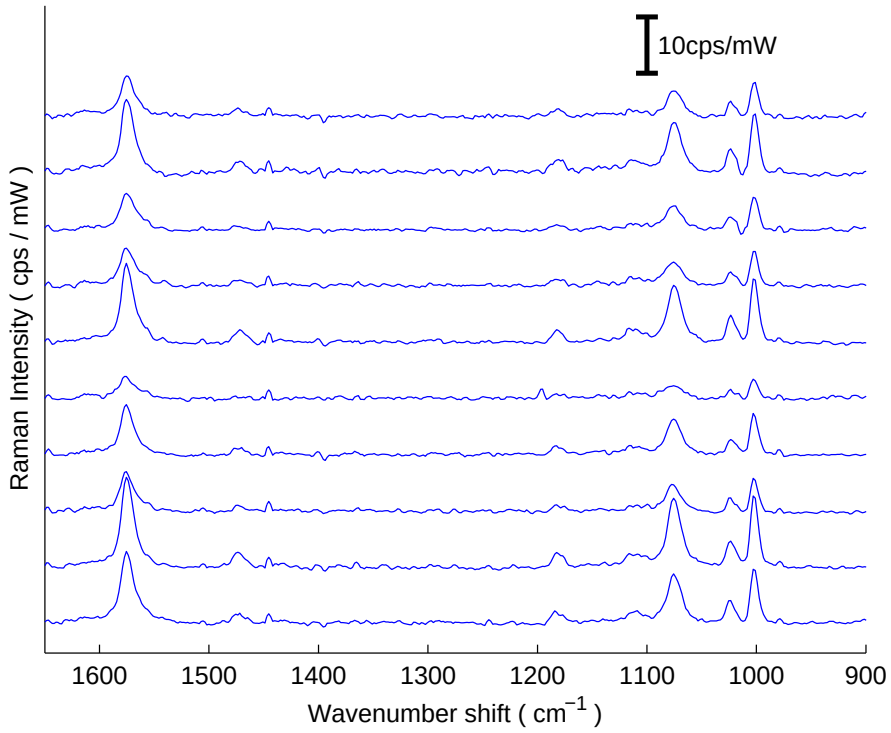

Fig. 6.21: Spectra for repeatability study. Spectra have been background subtracted and shifted vertically for clarity.

The variability recorded is qualitatively similar to the results achieved in Section 6.3 for samples etched > 8 minutes. Once again, it is proposed that the slight variations in surface coverage and inter-particle spacings of the silver islands on the surface of the wells is responsible for the large RSD.

This value is clearly too large for reliable quantitative measurements where a variability of less than 10% is typically desired. As an example, in the case of using SERS to monitor blood glucose levels for the purpose of providing feedback to a patient [Haynes et al., 2005], using a system where different sensors can vary their output by as much as 40% is clearly unacceptable.

One possible solution to reduce the variability is to provide the sensor with a known molecule at a known concentration with which its sensitivity can be calibrated (ie. an internal calibration standard). In their work on glucose detection, the Van Duyne group have used monolayers of thiol-terminated molecules on their substrates for the purpose

of trapping the glucose molecule close to the active surface [Haynes et al., 2005; Shefer-Peltier et al., 2002; Yonzon et al., 2004]. However, these thiols can also be employed as calibration standards. As thiol terminated molecules form stable monolayers on the surface of the sensor, their concentration should be uniform across multiple samples. Taking a spectrum of the functionalised surface before introducing the sample allows the performance of each different sensor to be determined. By then comparing the spectra of the molecule of interest to this reference spectrum, the sensor is now acting as a calibrated, quantitative system. In other words, as long as the spectra gathered from a sensor are compared against the calibration spectrum of that sensor (and not simply against some average), the variation between sensors can be reduced to an acceptable level.

As a preliminary example, Figure 6.22 shows the data from the repeatability study (Section 6.5) after normalising the spectra to the 1073 cm^{-1} peak. Normalising in this case simply means scaling the heights of the normalisation peak so that it is identical for all spectra. Doing so now reduces the RSD of the $\overline{I_{tp}}$ from 40% to 8%. It should be noted that in theory, for a data set such as this, normalising should result in zero RSD. It doesn't due to such conditions as the high noise level (ie. low signal-to-noise ratio) and thermal effects on the sample. It is, however, a measure of the system's repeatability for a "perfect" data set. After the normalisation process, the RSD value compares well to other quoted values for established techniques including a figure of 20% for roughened surfaces and 5% for carefully controlled colloidal solutions [Munro et al., 1995; Viets and Hill, 1998]. It also compares well with the 10% value quoted for a SERS optical fibre utilising immobilised silver colloids [Polwart et al., 2000].

Of course, the addition of a calibration molecule may result in undesirable spectral lines or prevent the molecule of interest from reaching the active surface. As such, calibration molecules must be carefully chosen so as to minimise the masking of relevant spectral features whenever possible.

6.6 Conclusions

The production of topologically identical nano-scale silica structures allows investigations into the effects of coating thicknesses to be conducted. From these tests, it can be concluded that etching the FIGH-30-100X fibre for over 10 minutes and coating

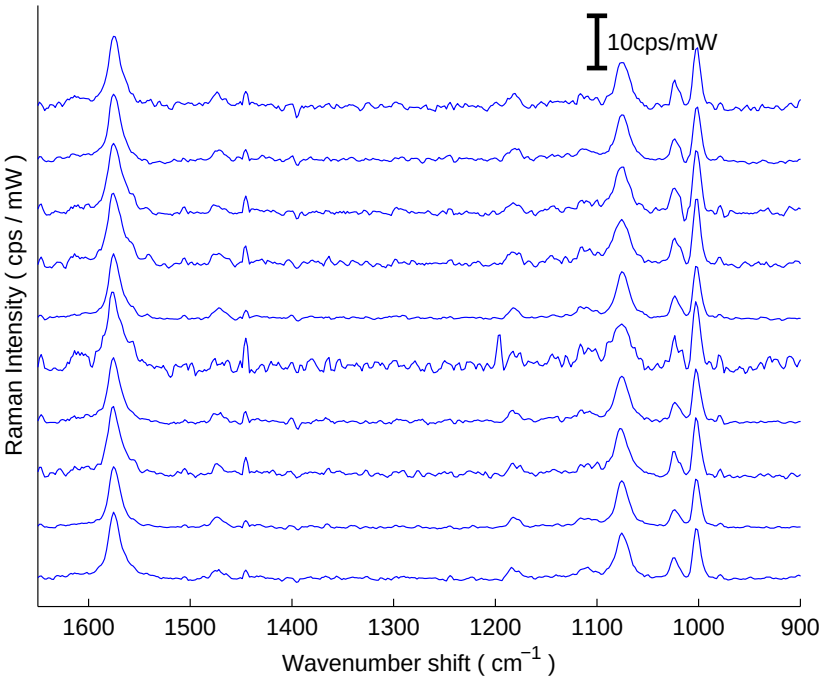

Fig. 6.22: Spectra for the repeatability study after normalising to the 1073 cm^{-1} peak. Spectra have been background subtracted and shifted vertically for clarity.

with 60 nm of silver produces the highest SERS enhancement factors for this surface topology using a 532 nm excitation. The signal count rates for these surfaces was approximately 1.5 orders of magnitude greater than those taken from a planar glass surface with a metal island film. Annealing the silver films appears to cause the metal islands to merge and the consequential reduction in nanoparticle sites results in a reduction in the SERS intensity.

It was found that the peak LSPR adsorption when coated with thin layers of silver was in the region of 700 nm. However, the data presented in this chapter was collected using a 532 nm source. Given that the LSPR correlates with the SERS enhancement factor, it may be possible to improve the sensitivity of the probe by moving to a longer excitation wavelength. This shift, however, must be balanced against the reduction in native Raman intensity as a function of the ω^4 frequency dependence.

Despite the structural uniformity generated by the etching process, a relatively large variation in signal strength was observed. This is most likely due to the random

nature of the metal islands formation on the surface of the well walls. Once again, highly oblique surface angles with respect to the metal source cause the deposited metal to form islands rather than a continuous film. Variations in the size and spacing of these islands result in variations in the SERS enhancement. Having found the sensors to produce quite variable enhancement factors now raises the importance of calibration. When using a SERS sensor simply for detection purposes (ie. qualitative), calibration is not necessary. As long as the sensor reliably produces a signal above an appropriate threshold, all is well. However, for a quantitative system this is unacceptable.

The solution (as presented in Section 6.5.2) is to expose the SERS substrates to molecules of known concentration and to use the recorded signal intensity to calibrate the sensor performance. In the preliminary experiment presented in Section 6.5.2, by calibrating to a peak of the thiophenol spectrum, the variability dropped from 40% to 8% which compares well with other substrate designs.

Chapter 7

Applications of the Nanostructured SERS Probe

In Chapter 1, a number of applications where a small fibre-based SERS sensor could be employed were discussed. Presented in this chapter is a selection of preliminary "proof of concept" results using the SERS fibres for a number of these uses, namely the detection of glucose, 2-chloroethyl ethyl sulfide (commonly known as half-mustard) and chlorsulfuron. The small number of fibre samples available at the time of writing placed severe limits on the number of experiments that could be conducted. However, the results shown here indicate the potential of the SERS fibre sensors.

As stated in the previous chapter, to use the nanostructured SERS fibre sensor for quantitative purposes requires some form of calibration. In this case, a monolayer of 1-decanethiol (1-DT) ($CH_3(CH_2)_9SH$) (Fig. 7.1) is used as a calibration molecule. Like the thiophenol used in Sections 6.3 and 6.5, 1-DT also forms a self-assembled monolayer on the silver coated surface via bonding of the thiol group. Because it forms a stable SAM, its concentration should be reasonably consistent from one sample to the next. As such, by normalising the results to the Raman intensity of the 1-DT peaks, the SERS enhancement variability between samples can be significantly reduced. Additionally, previous works have shown that the packing density, orientation and charge (hydrophobicity) of 1-DT allow it to act as an effective partition layer, bringing molecules of interest close to the active surface [Shefer-Peltier et al., 2002; Stuart et al., 2006a]. To demonstrate the calibration process, for all the results presented here, the target molecule's spectrum (which now is superimposed on the 1-DT monolayer

spectrum) is normalised to the 1124 cm^{-1} peak of a pure 1-DT monolayer spectrum. As such, in the figures presented, the cps/mW values are the raw data gathered from the 1-DT spectrum whereas the values for the analytes are scaled as appropriate.

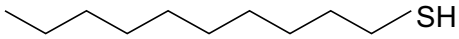

Fig. 7.1: 1-decanethiol molecule.

Although the results presented in this chapter only show a limited number of spectra per analyte (due to the limited number of substrates available) and hence are not strictly quantitative in nature, it is still important to demonstrate that spectral identification is indeed possible in the presence of the 1-DT partition layer. It should also be noted that as in the previous chapter, the spectra presented here were collected by backscattering off the active tip rather than through the fibre itself due to the internal scattering losses encountered. For the applications presented, a through-fibre measurement would be preferable and future work on the fibre design is intended to make this possible. Suggestions on how this may be achieved are presented in the thesis conclusions.

7.1 Glucose Detection

One of the most compelling applications of SERS is for the in-vivo detection and monitoring of medically relevant bio-molecules. Of these, the important challenge of continuous monitoring of blood glucose levels for the management of diabetes has prompted much interest. Presently, most people who suffer from diabetes monitor their blood glucose levels by drawing a small quantity of blood, typically from the finger tip, and testing it using an external device. For patients with acute diabetes, this procedure may need to be done several times a day causing considerable discomfort. However, it is proposed that a small, implantable SERS sensor may provide not only a minimally invasive testing procedure but may also offer the possibility of continuous monitoring [Stuart et al., 2005]. Ultimately this may be integrated with a miniature subcutaneous insulin pump for closed loop glycemic control [Newman and Turner, 2005].

As discussed in Chapter 1, the Van Duyne group have published several papers on the use of SERS sensors for the detection and monitoring of glucose including a recent

demonstration of in-vivo detection [Stuart et al., 2006b]. It should be noted though that in the latter experiment, a relatively large incision was required in the flank of the test animal for the placements and interrogation of the conventional planar SERS surface. However, if using a small fibre-based SERS sensor in an "optrode" configuration (ie. a single fibre for both excitation and collection), such an invasive procedure would not be required.

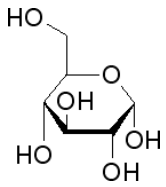

Fig. 7.2: $\alpha-$D glucose molecule. [Sigma-Aldrich-Glucose, 2008]

7.1.1 Experiment and Results

A SERS fibre probe (FIGH-30-100X fibre mounted in a Diamond FO ferrule) was prepared by etching for 20 minutes in the 10% BHF/HCl etchant and coated with 100 nm silver using the KJL unit. The Van Duyne group has previously experimented with various partition layers for the capture of glucose but for the purposes of this preliminary study, the simplest approach involving a single-component SAM of 1-DT was utilised [Shefer-Peltier et al., 2002]. As such, a 10 mM ethanolic solution of 1-DT (96%, Aldrich) was prepared and the sensor functionalised by immersing it in the solution for approximately 12 hours.

A 5,000 ppm (by mass) solution of $\alpha-$D glucose (96%, Aldrich) (Fig. 7.2) was prepared by dilution into phosphate buffered saline (pH 7.4, Sigma). This concentration is equivalent to the upper limit of physiologically attainable human glucose levels (typically 50 - 5,000 ppm). The probe was then immersed in a bath containing approximately 25 mL of this solution such that the active tip, facing upwards towards the collection lens, was just below the surface of the liquid. Spectra were collected using the RM2000 microscope (Section 2.5.1) fitted with the 632.8 nm Coherent 40.6" HeNe laser source and a 50× objective. The power at the sample was approximately 0.4 mW and five scans of 10 seconds each were averaged together.

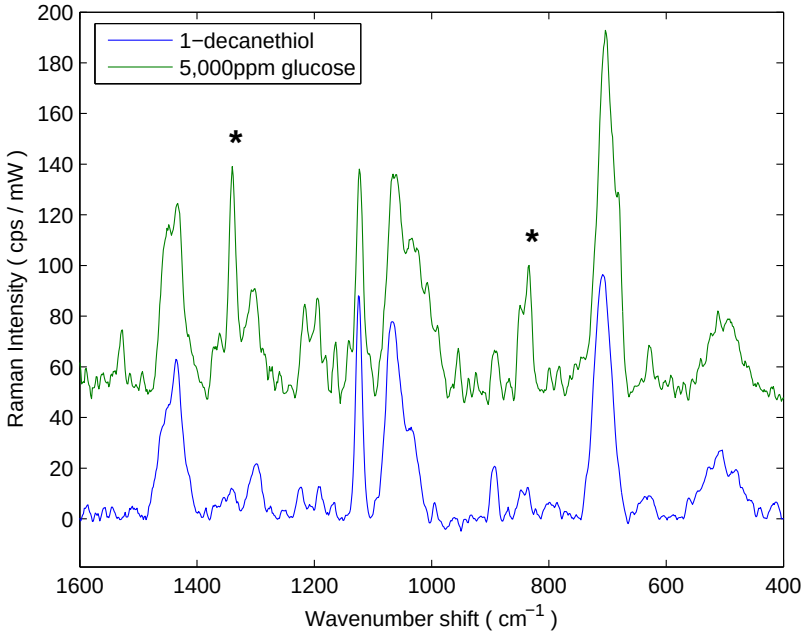

Fig. 7.3: 1-decanethiol monolayer and $\alpha-$D glucose + 1-DT monolayer spectra (after background subtraction) with the characteristic glucose peaks at 843 cm^{-1} and 1340 cm^{-1} identified by asterisks. The glucose spectrum is normalised to the 1124 cm^{-1} peak of 1-DT and is shifted vertically for clarity.

Figure 7.3 shows the spectra collected after undergoing background subtraction. The glucose (+ 1-DT) spectrum has been normalised to the 1124 cm^{-1} peak of the pure 1-DT spectrum and is shifted vertically for clarity. The characteristic glucose peaks at 834 and 1340 cm^{-1} can be clearly identified. The signal-to-noise ratio of the glucose peaks to the background Raman signal indicate the potential for the detection of lower glucose concentrations. Experiments are currently being conducted to determine if the sensor can detect the low end of the physiological levels (ie. 50 ppm). According to the results gathered in the previous chapter, using a thinner coating in the range of 60 - 80 nm and moving to a longer excitation wavelength may further improve the sensitivity. Problems were encountered with the stability of the silver coating in the saline solution during this experiment and this issue will require further attention in future work. Studies are also being conducted to determine what chemometric techniques may be applied to track changes in concentration.

7.2 CEES Detection

The detection of contaminants in drinking and agricultural water is another application especially suitable for SERS. Unlike other techniques such as IR absorption spectroscopy, SERS is relatively insensitive to the presence of water molecules. As such, contaminants can be readily identified from the spectra collected. Previous works have demonstrated the suitability of SERS for detecting naphthalene and polynuclear aromatic hydrocarbons in sea water [Murphy et al., 2000; Schmidt et al., 2004]. Of special interest in the current climate is the detection of contaminants in drinking water. To this end, a test was conducted to determine if the SERS fibre sensor could detect 2-chloroethyl ethyl sulfide (also known as CEES or half-mustard), a simulant for the nerve agent HD mustard [Stuart et al., 2006a]. Detecting molecules such as these is of particular importance for protecting potable water supplies against bio-terrorism attacks.

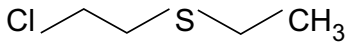

Fig. 7.4: CEES molecule.

7.2.1 Experiment and Results

A ferrule mounted SERS fibre probe was prepared by etching for 20 minutes in the 10% BHF/HCl etchant and coated with 2 nm of chromium and 100 nm of silver using the KJL and Emitech coaters respectively. The sensor was again functionalised by immersing in the 10 mM ethanolic solution of 1-DT for approximately 12 hours.

A 549 ppm ($\pm$0.5ppm, by mass) solution of CEES ($ClCH_2CH_2SC_2H_5$) (98%, Aldrich) was prepared by diluting in de-ionised water. Due to the toxic nature of CEES, the solution was placed into a modified sealed sample cell (volume $\approx$ 0.9 mL, optical path length $\approx$ 2 mm). The ferrule mounted SERS fibre was then inserted into a ferrule holder mounted above a hole drilled into the wall of the cell such that the active tip was exposed to the solution. A plastic cap was used to seal the sensor into the cell with a rubbed O-ring. The sensor was then left for five minutes to allow the CEES to migrate to the SERS surface.

SERS spectra were gathered using a Renishaw InVia microscope - an updated version of the RM2000 microscope. The InVia was fitted with a 785 nm diode laser for excitation and a 50× long working distance lens for spectral collection. Aside from the different laser wavelength, the operation of the microscope was identical to the RM2000 as discussed in Section 2.5.1. To collect the spectra, the laser was focussed through the sample cell containing the fluid onto the active tip of the sensor. Power at the sample was approximately 1.8 mW and five scans of 30 seconds each were averaged together. After collecting the spectrum for the 549 ppm solution, the cell was washed with water and filled with pure CEES. A second spectrum was then immediately recorded using the same setup. It was found that the glue used to fix the fibre inside the ferrule was dissolved by the solution leading to contamination of the sensor. Further effort is required to identify a more suitable adhesive.

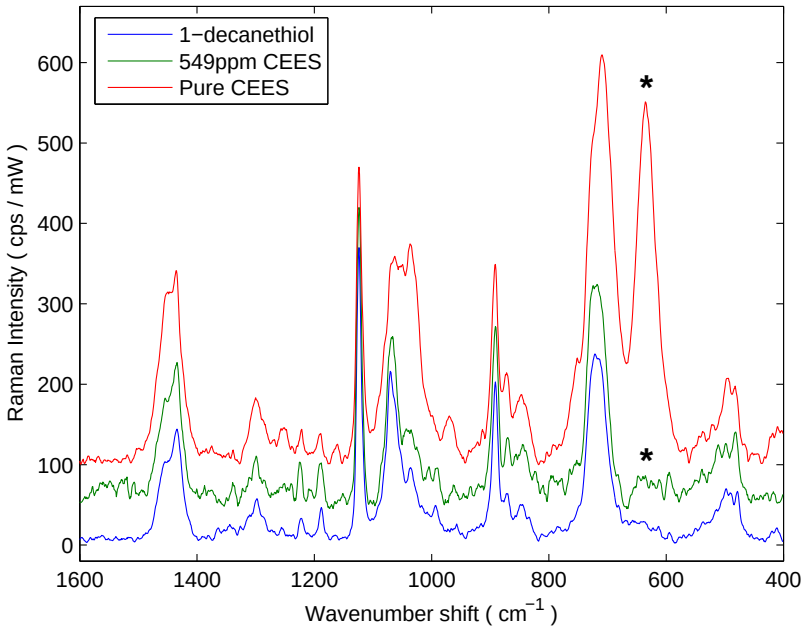

Fig. 7.5: 1-decanethiol monolayer and CEES + 1-DT monolayer spectra (after background subtraction) with the characteristic CEES peak at 637 cm^{-1} identified by an asterisk. The CEES spectra are normalised to the 1124 cm^{-1} peak of 1-DT and are shifted vertically for clarity.

Figure 7.5 shows the spectra gathered from the 549 ppm solution and the pure CEES after manual background subtraction. Both spectra have been normalised to the 1124 cm^{-1} peak of 1-DT and are shifted vertically for clarity. Only one CEES

characteristic peak at 637 cm^{-1} could be identified. On the spectrum of the pure CEES, this is clearly visible but on the 549 ppm solution, much less so. It is, however, still visible above the background level. Furthermore, when exposed to the pure CEES, the spectral intensities for the characteristic peaks continued to grow over time, revealing the dynamic process whereby the sample molecules penetrate the partition layer. As this progression occurred, additional spectral lines (such as the 1040 cm^{-1} peak visible in Fig. 7.5) became apparent.

Once again, according to the results gathered in the previous chapter, using a thinner silver coating in the rage of 60 - 80 nm may improve the sensitivity.

7.3 Chlorsulphuron Detection

Another application where a small and portable SERS device might find use is in the detection of environmental contamination as a result of agriculture. For this application, being able to use a low cost sensor and to bring the sensor to the investigation location rather than taking a sample back to a laboratory creates the potential for enormous savings in cost and time. Of particular interest in this field is the detection of sulfonylureas. Sulfonylureas are a class of herbicide used to control weeds during the growth of cereal crops. Chlorsulphuron ($C_{12}H_{12}ClN_5O_4S$) (Fig. 7.6) is a commonly used sulfonylurea as it requires very low concentrations (2 - 75 g/ha) to be effective [Sabater and Carrasco, 1997]. However, despite the low concentrations, leaching into the surrounding environment can cause damage to the neighbouring flora and fauna [Ahtiainen et al., 2003; DuPont, 2007; Sabater and Carrasco, 1997].

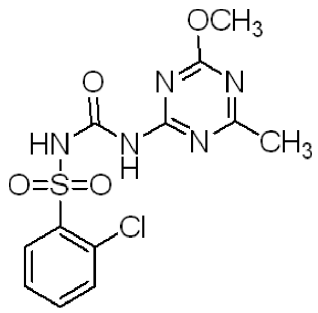

Fig. 7.6: Chlorsulphuron molecule. [Sigma-Alrich-Chlorsulphuron, 2008]

7.3.1 Experiment and Results

A SERS fibre probe was etched for 20 minutes in the 10% BHF/HCl etchant and coated with 2 nm of chromium and 60 nm of silver using the KJL and Emitech coaters respectively. The sensor was functionalised by immersing in the 10 mM ethanolic solution of 1-DT; in this instance for approximately 1 week. A solution of 10,000 ppm (by mass) chlorsulphuron (99.5%, Dr Ehrenstorfer GmbH) was prepared by diluting in methanol (>99.7%, Scharlau).

The 1-DT functionalised fibres were exposed to chlorsulphuron by dropping approximately 20 μL of the solution onto the active tip. The chlorsulphuron solution was then allowed to dry (approximately 30 seconds) and the spectrum recorded. The HJY microscope setup using 532 nm excitation (Section 6.3) was used to collect the spectra. However, for this test, laser power was increased to 1 mW. Spectral collection times remained the same at five averages of 10 seconds each.

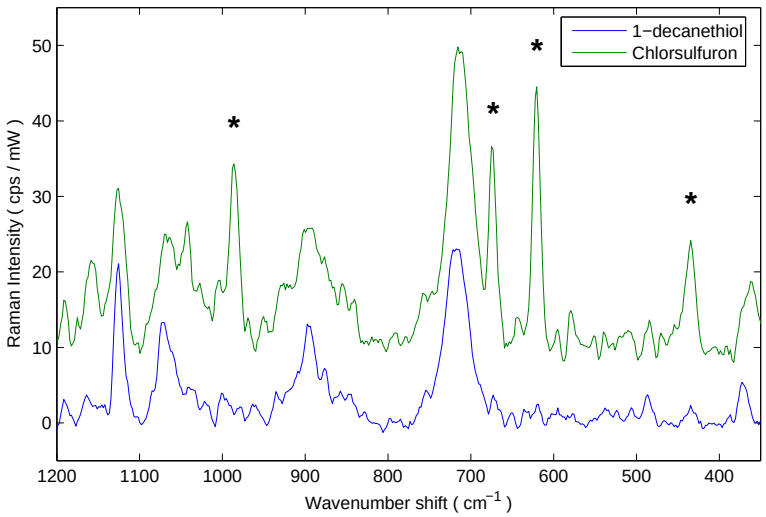

Fig. 7.7: 1-decanethiol monolayer and 10,000 ppm chlorsulphuron + 1-DT monolayer spectra (after background subtraction) with the characteristic chlorsulphuron peaks identified by asterisks. The chlorsulphuron spectrum is normalised to the 1124 cm^{-1} peak of 1-DT and is shifted vertically for clarity.

Figure 7.7 shows the spectra of 1-DT and 10,000 ppm chlorsulphuron. Spectra have undergone manual background subtraction and are presented as counts/second/mW. The chlorsulphuron spectrum has been scaled so that the 1124 cm^{-1} 1-DT peak is

the same height in both spectra. Asterisks indicate the most prominent characteristic chlorsulphuron peaks at 434, 620, 673 and 986 cm^{-1}.

In addition to the simple detection of chlorsulphuron, an additional test was performed to determine if the SERS sensor shows reversibility - in other words, the ability to detect both increasing and decreasing concentrations of the target analyte. For a sensor to be used in a continuous, on-line monitoring system, reversibility is a key feature. After collecting the spectra shown in Figure 7.7, the sensor was washed by spraying the surface with ethanol. A spectrum was then recorded of the washed sensor and the chlorsulphuron solution applied again. A second chlorsulphuron spectrum was collected before the wash routine was repeated.

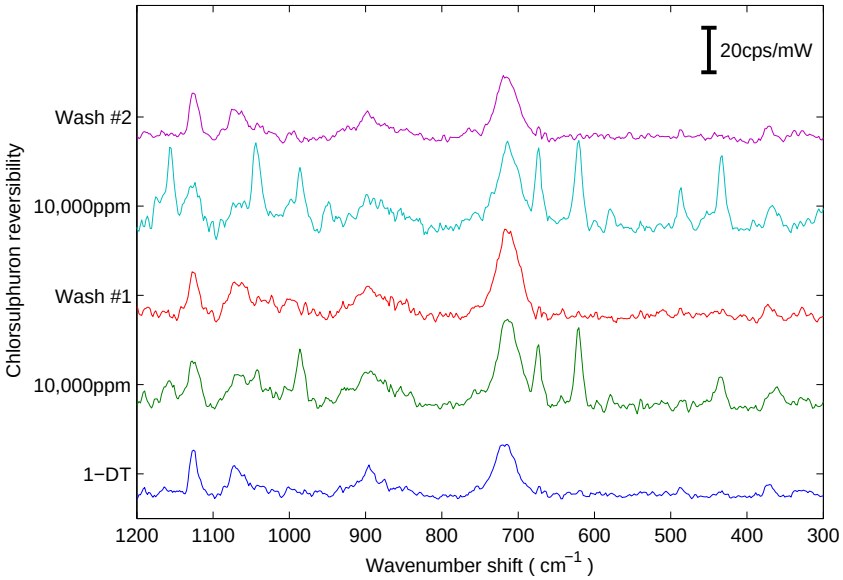

Fig. 7.8: Spectra gathered for the reversibility test. All spectra have undergone background subtraction, are normalised to the 1124 cm^{-1} peak of 1-DT and are shifted vertically for clarity.

Figure 7.8 shows the spectra collected for the reversibility test. As can be seen, the characteristic chlorsulphuron peaks at 434, 620, 673 and 986 cm^{-1} disappear after washing the sensor with ethanol thus indicating the lack of adherence to the surface and hence the reversibility of the sensor. Further experiments using more gentle rinsing processes are required to determine how many cycles are possible before the sensor is irreparably damaged.

7.4 Conclusions

The preliminary results presented in this chapter clearly demonstrate the potential of the SERS sensor for a variety of current chemical sensing challenges. In order to demonstrate the use of the sensor in a quantitative sense, the SERS fibres were coated with a monolayer of 1-DT. The spectra gathered from the target molecules were then normalised to the recorded 1-DT spectrum. Although only one measurement could be taken for each test (due to the limited number of sensors available for use), should a larger number of sensors be available, applying this calibration routine to them all would negate the effects of inter-sample variability.

Three important molecules have been detected using the SERS fibre sensors. As a test for biologically relevant molecules, a spectrum of 5,000 ppm glucose was successfully conducted. The signal-to-noise ratio of the resultant spectrum indicate lower detection limits are possible. Additional work is currently underway to further develop this technique for detecting glucose in-vivo. Tests for CEES, a simulant for the nerve agent HD mustard, indicate a detection limit of sub 1,000 ppm when diluted in water. Lastly, the common agricultural herbicide chlorsulphron could easily be detected at 10,000 ppm levels. Once again, there is clear scope to lower this detection limit as the measurements presented were collected over an extended period with a range of experimental parameters and therefore were not necessarily optimised according to the findings of the previous chapter.

It must be remembered that the three examples presented here were taken using three different microscopes, each with different excitation wavelengths. As such, no quantitative comparisons can be made as to the relative sensitivities to the target molecules. It is interesting from a qualitative point of view however, that the CEES experiment which used a 785 nm laser excitation produced higher cps/mW levels for

the baseline 1-DT spectrum than the 633 nm and 532 nm experiments did. While this result is far from conclusive (again, due to the very limited number of samples), the higher signal counts correlate with the LSPR measurements presented in Section 6.4 which indicate a high plasmon absorption in the 700 nm region. It is possible that the increase in LSPR strength at this wavelength is responsible for a higher SERS enhancement factor. Future work could be conducted to gather more evidence for this.

Chapter 8

Conclusions

8.1 Summary of the Project

Chemically etched nanostructured optical fibres are found to produce highly repeatable structured surfaces that, when coated with silver, can be used as SERS substrates. The work presented in this thesis has focussed on the design, prototyping, manufacturing and characterisation of such fibres.

Prototype SERS capable fibres were successfully produced by simply drawing commercial imaging fibres to smaller diameters by hand using a butane torch to soften the glass. With this method, fibres having an initial I_C of 4 μm were drawn to spacings of between 150 and 650 nm. Using a buffered hydrofluoric acid solution, the nano-scale imaging fibre cores were etched away leaving an array of structures formed by the remaining matrix material. It was found that after etching and coating with 100 nm of silver, SERS-capable fibres that had either closely packed rod-like structures (from small inter-core spacing) or triangular structures (found for fibre with $I_C \approx 400$ nm) produced the highest SERS enhancements at the excitation wavelength of 632.8 nm.

An accurate estimate of the size of the SERS enhancement is not easy to determine. The standard equation (Section 1.2.1) calculates the enhancement factor by comparing the NRS and SERS signal counts once normalised for the number of contributing molecules. When measuring the NRS signal from a solution, a reasonably accurate estimation of the number of contributing molecules can be made by simply calculating

the focal volume of the system. However, to find the actual number of molecules on the surface of the nanostructured fibre is, at this point in time, extremely challenging. Instead, an estimate of the number of SERS active molecules that could fit into the *focal plane* of the system was used. This simplification does not take into account the possible coverage on the walls of the etched wells and hence is likely to underestimate the number of contributing molecules. This in turn leads to an overestimation of the SERS enhancement. Furthermore, the enhancement, once found, can only be applied to a specific system. A change in the excitation wavelength, illumination lens, filters, gratings, etc will all alter the SERS enhancement. As a result of these factors, the signal was quoted as counts per second per milliwatt (cps/mW) as this is the observable quantity of practical interest. Nevertheless, for the sake of completeness, an estimation of the enhancement of the prototype fibres was performed (Appendix A) and was found to be in the range of $10^{5.3} - 10^{5.5}$ when using a Renishaw RM2000 Raman microscope and 632.8 nm laser excitation.

The transition from prototype nanostructured fibres made using a butane torch to a larger, commercial scale construction required several significant changes. Principal amongst these was the move to a large, annular furnace for softening the glass. When using the furnace instead of the torch, the amount of time the fibre spends at elevated temperatures can be dramatically increased. A computer simulation was written to determine how this increase would impact the diffusion of dopants within the fibre (and the resulting change in nanostructure). By using the Arrhenius equation and previously published diffusion coefficients, an estimation of the amount of diffusion (D_L) occurring within the fibre based on temperature and time can be made.

The simulation models a unit cell within the fibre structure. For each point in the simulation volume, an etch rate is assigned based on the distribution of dopants determined by the Arrhenius equation. The simulation then calculates the amount a particle will erode based on its exposure to the acid etchant and its etch rate. The output from the simulation was imported into an animation package for visualisation.

Several interesting features were shown by the simulation. Firstly, to create sharply defined structures (as seen in Section 3.5) requires an absolute minimum of diffusion. This implies very short heating times, which aren't practical in a commercial furnace. Secondly, as the D_L increases these predominantly 2 dimensional triangular structures give way to 3 dimensional pyramidal structures. These structures continue to occur up to the point where the diffusion length becomes greater than 25% of the inter-core

spacing. From this point onwards, the fibres instead produce a dimpled surface rather than defined pyramidal structures. This limit of keeping D_L to less than 25% of I_C (ie. $\xi_d \leq 25\%$) now dictates the parameters needed for successful commercial scale production.

Three attempts at commercial scale production were undertaken - two at OFTC and one with Fujikura Ltd. The first attempt at OFTC was deemed a failure due to excessive diffusion. A range of inter-core spacings from 130 - 260 nm were attempted. The estimated ξ_d ratios for these fibres was later found to be 160 - 220% which far exceeded the predicted simulation limit of 25%. As such, no nanostructure was observed after etching. The second attempt was conducted at a much lower temperature and a much faster draw speed. These changes produced a fibre with I_C of 400 nm and a ξ_d of approximately 20%. In this instance, etching produced well-defined nanostructures. Unfortunately, due to the increased internal strain induced by the draw process, the fibre produced was very weak and brittle. Consequently, only a short length of useful fibre was produced.

The lack of success with the OFTC facility prompted the move to Fujikura Ltd for further development. As stated earlier, due to commercial sensitivity, no details of the physical draw are available. However, the fibre has an I_C of 420 nm and by comparing the etched surfaces against the data produced by the simulation, the fibre appears to have a ξ_d ratio of approximately 20%. This is below the critical value and the fibre successfully produced nanostructures after etching. Several additional attempts at fibre manufacturing were undertaken by Fujikura but none have been as successful as of the time of writing this thesis. To aid in the preparation and handling of this fibre, a special ferrule was designed in conjunction with Diamond FO. The dimensions of the ferrule allow the fibre to integrate with standard fibre handling equipment.

Fujikura Ltd were able to produce approximately 2 m of nanostructured fibre which enabled a detailed characterisation experiment to be conducted. To determine the etch characteristics, 20 samples were prepared and etched for periods of 1 - 20 minutes in a modified BHF solution. This produced a range of structures from shallow bowls (1 to 3 minutes) to deep wells (4 to 7 minutes) and then pyramidal structures (> 8 minutes). Due to the increased diffusion, planar triangular structures that were seen in the prototype (hand-drawn) phase could not be reproduced. Once again, the observed progression matches the simulated results for a fibre with a ξ_d ratio of 20%.

To determine the relationship between nano-structure and SERS intensity, the fibres were coated with silver in thicknesses ranging from 20.5 to 100.0 nm. Samples were investigated using a Horiba Jobin-Yvon Modular Raman system with 532 nm excitation. It was found that when using this setup, the highest signal counts were achieved by samples etched for more than 8 minutes and coated with 60.2 nm of silver. Increasing the etch time from 8 minutes did not increase the count rate appreciably. This indicates that once in the pyramidal scheme, further etching does not produce an increase in signal. This correlates with the simulation output which indicated that the etch progression eventually reaches an equilibrium point where the surface is uniformly eroded without further structural changes.

While there was no significant increase in the signal counts after 8 minutes of etching, there was a large amount of variability. The etched fibres produced highly repeatable surface structures and hence an explanation of the signal variability focussed on the nature of the metal coating. As could be seen in Figure 6.16, the silver coating did not produce a continuous film. High resolution SEM images indicated that the coating instead consisted of small islands of silver. It is now believed that it is the EM field generated by, and between, these islands that produces a majority of the SERS counts, and that the contribution from the larger glass structures is less important. In other words, the presence of the steep walls of the etched wells (which cause the silver to form into discrete islands) is more significant than the pyramidal structures themselves.

The implications of this are very significant in terms of the project goals. While the glass surfaces are highly repeatable and controllable, the metal islands are not. This discrepancy contributes to the observed variability in the SERS intensities. To confirm this, a sample of 10 identically produced fibres were tested. The resultant relative standard deviation of the thiophenol peaks ($\overline{I_{tp}}$) was found to be 40%.

To enable SERS probes to be used as a quantitative tool, this variability must be reduced. The method employed in this work is to expose the probe to an internal calibration standard. By measuring the intensities of the standard molecule's peaks, a measure of the SERS performance for a particular probe can be determined. If the intensity of the target molecule's spectrum is then normalised to the calibration spectrum, the variability between samples can easily be accounted for. Applying this process to the spectra gathered for the repeatability measurements reduced the variability from 40% to 8%. This remaining variability can be attributed to such things

as errors in focussing the laser spot onto the target, fluctuations in laser intensity and thermal effects on the surface. For an ideal sample (Si wafer), the intrinsic variability in the system amounts to approximately 5%.

To demonstrate practical uses for the SERS probes, preliminary experiments were conducted on three analytes: $\alpha-$D glucose, CEES and chlorsulphuron were conducted. As a test of the calibration procedure, the probes were functionalised with a SAM of 1-decanethiol. Once the monolayer was applied, the probes were then exposed to the target molecules. The spectra recorded for each analyte were then normalised to the 1-DT spectrum gathered from the same probe, thus normalising the enhancement factors. Unfortunately, due to the limited number of SERS fibre probes available, only a small number of spectra for each analyte could be collected. However, the data gathered showed clear detection of 5,000 ppm glucose, 549 ppm CEES and 10,000 ppm chlorsulphuron with scope to improve the sensitivity limits for both glucose and chlorsulphuron. Reversibility of of the probes for measurement of chlorsulphuron was also demonstrated.

It should be remembered that at the time of writing, while the sensitivity of the sensors (in other words, the SERS enhancement) is relatively low compared to some reported techniques, this probe design offers many advantages over other chemical detection systems. Firstly, the measurements shown in the previous chapter took 50 seconds to collect. This compares very favourably with techniques such as LCMS/GCMS which can take from 10 minutes to upwards of an hour to conduct a single measurement [Berrada et al., 2000; Carabias-Martinez et al., 2004]. Secondly, no sample preparation was required. To gather the spectra, the probes were simply exposed to solutions of the analytes (ie. no pre-concentration steps were required). Such ease of preparation is an significant advantage for a system designed for on-line or field use. Thirdly, the experiment showed a single sensor could be washed and reused a number of times. Once again, for an on-line sensor, such reversibility is essential. Lastly, the probe itself is physically small. If the sensor can be coupled with a small form factor laser and spectrometer, a lightweight, portable SERS system is entirely feasible.

8.2 Recommendations for Future Work

Due to the costs and time required for the large scale manufacturing of the nanostructured optical fibre, only a small number of attempts could be conducted. Of these, only one production run conducted by Fujikura Ltd. was deemed successful in that (a) after etching it did produce nanostructures on the tip of the fibre and (b) enough uniform fibre was produced to enable characterisation. However, the critical dimensions such as inter-core spacing were chosen not by design but by practical considerations.

Should future attempts at manufacture be possible, there are a number of changes that can be suggested which might improve the SERS enhancement. Reducing the I_C ($\approx$ 420 nm for the current Fujikura fibre) by increasing the packing density of the cores is one such alteration. Doing so would result in two main changes. Firstly, the closer packing would produce smaller pyramid structures. Although the work conducted in the characterisation chapter indicate that the present pyramidal structures may not be generating the majority of the EM field, results gathered for hand-drawn fibres indicate that reducing their size might increase this value. Secondly, if the enhancement is relying on the metal particles on the walls of the wells, simply increasing the packing density of the wells increases the available surface area for such an effect to occur. This would, in turn, increase the number of potential 'hot spots' available in the focal area of a Raman microscope.

A future experiment to help confirm or deny the significance of the particles on the wall can also be conducted. One possible way would be to coat planar glass surfaces at oblique angles (ie. metal flux at more than $> 80^\circ$ from the surface normal for example) [Chaney et al., 2005]. Such an experiment should be able to show if there is a critical angle required to induce metal islands instead of a continuous film. If the metal islands are indeed responsible for the enhancement, there should be an increase in the SERS intensity at this point. Also, by using a planar glass substrate the resultant surface can be characterised by AFM, something which could not be done with the etched fibres.

Changes may also be made in the construction of the fibres. The current design used a germanium doped core with a fluorine doped cladding, both of which are at present unknown levels. However, other materials, in particular boron, phosphorus and aluminium, can also be used to dope glass. It may be possible that by incorporating

these elements into the glass, the diffusion lengths encountered during the draw process may be reduced. If this can be done, the fibres may be produced at a higher temperature, which would in turn reduce the stress experienced by the preform during manufacture and allow for easier fibre production.

The method of heating the glass to the softening temperature could also be modified. The fibres produced in this thesis were formed by heating the preform using an annular furnace. The size and dwell time inside the furnace led to relatively high levels of dopant diffusion. However, previous works have shown that imaging fibres can be drawn (tapered) by localised heating using a CO_2 laser [Hankus et al., 2004]. Additionally, by using a carefully drawn tapered fibre as opposed to a uniform drawn fibre, the internal scattering losses which, to date, have prevented through-fibre measurements may be alleviated [Hankus et al., 2006].

During the characterisation experiment, the Raman signal was excited by a 532 nm laser as this was the only wavelength that was available at the time. However, the LSPR measurements indicated a possible plasmon resonance closer to 700 nm. Moving to an excitation wavelength closer to this value may increase the EM field and hence the SERS enhancement factor. However, as stated earlier in the thesis, moving to a longer wavelength reduces the intrinsic Raman intensity as a result of the fourth power dependence on wavelength. Changing to a 632.8 nm laser, for example, reduces the native Raman intensity by half. Therefore the increase in SERS enhancement must be greater than the reduction in Raman signal to be of any value.

The results presented in this thesis show that the nanostructured SERS fibres have much potential. At the time of writing, there exists clear scope to further improve the sensitivity of the substrates. Experiments are currently being conducted to realise this improvement and to explore additional interesting applications of the probes.

Bibliography

J. H. Ahtiainen, P. Vanhala, and A. Myllymaki. Effects of different plant protection programs on soil microbes. *Ecotox. Environ. Safe.*, 54(1):56–64, 2003.

M. G. Albrecht and J. A. Creighton. Anomalously intense Raman spectra of pyridine at a silver electrode. *J. Am. Chem. Soc.*, 99(15):5215–5217, 1977.

R. F. Aroca, R. A. Alvarez-Puebla, N. Pieczonka, S. Sanchez-Cortez, and J. V. Garcia-Ramos. Surface-enhanced Raman scattering on colloidal nanostructures. *Advances in Colloid and Interface Science A Collection of Papers to mark the 65th Birthday of Professor Ludwig Brehmer*, 116(1-3):45–61, 2005.

G. A. P. Baker and D. S. P. Moore. Progress in plasmonic engineering of surface-enhanced raman-scattering substrates toward ultra-trace analysis. *Anal. Bioanal. Chem.*, 382(8):1751–1770, 2005.

D. D. Bernhard, S. Mall, and P. Pantano. Fabrication and characterization of microwell array chemical sensors. *Anal. Chem.*, 73(11):2484–2490, 2001.

H. Berrada, G. Font, and J. C. Molto. Indirect analysis of urea herbicides from environmental water using solid-phase microextraction. *J. Chromatogr. A*, 890(2): 303–312, 2000.

S. Borel, C. Arvet, J. Bilde, S. Harrison, and D. Louis. Isotropic etching of SiGe alloys with high selectivity to similar materials. *Microelectron. Eng.*, 73-74:301–305, 2004.

M. A. Bryant and J. E. Pemberton. Surface raman scattering of self-assembled monolayers formed from 1-alkanethiols at Ag. *J. Am. Chem. Soc.*, 113(10):3629–3637, 1991.

J. Buhler, F. P. Steiner, and H. Baltes. Silicon dioxide sacrificial layer etching in surface micromachining. *J. Micromech. Microeng.*, 7(1):1–13, 1997.

H. P. L. Buschman, M. G. Shim, and B. C. Wilson. In vivo Raman spectroscopy. In I.R. Lewis and H.G.M. Edwards, editors, *Handbook of Raman Spectroscopy*, pages 549–574. Marcel Dekker, New York, 2001.

R. Carabias-Martinez, E. Rodriguez-Gonzalo, E. Herrero-Hernandez, and J. Hernandez-Mendez. Simultaneous determination of phenyl- and sulfonylurea herbicides in water by solid-phase extraction and liquid chromatography with UV diode array or mass spectrometric detection. *Anal. Chim. Acta*, 517(1-2):71–79, 2004.

K. T. Carron and L. G. Hurley. Axial and azimuthal angle determination with surface-enhanced Raman spectroscopy: Thiophenol on copper, silver and gold metal surfaces. *J. Phys. Chem.*, 95(24):9979–9984, 1991.

H. S. Carslaw and J. C. Jaeger. *Conduction of heat in solids*. Clarendon Press, Oxford, 2nd edition, 1959.

S. B. Chaney, S. Shanmukh, R. A. Dluhy, and Y. P. Zhao. Aligned silver nanorod arrays produce high sensitivity surface-enhanced Raman spectroscopy substrates. *Appl. Phys. Lett.*, 87(3):1–3, 2005.

H. W. Deckman and J. H. Dunsmuir. Natural lithography. *Appl. Phys. Lett.*, 41(4): 377–379, 1982.

J. A. Dieringer, A. D. McFarland, N. C. Shah, D. A. Stuart, A. V. Whitney, C. R. Yonzon, M. A. Young, X. Y. Zhang, and R. P. Van Duyne. Surface enhanced Raman spectroscopy: new materials, concepts, characterization tools, and applications. *Faraday Discuss.*, 132:9–26, 2006.

S. D Druger and P. J. McNulty. Radiation pattern of Raman scattering from randomly oriented molecules in or near small particles. *Phys. Rev. A*, 29(3):1545–1547, 1984.

V. Dubaj, A. Mazzolini, A. Wood, and M. Harris. Optic fibre bundle contact imaging probe employing a laser scanning confocal microscope. *J. Microsc.*, 207:108–117, 2002.

DuPont. Chlorsulfuron material safety data sheet, 2007.

J. R. Epstein, A. P. K. Leung, K. Lee, and D. R. Walt. High-density microsphere-based fiber optic DNA microarrays. *Biosens. Bioelectron.*, 18:541–546, 2003.

P. Etchegoin, R. C. Maher, L. F. Cohen, H. Hartigan, R. J. C. Brown, M. J. T. Milton, and J. C. Gallop. New limits in ultrasensitive trace detection by surface enhanced Raman scattering (SERS). *Chem. Phys. Lett.*, 375(1-2):84–90, 2003.

M. Fleischmann, P. J. Hendra, and A. J. McQuillan. Raman spectra of pyridine adsorbed at a silver electrode. *Chem. Phys. Lett.*, 26(2):163–166, 1974.

R. Gessner, P. Rosch, W. Keifer, and J. Popp. Raman spectroscopy investigation of biological materials by use of etched and silver coated glass fiber tips. *Biopolymers*, 67(4-5):327–330, 2002.

R. J. Greco, C. E. Hartford, L. R. Haith, and M. L. Patton. Hydrofluoric acid-induced hypocalcemia. *J. Trauma*, 28(11):1593–1596, 1998.

A. J. Haes, W. P. Hall, L. Chang, W. L. Klein, and R. P. Van Duyne. A localized surface plasmon resonance biosensor: First steps toward an assay for alzheimer's disease. *Nano Letters*, 4(6):1029–1034, 2004.

M. E. Hankus, G. Gibson, N. Chandrasekharan, and B. M. Cullum. Surface-enhanced Raman scattering (SERS): nanoimaging probes for biological analysis. *Proceedings of* SPIE, 5588:106–116, 2004.

M. E. Hankus, H. Li, G. J. Gibson, and B. M. Cullum. Surface-enhanced Raman scattering-based nanoprobe for high-resolution, non-scanning chemical imaging. *Analytical Chemistry*, 78(21):7535–7546, 2006.

E. Hao and G. C. Schatz. Electromagnetic fields around silver nanoparticles and dimers. *J. Chem. Phys.*, 120(1):357–366, 2004.

C. L. Haynes and R. P. Van Duyne. Nanosphere lithography: A versatile nanofabriaction tool for studies of size-dependent nanoparticle optics. *J. Phys. Chem. B*, 105:5599–5611, 2001.

C. L. Haynes, A. D. McFarland, L. L. Zhao, R. P. Van Duyne, G. C. Schatz, L. Gunnarsson, J. Prikulis, B. Kasemo, and M. Kall. Nanoparticle optics: The importance of radiative dipole coupling in two-dimensional nanoparticle arrays. *J. Phys. Chem. B*, 107(30):7337–7342, 2003.

C. L. Haynes, C. R. Yonzon, X. Zhang, and R. P. Van Duyne. Surface-enhanced Raman sensors: early history and the development of sensors for quantitative biowarfare agent and glucose detection. *J. Raman Spectrosc.*, 36(6-7):471–484, 2005.

M. Hof. Basics of optical spectrscopy. In G. Gauglitz and T. Vo-Dinh, editors, *Handbook of Spectroscopy*, volume 1. Wiley-VCH, Weinheim, 2003.

D. L. Jeanmaire and R. P. Van Duyne. Surface Raman spectroelectrochemistry: Part I. Heterocyclic, aromatic, and aliphatic amines adsorbed on the anodized silver electrode. *J. Electroanal. Chem.*, 84(1):1–20, 1977.

M Kahl, E. Voges, S. Kostrewa, C. Viets, and W. Hill. Periodically structured metallic substrates for SERS. *Sens. Actuator B-Chem.*, 51:285–291, 1998.

V. Kenzin, A. Vais, A. Medvedev, and A. Maslii. Coulometric metal-coating thickness gauge with automatic dynamic correction of measuring conditions. *Meas. Tech.*, 39 (2):158–161, 1996.

I. Khan, D. Cunningham, R. E. Littleford, D. Graham, W. E. Smith, and D. W. McComb. From micro to nano: Analysis of surface-enhanced resonance raman spectroscopy active sites via multiscale correlations. *Analytical Chemistry*, 78(1): 224–230, 2006.

H. Kikyuama, N. Miki, K. Saka, J. A. Takano, I. A. Kawanabe, M. A. Miyashita, and T. A. Ohmi. Principles of wet chemical processing in ULSI microfabrication. *IEEE Transactions on Semiconductor Manufacturing*, 4(1):26–35, 1991.

K. Kneipp, H. Kneipp, and H. G. Bohr. Single-molecule SERS spectroscopy. In *Surface-Enhanced Raman Scattering: Physics and Applications*, volume 103 of *Top. Appl. Phys.*, pages 261–277. 2006.

A Kosiorek, W. Kandulski, P Chudzinski, K Kempa, and M Giersig. Shadow nanosphere lithography: Simulation and experiment. *Nano Lett.*, 4(7):1359–1363, 2004.

P. E. Laibinis, G. M. Whitesides, D. L. Allara, Y. Tao, A. N. Parikh, and R. G. Nuzzo. Comparison of the structures and wetting properties of self-assembled monolayers of n-Alkanethiols on the coinage metal surfaces, Cu, Ag, Au. *J. Am. Chem. Soc.*, 113: 7152–7167, 1991.

K. J. Laidler. The development of the Arrhenius equation. *J. Chem. Educ.*, 61(6): 494–498, 1984.

E. C. Le Ru and P. G. Etchegoin. Surface-enhanced Raman scattering (SERS) and surface-enhanced fluorescence (SEF) in the context of modified spontaneous emission, 2005. URL `http://www.citebase.org/abstract?id=oai:arXiv.org:physics/0509154`.

F. M. Liu, P. A. Kollensperger, M. Green, A. E. G. Cass, and L. F. Cohen. A note on distance dependence in surface enhanced Raman spectroscopy. *Chem. Phys. Lett.*, 430(1-3):173–176, 2006.

A. Lucotti and G. Zerbi. Fiber-optic SERS sensor with optimized geometry. *Sens. Actuator B-Chem*, 121(2):356–364, 2007.

K. Lyytikainen, S. T. Huntington, Carter A. L. G., P. McNamara, S. Fleming, J. Abramczyk, I. Kaplin, and G. Schotz. Dopant diffusion during optical fibre drawing. *Opt. Express*, 12(6):972–977, 2004.

J. B. MacChesney, P. B. O'Connor, F. V. DiMarcello, J. R. Simpson, and P. D. Lazay. Preparation of low loss optical fibers using simultaneous vapor-phase deposition and fusion. In *10th International Congress on Glass*, volume 6, pages 50–54, Kyoto, Japan, 1974. Ceramics Society.

A. Mahadevan-Jansen. Raman spectroscopy: From benchtop to bedside. In T. Vo-Dinh, editor, *Biomedical Photonics Handbook*. CRC Press, Boca Raton, 2003.

M. Moskovits. Surface-enhanced Raman spectroscopy: a brief retrospective. *J. Raman Spectrosc.*, 36(6-7):485–496, 2005.

M. Moskovits. Surface roughness and the enhanced intensity of Raman scattering by molecules adsorbed on metals. *J. Chem. Phys.*, 69(9):4159–4161, 1978.

C. H. Munro, W. E. Smith, M. Garner, J. Clarkson, and P. C. White. Characterization of the surface of a citrate-reduced colloid optimized for use as a substrate for surface-enhanced resonance Raman scattering. *Langmuir*, 11:3712–3720, 1995.

T. Murphy, S Lucht, H Schmidt, and H.-D. Kronfeldt. Surface-enhanced Raman scattering (SERS) system for continous measurements of chemicals in sea-water. *J. Raman Spectrosc.*, 31:943–948, 2000.

L. A. Nafie. Theory of Raman scattering. In I.R. Lewis and H.G.M. Edwards, editors, *Handbook of Raman Spectroscopy*, pages 1–10. Marcel Dekker, New York, 2001.

J. D. Newman and A. P. F. Turner. Home blood glucose biosensors: a commercial perspective. *Biosens. Bioelectron.*, 20(12):2435–2453, 2005.

NICNAS. Hydrofluoric acid - priority existing chemical assessment report. Technical report, National Industrial Chemical Notification and Assessment Scheme, 2001.

A. Otto. The 'chemical' (electronic) contribution to surface-enhanced Raman scattering. *J. Raman Spectrosc.*, 36(6-7):497–509, 2005.

P. Pace, S. T. Huntington, K. Lyytikainen, A. Roberts, and J. D. Love. Refractive index profiles of Ge-doped optical fibers with nanometer spatial resolution using atomic force microscopy. *Opt. Express*, 12(7):1452–1457, 2004.

P. Pantano and D. R. Walt. Ordered nanowell arrays. *Chem. Mater.*, 8:2832–2835, 1996.

M. C. Paul, R. Sen, and T. Bandyopadhyay. Fluorine incorporation in silica glass by MCVD process a critical study. *J. Mater. Sci.*, 32(13):3511–3516, 1997.

N. M. B. Perney, J. J. Baumberg, M. E. Zoorob, M. D. B. Charlton, S. Mahnkopf, and C. M. Netti. Tuning localized plasmons in nanostructured substrates for surface-enhanced Raman scattering. *Opt. Express*, 14(2):847–857, 2006.

E. Polwart, R. L. Keir, C. M. Davidson, W. E. Smith, and D. A. Sadler. Novel SERS-active optical fibres prepared by the immobilization of silver colloidal particles. *Appl. Spectrosc.*, 54(4):522–527, 2000.

J. Prikulis, K. V. G. K. Murty, H. Olin, and M. Kall. Large-area topography analysis and near-field Raman spectroscopy using bent fibre probes. *J. Microsc.*, 210(3): 269–273, 2003.

R. A. Rudder, R. E. Thomas, and R. J. Nemanich. Remote plasma processing for silicon wafer cleaning. In W. Kern, editor, *Handbook of Semiconductor Wafer Cleaning Technology: Science, Technology and Application*. Noyes Publications, Park Ridge, 1993.

C. Sabater and J. M. Carrasco. Effecs of chlorsulfuron on growth of three freshwater species of phytoplankton. *Bull. Environ. Contam. Toxicol.*, 58(5):807–813, 1997.

M. Sackmann, S. Bom, T. Balster, and A. Materny. Nanostructured gold surfaces as reproducible substrates for surface-enhanced Raman spectroscopy. *J. Raman Spectrosc.*, 38(3):277–282, 2007.

G. C. Schatz and R. P. Van Duyne. Electromagnetic mechanism of surface-enhanced spectroscopy. In John M. Chalmers and Peter R. Griffiths, editors, *Handbook of Vibrational Spectroscopy*, volume 1, pages 1–16. John Wiley and Sons Ltd, Chichester, 2002.

H Schmidt, B. H. Nguyen, J. Pfannkuche, H. Amann, H.-D. Kronfeldt, and G. Kowalewska. In situ detection of PAHs in seawater using surface enhanced Raman scattering (SERS). *Mar. Poll. Bull.*, 49:229–234, 2004.

F. Schreiber. Structure and growth of self-assembling monolayers. *Prog. Surf. Sci.*, 65: 151–256, 2000.

A. Sengupta, M. L. Laucks, N. Dildine, E. Drapala, and E. J. Davis. Bioaerosol characterization by surface-enhanced Raman spectroscopy (SERS). *J. Aerosol. Sci.*, 36(5-6):651–664, 2005.

K. E. Shefer-Peltier, C. L. Haynes, M. R. Glucksberg, and R. P. Van Duyne. Towards a glucose biosensor based on surface-enhanced Raman scattering. *J. Am. Chem. Soc.*, 125:588–593, 2002.

Sigma-Aldrich-Glucose. α-D glucose data sheet, 2008. URL `http://www.sigmaaldrich.com/catalog/search/ProductDetail/ALDRICH/158968`.

Sigma-Alrich-Chlorsulphuron. Chlosulphuron data sheet, 2008. URL `http://www.sigmaaldrich.com/catalog/search/ProductDetail/RIEDEL/34322`.

Sigma-Alrich-Thiophenol. Thiophenol data sheet, 2008. URL `http://www.sigmaaldrich.com/catalog/search/ProductDetail/ALDRICH/240249`.

W. E. Smith and C. Rodger. Surface-enhanced Raman scattering. In John M. Chalmers and Peter R. Griffiths, editors, *Handbook of Vibrational Spectroscopy*, volume 1, pages 775–784. Wiley, Chichester, 2002.

L. N. Song, S. Ahn, and D. R. Walt. Fiber-optic microsphere-based arrays for multiplexed biological warfare agent detection. *Anal. Chem.*, 78(4):1023–1033, 2006.

M. Stjernström and J. Roeraade. Method for fabrication of microfluidic systems in glass. *Journal Micromech. Microeng.*, 8:33–38, 1998.

P. R. Stoddart and N. Brack. Physical techniques for cell surface probing and manipulation. In E.P Ivanova, editor, *Nanoscale Structure and Properties of Microbial Cell Surfaces*, pages 1–58. Nova Science Publishers, Inc., New York, 2007.

D. L. Stokes and T. Vo-Dinh. Development of an integrated single-fibre SERS sensor. *Sens. Actuator B-Chem.*, 69:28–36, 1999.

D. A. Stuart, C. R. Yonzon, X. Zhang, O. Lyandres, N. C. Shah, M. R. Glucksberg, J. T. Walsh, and R. P. Van Duyne. Glucose sensing using near-infrared surface-enhanced raman spectroscopy: Gold surfaces, 10-day stability, and improved accuracy. *Anal. Chem.*, 77(13):4013–4019, 2005.

D. A. Stuart, K. B. Biggs, and R. P. Van Duyne. Surface-enhanced Raman spectroscopy of half-mustard agent. *Analyst*, 131(4):568–572, 2006a.

D. A. Stuart, J. M. Yuen, N. Shah, O. Lyandres, C. R. Yonzon, M. R. Glucksberg, J. T. Walsh, and R. P. Van Duyne. In vivo glucose measurement by surface-enhanced raman spectroscopy. *Anal. Chem.*, 78(20):7211–7215, 2006b.

X. Sun, R. Hong, H. Hou, Z. Fan, and J. Shao. Thickness dependence of structure and optical properties of silver films deposited by magnetron sputtering. *Thin Solid Films*, 515(17):6962–6966, 2007.

R. P. Van Duyne, J. C. Hulteen, and D. A. Treichel. Atomic force microscopy and surface-enhanced Raman spectroscopy. Ag island films and Ag films over polymer nanosphere surfaces supported on glass. *J. Chem. Phys.*, 99(3):2101–2115, 1993.

C. Viets and W. Hill. Fibre-optic SERS sensors with conically etched tips. *J. Mol. Struct.*, 563-564:163–166, 2001.

C. Viets and W. Hill. Comparison of fibre-optic SERS sensors with differently prepared tips. *Sens. Actuator B-Chem.*, 51:92–99, 1998.

T. Vo-Dinh, L. R. Allain, and D. L. Stokes. Cancer gene detection using surface-enhanced Raman scattering (SERS). *J. Raman Spectrosc.*, 33(7):511–516, 2002.

T. Vo-Dinh, F. Yan, and M. B. Wabuyele. Surface-enhanced Raman scattering for medical diagnostics and biological imaging. *J. Raman Spectrosc.*, 36(6-7):640–647, 2005.

E. Vogel, W. Kiefer, V. Deckert, and D. Zeisel. Laser-deposited silver island films: An investigation of their structure, optical properties and SERS activity. *J. Raman Spectrosc.*, 29(8):693–702, 1998.

T. Vosgrone, A. J. Meixner, A. Anders, H. Dietz, G. Sandmann, and W. Plieth. Electrochemically deposited silver particles for surface enhanced Raman spectroscopy. *Surf. Sci.*, 597(1-3):102–109, 2005.

L. Wan, M. Terashima, H. Noda, and M. Osawa. Molecular orientation and ordered structure of benzenethiol adsorbed on gold(111). *J. Phys. Chem. B*, 104:3563–3569, 2000.

D. A. Weitz, S. Garoff, J. I. Gersten, and N. Abraham. The enhancement of Raman scattering, resonance Raman scattering, and fluorescence from molecules adsorbed on a rough silver surface. *J. Chem. Phys.*, 78(9):5324–5338, 1983.

C. M. Whelan, M. R. Smyth, and C. L. Barnes. HREELS, XPS, and electrochemical study of benzenethiol adsorption on Au(111). *Langmuir*, 15:116–126, 1999.

K. R. Williams and R. S. Muller. Etch rates for micromachining processing. *J. Microelectromech. Syst.*, 5(4):256–269, 1996.

K. R. Williams, K. Gupta, and M. Wasilik. Etch rates for micromachining processing - part II. *J. Microelectromech. Syst.*, 12(6):761–778, 2003.

K. Wygladacz, A. Radu, C. Xu, Y. Qin, and E. Bakker. Fiber-optic microsensor array based on fluorescent bulk optode microspheres for the trace analysis of silver ions. *Anal. Chem.*, 77(15):4706–4712, 2005.

D. Y. Xia and S. R. J. Brueck. A facile approach to directed assembly of patterns of nanoparticles using interference lithography and spin coating. *Nano Lett.*, 4(7): 1295–1299, 2004.

G. Xu, M. Tazawa, P. Jin, and S. Nakao. Surface plasmon resonance of sputtered Ag films: substrate and mass thickness dependence. *Appl. Phys. A*, 80:1535–1540, 2005.

X. Xu, Z. Tang, Z. Fan, and J. Shao. Effect of chromium intermediate layer on properties of silver coatings. *Opt. Eng.*, 43(4):971–974, 2004.

G Yang and G Liu. New insights for self-assembled monolayers of organothiols on Au(111) revealed by scanning tunneling microscopy. *J. Phys. Chem. B*, 107:8746–8759, 2003.

C. R. Yonzon, C. L. Haynes, X. Zhang, J. T. Jr. Walsh, and R. P. Van Duyne. A glucose biosensor based on surface-enhanced Raman scattering: Improved partition layer, temporal stability, reversibility, and resistance to serum protein interference. *Anal. Chem.*, 76(1):78–85, 2004.

C. R. Yonzon, D. A. Stuart, X. Zhang, A. D. McFarland, C. L. Haynes, and R. P. Van Duyne. Towards advanced chemical and biological nanosensors - an overview. *Talanta*, 67:438–448, 2005.

S. Zou and G. C. Schatz. Silver nanoparticle array structures that produce giant enhancements in electromagnetic fields. *Chemical Physics Letters*, 403(1-3):62–67, 2005.

Appendix A

Appendix A

The following is a breakdown of the calculations used to determine the signal enhancement factor. The numbers shown here are for the example presented in Section 3.4.3.1 for a hand-drawn fibre with an inter-core spacing of 238 nm etched for one minute in a BHF/HCl etchant. The signal counts are for the peak at 1000 cm^{-1} after background subtraction. The calculation is the same for the other enhancement factors presented with the only difference being the counts per second per milliwatt of the SERS signal and the numerical aperture of the objective lens used.

Attribute	Value
Wavelength (λ)	632.8nm
Numerical Aperture (SERS) (N.A.)	0.4
Numerical Aperture (NRS) (N.A.)	0.55
Thiophenol packing density	$0.2338nm^2$
Thiophenol density in liquid	1.078
Thiophenol molecular weight	110.18 amu
Avagadros number (A)	6.0221415×10^{23}
SERS signal counts	5673 cps/mW
NRS signal counts	40 cps/mW

Table A.1: Values used for SERS enhancement calculation. Note that different lenses were used to collect the SERS and NRS spectra.

The packing density value shown in Table A.1 is for the adsorption of thiophenol onto gold [Wan et al., 2000] whereas the SERS data shown here was collected on a

silver substrate. A reliable value for the adsorption onto silver could not be found. However, studies of the packing density of alkanethiols (chains of carbon with a thiol group) indicate only a small percentage difference between the densities on silver and gold [Laibinis et al., 1991].

For the SERS calculation:

Spot size ($1/e$ diameter):

$$S = 0.61 \times \frac{\lambda}{\text{N.A.}} = 0.61 \times \frac{632.8}{0.4} = 965.02 \text{ nm} \tag{A.1}$$

Number of molecules in the spot:

$$M = \frac{\pi \left(\frac{S}{2}\right)^2}{\text{packing density}} = \frac{\pi \left(\frac{965.02}{2}\right)^2}{0.2338} = 3,128,369 \tag{A.2}$$

Therefore counts/second/mW/molecule for the SERS signal = $1.813404882 \times 10^{-3}$.

For the NRS calculation:

Spot size ($1/e$ diameter):

$$S = 0.61 \times \frac{\lambda}{\text{N.A.}} = 0.61 \times \frac{632.8}{0.55} = 701.83 \text{ nm} \tag{A.3}$$

Depth of field (nm):

$$DOF = \frac{\lambda}{(\text{N.A.})^2} = \frac{632.8}{0.55^2} = 2,092 \text{ nm} \tag{A.4}$$

Using the depth of field (DOF) and the spot size (S) as the length and diameter of a cylinder respectively give a focal volume (V) of 8.0928×10^{-13} cubic centimetres.

Given that 1 cc of water weighs 1 gram and thiophenol has a density 1.078 times that of water, 1 cc of thiophenol weighs 1.078 grams. If 1 mole of thiophenol weighs 110.18 grams, the number of moles in 1 cc of thiophenol is 1.078 / 110.18 = 0.00978399.

Number of molecules in the focal volume:

$$\begin{aligned} M &= 0.00978399 \times V \times A \\ &= 0.00978399 \times (8.0928 \times 10^{-13}) \times (6.023 \times 10^{23}) = 4,768,997,127 \end{aligned} \quad \text{(A.5)}$$

Therefore counts/second/mW/molecule for the NRS signal = $8.388703373 \times 10^{-9}$

The ratio of signal counts between the SERS signal and the NRS signal = 216,172:1 $\approx 10^{5.33}$

As was mentioned in Section 3.4.3.1, there are many errors associated with this value (predominantly the number of molecules contributing to the signal) which is why only one or two significant figures are used when describing enhancement in the text.

Appendix B

Appendix B

The following is the detailed code for the critical functions of the computer simulation. The pseudo code is shown below:

```
(1) calculate possible exposures

loop
{
(2) for every element
    {
    if not acid
        {
            determine exposure and erode element
        }
    }
(3) for every element
    {
        if amount remaining <= 0
        {
            particle becomes acid element;
        }
    }

(4) find surface
}
```

```
Function 1.
void DetermineRates()
{
    for(int i=0; i < 25; i++)
    {
        exposures[i] = sinf((PI/2.0f)*((float)i/25.0f))*2.0f;
        exposures[i] = exposures[i] * etchScale * STEP_TIME;
    }
}
```

The second line of the looping function includes factors for altering the scale of the etching program as well as a scaling factor based on the number of steps performed per simulated second of etching.

Having determined the possible amounts an element can be exposed, the program runs the following functions as many times as needed (note that for convenience, an element is considered acidic if its etch rate is < 0):

```
Function 2.
void ExposeMolecule()
{
    int exposure;
    for(int i = 0; i < NUMX; i++)
    {
        for(int j = 0; j < NUMY; j++)
        {
            for(int k = 0; k < NUMZ; k++)
            {
                exposure = 0;

                // If not acid
                if(molecules[i][j][k].rate >0)
                {
                    // Look at all the neighbours:
                    for(int m = i-1; m <= i+1; m++)
                    {
                        for(int n = j-1; n <= j+1; n++)
                        {
                            for(int o = k-1; o <= k+1; o++)
                            {
                                int a=m;
```

```
                                int b=n;

                                // Take into account axis of symmetry
                                if(m<0)
                                    a=1;
                                else if(m>=NUMX)
                                    a=NUMX-1;
                                if(n<0)
                                    b=1;
                                else if(n>=NUMY)
                                    b=NUMY-1;

                                // If the neighbour is acid:
                                if(molecules[a][b][o].rate <0)
                                    exposure++;
                            }
                        }
                    }

                    // If the element has been exposed:
                    if(exposure>0)
                        molecules[i][j][k].etched -= ...
                          molecules[i][j][k].rate*exposures[exposure];

                }
            }
        }
    }
}
```

After determining the exposure of the element and etching it, the simulation now checks if a particle has been completely eroded away:

```
Function 3.
void LoseMolecule()
{
    for(int x = 0; x < NUMX; x++)
    {
        for(int y = 0; y < NUMY; y++)
        {
            for(int z = 0; z < NUMZ; z++)
```

```
            {
                if(molecules[x][y][z].etched <= 0)
                    molecules[x][y][z].rate = -1;
            }
        }
    }
}
```

Now the remaining surface can be found:

```
Function 4.
void FindSurface()
{
    for(int i = 0; i < NUMX; i++)
    {
        for(int j = 0; j < NUMY; j++)
        {
            for(int k = 0; k < NUMZ; k++)
            {
                if(molecules[i][j][k].etched > 0)
                {
                    // Find the surface
                    surface[i][j] = k-molecules[i][j][k].etched+1;
                    break;
                }
            }
        }
    }
}
```

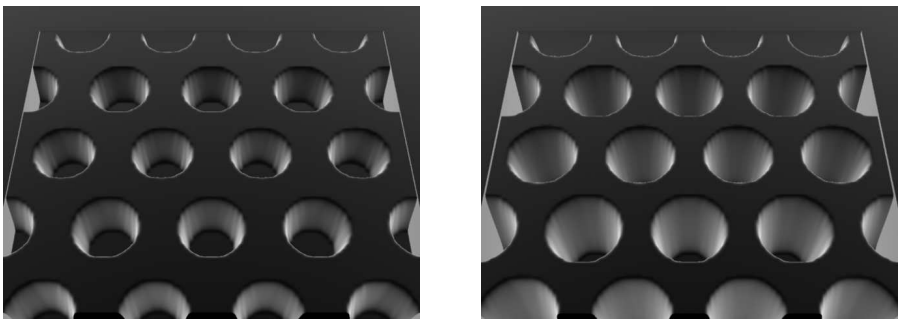

(a) 5 s

(b) 10 s

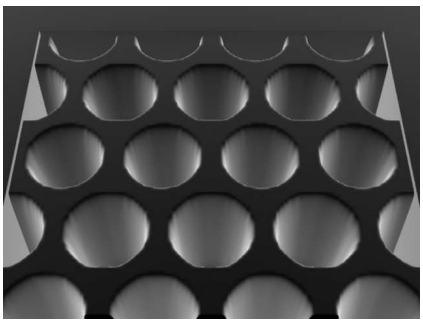

(c) 15 s

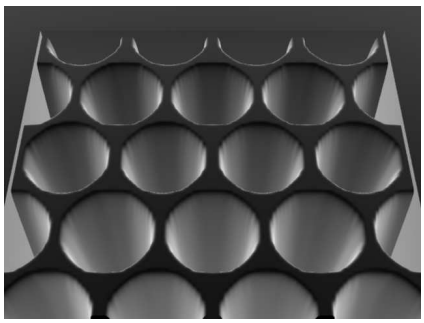

(d) 20 s

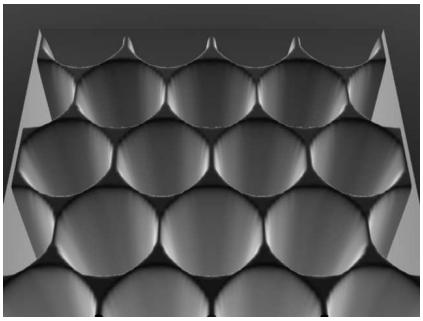

(e) 25 s

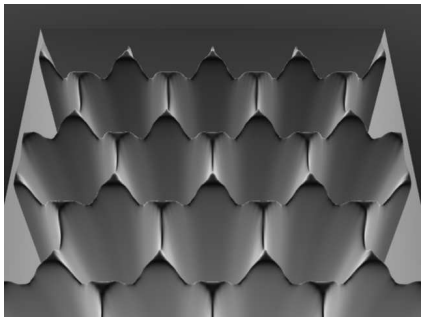

(f) 30 s

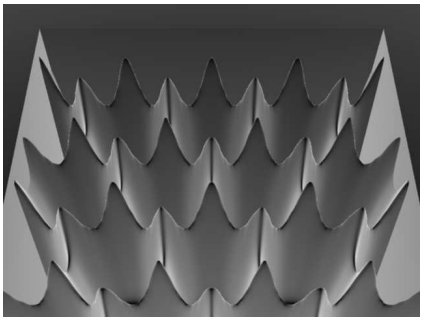

(g) 35 s

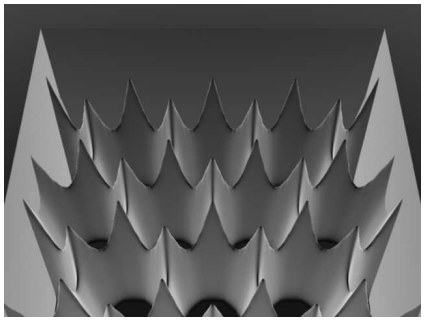

(h) 40 s

Fig. B.1: Simulation output for fibre with no diffusion.

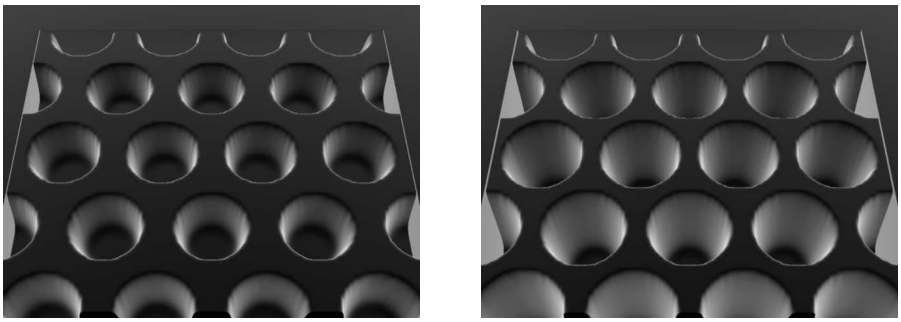

(a) 5 s

(b) 10 s

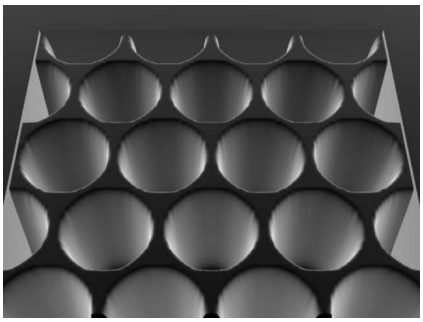

(c) 15 s

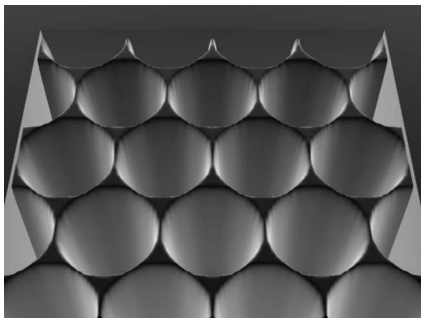

(d) 20 s

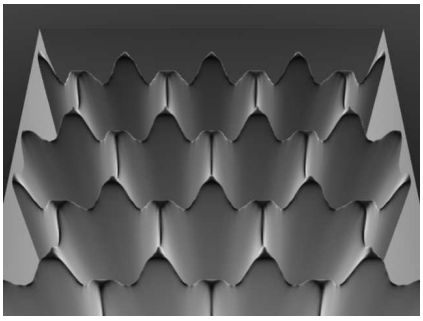

(e) 25 s

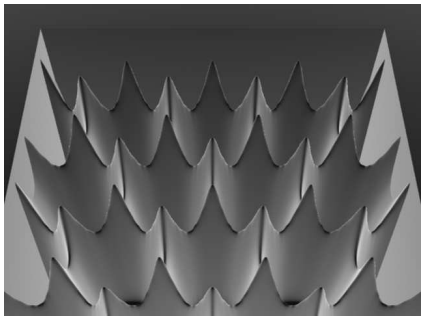

(f) 30 s

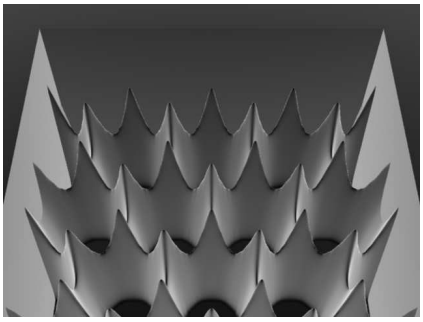

(g) 35 s

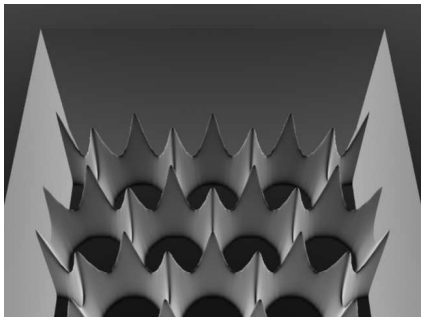

(h) 40 s

Fig. B.2: Simulation output for fibre with $\xi_d = 5\%$.

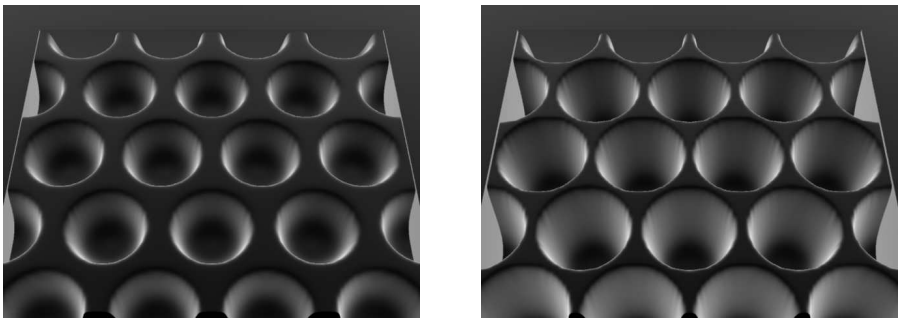

(a) 5 s

(b) 10 s

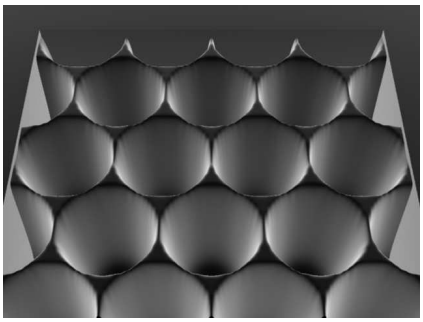

(c) 15 s

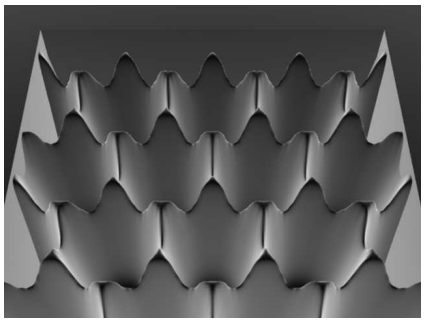

(d) 20 s

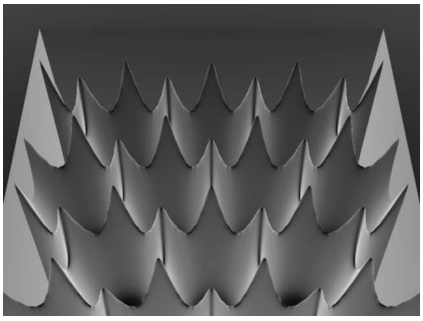

(e) 25 s

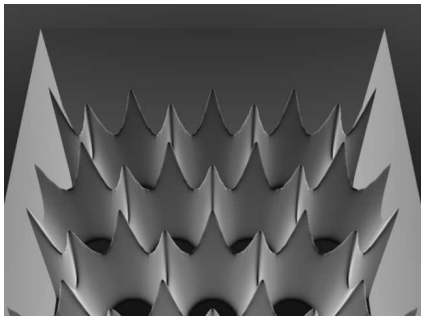

(f) 30 s

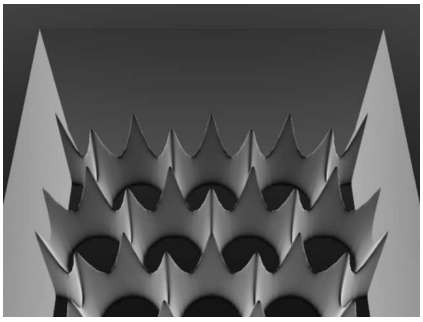

(g) 35 s

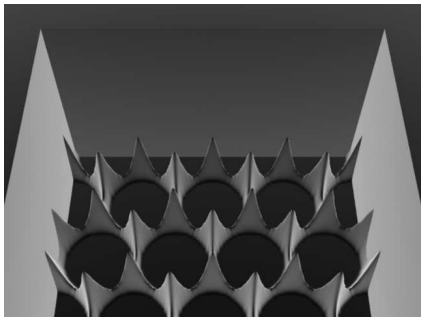

(h) 40 s

Fig. B.3: Simulation output for fibre with $\xi_d = 10\%$.

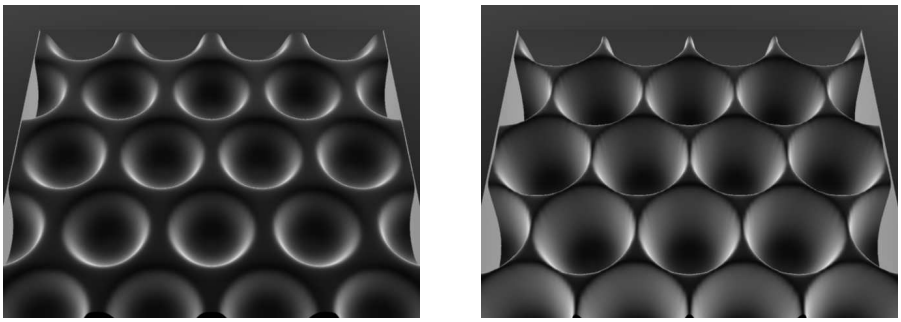

(a) 5 s

(b) 10 s

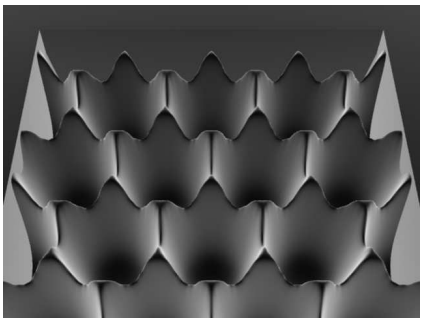

(c) 15 s

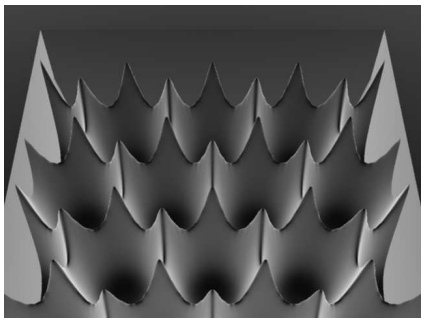

(d) 20 s

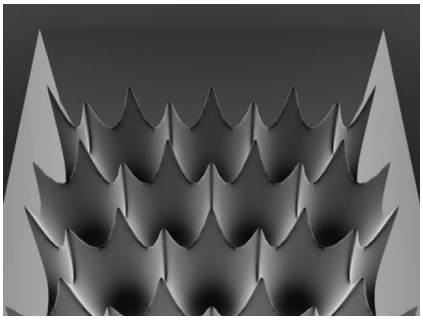

(e) 25 s

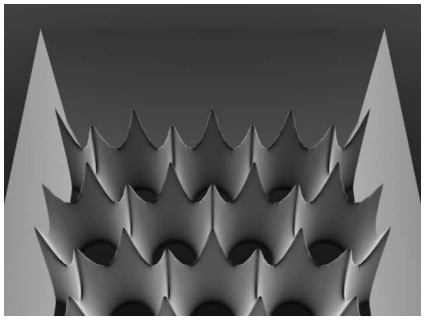

(f) 30 s

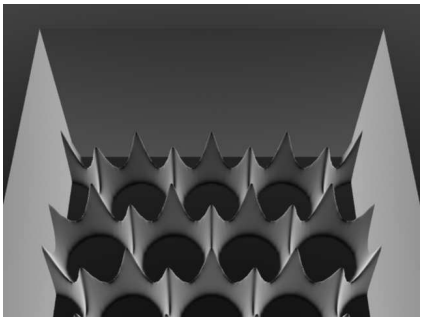

(g) 35 s

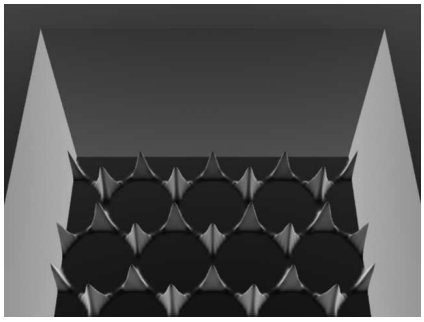

(h) 40 s

Fig. B.4: Simulation output for fibre with $\xi_d = 15\%$.

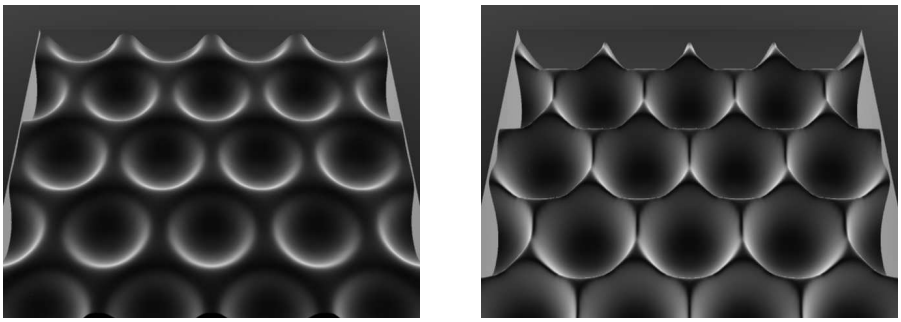

(a) 5 s

(b) 10 s

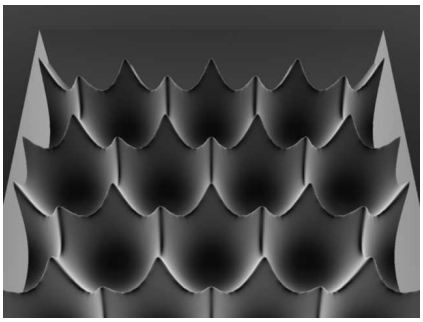

(c) 15 s

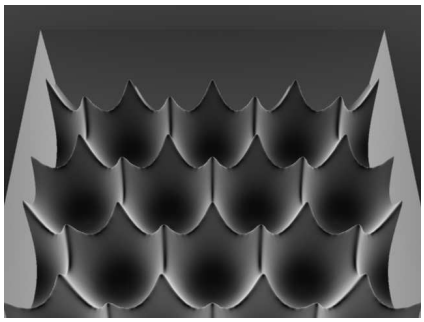

(d) 20 s

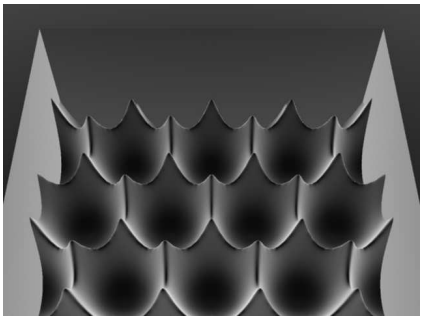

(e) 25 s

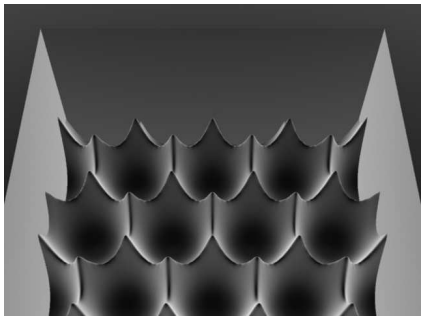

(f) 30 s

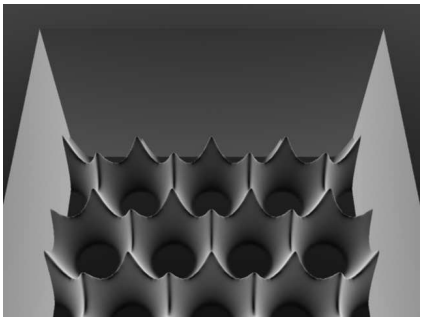

(g) 35 s

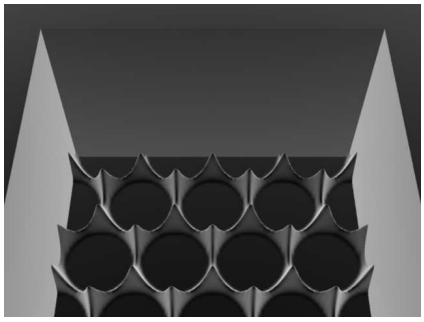

(h) 40 s

Fig. B.5: Simulation output for fibre with $\xi_d = 20\%$.

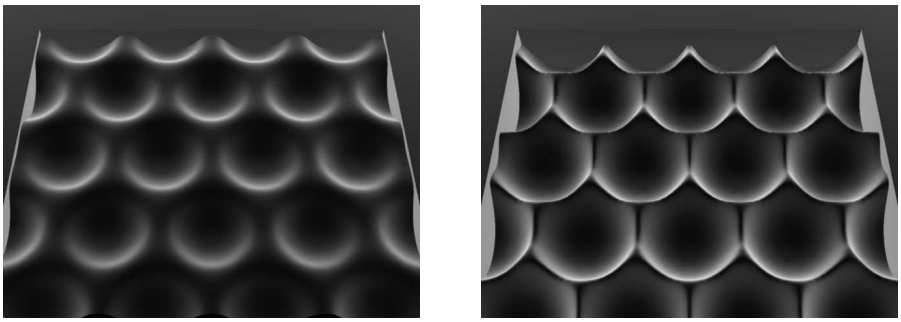

(a) 5 s

(b) 10 s

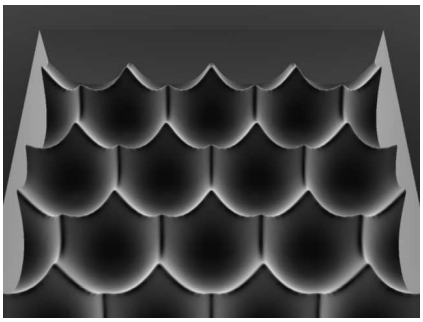

(c) 15 s

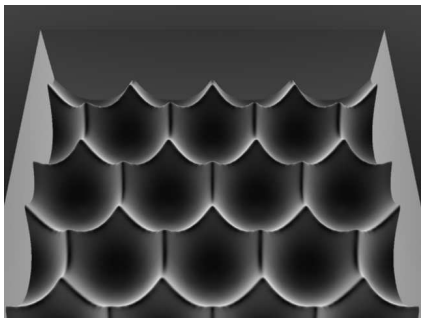

(d) 20 s

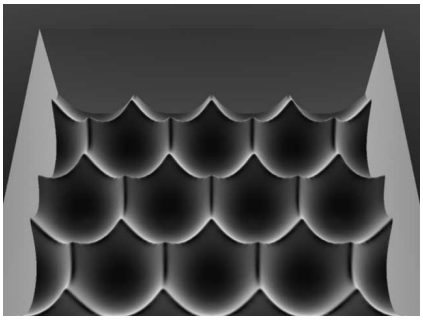

(e) 25 s

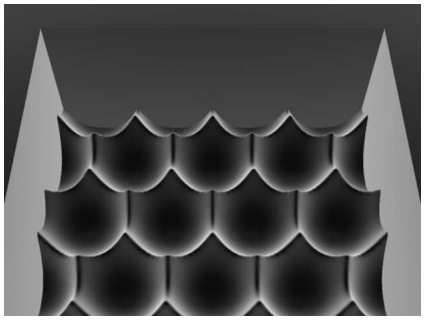

(f) 30 s

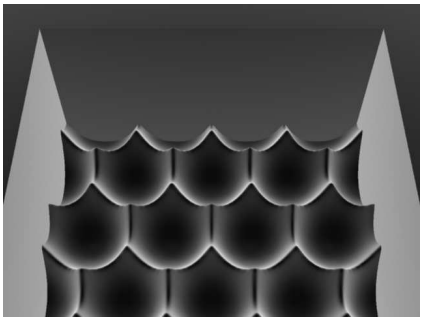

(g) 35 s

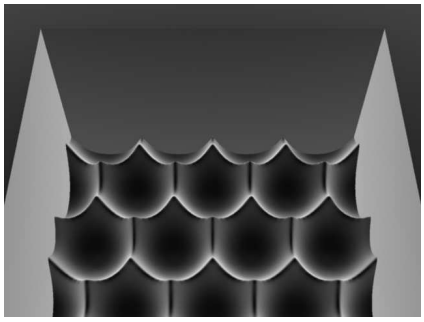

(h) 40 s

Fig. B.6: Simulation output for fibre with $\xi_d = 25\%$.

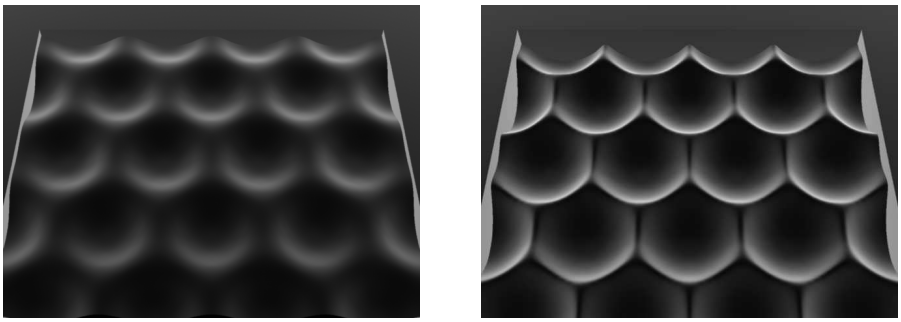

(a) 5 s

(b) 10 s

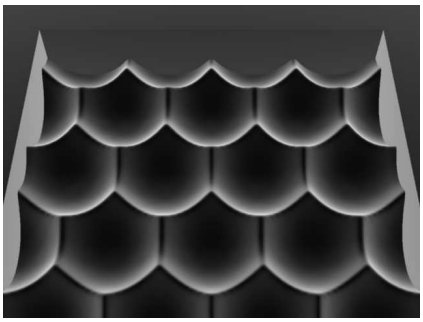

(c) 15 s

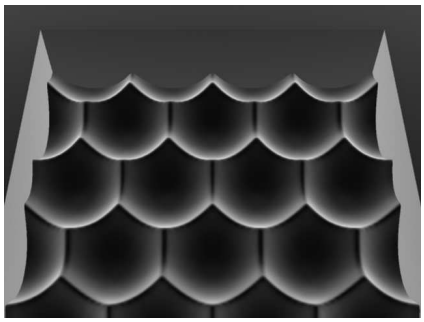

(d) 20 s

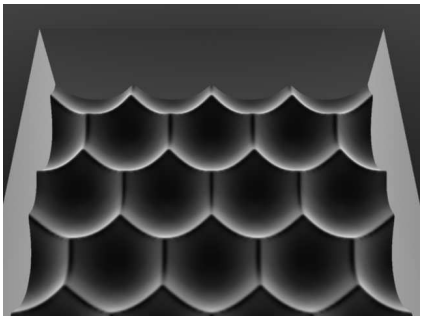

(e) 25 s

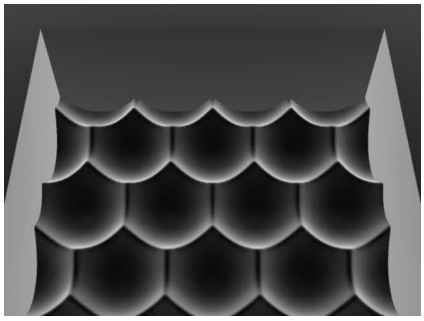

(f) 30 s

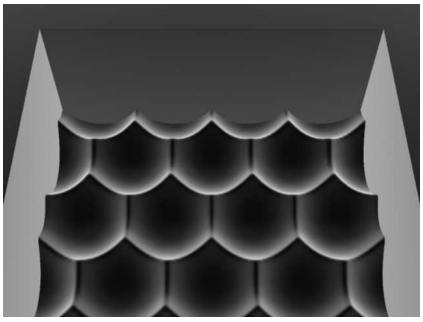

(g) 35 s

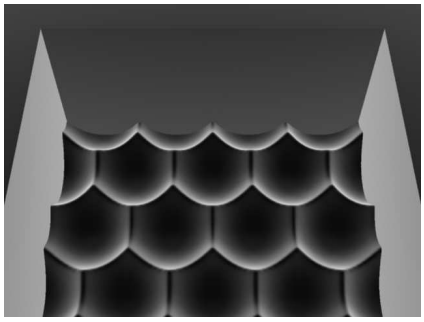

(h) 40 s

Fig. B.7: Simulation output for fibre with $\xi_d = 30\%$.

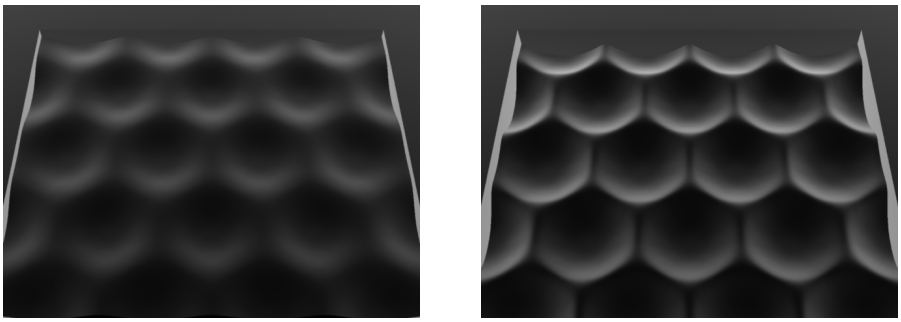

(a) 5 s

(b) 10 s

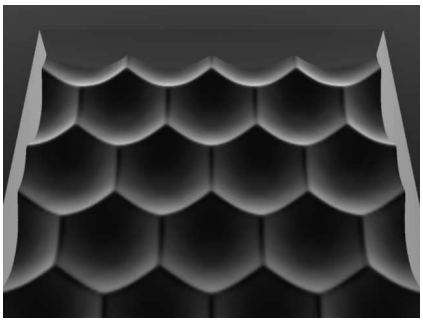

(c) 15 s

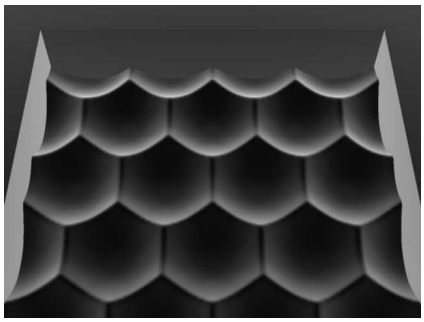

(d) 20 s

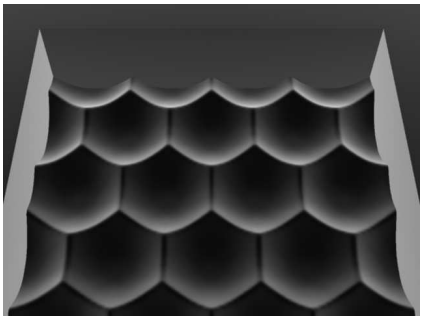

(e) 25 s

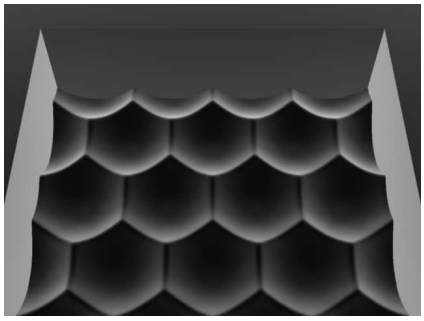

(f) 30 s

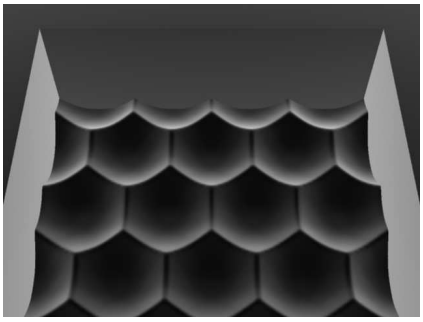

(g) 35 s

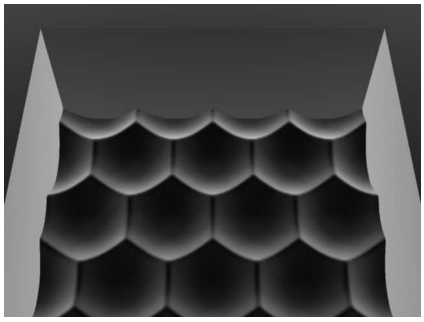

(h) 40 s

Fig. B.8: Simulation output for fibre with $\xi_d = 35\%$.

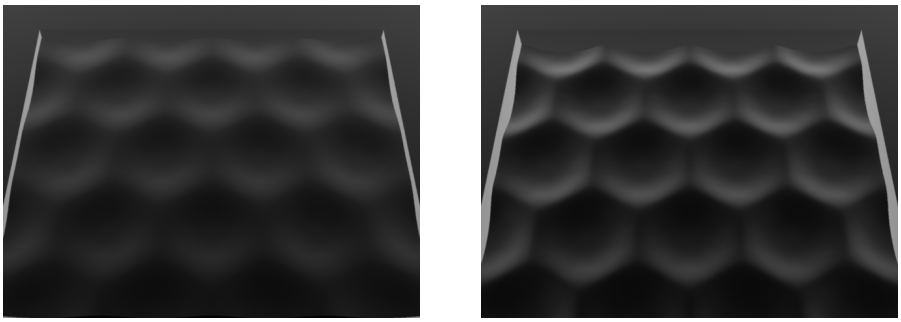

(a) 5 s

(b) 10 s

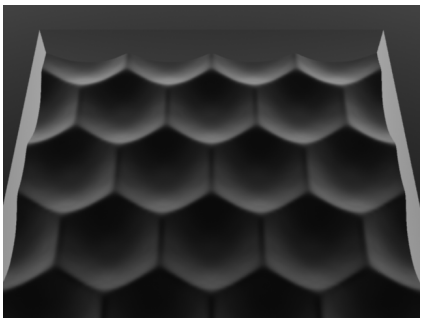

(c) 15 s

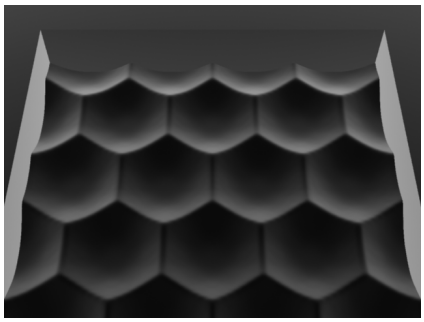

(d) 20 s

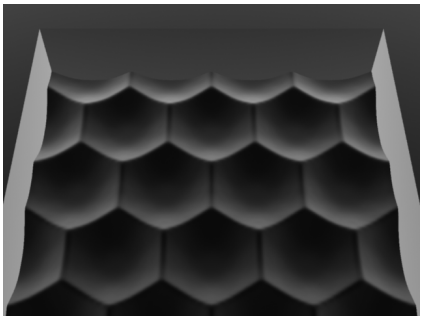

(e) 25 s

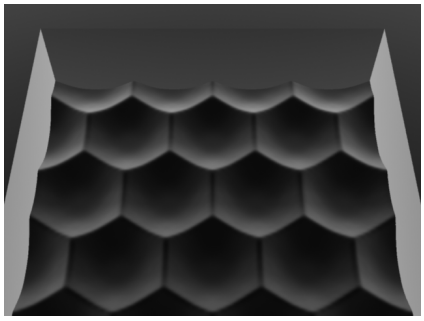

(f) 30 s

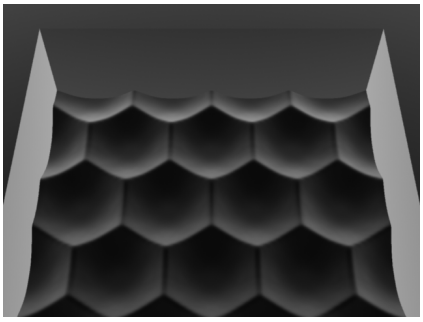

(g) 35 s

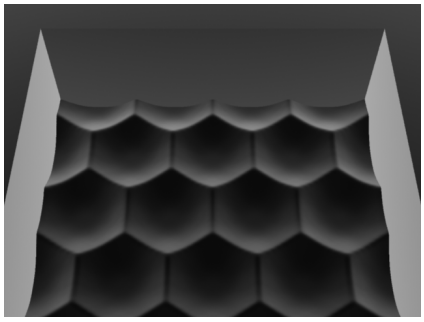

(h) 40 s

Fig. B.9: Simulation output for fibre with $\xi_d = 40\%$.

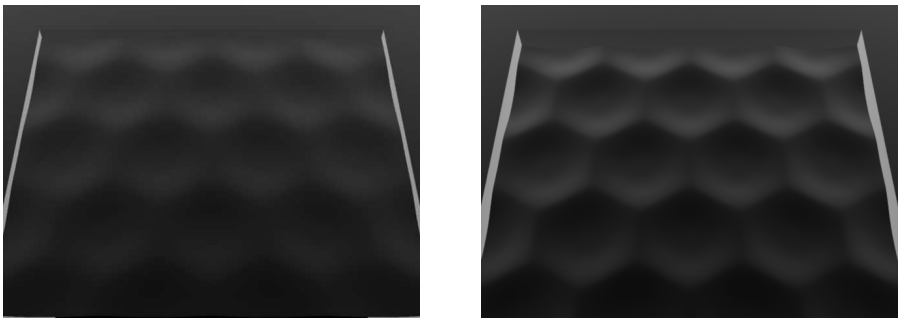

(a) 5 s

(b) 10 s

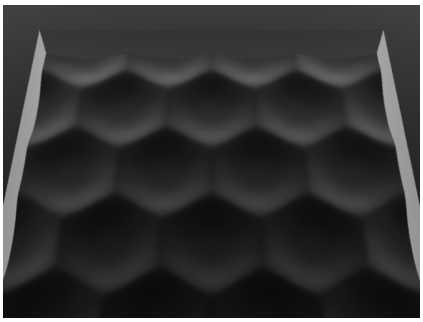

(c) 15 s

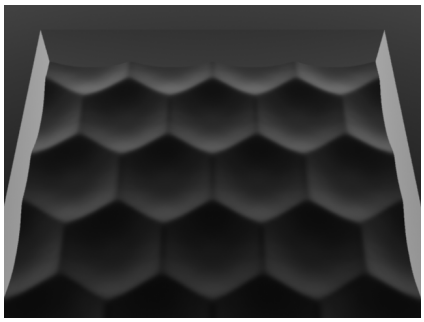

(d) 20 s

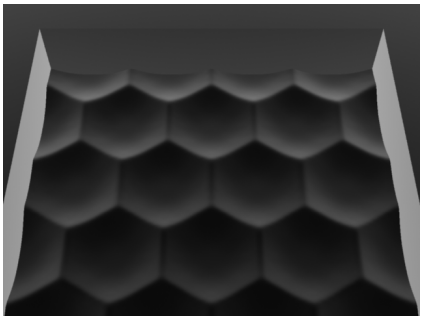

(e) 25 s

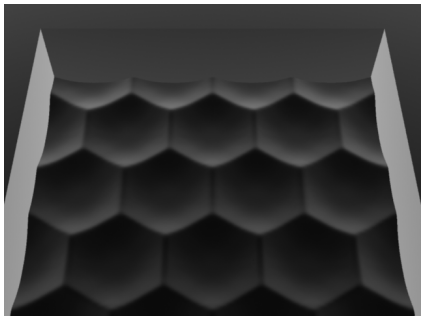

(f) 30 s

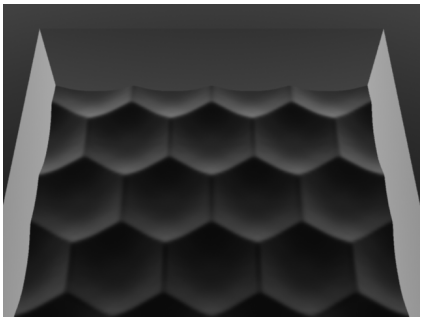

(g) 35 s

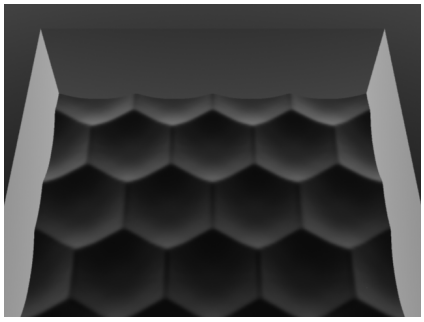

(h) 40 s

Fig. B.10: Simulation output for fibre with $\xi_d = 45\%$.

Publications

Some of the material presented in this thesis has appeared in the following publications and presentations:

D. J. White and P. R. Stoddart, *Advances in the nano-engineering of Surface-Enhanced Raman Scattering substrates*, in Nanotechnology Research: New Nanostructures and Materials, Ed. Xiaohua Huang, Nova Science Publishers, Inc. (in press)

D. J. White, A. P. Mazzolini, P. R. Stoddart, *Fabrication of a range of SERS substrates on nanostructured multicore optical fibres*, J. Raman Spec., 38, 377-382, (2007)

D. J. White and P. R. Stoddart, *Nanostructured optical fibre with surface-enhanced Raman scattering functionality*, Opt. Lett., 30 (6), 598-600 (2005)

D. J. White and P. R. Stoddart, *Nanostructured optical fibre for glucose detection by surface-enhanced Raman scattering*, presented at the Asian and Pacific Rim Symposium on Biophotonics (APBP) (2007)

D. J. White, A. P. Mazzolini, P. R. Stoddart, *Nanostructured optical fiber for miniaturized SERS probes*, presented at the International Conference on Raman Spectroscopy (ICORS) (2006)

D. J. White, A. P. Mazzolini, P. R. Stoddart, *Nanostructured optical fibre for chemical sensing using surface-enhanced Raman scattering*, presented at the Australian Conference on Optical Fibre Technology (ACOFT) (2006)

D. J. White and P. R. Stoddart, *Nanostructured optical fiber for trace chemical sensing by surface-enhanced Raman scattering*, presented at the Optical Fibre Sensors (OFS) conference (2006)

D. J. White, A. P. Mazzolini, P. R. Stoddart, *Surface-enhanced Raman scattering on nanostructured optical fibre tips*, presented at the Australasian Conference on Optics and Laser Spectroscopy (ACOLS) (2005)

D. J. White and P. R. Stoddart, *Fibre optic SERS Sensors with well defined nanoscale structures*, presented at the International Conference on Raman Spectroscopy (ICORS) (2004)

Additional Files

The attached disk contains the following directories and files:

1. Individual
→ 9 videos each 40 seconds long showing the etch progression for $\xi_d = 0\%$ to 45%

2. Combined
→ 2 video showing the etch progression for $\xi_d = 5\%$ to 45% on the one screen and real SEM images of the FIGH-30-100X fibre etching.

3. Extras
→ 3 videos of $\xi_d = 10\%$ and $\xi_d = 25\%$ showing detail of the tips

All videos are compressed using the DivX6 codec. A copy of the codec is included and may need to be installed. Alternatively, codecs and player software may be downloaded from http://www.divx.com

Note that while the videos in the last folder are made to resemble the images gathered using electron microscopes, they are not real and are entirely a product of the simulation, animation and rendering packages.

If you have any problems viewing the movies, please contact the author at dwhite@swin.edu.au